BOOK OF EXTENDED ABSTRACTS

http://lip-conference.org/

13th International Conference Series on

Laser-light and Interactions with Particles

Optical Particle Characterization follow-up !

(LIP2022)

August 21-26th, 2022,

Institute of Physics, Polish Academy of Sciences

Warsaw, Poland

Organizer

Polish Physical Society (PPS)

Sponsoring and Partnering Organizations

Polish Ministry of Science and Education

The conference is co-funded by the 'Excellent Science' programme of the Polish Ministry of Science and Education

Institute of Physics (IF-PAN) – co-organizer

European Physical Society (EPS)*

French Association for the Promotion of Laser Techniques (AFVL)

Conference Management Software (COMS Optics and Lasers)

Electromagnetic and Light Scattering by Particles Newsletter (ELS Newsletter)

Laboratory CORIA, UMR 6614, CNRS, INSA Rouen & Normandy University

Laboratory IUSTI, UMR 7343, CNRS & Aix-Marseille University

Light Scattering Information Portal for the light scattering community (SCATTPORT)

Photoniques

European Optical Society (EOS)

Optical Society of America (OSA)

* The European Physical Society will support a researcher working in Africa for attending the LIP2022 conference in the framework of the International Year of Basic Science for Sustainable Development (IYBSSD 2022).

PREFACE

This Book of Abstracts contains the extended abstracts of keynote lectures and papers which have been presented (whether locally or remotely) during the 13th International Conference on Laser-light and Interactions with Particles (LIP2022) which is an Optical Particle Characterization follow-up, held in Warsaw, Poland from August 21th to 26th. This event has been organized under the auspices of the Polish Physical Society and the Institute of Physics, Polish Academy of Sciences.

This conference series was created in Rouen, in 1987 (conveners: G. Gouesbet, G. Gréhan), under the title "Optical Particle Sizing, theory and practice (OPS)". At this time, after the successful development of laser based methods allowing one to measure the velocities of particles embedded in flows, particularly the "Laser Doppler Velocimeter", the current challenge was the extension of such methods to the simultaneous measurements of velocities and sizes of individual particles in flows. This was as well the time when a theory, named generalized Lorenz-Mie theory, was mature enough for the design of laser-based techniques interacting with particles, and for the interpretation of measured data. The conferences were intended to take place every three years.

The second OPS conference has been held in Phoenix, Arizona, USA, in 1990 (convener: D. Hirleman), followed in 1993 by Yokohama, Japan (convener: M. Maeda), Nuremberg, Germany, in 1995 (convener: F. Durst), Minneapolis, USA, in 1998 (convener: A. Naqwi). To account for the rapid developments and demands in the .eld, the title of the conference was changed to "Optical Particle Characterization (OPC)" at the occasion of the 6th edition held in Brighton, England, in 2001 (convener: A. Jones), followed by Kyoto, Japan, in 2004 (convener: M. Itoh) and by Graz, Austria, in 2007 (convener: O. Glätter). The conference returned to its roots in Rouen, France, 2012 (G. Gouesbet, G. Gréhan) where it was decided to change its title to "Laser-light and Interactions with Particles (LIP)" to take into account, once more, of the evolution of the field. Beside "Optical Particle Characterization", the new conference encompasses all light scattering theories dealing with structured light scattering (Generalized Lorenz-Mie theory, Extended Boundary Condition Method, ray optics, discrete dipole approximation and numerical techniques), mechanical effects of light, resonances. All kinds of structured beams are considered, not only Gaussian beams, but as well various kinds of laser sheets, non-di¤racting beams, helical beams, laser pulses and, due to analogies with EM scattering, acoustical scattering was welcome as well. Covered applications are many, such as to multiphase flows, aerosols and atmospheric environment sciences, biomedical optical engineering, optical levitation and manipulation of objects (particularly optical tweezers), plasma physics, etc.

Rouen conference has been followed by Marseille, France, 2014 (F.R.A. Onofri and B. Stout) and Xian, China, 2016 (Yiping Han, Lixin Guo). In 2018, the 12th LIP conference took place at the Texas A&M University, College Station, USA under the chairs of P. Yang, G. Kattawar and E. Fry jointly with the "Electromagnetic and Light Scattering by Nonspherical Particles" conference ELSXVII.

The 13th LIP-conference was scheduled to be held in Warsaw, Poland, 2020, under the local chairs of D. Jakubczyk and M. Kolwas but this edition has been made impossible due to the Covid pandemic. Although this pandemic is still active, and notwithstanding the difficulties

imposed by the global situation, including the invasion of Ukraine which has a Western border with Poland, the 13th LIP-conference has eventually been held in Warsaw, from August 21th to August 26th, 2022, in the format of a hybrid conference.

Since the Rouen conference of 2012, a special issue of the Journal of Quantitative Spectroscopy and Radiative Transfer, including at the occasion of the "no-shown" 2020 conference, has been published, with G. Gouesbet and M. Brunel as guest editors in 2012 (see volume 126 of the journal), afterward with G. Gouesbet and F.R.A. Onofri as guest editors (see volumes 162 and 195 of the journal) for the 2014 and 2016 editions. These special issues, up to the 2016 conference included, have been published in a single volume. Since the 2018 edition included, papers associated with the LIP-conferences (based on the topics discussed, but not necessarily presented during the conference) have been published in virtual topical issues, the word "virtual" meaning that the papers have been published once they have been accepted, without having to wait for the rest of the manuscripts being reviewed/accepted. The virtual special issue of the Warsaw 2022 conference is currently under progress [1]

Finally, we would like to take the opportunity of this preface to express our thanks to those who contributed to the organization of the conference, in particular for the assistance of the Scientific and Advisory committees (see [2]), and of the local organizing committee (Anastasiya Derkachova, Gennadiy Derkachov, Krystyna Kolwas, Sławomir Palesa, Yaroslav Shopa, Jacek Szczepkowski, Mariusz Woźniak) whose work has been made more difficult by the current circumstances, and still more particularly to the participants (whether they were locally present or remotely connected) which are essential to the success of any conference. We also address all our thanks to the sponsors, the Polish Physical Society, the Polish Ministry of Education and Science ("Excellent Science" program), the French National Center for Scientific Research and the European Physical Society, without whom the organization would not have been possible. Our thanks go also to the partners of this conference who contributed to the outreach of this conference: AFVL, COMS Optics and Lasers, ELS Newsletter, SCATTPORT, EOS and OSA [2].

For the organizing committee, Warsaw Poland August 21st 2022,

Gérard Gouesbet, Fabrice Onofri, Daniel Jakubczyk, Maciej Kolwas (co-chair).

[1] Forthcoming topical issue "Laser-light and Interactions with Particles 2022, JQSRT, 2022, https://www.journals.elsevier.com/journal-of-quantitative-spectroscopy-and-radiative-transfer/forthcoming-special-issues

[2] Committees, sponsors & partners, LIP2022, http://lip-conference.org/.

Scientific Committee

Z.S. WU
SCHOOL OF SCIENCE, XIDIAN UNIVERSITY, XIDIAN, CHINA
wuzhs@mail.xidian.edu.cn - https://en.xidian.edu.cn/info/1043/1247.htm

ADVISORY COMMITTEE

Y. AIZU
MURORAN INSTITUTE OF TECHNOLOGY, MURORAN, JAPAN
aizu@mmm.muroran-it.ac.jp - http://rd-soran.muroran-it.ac.jp/profile/...
L. A. AMBROSIO
UNIVERSITY OF SAO PAULO, USP, BRAZIL
leo@sc.usp.br - http://www.sel.eesc.usp.br/leonardo/
M. BRUNEL
LASER/PARTICLE(S) INTERACTION, CORIA, NORMANDY UNIVERSITY, ROUEN, FRANCE
marc.brunel@coria.fr - http://www.coria.fr/spip.php?auteur8&ong=739&lang=en
R. CHAKRABARTY
DIVISION OF ATMOSPHERIC SCIENCES - DESERT RESEARCH INSTITUTE, RENO, USA
rajan.chakrabarty@dri.edu - http://www.dri.edu/rajan-chakrabarty
L. TSANG
DEPT. ELECTR. ENG. AND COMPUTER SCI., UNIVERSITY OF MICHIGAN, MI, USA
leutsang@umich.edu - https://web.eecs.umich.edu/~leutsang/
Y.E. GEINTS
ZUEV INSTITUTE OF ATMOSPHERIC OPTICS, RAS, TOMSK, RUSSIA
ygeints@iao.ru - http://www.iao.ru/en/home/
D. GRIER
DEPARTMENT OF PHYSICS AND CENTER FOR SOFT MATTER RESEARCH, NEW-YORK UNIVERSITY, NEW-YORK, USA
david.grier@nyu.edu - http://physics.nyu.edu/grierlab/home.html
S. HANNA
NANOPHYSICS AND SOFT MATTER, UNIVERSITY OF BRISTOL, BRISTOL, UK
S.Hanna@bristol.ac.uk - http://www.bristol.ac.uk/~/simon-hanna/overview.html
M. KOLWAS
INSTITUT OF PHYSICS, POLISH ACADEMY OF SCIENCES, WARSAW, POLAND
Maciej.Kolwas@ifpan.edu.pl - http://www.ifpan.edu.pl/ON-2/on22/staff/kolwas.html
F. LEMOINE
SPRAY COMBUSTION AND OPTICAL DIAGNOSTICS, LEMTA, UNIVERSITY OF LORRAINE, NANCY, FRANCE
fabrice.lemoine@ensem.inpl-nancy.fr - https://www.researchgate.net/profile/F-Lemoine
F. G. MITRI
CHEVRON, AREA 52 TECHNOLOGY, SANTA FE, NM, USA
fmitri@gmail.com - http://fmitri.wix.com/mitri
A.A.R. NEVES
FEDERAL UNIVERSITY OF ABC, SANTO ANDRÉ, BRAZIL
antonio.neves@ufabc.edu.br - http://www.ufabc.edu.br/
T. NIEMINEN
DEPT. OF PHYSICS, UNIVERSITY OF QUEENSLAND, BRISBANE, AUSTRALIA
timo@physics.uq.edu.au - http://www.physics.uq.edu.au/people/nieminen/

B. POULIGNY
CRPP, NATIONAL CENTER FOR SCIENTIFIC RESEARCH, PESSAC, FRANCE
pouligny@crpp-bordeaux.cnrs.fr - http://www.crpp-bordeaux.cnrs.fr/
H.-H. QIU
DEPT. MECH. ENGINEERING, HONG KONG UNIVERSITY OF SCIENCE & TECHNOLOGY, KOWLOON, HONG KONG
meqiu@ust.hk - https://www.mae.ust.hk/~meqiu/index3.html
K-F. REN
LASER SOURCES AND DENSE MEDIA DIAGNOSTICS, CORIA, NORMANDY UNIVERSITY, ROUEN, FRANCE
fang.ren@coria.fr - http://www.coria.fr/spip.php?auteur970&lang=en
N. ROTH
INSTITUTE OF AEROSPACE THERMODYNAMICS, STUTTGART UNIVERSITY, STUTTGART, GERMANY
Norbert.Roth@itlr.uni-stuttgart.de - https://www.project.uni-stuttgart.de/dropit/team_and_institutes/team/Roth-00015/
M. ŠILER
INSTITUTE OF SCIENTIFIC INSTRUMENTS OF THE ASCR, BRNO, CZECH REPUBLIC
siler@isibrno.cz - https://www.isibrno.cz/en/mgr-martin-siler-phd
A.M.K.P. TAYLOR
DEPARTMENT OF MECHANICAL ENGINEERING, IMPERIAL COLLEGE, LONDON, UK
a.m.taylor@imperial.ac.uk - http://www3.imperial.ac.uk/people/a.m.taylor
X.M. SUN
SCHOOL OF ELECTRICAL AND ELECTRONIC ENGINEERING, SHANDONG UNIVERSITY OF TECHNOLOGY, ZIBO, CHINA,
xmsun@mail.xidian.edu.cn - http://www.sdut.edu.cn/en/Colleges.htm
M.R. VETRANO
DEPARTMENT OF MECHANICAL ENGINEERING, KU LEUVEN, LEUVEN, BELGIUM,
rosaria.vetrano@kuleuven.be - https://www.kuleuven.be/wieiswie/en/person/00112909
J. J. WANG
SCHOOL OF SCIENCE, XIDIAN UNIVERSITY, XI'AN, CHINA
wangjiajie@xidian.edu.cn - https://en.xidian.edu.cn/info/1018/1092.htm
S. WILL
FRIEDRICH-ALEXANDER-UNIVERSITÄT, ERLANGEN-NÜRNBERG, LTT, ERLANGEN, GERMANY
stefan.will@fau.de - https://www.ltt.tf.fau.eu/person/stefan-will/
F. XU
THE UNIVERSITY OF OKLAHOMA NATIONAL WEATHER CENTER, NORMAN, USA
fengxu@ou.edu - http://meteorology.ou.edu/member/feng-xu/
R. XU
MICROMERITICS INSTRUMENT CORP., SHANGHAI, CHINA
Ren.Xu@micromeritics.com - http://www.micromeritics.com/...
M. YURKIN
VOEVODSKY INST. OF CHEM. KINETICS AND COMB., NOVOSIBIRSK, RUSSIA
yurkin@gmail.com - http://www.kinetics.nsc.ru/CMS/index.php?id=392

ORGANIZING COMMITTEE & LOCAL ORGANIZATION

D. JAKUBCZYK (CO-CHAIR), IP-PAS, WARSAW, POLAND
M. KOLWAS (CO-CHAIR), IP-PAS, WARSAW, POLAND
F. ONOFRI, IUSTI, CNRS, MARSEILLE, FRANCE
G. GOUESBET, CORIA, INSA DE ROUEN,SAINT-ETIENNE DU ROUVRAY, FRANCE
A. DERKACHOVA, IP-PAS, WARSAW, POLAND
G. DERKACHOV, IP-PAS, WARSAW, POLAND
K. KOLWAS, IP-PAS, WARSAW, POLAND
S. PALESA, IP-PAS, WARSAW, POLAND
Y. SHOPA, CARDINAL STEFAN WYSZYŃSKI UNIVERSITY IN WARSAW, POLAND
M. WOZNIAK, PIT-RADWAR S.A., WARSAW, POLAND

Conference secretariat:

Dr A. DERKACHOVA - Institute of Physics Al. Lotnikow 32/46 02-668 Warsaw, Poland Ph: (+48) 22 116-32-77 mobile: (+48) 514-628-350,
Dr M. WOZNIAK - PIT-RADWAR S.A. Poligonowa 30, 04-051 Warsaw, Poland tel.: (+48) 22 540 22 00 mobile: (+48) 693-087-455
email: contact@lip-conference.org

List of Contents

Keynote Lectures

Beam Shape Description and Effects

Droplets

SUSPENSIONS

FORCES & PROPERTIES

FORCES & TRAPPING

BEAMS & SURFACES

MISCELLANEOUS

AEROSOLS

BIOMEDIA

PLASMONICS & NANOPARTICLES

KEYNOTE LECTURES

13th International Conference Series on
Laser-light and Interactions with Particles
Optical Particle Characterization follow-up !
August 21-26th, 2022, Warsaw, Poland

STRUCTURED FIELDS CONSTRUCTED FROM SUPERPOSITIONS OF NONDIFFRACTING BEAMS

Leonardo André AMBROSIO

[1] Department of Electrical and Computer Engineering. São Carlos School of Engineering, University of São Paulo. 400 Trabalhador são-carlense Ave. 13566-590, São Carlos, SP, Brazil.

leo@sc.usp.br

Abstract

In this talk a new technique for creating linear, superficial or volumetric nondiffracting beams and pulses is presented. Such beams and pulses are called Frozen Waves (FWs) and can be constructed from discrete or continuous superpositions of arbitrary-order Bessel beams, allowing both the theoretician and the experimentalist to conceive, design and produce arbitrary-shaped, diffractionless and even dispersion-free structured light fields along lines, surfaces and volumes, even in lossy and dispersive media.

1 Frozen Waves

In microwaves, optics and photonics, it is usually desired or required to confine or structure light at different spatial scales. Specifications on the practical application envisioned might demand a significant set of requirements such as loss compensation, distortion minimization, reduction of scattered fields, maximization of transmitted fields and so on. Also of importance, overcoming diffraction is of utmost importance in a wide range of problems in physics and engineering, such as in free space communication, remote sensing, optical alignment, atom guiding, optical nanochannel fabrication, optical manipulation in optical tweezers systems and volumetric displays, to mention a few.

Perhaps the two most notable examples of non-diffracting electromagnetic waves are the uniform plane wave and Bessel beams. Mathematically, the former emerges from the vector wave equation when the method of separation of variables is introduced using a Cartesian coordinate system, while the latter is derived in an analogous fashion, but using a cylindrical coordinate system. By "non-diffracting" it is usually meant "that can overcome diffraction".

Physically-realizable versions of Bessel beams, as first demonstrated by Durnin, Miceli Jr. and Eberly, can only resist to the natural spatial widening imposed by diffraction up to a certain distance [1]. This reflects the limited power availability or, in other words, the lack of an infinite amount of energy to recompose the transverse field profile indefinitely along propagation [1-3]. Therefore, truncated apertures can only produce pseudo nondiffracting beams.

Resistance to diffraction implies propagation invariance, so Bessel beams have expected properties such as depth of focus and self-healing [4]. Advantageously as it may seem in several applications – e.g., in optical trapping systems in allowing for simultaneous traps at multiple planes [5,6] – it must be recognized that the longitudinal field pattern of Bessel beams lacks flexibility in the sense of, just like other diffracting and nondiffracting beams, not allowing for an immediate structuring of its intensity. It would certainly be useful that, while still preserving their nondiffracting properties, Bessel beams could be used as building blocks for new exciting structured light beams.

In this talk, I shall explore a particular class of structured nondiffracting beams called *Frozen Waves* (FW). Such beams are constructed from superpositions of Bessel beams of arbitrary order and, although first theoretically presented in 2004 by Zamboni-Rached [7], they have only recently been experimentally explored in practical applications [8-10].

Like Bessel beams, FWs are solutions to either the scalar or the vector wave equation in cylindrical coordinates. Historically, they were first investigated for lossless simple media in terms of a discrete superposition of co-linear, co-propagating zeroth order scalar Bessel beams [7], all with the same operating frequency but carrying distinct longitudinal (or, alternatively, transverse) wave numbers. This means that each Bessel beam in the superposition has its own half-cone (or axicon) angle. By suitably weighting their amplitude and phase, it is permissible to expect that the resulting field can be adjusted to achieve any desired longitudinal intensity pattern, at least within the diffraction limit.

Today, the name *Frozen Wave* is recognized as designating a whole family of structured light fields not only constructed from scalar but from vector Bessel beams as well. Also, theoretical extensions to arbitrary-order FWs soon appeared, with new variants incorporating attenuation-resistant properties for propagation along lossy simple media. Dispersion-free versions of FWs known as "Diffraction-Dispersion-Attenuation Resistant Vortex Pulses" were proposed for propagation along absorbing media. Multichromatic FWs came as a generalization of the concept of monochromatic FWs envisioning wavelength and topological charge management along the axis of propagation. Generalizations for superpositions of FWs of different orders, or for a single FW composed of Bessel

beams of different orders revealed the potential of such optical fields as alternative beams for atom guiding and optical trapping, and propagation along stratified media has been investigated. Proposals of finite-energy FWs designed from *continuous* superpositions of Bessel beams were presented. Descriptions of specific types of FWs have been given in terms of beam shape coefficients in the framework of the Generalized Lorenz-Mie theory (GLMT). From a theoretical and computational point of view, investigations on FWs have significantly developed during the past eighteen years [11-22].

The first experimental demonstration and generation of a FW was realized by Vieira and coworkers in 2012 by having recourse to a holographic setup for the reconstruction of computer-generated holograms [23]. However, it was not until 2020 when the first practical use of FWs was proposed by Suarez *et al.* in optical trapping and manipulation of microparticles from non-thermal (scattering and gradient) forces [8]. The ability of FWs to hold and move small particles was firmly demonstrated.

In 2018, Ambrosio proposed a theoretical extension of the concept of a FW that allows modelling or structuring light on a plane in a lossless medium, subsequently extended to lossy media [24,25]. To do so, parallel co-propagating FWs are superposed in space, with their longitudinal patterns adjusted so as to form a two-dimensional intensity pattern that can be chosen *a priori*. The difference from other techniques available for the generation of two-dimensional field patterns is that the intended profile lies on a plane that includes the axis of propagation and, up to certain limits, the self-healing property of Bessel beams can still be used with advantage.

A few months ago, a successful demonstration of the experimental demonstration of two-dimensional FWs was presented envisioning application in three-dimensional holography [9,10]. Two-dimensional FWs or, alternatively, *holographic light sheets* [10], now represents a new approach to holographic projection beyond, e.g., Fourier and Fresnel holography. It is also expected that FWs will find room in 2D and 3D imaging and printing, micromachining techniques for optical nanochannel fabrication and volumetric displays, among others. Recently, the first theoretical predictions on the asymmetry factor in photophoresis with FWs has been made [26]. This represents a first step towards the analysis of optical forces from thermal origins (photophoretic forces) exerted by FWs, envisioning the incorporation of such optical wave fields in the trapping system of volumetric photophoretic-trap displays [27]. I intend to discuss more on FWs and their applications and tentatively provide an updated but otherwise non-exhaustive list of references for those interested in the subject during the lecture.

2 Acknowledgement

The author thanks the National Council for Scientific and Technological Development (CNPq) (426990/2018-8, 309201/2021-7) for supporting this work.

3 References

[1] Durnin J., Miceli Jr. J. J., Eberly J. H., Diffraction-free beams, Phys. Rev. Lett. 58(15):1499–1501 (1987).

[2] Durnin J., Exact solutions for nondiffracting beams. I. The scalar theory, J. Opt. Soc. Am. A 4(4):651–654 (1987).

[3] Durnin J., Miceli J. J., Eberly J. H., Comparison of Bessel and Gaussian beams, Opt. Lett. 13(2):79–80 (1988).

[4] McGloin D., Dholakia K., Bessel beams: Diffraction in a new light, Contemporary Phys. 46(1):15-28 (2010).

[5] Arlt J., Garcés-Chávez V., Sibbett W., Dholakia K., Optical micromanipulation using a Bessel light beam, Opt. Commun. 197(4-6):239–245 (2001).

[6] Garcés-Chávez V., McGloin D., Melville H., Sibbett W., Dholakia K., Simultaneous micromanipulation in multiple planes using a self-reconstructing light beam, Nature 419:145–147 (2002).

[7] Zamboni-Rached M., Stationary optical wave fields with arbitrary longitudinal shape by superposing equal frequency Bessel beams: Frozen Waves, Opt. Express, 12(17):4001–4006 (2004).

[8] Suarez R. A. B., Ambrosio L. A., Neves A. A. R., Zamboni-Rached M., Gesualdi M. R. R., Experimental optical trapping with frozen waves, Opt. Lett. 45(9):2514-2517 (2020).

[9] Dorrah A. H., Bordoloi P., Angelis V. S., Sarro J. O., Zamboni-Rached M., Ambrosio L. A., Capasso F., Longitudinally Structured Light Sheets for 3D Holography, CLEO Conference, paper FM2H.2, 07-12 May, San Jose, California, USA, 2022.

[10] Dorrah A. H., Bordoloi P., Angelis V. S., Sarro J. O., Zamboni-Rached M., Ambrosio L. A., Capasso F., Towards three-dimensional holography with longitudinally structured light sheets, submitted to Nature Photonics, 2022.

[11] Zamboni-Rached M., Recami E., Hernández-Figueroa H. E., Theory of "frozen waves": modeling the shape of stationary wave fields. J. Opt. Soc. Am. A 22(11):2465–2475 (2005).

[12] Zamboni-Rached M., Ambrosio L. A., Hernández-Figueroa H. E., Diffraction–attenuation resistant beams: their higher-order versions and finite-aperture generations, Appl. Opt. 49(30):5861-5869 (2010).

[13] Zamboni-Rached, Mojahedi M., Fusion Between Frozen-Wave-Type Beams and Airy-Type Pulses: Diffraction-Dispersion-Attenuation Resistant Vortex Pulses in Absorbing Media, arXiv:1809.08740 (2018).

[14] Dorrah A. H., Zamboni-Rached M., Mojahedi M., Wavelength and topological charge management along the axis of propagation of multichromatic non-diffracting beams, J. Opt. Soc. Am. B 36(7):1867-1872 (2019).

[15] Pachon E. G. P., Zamboni-Rached M., Dorrah A. H., Mojahedi M., Gesualdi M. R. R., Cabrera G. G., Architecting new diffraction-resistant light structures and their possible applications in atom guidance, Opt. Express 24(22):25403-25408 (2016).

[16] Ambrosio L. A., Circularly symmetric frozen waves: Vector approach for light scattering calculations, J. Quant. Spectrosc. Radiat. Transfer 204: 112-119 (2018).

[17] Lourenço-Vittorino G. A., Zamboni-Rached M., Modeling the longitudinal intensity pattern of diffraction resistant beams in stratified media, Appl. Opt. 57(20):5643-5651 (2018).

[18] Zamboni-Rached M., Ambrosio L. A., Dorrah A. H., Mojahedi M., Structuring light under different polarization states within micrometer domains: exact analysis from the Maxwell equations, Opt. Express 25(9):10051-10056 (2017).

[19] Ambrosio L. A., Zamboni-Rached, Optical forces experienced by arbitrary-sized spherical scatterers from superpositions of equal-frequency Bessel beams, J. Opt. Soc. Am. B 32(5):B37-B46 (2015).

[20] Ambrosio L. A., Zamboni-Rached M., Gouesbet G., Discrete vector frozen waves in generalized Lorenz–Mie theory: linear, azimuthal, and radial polarizations, Appl. Opt. 57(12):3293-3300 (2018).

[21] Ambrosio L. A., Zamboni-Rached M., Gouesbet G., Zeroth-order continuous vector frozen waves for light scattering: exact multipole expansion in the generalized Lorenz–Mie theory, J. Opt. Soc. Am. B 36(1):81-89 (2019).

[22] Ambrosio L. A., Votto L. F. M., Gouesbet G., Wang J., Assessing the validity of the localized approximation for discrete superpositions of Bessel beams, J. Opt. Soc. Am. B 35(11):2690-2698 (2018).

[23] Vieira T. A., Gesualdi M. R. R., Zamboni-Rached M., Frozen waves: experimental Generation, Opt. Lett. 37(11):2034-2036 (2012).

[24] Ambrosio L. A., Millimeter-structured nondiffracting surface beams, J. Opt. Soc. Am. B 36(3):638-645 (2019).

[25] Sarro J. O., Ambrosio L. A., Surface beams resistant to diffraction and attenuation and structured at the millimeter scale, J. Opt. Soc. Am. B 38(3):677-684 (2021).

[26] Maia A. V. A., Rocha B. H. D, Ambrosio L. A., Photophoretic Asymmetry Factor of On-Axis Non-Diffracting Frozen Waves and Dielectric Micro-Spheres, to be presented at Latin America Optics and Photonics (LAOP/Optica), 7-11 August, Recife, Brazil, 2022.

EXHALED SALIVA DROPLETS AND AEROSOLS MEASURED IN TIME AND 3D SPACE: QUANTIFICATION OF SARS-COV-2 FLOW RATES

Edouard BERROCAL

**Corresponding author: edouard.berrocal@forbrf.lth.se*

Abstract

Understanding the airborne transmission of pathogens, such as SARS-CoV-2, requires accurate measurements of the exhaled particles. This presentation describes how the size and velocity of the ejected saliva droplets and aerosols can be measured near the mouth. These measurements have been applied when speaking and coughing. The tracking of each detected particle has been achieved in 3D at 15 000 images per seconds. The sizing of the particles has been reached using laser light scattering detected in the semi-forward direction. The evaporation of water content in the particles is analyzed to deduce the transition from saliva droplets to solid aerosols. Using the measured volume of the particles ejected over time, together with a concentration of SARS-CoV-2 in saliva, an estimation of the flow rate emission of virions has been deduced.

13th International Conference Series on
Laser-light and Interactions with Particles
Optical Particle Characterization follow-up !
August 21-26th, 2022, Warsaw, Poland

HOLOGRAPHIC PARTICLE CHARACTERIZATION: UNVEILING THE COMPOSITION AND DYNAMICS OF COLLOIDAL DISPERSIONS WITH HOLOGRAPHIC VIDEO MICROSCOPY

David G. GRIER[1,*], Lauren E. ALTMAN[1], Kaitlynn SNYDER[1] and Rushna QUDDUS[2]

[1] Department of Physics and Center for Soft Matter Research, New York University, New York, NY 10003, USA
[2] Department of Chemistry, New York University, New York, NY 10003, USA

Corresponding author: david.grier@nyu.edu

Abstract

Holograms of colloidal particles recorded with in-line holographic video microscopy encode detailed information on each particle's three-dimension position, size, shape, orientation and composition. Extracting that information is an example of a highly nonlinear inverse problem whose solution has been sought with generative models based on the generalized Lorenz-Mie theory of light scattering [1–3]. Real-time implementations of Lorenz-Mie analysis yield the position, size and refractive index of individual colloidal spheres with extraordinary precision [4]. The same approach can be applied to more general types of particles through Maxwell Garnett effective-medium theory [5–7]. This wealth of information has immediate applications in areas as diverse as soft condensed matter physics, physical chemistry, biopharmaceutical manufacturing and medical diagnostics. These applications are being further accelerated through the recent development of machine-learning implementations [8] that also cast new light on the Lorenz-Mie framework.

1 Holographic Particle Characterization

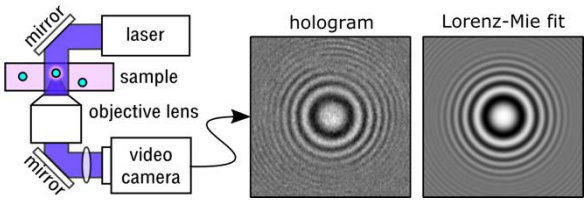

Figure 1 *An in-line holographic microscope illuminates a colloidal sample with a collimated laser beam. The interference pattern formed by the scattered and incident waves is magnified by a microscope and recorded with a video camera. Fitting to predictions of Lorenz-Mie theory yields tracking and characterization data.*

Figure 1 illustrates the deceptively simple principle of holographic particle characterization. Colloidal particles dispersed in a fluid sample are illuminated by a collimated laser beam. The light they scatter interferes with the rest of the beam in the focal plane of a microscope. The intensity of the magnified interference pattern is recorded with a video camera and is interpreted by quantitative comparison with a generative model for the image-formation process.

1.1 Lorenz-Mie Analysis

If the incident light is modelled as a unit-intensity plane wave propagating along $\hat{z}$ and linearly polarized along $\hat{x}$, the hologram of a particle at $\mathbf{r}_p$ has the form [4]

$$b(\mathbf{r}) = \left|\hat{x} + e^{-ikz_p}\,\mathbf{f}_s\left(k(\mathbf{r}-\mathbf{r}_p)\right)\right|^2 \qquad (1)$$

where k is the wavenumber of light in the medium and $\mathbf{f}_s(k\mathbf{r})$ is the Lorenz-Mie scattering function describing the particle's scattering properties. Lengths in Eq. (1) are scaled by the magnification of the microscope. Experimentally recorded holograms can be cast into this form by subtracting the dark count of the camera and then normalizing by a background image. For an isotropic homogeneous sphere, the scattering function is parameterized by the diameter, d_p, and the refractive index, n_p. A fit, such of the example in Fig. 1, is obtained by optimizing five parameters: $\mathbf{r}_p$, d_p, and n_p.

A well-converged fit typically yields the position of a micrometre-scale colloidal sphere with nanometre-scale precision over a range of more than 100 μm, and also resolves the diameter with nanometer precision and the refractive index to within a part per thousand [9]. The performance has been reported for particles ranging in diameter from 500 nm to 20 μm dispersed at concentrations from 10^3 particles/mL to 10^7 particles/mL. Optimized software implementations can analyse a single sphere's hologram in a few milliseconds, permitting real-time analysis of large populations of particles. As a particle-resolved measurement technique, furthermore, holographic particle characterization is uniquely able to identify and differentiate multiple classes of particles in heterogeneous dispersions.

1.2 Generalized Lorenz-Mie Analysis

The generative model in Eq. (1) can be extended to accommodate more general types of particles, such as core-shell spheres and aggregates of nanoparticles [10, 11]. These generalizations, however, increase the dimensionality of the inverse problem and greatly increase the time and computational power required to find solutions [12]. Additional amplitude and phase factors can be incorporated into the image-formation model to account for aberrations and other defects in the imaging systems. Still more sophisticated generative models based on the Debye-Wolf integral formalism can be used to more fully account for spatially varying phase delays and polarization rotation in

the imaging system [13, 14]. Such elaborations have been used successfully to measure colloidal interactions and to track the motions of colloidal clusters.

1.3 Effective-Sphere Analysis

Holograms of general particles also can be analysed with the computationally efficient generative model for homogeneous spheres. The estimated values of d_p and n_p then reflect properties of an effective sphere that encloses all of the phases that make up the actual particle. These effective-sphere parameters can offer insights into the particle's actual properties.

A porous particle, for example, includes a matrix composed of a material of refractive index n_0 that fills a fraction, ϕ, of its volume and also the fluid medium with refractive index n_m that fills the rest of the volume. Provided the pores are smaller than the wavelength of light, the measured refractive index is given by Maxwell Garnett effective-medium theory as [7]

$$n_{\mathrm{P}} = n_m \sqrt{\frac{1+2\phi\, L(m_0)}{1-\phi\, L(m_0)}}, \qquad (2)$$

where

$$L(m) = \frac{m-1}{m+2} \qquad (3)$$

is the Lorentz-Lorenz function and $m_0 = n_0/n_m$. This model has proved effective for monitoring molecules infiltrating nanoporous colloidal spheres [7] and for measuring the fractal dimensions of nanoparticle agglomerates [15, 16] and protein aggregates [17].

While effective-sphere analysis lacks the rigor of a detailed model for light-scattering by a structured particle, its speed and generality create opportunities for practical applications.

1.4 Machine-Learning Implementation

Holographic particle characterization involves challenging image-analysis problems that can be addressed effectively with machine-learning techniques. Figure 2 schematically presents an end-to-end implementation [8]. The analytical pipeline takes as its input a normalized hologram containing an unknown number of features associated with colloidal scatterers. The first stage uses a convolutional neural network [18] to identify features of interest, to estimate the centroid coordinates, x_p and y_p, for each feature, and to estimate the feature's extent, w_p, in the field of view. The feature is then cropped, scaled to a standard size and then fed into a second network that estimates the particle's axial position, z_p, diameter, d_p, and refractive index, n_p. Both stages consist of convolutional neural networks (CL) whose abstract outputs are parsed into physically relevant parameters using fully-connected neural layers (FC).

The complete network in Fig. 2 has more than 60,000 parameters whose values are optimized through training on several thousand sample holograms that span the anticipated range of single-particle properties and particle numbers in the field of view. Most such training processes require experimental images, each of which must be annotated with ground-truth results. Fortunately, the training and validation data for holographic particle characterization can be computed with the generative model from Eq. (1) and therefore can span a much wider parameter domain than could be accessed with experimental data. In practice, a well-trained neural-network implementation performs far better than conventional particle-tracking algorithms for detecting and localizing holographic features and can rival the precision of nonlinear least-squares fitting for estimating the particles' positions and individual characteristics. The parameters for the estimation module fit within 200 kbytes of storage, which is remarkable given the complexity of the underlying Lorenz-Mie theory. The machine-learning implementation, moreover, is exceptionally fast and can support real-time analysis for high-throughput applications.

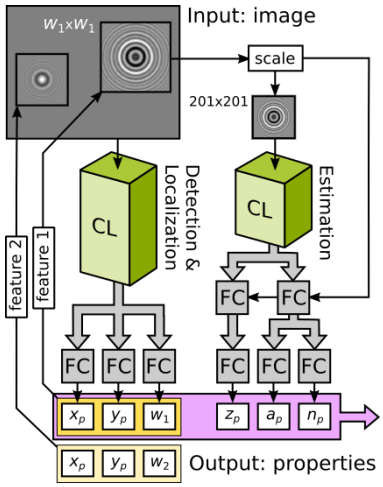

Figure 2 *The CATCH deep neural network for holographic particle tracking and characterization uses a combination of convolutional layers (CL) and fully-connected layers (FC) to detect and localize features of interest in a normalized hologram, and then to perform regression on each feature to estimate the associated particle's three-dimensional position,* $\boldsymbol{r}_p = (x_p, y_p, z_p)$*, radius* a_p *and refractive index* n_p*. From [8].*

2 Applications

Quantitative analysis of colloidal holograms provides an unprecedented wealth of particle-resolved tracking and characterization data with important real-world applications. Two examples illustrate the value of the extra dimensions of information provided by holographic particle characterization and the utility of the effective-sphere interpretation for fast precision monitoring of molecular-scale processes.

2.1 Differentiation of Particles in Biopharmaceuticals

Biopharmaceutical products consist of therapeutic proteins dissolved in buffer along with surfactants and other excipients intended to improve performance and prolong shelf life. These products fail if the highly concentrated proteins bind to each other, forming insoluble micrometer-scale aggregates. Not only are the aggregates

ineffective as therapeutic agents, but they can trigger dangerous immune responses. Detecting aggregates is challenging because typical formulations are full of other micrometer-scale particles such as inert silicone oil droplets, glass and metal microparticles from the manufacturing process, and benign aggregates formed from breakdown products of surfactants. All of these are indistinguishable to conventional particle-characterization techniques.

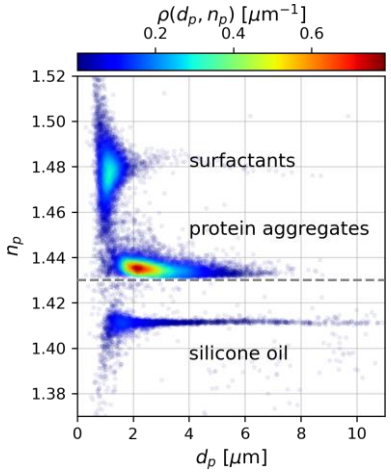

Figure 3 *Holographic differentiation of particles in a biopharmaceutical formulation. Each point represents the properties of one particle and is coloured by the observed probability density of measurements. Three populations of particles are differentiated by refractive index. From [19].*

Figure 3 shows experimental results for holographic characterization of a model biopharmaceutical formulation that was caused to fail through heat treatment [19]. Each point in the scatter plot represents the diameter and refractive index of one particle in the sample. Points are coloured by the local density of measurements, $\rho(d_p, n_p)$.

Three categories of particles are clearly resolved in this joint distribution. On the basis of their refractive indexes, they can be identified as silicone oil droplets, surfactant aggregates and protein aggregates. Whereas the droplets are spherical, the other major particle types are fractal aggregates whose measured properties can be interpreted with the effective-sphere model.

The various types of particles in this heterogeneous dispersion could not have been distinguished by size alone. Because the measurement is performed in a known sample volume, moreover, the absolute concentrations and size distributions of each type can be obtained with very high precision. All of this information is invaluable for optimizing the formulation of biopharmaceutical products and for monitoring their manufacturing processes.

2.2 Holographic Molecular Binding Assays

Holographic characterization can resolve the diameter of a micrometre-scale sphere with nanometre precision. This resolution is good enough to monitor a coating of molecules forming on the surface of a sphere [20, 21]. Rather than analysing the sphere with the generative model for a core-shell sphere, we instead can use the fast and stable analysis for a homogeneous sphere and interpret the results with the effective-sphere model.

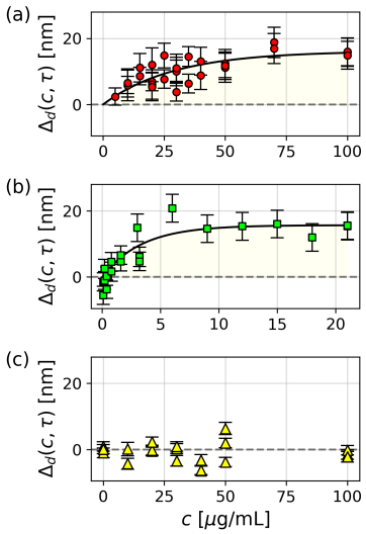

Figure 4 *Holographic molecular binding assay in which the effective diameter of functionalized probe beads increases by an amount Δ_d because of molecules binding to the surface from a solution of concentration c after incubation time τ. (a) Assay for the antibody IgG. (b) Assay for the antibody IgM. (c) Control measurements with alcohol dehydrogenase (ADH) show no binding. Solid curves are fits to Eq. (4). From [22].*

The data in Fig. 4 show typical results for holographic analysis of molecular binding to the surfaces of functionalized colloidal beads [22]. The probe beads have micrometre-diameter cores of polystyrene and are coated with protein A, a molecule that selectively and strongly binds antibodies. Any antibodies in solution will stick to the binding sites with a rate constant k, increasing the bead's apparent diameter by an amount

$$\Delta_d(c, \tau) = 2\delta\,(1 - e^{-kc\tau}) \qquad (4)$$

that depends on the concentration of antibodies, c, and the incubation time τ. The parameter δ describes the increase in the effective sphere's diameter when its binding sites are saturated. Rate constants inferred from holographically measured kinetic binding curves agree with literature values obtained with conventional biochemical assays [22]. Holographic assays can be performed on far smaller sample volumes, require far fewer preparatory and analytical steps, and lend themselves to multiplexing on the basis of the size and composition of the substrate beads. These fast and precise assays make full use of the nanometre precision for particle sizing made available through holographic microscopy.

3 Discussion

Holographic microscopy encodes a treasure trove of information about colloidal materials into a readily accessible video data stream. A lot of that information can be extracted in real time through analysis with generative models for the image formation process. Even an idealized model for light scattering by homogeneous spheres can cast

valuable light on the properties and microscopic dynamics of complex heterogeneous colloidal dispersions. The nature, quantity and quality of information accessible through holographic particle characterization is enabling exciting new academic and industrial applications. This comparatively new field is growing rapidly, driven both by advances in analytical software and hardware, and also by ongoing discoveries of new systems and phenomena that can be probed holographically.

4 Acknowledgement

This work was supported by the National Institutes of Health of the United States through Award Number R44TR001590 and by the National Science Foundation of the United States through Awards Number DMR-2027103 and DMR-2104837.

5 References

[1] C.F. Bohren, and D.R. Huffman, Absorption and scattering of light by small particles (Wiley, 1983)

[2] M.I. Mishchenko, L.D. Travis, and A.A. Lacis, *Scattering, Absorption, and Emission of Light by Small Particles* (Cambridge University Press, 2002)

[3] G. Gouesbet, and G. Gréhan, *Generalized Lorenz-Mie theories* (Springer, 2011)

[4] Lee, S.-H., Roichman, Y., Yi, G.-R., Kim, S.-H., Yang, S.-M., van Blaaderen, A., van Oostrum, P., Grier, D.G., Characterizing and tracking single colloidal particles with video holographic microscopy, Optics Express 15, 18275–18282 (2007)

[5] Markel, V.A., Introduction to the Maxwell Garnett approximation: tutorial, Journal of the Optical Society of America A 33, 1244–1256 (2016)

[6] Cheong, F.C., Xiao, K., Pine, D.J., Grier, D.G., Holographic characterization of individual colloidal spheres' porosities, Soft Matter 7, 6816–6819 (2011)

[7] Odete, M.A., Cheong, F.C., Winters, A., Elliott, J.J., Philips, L.A., Grier, D.G., The role of the medium in the effective-sphere interpretation of holographic particle characterization data, Soft Matter 16, 891–898 (2020)

[8] Altman, L.E., Grier, D.G., CATCH: Characterizing and Tracking Colloids Holographically Using Deep Neural Networks, Journal of Physical Chemistry B 124, 1602–1610 (2020)

[9] Krishnatreya, B.J., Colen-Landy, A., Hasebe, P., Bell, B.A., Jones, J.R., Sunda-Meya, A., Grier, D.G., Measuring Boltzmann's constant through holographic video microscopy of a single sphere, American Journal of Physics 82, 23–31 (2014)

[10] Fung, J., Perry, R.W., Dimiduk, T.G., Manoharan, V.N., Imaging multiple colloidal particles by fitting electromagnetic scattering solutions to digital holograms, Journal of Quantitative Spectroscopy and Radiative Transfer 113, 2482–2489 (2012)

[11] Perry, R.W., Meng, G., Dimiduk, T.G., Fung, J., Manoharan, V.N., Real-space studies of the structure and dynamics of self-assembled colloidal clusters, Faraday Discussions 159, 211–234 (2013)

[12] Barkley, S., Dimiduk, T., Fung, J., Kaz, D., Manoharan, V.N., McGorty, R., Perry, R., Wang, A., Holographic Microscopy with Python and HoloPy, Computing in Science and Engineering 22, 72-82 (2020)

[13] Leahy, B., Leahy, B., Alexander, R., Alexander, R., Martin, C., Barkley, S., Manoharan, V.N., Manoharan, V.N., Large depth-of-field tracking of colloidal spheres in holographic microscopy by modeling the objective lens, Optics Express 28, 1061–1075 (2020)

[14] Alexander, R., Leahy, B., Manoharan, V.N., Precise measurements in digital holographic microscopy by modeling the optical train, Journal of Applied Physics 128, 060902 (2020)

[15] Wang, C., Cheong, F.C., Ruffner, D.B., Zhong, X., Ward, M.D., Grier, D.G., Holographic characterization of colloidal fractal aggregates, Soft Matter 12, 8774–8780 (2016)

[16] Fung, J., Hoang, S., Computational assessment of an effective-sphere model for characterizing colloidal fractal aggregates with holographic microscopy, Journal of Quantitative Spectroscopy and Radiative Transfer 236, 106591 (2019)

[17] Wang, C., Zhong, X., Ruffner, D.B., Stutt, A., Philips, L.A., Ward, M.D., Grier, D.G., Holographic characterization of protein aggregates, Journal of Pharmaceutical Sciences 105, 1074–1085 (2016)

[18] Redmon, J., Farhadi, A.: YOLOv3: An Incremental Improvement. CoRR. abs/1804.02767, (2018)

[19] Winters, A., Cheong, F.C., Odete, M.A., Lumer, J., Ruffner, D.B., Mishra, K.I., Philips, L.A., Quantitative differentiation of protein aggregates from other subvisible particles in viscous mixtures through holographic characterization, Journal of Pharmaceutical Sciences 109, 2405–2412 (2020)

[20] Cheong, F.C., Sun, B., Dreyfus, R., Amato-Grill, J., Xiao, K., Dixon, L., Grier, D.G., Flow visualization and flow cytometry with holographic video microscopy, Optics Express 17, 13071–13079 (2009)

[21] Zagzag, Y., Soddu, M.F., Hollingsworth, A.D., Grier, D.G., Holographic molecular binding assays, Scientific Reports 10, 1–7 (2020)

[22] Snyder, K., Quddus, R., Hollingsworth, A.D., Kirshenbaum, K., Grier, D.G., Holographic immunoassays: direct detection of antibodies binding to colloidal spheres, Soft Matter 16, 10180–10186 (2020)

TAILORED OPTICAL AND ACOUSTIC TRAPS FOR ORGANOID RESEARCH

Monika RITSCH-MARTE

Biomedical Optics, Medical University of Innsbruck, Austria

**Corresponding author: monika.ritsch-marte@i-med.ac.at*

Abstract

Optical imaging of trapped bio-samples poses a serious challenge for large living specimens, such as developing embryos organoids.

A customized combination of optical tweezers and standing ultrasound waves represents a flexible solution to this problem, facilitating 3D-manipulation and volumetric imaging.

IN *VIVO* IMAGING BY SPATIO-TEMPORAL OPTICAL COHERENCE TECHNIQUES

Maciej WOJTKOWSKI [1,*], Dawid BORYCKI[1]

[1] International Centre for Translational Eye Research,
Institute of Physical Chemistry Polish Academy of Science,
Kasprzaka Str. 44/52 01-224 Warsaw, Poland

**Corresponding author: mwojtkowski@ichf.edu.pl*

Abstract

The main physical limitation of the in vivo microscopic imaging is associated with light scattering introduced by irregular and often discontinuous distribution of refractive index. Scattering of light limits the number of ballistic photons delivered to and received from the sample. In our work we try to solve these fundamental physical limitations by developing new optical coherence imaging techniques, which utilize spatio-temporally partially coherent light with access to intensity and phase of detected radiation. In our research activity we focus on developing new optical methods that enable to image biological objects in vivo and in minimally invasive way. We went long way covering significant spectrum of various sizes of objects – from organ-size scale up to internal structure of a single cell.

1 Spatio-Temporal Optical Coherence Imaging

Non-invasive optical imaging of biological tissues at the cellular level is one of the fundamental scientific challenges of modern physical optics. From a physical point of view, biological tissue is very often characterized by optical inhomogeneities with sizes smaller or comparable to the wavelength of light. The description of light propagation in such media goes beyond the framework of diffraction theory, and requires the use of statistical optics techniques. For this reason, in order to describe the physical effect of perturbations on the formation of optical reconstruction in such media, we introduced and then experimentally verified the model using the formalism of the matrix of the spectral degree of coherence of light, G [1-3]. This formalism describes the process of disruption of image reconstruction in the presence of optical inhomogeneities in the form of spatio-temporal correlations. Quantifying these correlations allows us to distinguish useful signal from noise, leading to so-called optical crosstalk. The non-crosstalk signal associated with ballistic photons corresponds to the diagonal elements of the G matrix, in contrast to the noise, which is associated with the extra-diagonal elements of the G matrix. In view of this, in order to remove optical crosstalk, the phase of the incident optical field must be suitably modulated in order to obtain a diagonal G matrix after averaging multiple realizations of the optical fields.

In order to experimentally validate this approach, we used full-field swept-source optical coherence tomography (FF-SS-OCT) interferometry of partially coherent light with parallel Fourier domain detection [4, 5]. With interferometry, we gain access to additional information encoded in the phase of the optical field. This additional information has been crucial for quantifying and controlling

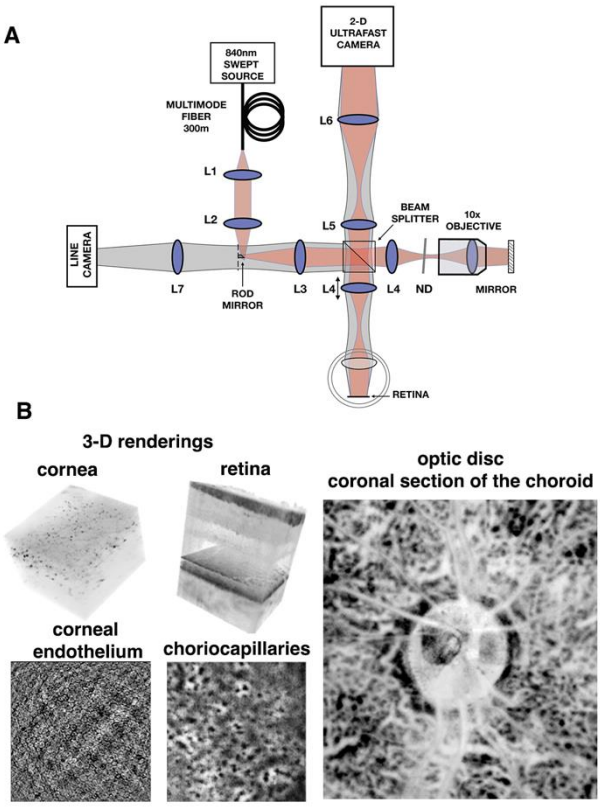

imaging perturbations in the presence of optical inhomogeneities in the medium.

Figure 1 *Spatio-Temporal Optical Coherence Imaging:* ***A.*** *STOC-T system using a long multimode fiber for spatial light decoherence.* ***B.*** *examples of volumetric imaging of the cornea and retina of the human eye.*

In practice, these disturbances lead to optical crosstalk, which creates coherent noise that reduces resolution and

imaging range. As a result, this limits the widespread adaptation of imaging interferometric methods such as FF-SS-OCT for practical and clinical applications for non-invasive imaging of biological tissue. To address this problem, we performed experimental (hardware) diagonalization of the G matrix using spatio-temporal modulation of incident light on the sample [2]. By appropriately parameterizing this modulation, we removed spatial coherence, which is confirmed by diagonalizing the coherence matrix. As a final result, we were able to visualize a static object hidden under a strongly scattering layer (ex vivo rat skin). With this, we obtained a new way of modulating light, which we called spatio-temporal optical coherence STOC imaging. We define imaging techniques that use STOC in general as **(**STOC**)** optical tomography (STOC-T).

Based on this research, we took on another challenge in which we sought to create an optimal and fast way to modulate the coherence of light. After analyzing multiple technologies, we used a very fast deformable membrane that effectively acts as a random phase mask. In addition, we combined this modulation with angle-varying sample illumination [5]. Using this method, we showed that we could control the spatial coherence of the light. We proved this by arbitrarily selecting the spatial coherence gate in the imaging system. Using this approach, we redesigned the optical system to adapt it for in vivo imaging of the human fundus. Our research hypothesis was that removing the optical crosstalk would allow non-invasive imaging of the deep layers of the retina (known as the choroid). This has not been possible so far with classical optical tomography with partially coherent light interferometry, as well as the FF-SS-OCT technique due to multiple light scattering. In a later phase of the work, we optimized the system using a multimode optical fiber to introduce spatial decorrelation of the incident light on the measured object (Fig. 1A.). In this configuration, the decorrelation is done by introducing a delay between spatial modes by the coherence time of the light source. In this way, the interferometric system gets rid of parasitic signals from multiple scatterers and minimizes speckle contrast.

We demonstrated high-resolution, high-speed, non-contact volumetric imaging of the cornea in vivo [6, 7]. The spatial coherence of the laser source was suppressed to prevent it from focusing on the macula on the retina, thereby exceeding the maximum allowable light intensity. The inherently volumetric nature of the acquired data made it possible to align the curved layers of the cornea. The images obtained revealed the cellular structures of the cornea, such as the epithelium, stroma and endothelium, as well as the subbasal and midbasal nerves (Fig. 1B.). The second application was in vivo imaging of the human retina. Figure 1B. shows STOC-T's capabilities in this area. STOC-T offers visualization of the anatomical details of the retina in en face projection without the need for complex hardware adaptive optics, yielding results previously unattainable for OCT **[8]**. Particularly noteworthy are images of the structure of the choroid, which is unavailable for measurement by other optical methods.

As part of our work, we developed a new approach to control the coherence of light used in imaging. As a result, we created a new tool for imaging biological objects, which we called spatio-temporal optical coherence tomography (STOC-T). Specifically, the removal of optical field perturbations from optical inhomogeneities of the medium (biological tissue), allows us to non-invasively image deeper layers of the specimen. This unique feature also allows us to quantitatively analyze the dynamics of blood flows in the deep layers of the sample. The new STOC-T method for imaging biological structures of the eye enables in-vivo imaging with microscopic accuracy, but the final imaging results require additional iterative geometric aberration correction algorithms to obtain sharp images.

2 Acknowledgement

Work supported by grant from National Science Centre (2016/22/A/ST2/00313);

3 References

[1] D. Borycki, M. Nowakowski, and M. Wojtkowski, "Control of the optical field coherence by spatiotemporal light modulation," Optics letters **38**, 4817-4820 (2013).

[2] D. Borycki, M. Hamkało, M. Nowakowski, M. Szkulmowski, and M. Wojtkowski, "Spatiotemporal optical coherence (STOC) manipulation suppresses coherent cross-talk in full-field swept-source optical coherence tomography," Biomedical Optics Express **10**, 2032-2054 (2019).

[3] M. Wojtkowski, P. Stremplewski, E. Auksorius, and D. Borycki, "Spatio-Temporal Optical Coherence Imaging - a new tool for in vivo microscopy," Photonics Letters of Poland **11**, 45-50 (2019).

[4] E. Auksorius, D. Borycki, and M. Wojtkowski, "Crosstalk-free volumetric in vivo imaging of a human retina with Fourier-domain full-field optical coherence tomography," Biomed Opt Express **10**, 6390-6407 (2019).

[5] P. Stremplewski, E. Auksorius, P. Wnuk, L. Kozon, P. Garstecki, and M. Wojtkowski, "In vivo volumetric imaging by crosstalk-free full-field OCT," Optica **6**, 608-617 (2019).

[6] E. Auksorius, D. Borycki, P. Stremplewski, K. Lizewski, S. Tomczewski, P. Niedzwiedziuk, B. L. Sikorski, and M. Wojtkowski, "In vivo imaging of the human cornea with high-speed and high-resolution Fourier-domain full-field optical coherence tomography," Biomed Opt Express **11**, 2849-2865 (2020).

[7] D. Borycki, E. Auksorius, P. Wegrzyn, and M. Wojtkowski, "Computational aberration correction in spatiotemporal optical coherence (STOC) imaging," Optics letters **45**, 1293-1296 (2020).

[8] E. Auksorius, D. Borycki, and M. Wojtkowski, "Multimode fiber enables control of spatial coherence in Fourier-domain full-field optical coherence tomography for in vivo corneal imaging," Optics letters **46**, 1413-1416 (2021).

Beam Shape Description and Effects

13th International Conference Series on
Laser-light and Interactions with Particles
Optical Particle Characterization follow-up !
August 21-26th, 2022, Warsaw, Poland

DIVERGING AND CONVERGING SCHEMES OF APPROXIMATIONS FOR GAUSSIAN BEAMS

Gérard GOUESBET[1], Jianqi SHEN[2] and Leonardo André AMBROSIO[3]

[1] Coria, Normandie University, Saint-Etienne du Rouvray, 76800, France
[2] College of Science, University of Shanghai for Science and Technology, Shanghai, 200093, China
[3] Department of Electrical and Computer Engineering, Sao Paulo University, Sao Paulo, 13566-590, Brazil
Corresponding author: gouesbet@coria.fr

Abstract

EM Gaussian beams are the most celebrated and used kind of laser beams, and their description for various applications, such as light scattering and optical particle characterization, has therefore a long and venerable history. To this aim, the Davis scheme of approximations has been one of the most celebrated. An overlooked paper has nevertheless established a quite unexpected result, namely that this scheme is actually divergent. Our presentation will discuss the main features of this divergence and recall the existence of convergence schemes which have been deduced from the divergent Davis scheme.

1 The Davis scheme and its divergence.

The Davis scheme of approximations relies on the introduction of an x-polarized potential vector [1-2], from which we may deduce electric and magnetic field components in the Lorentz gauge. The Gaussian beam is characterized by a small parameter denoted "s" and called the beam confinement factor (or beam shape factor). The x-component of the potential vector satisfies the Helmholtz equation. The solution is searched under the form of an infinite series in terms of even powers of "s". Only the first-order, third-order and fifth-order approximations which respectively contain terms up to $O(s^2)$, $O(s^4)$ and $O(s^6)$ are explicitly known. None of the approximations in the scheme satisfies Maxwell's equations which are only satisfied in the infinite-order limit. Nevertheless, the first three terms of the series are sufficient to obtain, in practice, a good description of a Gaussian beam. The convergence of the whole series, considering the small value of the beam confinement factor (0 for a plane wave, typically 10^{-3} for a moderate focusing, and 1/6 for an extreme focused case when the wave-length is about equal to the beam waist radius of the beam), has been considered as guaranteed. In a very overlooked paper [4], it has surprisingly been demonstrated that the series is actually divergent.

The demonstration of the divergence is sophisticated and relies on the study of a partial differential equation for the x-component of the potential vector whose solution is researched under the form of infinite series defined by recurrence relations between expansion coefficients. The study of the successive terms of the series shows that the series, to begin with, converges to a satisfactory solution, before diverging. We shall return to such a behaviour later.

2 Convergent schemes.

From the divergent Davis scheme, two convergent schemes have been however developed and are known since a long time.

The first one is the localized approximation schemes whose convergence is ensured by the fact that they produce closed-form expressions, whose validity in the case of Gaussian beams has been established both for on-axis configurations [5] and for off-axis configurations [6]. These closed-form expressions provide the evaluation of the beam shape coefficients which encode the structure of the beam and from which we may evaluate all field components of the Gaussian beam.

The second one relies on the evaluation of the beam shape coefficients directly from the first-order, third-order and fifth-order Davis approximations. It is found, after a significant amount of calculation, that for each of these cases, the beam shape coefficients are the summation of terms which do not depend on the coordinates and on non-constant terms which do depend on the coordinates. These coordinate-dependent terms are artefacts produced by the fact that the Davis beam approximations do not satisfy Maxwell's equations. Once they are removed, we obtain beam descriptions which exactly satisfy Maxwell's equations. For instance, in the simple case when the beam waist centre of the beam is located at the origin of the coordinates, the beam shape coefficients simply read as $[1-(n-1)(n+2)s^2]$ for the first-order Davis beams, and similar simple although longer expressions for the third-order and for the fifth-order Davis beams.

We have then defined standard beams as the infinite generalization of the beams defined by the first Davis beams when the artefacts are removed.

In a first version, called standard beams, we obtain a satisfactory description of Gaussian beams, but the series obtained possessed a limited radius of convergence. An improved standard beam scheme has afterward been designed whose convergence was guaranteed [7].

3 Complementary discussion

The divergent series of the Davis is an example of asymptotic series which is reminiscent of asymptotic series encountered in quantum electrodynamics. Such series are non-convergent series which however provide a correct result if we limit ourselves to a few terms. A paradigmatic example is the evaluation of the electron g-factor which is a dimensionless magnetic moment. It may evaluated by a series reading as $g/2=1+C(1)\alpha+C(2)\alpha^2+\ldots$

In this series, α is a small parameter (the fine structure constant) equal to 1/137.035…, from which we might have expected a fast convergence of the series. Such is not the case however, and the calculations of the successive coefficients, relying on an evaluation of an increasing number of integrals related to Feynman diagrams, become more and more complicated. For instance, the calculation of C(3) requires the evaluation of 72 integrals while C(4) requires the evaluation of 891 integrals [8]. The theoretical value, obtained by summing only such few terms, is found to be 1. 001 159 652 181 [9] to be compared with an experimental value equal to 1.001 159 652 180 [10]. The origin of the divergence of such series in QED is attributed to the punctual character of "lines" in the Feynman diagrams and have at least a possible solution in the framework of superstring theories when the "lines" of the Feynman diagrams are replaced by "tubes". This means that infinities in quantum electrodynamics might have and certainly have a deep physical meaning.

The question is then open to know whether the divergence of the Davis scheme is purely "accidental" or whether there is a deep physical meaning as well behind such a behavior.

4 References

[1] L.W. Davis. Theory of electromagnetic beams. Physical Review, 19, 3, 1177-1179, 1979.

[2] J.P. Barton and D.R. Alexander. Fifth-order corrected electromagnetic field components for fundamental Gaussian beams. Journal of Applied Physics, 66, 7, 2800-2802, 1989.

[3] G. Gouesbet, J.A. Lock, G. Gréhan. Partial wave representations of laser beams for use in light scattering calculations, Applied Optics, 34, 12, 2133-2143, 1995.

[4] G.-Z. Wang and J.F. Webb. New method to get fundamental Gaussian beam's perturbation solution and its global property. Appl. Phys. B. 93, 345-348, 2008.

[5] J.A. Lock and G. Gouesbet. Rigorous justification of the localized approximation to the beam shape coefficients in generalized Lorenz-Mie theory. I. On-axis beams. Journal of the Optical Society of America A, 11, 9, 2503-2515, 1994

[6] G. Gouesbet, J.A. Lock. Rigorous justification of the localized approximation to the beam shape coefficients in generalized Lorenz-Mie theory. II. Off-axis beams. Journal of the Optical Society of America A. 11, 9, 2516-2525, 1994.

[7] H. Polaert, G. Gréhan and G. Gouesbet. Improved standard beams with applications to reverse radiation pressure. Applied Optics. 37, 12, 2435-2440, 1998.

[8] G. Gabrielse, D. Hannecke, T. Kinoshita, M. Nio and B. Odom. New determination of the fine structure constant from the electron g value and QED. Physical Review Letters. 97, Article 030802, 2006.

[9] R. Bouchendira, P. Cladé, S. Guellafi-Khélifa, F. Nez and F. Biraben. New determination of the fine structure constant and test of the quantum electrodynamics. Physical Review Letters. 106, Article 080801, 2011.

[10] D. Hannecke, S. Fogwell and G. Gabrielse. New measurement of the electron magnetic moment and the fine structure constant. Physical Review Letters. 100, Article 120801, 2008.

13th International Conference Series on
Laser-light and Interactions with Particles
Optical Particle Characterization follow-up !
August 21-26th, 2022, Warsaw, Poland

ANALYTICAL SOLUTIONS TO CLASSES OF INTEGRALS WITH PRODUCTS OF BESSEL FUNCTIONS OF THE FIRST KIND AND THEIR DERIVATIVES

Leonardo André AMBROSIO[1,*], Gérard GOUESBET[2] and Jiajie WANG[3]

[1] Department of Electrical and Computer Engineering. São Carlos School of Engineering, University of São Paulo. 400 Trabalhador são-carlense Ave. 13566-590, São Carlos, SP, Brazil.
[2] CORIA-UMR 6614 - Normandie Université. CNRS-Université et INSA de Rouen. Campus Universitaire du Madrillet. 76800, Saint-Etienne du Rouvray, France.
[3] School of Physics, Xidian University, 710071, Xi'an, China.

Corresponding author: leo@sc.usp.br

Abstract

Recently, attention has been paid to light scattering problems involving photophoresis with arbitrary-shaped beams. In particular, the determination of longitudinal and transverse photophoretic asymmetry factors (PAFs) plays a crucial role in the scattering problem by lossy microparticles, since such factors are proportional to photophoretic optical forces. Here, we show that semi-analytical formulas recently presented for PAFs associated with light scattering by lossy infinite cylinders, relying on integrals with products of Bessel functions of the first kind and their derivatives, can actually be given a complete analytical form, therefore speeding up calculations in light-matter interaction between an incident optical field and a cylindrical scatterer with unbalanced heat absorption. To the best of the authors knowledge, the solutions to such integrals are not available in the literature.

1 Introduction

When a lossy and homogeneous rigid microparticle absorbs light, unbalanced heat absorption takes place that gives rise to thermal forces called photophoretic forces $\mathbf{F}_{ph}$ [1-6]. The determination of such forces is usually accomplished by first finding quantities called (photophoretic) asymmetry factors (PAFs), J_1 [1], or asymmetry vectors, $\mathbf{r}_{as}$ [7]. For instance, under uniform plane wave illumination and assuming propagation along $+z$, $\mathbf{F}_{ph} = \hat{\mathbf{z}} F_z \propto \hat{\mathbf{z}} J_1$, the proportionality depends on hydrodynamic and thermal properties of the external fluid and the particle [1,7].

In a series of recent works, Mitri explored the interaction between a lossy infinite cylinder and arbitrary-shaped beams and provided expressions for the PAFs using a semi-analytic approach. This approach, based on a partial wave expansion of the internal fields, has been shown to be valid either for isolated dielectric or magnetodielectric cylinders or for cylinders close to planar boundaries and corner spaces [8-10].

A common fact about all the expressions for the PAFs available in these works is the presence of integrals of the following form:

$$I_1^{\pm} = \int_0^1 \xi^2 J_n\left(m_c ka\xi\right) J_{n\pm1}\left(m_c^* ka\xi\right) d\xi \tag{1}$$

and

$$I_2^{\pm} = \int_0^1 \left[\frac{n(n\pm1)}{|m_c|^2 (ka)^2} J_n\left(m_c ka\xi\right) J_{n\pm1}\left(m_c^* ka\xi\right) + \xi^2 J_n'\left(m_c ka\xi\right) J_{n\pm1}'\left(m_c^* ka\xi\right) \right] d\xi \tag{2}$$

In Eqs. (1) and (2), n is an integer ($-\infty \le n \le \infty$), $J_n(x)$ are Bessel functions of the first kind, a is the radius and m_c is the complex relative refractive index of the cylinder with respect to the surroundings, respectively, $k = 2\pi/\lambda$ is the wave number in the external medium, λ being the wavelength. A prime denotes differentiation with respect to the argument, and an asterisk denotes complex conjugation.

Due to the lack of known available analytical solutions to Eqs. (1) and (2), in [8-10] numerical techniques are employed in order to have accurate values of $I_1^{\pm}$ and $I_2^{\pm}$. However, here we show that these integrals can actually be solved after a great deal of algebra.

2 Analytical Expressions for $I_1^{\pm}$ and $I_2^{\pm}$

To solve Eq. (1), we define new variables $\rho = x\xi$, with $x = ka$ being the size parameter of the scatterer. Then, we consider a similar integral, valid for arbitrary real (not necessarily real) ν:

$$\frac{1}{x^3}\int_0^x \rho^2 J_\nu\left(m_c\rho\right) J_{\nu\pm1}^*\left(m_c\rho\right) d\rho \tag{3}$$

Next, we make use of the recurrence relation $J_{\nu\mp1}(m_c\rho) = (\nu/m_c\rho) J_\nu(m_c\rho) \pm J_\nu'(m_c\rho)$ to break Eq. (3) into two integrals:

$$\frac{1}{x^3}\int_0^x \rho^2 J_\nu\left(m_c\rho\right) J_{\nu\pm1}^*\left(m_c\rho\right) d\rho = \frac{1}{x^3}\frac{\nu}{m_c^*}\int_0^x \rho \left|J_\nu\left(m_c\rho\right)\right|^2 d\rho \mp \frac{1}{x^3}\int_0^x \rho^2 J_\nu\left(m_c\rho\right) J_\nu'^*\left(m_c\rho\right) d\rho \tag{4}$$

The first integral in the r.h.s. of Eq. (4) can be solved using a similar indefinite integral available in [11], see item 5.54, p. 639, or in [12], see (8), Sec. 5.11 where ν is an integer, and one gets:

$$\bar{R}_\nu \equiv \int_0^x \rho \left| J_\nu(m_c\rho) \right|^2 d\rho = \frac{\mathrm{Im}\left[m_c x J_{\nu+1}(m_c x) J_\nu^*(m_c x) \right]}{\mathrm{Im}(m_c^2)} \qquad (5)$$

For the second integral in the r.h.s. of Eq. (4), one works out Eqs. (60) and (61) of [5], which are expressed in terms of Ricatti-Bessel functions. After some arrangement and simplification, and performing a substitution of the form $\nu \to \nu - 1/2$, one has

$$\begin{aligned} \bar{S}_\nu &\equiv \int_0^x \rho^2 J_\nu^*(m_c\rho) J_\nu'(m_c\rho) d\rho \\ &= -\frac{i}{2\,\mathrm{Im}(m_c^2)} \left\{ x^2 \left[m_c \left| J_\nu(m_c x) \right|^2 + m_c^* \left| J_{\nu+1}(m_c x) \right|^2 \right] \right. \qquad (6) \\ &\left. -2\left[m_c + \nu \frac{\mathrm{Re}(m_c^2)}{m_c} \right] \bar{R}_\nu + 2\nu m_c^* \bar{R}_{\nu+1} \right\} \end{aligned}$$

Imposing $\nu = n$, substituting Eqs. (5) and (6) in (4) and after some simplification, one finally arrives at

$$I_1^\pm = \frac{1}{x^3} \left[\frac{n}{m_c^*} \bar{R}_n \mp (\bar{S}_n)^* \right] \qquad (7)$$

Equation (7) shows that a full analytical solution can be given to Eq. (1). Similarly, one can also solve for Eq. (2). Although straightforward, we shall here omit the details, which involves the use of recurrence relations to break into parts and rewrite the term with products between derivatives of Bessel functions in the second line of Eq. (2). One then performs some rearrangements and identifies each new integral either with either $\bar{R}_\nu$, $\bar{S}_\nu$ or $I_1^\pm$. After some algebra and simplification, one can then show that:

$$I_2^\pm = \frac{1}{x^3} \left(\frac{n \pm 1}{m_c^*} \bar{R}_{n\pm1} \pm \bar{S}_n \right) \qquad (8)$$

The validity of Eqs. (7) and (8) have been assessed by running computer simulations. They have been compared with the integrals with Eqs. (1) and (2) by implementing them using the commercial software *Wolfram Mathematica 12.1 Student Edition*. The code was then run on a personal computer [Intel(R) Core(TM) i7-3630QM CPU @ 2.40GHz, 16.0 GB]. Elapsed times for each case have also been computed and saved for comparison.

The solutions provided by Eqs. (7) and (8) can be used to evaluate the PAFs for infinite homogenous cylinders. As we intend to show during the conference, divergences between Eqs. (1), (2) and Eqs. (7), (8) are attributed to numerical errors and can be made smaller by increasing the numerical precision. Computational burden is reduced by approximately two orders of magnitude.

3 Conclusions

We have here derived exact and analytical solutions to integrals with products of Bessel functions of the first kind and their derivatives which, to the best of the authors knowledge, are not available anywhere in the literature. Such solutions are of special importance in light scattering problems by lossy and homogenous infinite cylinders, mainly in the determination of photophoretic asymmetry factors. However, it is expected that the present work serves as a first step towards new analytical solutions to classes of integrals involving products of Bessel functions of different kinds and their derivatives, as happens to be observed when the cylinder is not electromagnetically homogeneous. A similar problem might occur for multi-layered/coated spheres, and the results here presented can certainly be of help in putting aside semi-analytical methods in the analysis of photophoretic forces and asymmetry factors for arbitrary shaped beams in generalized Lorenz-Mie theories.

4 Acknowledgement

L. A. Ambrosio thanks the National Council for Scientific and Technological Development (CNPq) (426990/2018-8, 309201/2021-7) for supporting this work.

5 References

[1] Yalamov Y.I. Kutukov V., Shchukin E., Theory of the photophoretic motion of a large-size volatile aerosol particle, J. Colloid Interface Science 57(3):564-571 (1976)

[2] Reed L.D., Low Knudsen number photophoresis, J. Aero. Sci. 8(2): 123-131 (1977)

[3] Pluchino A.B., Photophoretic force on particles for low Knudsen number, Appl. Opt. 22(1):103-106 (1983)

[4] Greene W.M., Spjut R.E., Bar-Ziv E., Sarofim A.F., Longwell J.P., Photophoresis of irradiated spheres: absorption centers, J. Opt. Soc. Am. B 2(6): 998-1004 (1985)

[5] Mackowski D., Photophoresis of aerosol particles in the free molecular and slip-flow regimes, Intl. J. Heat Mass Trans. 32(5): 843-854 (1989)

[6] Horvarth H., Photophoresis – a Forgotten Force ??, KONA Powder Part. J. 31:181-199 (2014)

[7] Zulehner W., Rohatschek H., Representation and calculations of photophoretic forces and torques, J. Aero. Sci. 26(2): 201-210 (1995)

[8] Mitri F.G., Photophoretic asymmetry factors for an absorptive dielectric cylinder near a reflecting planar boundary, J. Opt. Soc. Am. A 38(12):1901-1910 (2021)

[9] Mitri F.G., Longitudinal and transverse PAFs for an absorptive magneto-dielectric circular cylinder in light-sheets of arbitrary wavefronts and polarization, Appl. Opt. 60(26): 7937-7944 (2021)

[10] Mitri F.G., Effect of a perfectly conducting corner space on the PAFs for an absorptive dielectric circular cylinder, J. Opt. Soc. Am. B 38(12):2910-2919 (2021)

[11] I.S. Gradshteyn, and I.M. Ruzhik, Table of Integrals, Series and Products (Academic Press, Burlington, MA, USA, 2007).

[12] Watson G.N., A Treatise on the Theory of Bessel Functions (Cambridge University Press, Cambridge, UK, 1944.

13th International Conference Series on
Laser-light and Interactions with Particles
Optical Particle Characterization follow-up !
August 21-26th, 2022, Warsaw, Poland

SHAPE SENSITIVE INTENSITY FLUCTUATIONS USING STRUCTURED ILLUMINATION

Shubham DAWDA, Zhean SHEN and Aristide DOGARIU*

CREOL, The College of Optics and Photonics, University of Central Florida, 4304 Scorpius Street, Orlando, Florida, 32816, USA.

*Corresponding author: adogariu@creol.ucf.edu

Abstract

We describe the intensity fluctuations due to scattering from sparse distributions of axisymmetric dipolar particles illuminated by space-polarization entangled fields. We show that, unlike traditional type of illumination, this approach permits controlling the scattering regime and, in certain conditions, provides means to optimize the retrieval of asymmetry factors using the scattered intensity measured by a single detector.

1 Introduction

Traditional techniques for particle characterization by light scattering are based on well-defined interaction volumes [1, 2]. However, space-polarization entangled fields allow changing this paradigm and divide the interaction volume into distinct regions illuminated with different polarization states [3, 4]. Further, it is known that a polarimetric analysis of scattered fluctuations enables a more detailed characterization of random media [5]. In this work, we study the light scattering from a sparse group of anisotropic but axisymmetric particles illuminated by such a structured field and demonstrate that the contrast of intensity fluctuations is highly sensitive to particle anisotropy. The concepts and results of this work should be of interest for remote sensing and the characterization of particulate matter.

2 Scattering from 2 axisymmetric dipoles

The anisotropic polarizability of a single scattering object can be obtained by analyzing the statistical moments of polarimetrically measured intensity distributions[6, 7]. Here we start by examining the canonical example of two identical axisymmetric dipoles that are coherently excited. The particle's polarizability tensor is a diagonal matrix $\boldsymbol{\alpha} = diag(\alpha_1, \alpha_2, \alpha_2)$ characterized by the aspect ratio $r = \frac{\alpha_1}{\alpha_2}$. These scattering centers are at different but fixed spatial locations. Their orientations are independent of each other and are uniformly randomly distributed during the measurement. Let E_1 and E_2 be the projections of the fields scattered from each dipole onto a common polarization state. It can be shown that the first and second moments of the far-field scattered intensity, $I = E^2 = (E_1 + E_2)^2$, are

$$\begin{aligned} \langle I \rangle_o &= \langle E_1^2 \rangle_o + \langle E_2^2 \rangle_o + 2\langle E_1 \rangle_o \langle E_2 \rangle_o \\ \langle I^2 \rangle_o &= \langle E_1^4 \rangle_o + \langle E_2^4 \rangle_o + 6\langle E_1^2 \rangle_o \langle E_2^2 \rangle_o + \\ &\quad 4\langle E_1^3 \rangle_o \langle E_2 \rangle_o + 4\langle E_1 \rangle_o \langle E_2^3 \rangle_o, \end{aligned} \tag{1}$$

where $\langle \dots \rangle_o$ represents orientation averaging.

In the following, we will analyze the contrast $C = \frac{Var(I)}{\langle I \rangle_o^2}$ of intensity fluctuations for two types of illuminations shown in Figure 1. Each of the two dipoles can be excited by a field that is either parallel or orthogonal to the orientation of the analyzer generating "parallel" $E_\parallel$ or "crossed" $E_\times$ scattered fields, respectively. When both excitations are parallel to the analyzer orientation, $\langle E_1^k \rangle_o = \langle E_2^k \rangle_o = \langle E_\parallel^k \rangle_o$ in Eq. (1) and the contrast can be written as

$$C_1 = \frac{\langle E_\parallel^4 \rangle_o + 3\langle E_\parallel^2 \rangle_o^2 + 4\langle E_\parallel^3 \rangle_o \langle E_\parallel \rangle_o}{2\left(\langle E_\parallel^2 \rangle_o + \langle E_\parallel \rangle_o^2\right)^2} - 1 \tag{2}$$

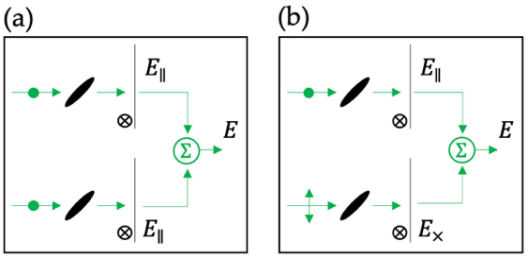

Figure 1 *Detected field E is generated by the coherent superposition of scattered fields from two independent dipoles, which are (a) both excited by field vectors parallel to analyzer orientation and (b) one of them is excited by field vector parallel and the other by a field orthogonal to the analyzer.*

When one of the excitation fields is "crossed", it can be shown that $\langle E_\times \rangle_o = \langle E_\times^3 \rangle_o = 0$ in Eq. (1) and the contrast becomes

$$C_2 = \frac{\langle E_\parallel^4 \rangle_o + \langle E_\times^4 \rangle_o + 6\langle E_\parallel^2 \rangle_o \langle E_\times^2 \rangle_o}{\left(\langle E_\parallel^2 \rangle_o + \langle E_\times^2 \rangle_o\right)^2} - 1. \tag{3}$$

Since the scatterers are axisymmetric, the contrasts will depend on their aspect ratio r ($r > 1$ for prolate, $r < 1$ for oblate, and $r = 1$ for spherical particles). The two contrasts C_1 and C_2 are plotted in Figure 2 for the case where the dipoles are illuminated by equally intense fields. We note that, within a certain range of aspect ratios, $\frac{dC_2}{dr} > \frac{dC_1}{dr}$, which suggests that the statistical properties of the intensity fluctuations are more sensitive to shape when the excitation field are not both parallel to the analyzer's orientation.

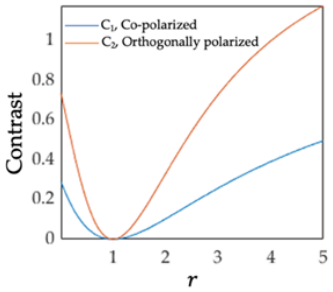

Figure 2 *Contrast of intensity fluctuations as function of aspect ratio when both excitation fields are parallel and when one of them is orthogonal to the direction of the analyser.*

3 Scattering from group of axisymmetric particles

Let us now consider a more realistic situation where N identical axisymmetric randomly orienting dipolar particles are randomly positioned in space. The particle group is sufficiently sparse such that it scatters light in the so-called "single scattering" regime. Unlike the previous section, this process now is characterized by two stochastic parameters: random orientations and random positions.

When the particle group is excited by a space-polarization entangled field such as, for instance, a cylindrical vector beam, the total interaction volume can be considered as two distinct orthogonally polarized regions. Effectively, a fraction $\nu \cdot N$ of all particles is excited by a field polarized parallel to the analyzer (co-polarized) and the rest of the particles are excited by a field polarized perpendicular to the analyzer (cross-polarized) as schematically shown in Figure 3.

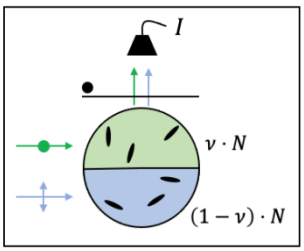

Figure 3 *Schematic of two spatially distinct and orthogonally polarized regions containing different numbers of identical, anisotropic, and randomly oriented particles.*

When the final scattered field is modelled as a 2D random walk in the complex plane with distributed step lengths and uncorrelated particle positions and amplitudes [8, 9], the contrast is given by

$$C_{\parallel+\times} = 1 + \frac{1}{N}\left(\frac{\nu\left(\langle E_\parallel^4\rangle_o - 2\langle E_\parallel^2\rangle_o^2\right) + (1-\nu)(\langle E_\times^4\rangle_o - 2\langle E_\times^2\rangle_o^2)}{\left(\nu\langle E_\parallel^2\rangle_o + (1-\nu)\langle E_\times^2\rangle_o\right)^2}\right) \quad (4)$$

where $E_\parallel$ and $E_\times$ are scattered fields from a single dipole excited under co-polarized and cross-polarized conditions, respectively. In Eq. (4), setting $\nu = 0$ and $\nu = 1$ gives the contrast for the cross and co-polarized excitations of a single interaction volume and setting $\nu \in (0,1)$ gives the contrast for different volume ratios of orthogonally polarized interaction volume. These contrasts are plotted in Figure 4 as a function of aspect ratio for the case of $N = 100$ particles.

There are three key features to note. First, in a cross-polarized setting ($\nu = 0$), the contrast is independent of particle shape. Second, within a certain range of aspect ratios, the sensitivity of contrast to particle shape is higher for $\nu < 1$ than that for $\nu = 1$. Third, the sensitivity of contrast is maximized when ν is minimized.

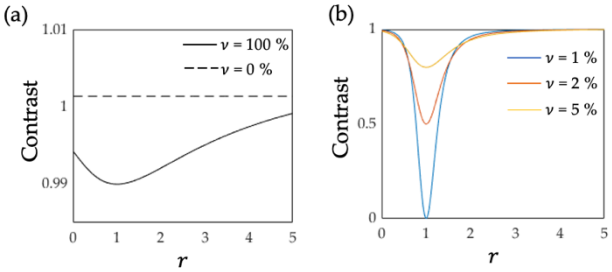

Figure 4 *Contrast of intensity fluctuations as a function of aspect ratio for 100 particles distributed (a) in a single co and cross-polarized and (b) two orthogonally polarized interaction volumes.*

4 Discussion and Conclusions

The improved sensitivity can be understood by considering the length distributions and number of steps in the random walk model. Analyzing the orientation averaged scattered intensities indicates that when excited by identical fields, the intensity scattered by a single axisymmetric dipole is, on average, higher in the co-polarized setting. Hence, when a subset of all particles is excited in this manner, the magnitude of the associated phasors are increased compared to the ones corresponding to the cross-polarized particles. From a macroscopic point of view, the space-polarization structuring effectively reduces the total number of particles contributing to the final field leading to a non-gaussian distribution of measured intensities [8, 10].

Since the mismatch between co and cross-polarized scattered intensities reaches a maximum around $r = 1$, the effective number reduction is most prominent for particle aspect ratios close to 1. Consequently, the highest sensitivity enhancement is observed around $r = 1$, which could be an appealing practical characteristic. Furthermore, adjusting the volume ratio ν allows control over the range of aspect ratios within which this improvement occurs.

In conclusion, we modeled the fluctuations of intensity scattered from a sparse distribution of subwavelength axisymmetric particles excited by space-polarization entangled fields. We demonstrate that by tuning the polarization state of the illumination across distinct spatial regions one can isolate the volume of interaction and effectively control the number of particles contributing to the detected intensity. This all-optical procedure permits establishing the desired regime of non-gaussian intensity

fluctuations in which the sensitivity to scatterers' asymmetry can be optimized. The results presented here should be of interest for characterizing non-spherical particles for biosensing[11, 12], monitoring polymerization[13, 14] and characterizing naturally occurring random media[15].

5 References

[1] [B. J. Berne and R. Pecora, Dynamic light scattering: with applications to chemistry, biology, and physics. Dover Publications, 2000.

[2] J. G. Walker, P. C. Y. Chang, K. I. Hopcraft, and E. Mozaffari, "Independent particle size and shape estimation from polarization fluctuation spectroscopy," Measurement Science and Technology, vol. 15, no. 5, pp. 771-776, 2004/03/26 2004, doi: 10.1088/0957-0233/15/5/001.

[3] Z. Bouchal and M. Olivík, "Non-diffractive Vector Bessel Beams," Journal of Modern Optics, vol. 42, no. 8, pp. 1555-1566, 1995/08/01 1995, doi: 10.1080/09500349514551361.

[4] A. Aiello, F. Töppel, C. Marquardt, E. Giacobino, and G. Leuchs, "Quantum–like nonseparable structures in optical beams," New Journal of Physics, vol. 17, no. 4, p. 043024, 2015/04/15 2015, doi: 10.1088/1367-2630/17/4/043024.

[5] Photopolarimetry in Remote Sensing. Kluwer Academic Publishers, 2004.

[6] D. Haefner, S. Sukhov, and A. Dogariu, "Stochastic Scattering Polarimetry," Physical Review Letters, vol. 100, no. 4, p. 043901, 01/28/ 2008, doi: 10.1103/PhysRevLett.100.043901.

[7] S. Sukhov, D. Haefner, and A. Dogariu, "Stochastic sensing of relative anisotropic polarizabilities," Physical Review A, vol. 77, no. 4, p. 043820, 04/16/ 2008, doi: 10.1103/PhysRevA.77.043820.

[8] A. P. Bates, K. I. Hopcraft, and E. Jakeman, "Particle shape determination from polarization fluctuations of scattered radiation," J. Opt. Soc. Am. A, vol. 14, no. 12, pp. 3372-3378, 1997/12/01 1997, doi: 10.1364/JOSAA.14.003372.

[9] E. Jakeman and K. D. Ridley, Modeling Fluctuations in Scattered Waves, 1 ed. CRC Press, 2006.

[10] E. Jakeman, "Polarization characteristics of non-Gaussian scattering by small particles," Waves in Random Media, vol. 5, no. 4, pp. 427-442, 1995/10 1995, doi: 10.1088/0959-7174/5/4/004.

[11] R. Chandrasekaran, T. Madheswaran, N. Tharmalingam, R. J. C. Bose, H. Park, and D.-H. Ha, "Labeling and tracking cells with gold nanoparticles," Drug Discovery Today, vol. 26, no. 1, pp. 94-105, 2021/01/01/ 2021, doi: https://doi.org/10.1016/j.drudis.2020.10.020.

[12] X. Yang, M. Yang, B. Pang, M. Vara, and Y. Xia, "Gold Nanomaterials at Work in Biomedicine," Chemical Reviews, vol. 115, no. 19, pp. 10410-10488, 2015/10/14 2015, doi: 10.1021/acs.chemrev.5b00193.

[13] R. Wu, J. R. Guzman-Sepulveda, A. P. Kalra, J. A. Tuszynski, and A. Dogariu, "Thermal hysteresis in microtubule assembly/disassembly dynamics: The aging-induced degradation of tubulin dimers," Biochemistry and Biophysics Reports, vol. 29, p. 101199, 2022/03/01/ 2022, doi: https://doi.org/10.1016/j.bbrep.2021.101199.

[14] H. J.J. and J. T., "Online Monitoring of Polymerizations: Current Status," European Journal of Organic Chemistry, 2017.

[15]] P. Piedra, A. Kalume, E. Zubko, D. Mackowski, Y.-L. Pan, and G. Videen, "Particle-shape classification using light scattering: An exercise in deep learning," Journal of Quantitative Spectroscopy and Radiative Transfer, vol. 231, pp. 140-156, 2019/07/01/ 2019, doi: https://doi.org/10.1016/j.jqsrt.2019.04.013.

DROPLETS

OPTICAL LATTICES AND STRUCTURAL TRANSITIONS IN MICRODROPLETS OF COLLOIDAL SUSPENSION PROBED WITH LUMINESCENT NANOPARTICLES.

Yaroslav SHOPA [1], Maciej KOLWAS [2], Izabela KAMIŃSKA [2], Gennadiy DERKACHOV [2], Kwasi NYANDEY [2-3], Tomasz JAKUBCZYK [4], Tomasz WOJCIECHOWSKI [2-5] and Daniel JAKUBCZYK [2,*]

[1] Faculty of Mathematics and Natural Sciences. College of Sciences, Cardinal Stefan Wyszyński University in Warsaw, Warsaw, 01-815, Poland
[2] Institute of Physics, Polish Academy of Sciences, Warsaw, 02-668, Poland
[3] Laser and Fibre Optics Centre, Department of Physics, School of Physical Sciences, College of Agriculture and Natural Sciences, University of Cape Coast, Cape Coast, Ghana
[4] Institute of Control and Computation Engineering, Warsaw University of Technology, Warsaw, 00-665, Poland
[5] International Research Centre MagTop, Institute of Physics, Polish Academy of Sciences, Warsaw, 02-668, Poland

Corresponding author: jakub@ifpan.edu.pl

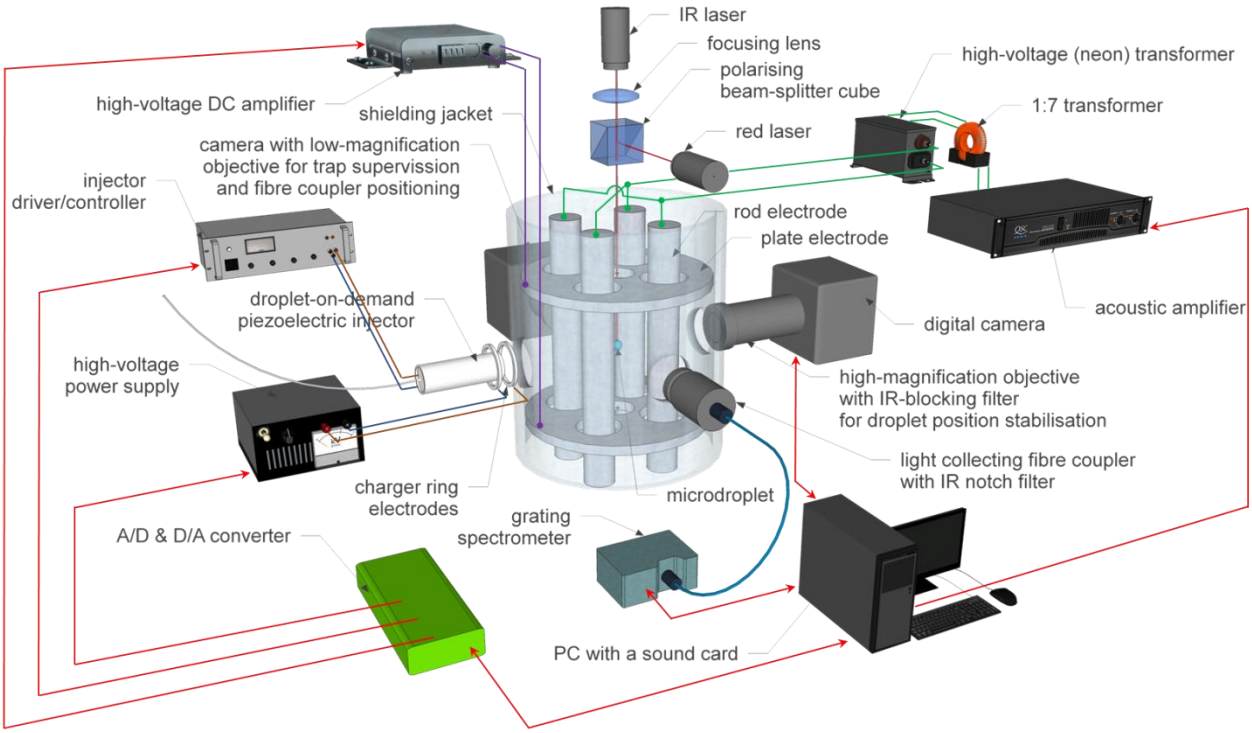

Figure 1 *Experimental setup schematic visualisation.*

Abstract

Luminescent nanoparticles (LNPs) were used as nano-probes to investigate possible evolution scenarios of slowly evaporating free microdroplets of (light-absorbing) suspension. Single microdroplets were kept in a linear electrodynamic quadrupole trap. It was found that intense (~50 W/mm^2) laser light may influence the distribution of light-absorbing nanoparticles in the microdroplet. Since the microdroplet acted as an optical spherical resonance cavity, the interaction of nanoparticles with light reflected the internal light field mode structure. Such interaction becomes nonlinear via positive feedback. It led, among others, to a very significant increase in modulation depth and narrowing of spherical cavity resonance maxima (of whispering gallery modes observed both in luminescence and scattering. Though such nonlinear phenomena are not expected to be induced by solar light intensities, they should be considered for freely propagating laser beams at light intensities much lower than those usually associated with non-linear optical phenomena.

1 Experimental setup and procedures

The experiments were conducted in a linear electrodynamic quadrupole trap (LEQT) (compare [1]) equipped with two plate electrodes perpendicular to the trap axis

(Figure. 1). The LEQT axis was kept in vertical position – an orientation/symmetry favourable for balancing the levitated microdroplet weight and eventual other forces along this axis (see below). Electrically charged droplets were confined horizontally with the quadrupolar AC field of rod electrodes, while vertical confinement was achieved with the DC field of plate electrodes. The field between the plates electrodes in the presented configuration is not homogeneous but exhibits a gradient, which enables translating of microdroplets vertically by varying the applied voltage. The (vertical) position of the levitating microdroplet was observed with a digital camera (Smartek, GC651MP, equipped with IR filters) through a high-magnification microscope with the resolution of ~1 μm/pixel. This enabled setting up a stabilization loop and keeping the droplet at the desired vertical location – on the (horizontal) axis of the light-collecting optics. In order to find this point, an analogue camera with medium-magnification objective was placed in front of light-collecting optics. This camera also enabled supervision of the volume of the trap and detecting unwanted stray microdroplets /microparticles.

The trap had aluminium shielding jacket, which screened it from external (static) fields and minimized thermal gradients along the wall. The trap with shielding was kept in an air-tight chamber (not shown in the figure) with windowed ports.

Microdroplets were delivered to the trap with a droplet-on-demand piezoelectric injector equipped at the nozzle with annular electrodes for droplet charging. The charging high voltage was switched on only for the droplet injection while off directly afterwards, in order not to influence the trapping field during the stabilising loop operation.

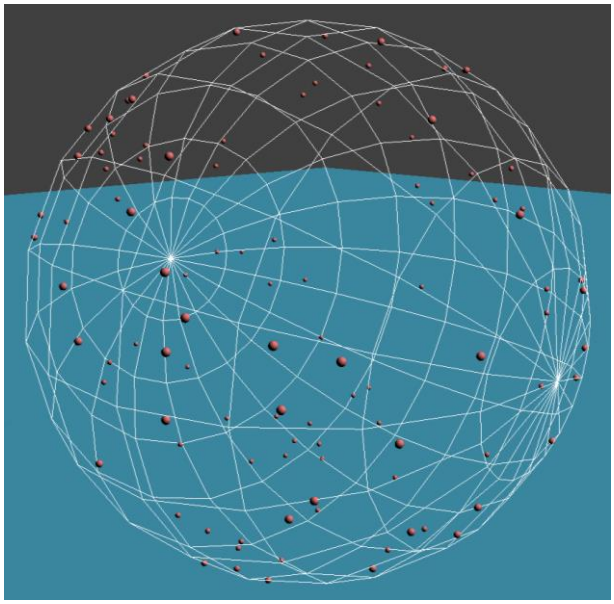

Figure 2 *Visualization of a distribution of 102 LNPs in a microdroplet obtained with the evolution numerical model. The LNP and microdroplet radii were 435 nm and 39 μm respectively. Coulomb repulsion was taken into consideration, but no interaction with light.*

In the presented experiments, the microdroplets were formed from a suspension of Gd_2O_3: 1% Nd^{3+} LNPs in tetraethylene glycol. The LNPs were produced in-lab with the homogeneous precipitation method (compare [2]). 0.89 g of gadolinium nitrate $Gd(NO_3)_3 \cdot 5H_2O$ and 3.6 mg of neodymium chloride $NdCl_3 \cdot 6H_2O$ were used for the synthesis. 3.6 g of urea $CO(NH_2)_2$ were used as the reducing agent. An aqueous solution (200 ml) of oxidants and reducing agent was prepared, which was heated to 85°C and shaken in a water bath for 4 h. The obtained nanoparticles were washed in distilled water four times and centrifuged in a laboratory centrifuge. Centrifugation parameters: 6000 rpm, 15°C, 15 minutes. A white powder was obtained which was dried overnight in a drying oven. Next, the nanoparticles were calcined in a laboratory furnace at 900°C for 3h. We used LNPs with the diameter of 870±5 nm (compare Figure. 2). The dispersion medium was chosen for its very low volatility and high polarizability. Slow evaporation of the droplet enabled long integration time in light-detection scheme, while high polarizability ensures easy and stable microdroplet charging. The initial LNPs concentration in the prepared suspension was ~5 mg/ml (which corresponds to ~10 LNPs in a 12-nm-radius droplet). However, due to the density of Gd_2O_3 (7.1 g/cm^3) being much higher than that of tetraethylene glycol (1.1 g/cm^3), sedimentation readily manifests, leading to significant variation in the actual initial LNPs concentration in microdroplets. We tried to avoid this by conducting suspension preparation, injector loading and droplet injection (experiment) in quick succession.

The levitating microdroplet was illuminated with two perpendicularly polarized CW laser beams of two wavelengths: 805 nm (IR, 1.6 W) and 655 nm (red, 30 mW). Both beams were used for scattering measurements, while the IR was also used for luminescence excitation, and the red for droplet position stabilization.

For optical probing of the microdroplet we used Nd^{3+} luminescence at 5 close-lying spectral lines: 879, 892, 894, 911, 927 nm. In particular the 892-894 nm doublet presented a valuable sounding tool. The experiments on luminescence of Gd_2O_3:Nd^{3+}, were conducted with FT spectrometer (Bomem, DA8) equipped with PMT (ФЭУ-62) covering the spectral range of 400-1100 nm, showed that the luminescence intensity of Nd^{3+} at the 5 lines mentioned above is comparable to the intensity at 1064 nm – usually the most prominent Nd^{3+} line. For the presented preliminary experiments we used a small grating spectrometer with a Si detector (Ocean Optics USB4000, 25 μm slit), which was much easier to integrate with the LEQT.

In order to obtain a measurable luminescence signal, the IR beam was (mildly) focused. In consequence, it exerted significant forces, both gradient and photophoretic – thus the choice of the trap type – LEQT and

geometry/orientation. By following the stabilizing loop DC voltage, the forces could be balanced and measured, thus providing additional information.

The scattered light (red and IR) as well as the luminescence were collected with a dedicated objective with aspheric achromatic optics. The objective was equipped with a notch filter (805 nm, OD 6) and coupled to a multimode 600-μm-core fibre feeding the light to a grating spectrometer. Reasonable luminescence signals were obtained for exposition/integration times ~1 s, which set the luminescence and scattering signals temporal resolution. However, the temporal resolution of the vertical force measurement was limited only by the camera frame rate (~50 fps), which yielded ~20 ms. The evolutions of each spectral line intensity was extracted from obtained spectra sequences.

2 Experimental results

A very interesting phenomenon could be observed for a relatively low concentration of LNPs (compare [3–5]). For initial concentration of 1 mg/ml and a microdroplet of 39 μm radius, there are ~102 LNPs in the droplet (compare Figure. 2). When evenly distributed on the droplet surface, their average distance would be ~15 μm. Since the microdroplet was evaporating very slowly (~0.35 nm/s), many optical cavity resonances could be observed.

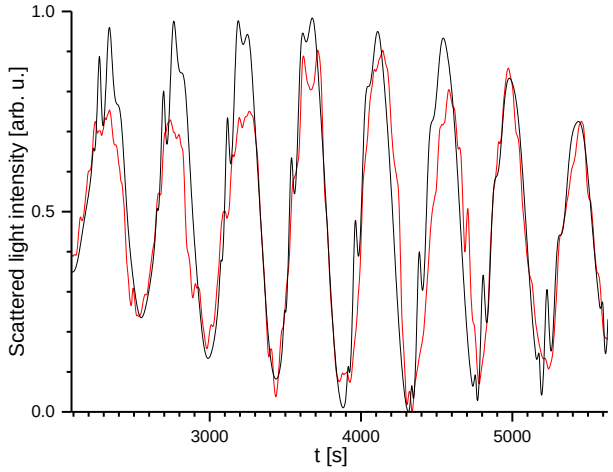

Figure 3 *Evolution of scattered light intensity at 654 nm. Red – mildly smoothed experimental results (LOWESS, 19/3055 of range window), black – Mie theory prediction for a weakly absorbing sphere (see text).*

Due to low LNPs concentration, the broad resonances of a microdroplet as a whole are plainly visible both in scattering as in luminescence all the time. The effective absorption of radiation by the droplet was small – the resonances modulation depth was generally high. Under closer scrutiny (Figure. 3), a fine resonance structure can also be detected, again, both in scattering and luminescence.

The broad resonance structure of scattered light intensity could be nicely fitted with Mie theory, while for the fine structure, only some of the peaks positions could be reproduced with a reasonable accuracy. This is only to be expected, since the field modes responsible for the narrow resonances are located close to the microdroplet surface, where LNPs proceed to concentrate and the medium inhomogeneity is highest. The effective imaginary part of the refractive index $\Im(n)$ at 654 nm, estimated with the fitting was $5 \cdot 10^{-5}$i.

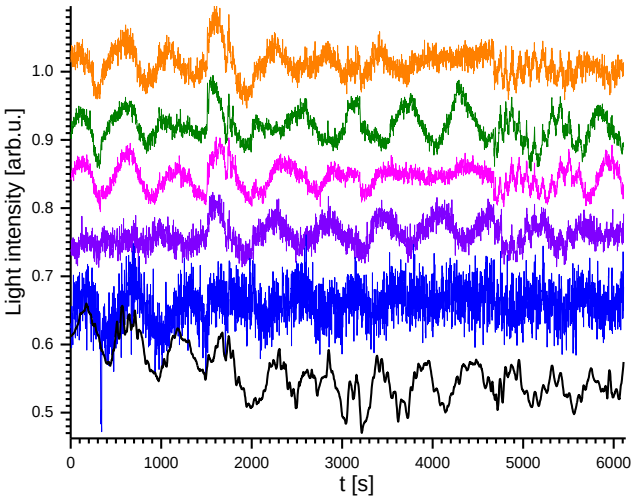

Figure 4 *An evolution of light intensities representative for low LNPs concentration: black line – scattering near the excitation wavelength (805 nm), color lines – luminescence: orange – 879 nm, green – 894 nm, pink – 911 nm, violet – 927 nm, blue – 942 nm. The vertical scaling of each graph trace is independent.*

The luminescence signal is more difficult to interpret as carrying more information and hence also more interesting. The exact shape of luminescence signal cannot be predicted at this stage of the model development (compare Figure. 6), since the details of coupling/interaction of luminescent nanoparticles with the internal light fields of the microdroplet (excitation and luminescence) is unknown. Interestingly, the fine resonance structure of the signal precisely corresponds such structure in the scattering signal. Since the resonances of the internal field

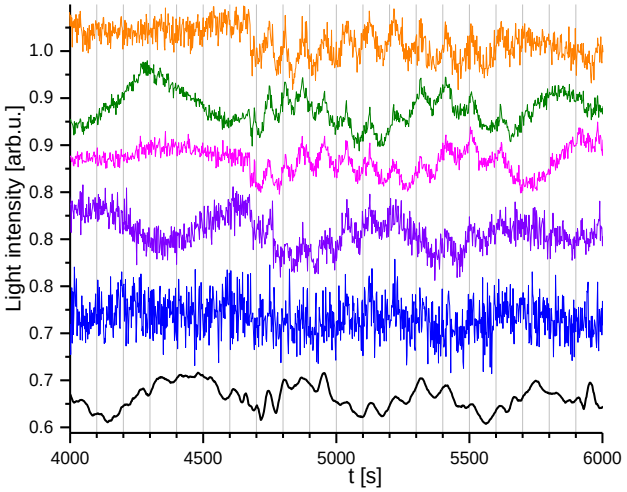

Figure 5 *Magnification of ROI from Figure. 4: spherical resonator mode – LNPs lattice resonance.*

correspond to those of scattering, it can be inferred that the correspondence results from absorption of 805-nm-wavelength internal field higher modes by near-surface LNPs. The slow oscillations visible in the signal correspond to lower modes of internal field – distributed more evenly in the droplet volume – and exhibit influence of microdroplet eigenmodes at the wavelength of the luminescence (compare Figure. 6). Some synchronization with the excitation field (805 nm) modes seems to persist, in particular when that field is stronger at the beginning of the droplet evolution. This may indicate some influence of strong excitation field modal structure, either via LNPs ordering (with photophoretic or gradient forces) or by creating an ordered distribution of refractive index via local heating due to absorption in the medium (for 805 nm $\Im(n)$ is over an order of magnitude higher than for 654).

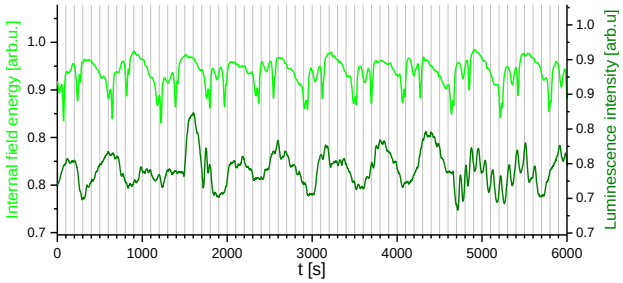

Figure 6 *Dark green – mildly smoothed (Savitzky–Golay, 25/3055 of range window) luminescence signal at 984 nm (compare Figures. 4 and 5); light green – corresponding total internal field (energy) calculated with Mie theory for $\Im(n)$ found previously in NIR region.*

For the most part of the observed microdroplet evolution the modulation depth of the fine structure seems in accordance with the $\Im(n)$ found (Figure. 6). However, at a certain moment (4675 s, see Figures. 4–6) the luminescence signal slightly but abruptly falls and the fine structure modulation depth becomes very significant. Furthermore, each constructive fine resonance peak exhibits a very narrow central maximum. Higher modulation depth is also visible in scattering at excitation wavelength. Again, the fine signal structure is in synchronisity with such strutcture of the excitation field, while the broad structure is not and corresponds to eigenmodes at luminescence lines. The proposed scenario is that the surface LNPs are ordered by the excitation filed via photophoretic forces, which direct LNPs to local field minima – hence slight decrease of overall luminescence intensity – thus forming an LNPs latice (near the droplet surface), which in resonance with the excitation field (modes). The process provides a positive feedback (stronger field – finer positioning in the node), which results in narrowing of resonance maxima. For some time the LNPs latice follow the evolution of field nodes, but due to microdroplet movements/rotations the order is gradually lost. As can be seen in Figure. 2, forming of LNPs lattice by Coulomb forces is out of question for such a low concentration fo LNPs.

The onset of the same phenomenon can also be spotted at 1749 s. However, the manifestation was much shorter.

3 Acknowledgement

This research was funded in whole or in part by National Science Centre, Poland, grant 2021/41/B/ST3/00069. For the purpose of Open Access, the author has applied a CC-BY public copyright license to any Author Accepted Manuscript (AAM) version arising from this submission.

4 References

[1] Woźniak M., Archer J., Wojciechowski T., Derkachov G., Jakubczyk T., Kolwas K., Kolwas M., Jakubczyk D., Application of a linear electrodynamic quadrupole trap for production of nanoparticle aggregates from drying microdroplets of colloidal suspension, Journal of Instrumentation, 14: P12007 (18pp) (2019)

[2] Kaminska, I. et al. Single-step synthesis of Er3+ and Yb3+ ions doped molybdate/Gd2O3 core-shell nanoparticles for biomedical imaging, Nanotechnology, 29: 025702 (19pp) (2018)

[3] Kolwas M., Jakubczyk D., Archer J., Do Duc T., Evolution of mass, surface layer composition and light scattering of evaporating, single microdropletes of SDS/DEG suspension. Shrinking droplet surface as the micelles generator, Journal of Quantitative Spectroscopy & Radiative Transfer, 258 :107396 (10pp) (2021)

[4] Kolwas M.., Kolwas, K., Jakubczyk, D., Derkachov G., Collective Scattering of Light on Gold Nanospheres Dispersed in Diethylene Glycol Microdroplet, Acta Physica Polonica A, 131:288-293 (2017)

[5] Kolwas M., Kolwas K., Derkachov G., Jakubczyk D., Surface Diagnostics of Evaporating Droplet of Nanospheres Suspension; Fano Interference and Surface Pressure, Phys. Chem. Chem. Phys., 17:6881-6888 (2015)

13th International Conference Series on
Laser-light and Interactions with Particles
Optical Particle Characterization follow-up !
August 21-26th, 2022, Warsaw, Poland

ASSESSMENT OF NON DIFFRACTIVE CONTRIBUTIONS IN THE FORMATION AND ANALYSIS OF DIGITAL HOLOGRAMS

Fabrice R.A. ONOFRI

[1] Aix-Marseille Université, CNRS, IUSTI, UMR 7343, 13453 Marseille Cedex 13, France
*Corresponding author: fabrice.onofri@univ-amu.fr

Abstract

The influence of non-diffractive scattering mechanisms in the formation and analysis of Digital-In-Line (DIH) holograms is studied. The electromagnetic calculations are performed with the Generalized Lorenz-Mie Theory (GLMT), as well as Debye's series and the localization principle. Numerical results clearly demonstrate the importance to account for partially refracted waves and, to a lesser extend, of edge waves effects.

1 Introduction

DIH is generally considered to be a laser diffraction technique operating in the near-field (i.e. for Fresnel numbers, $F \geq 1$ [1]). As the result of a pure diffraction process, induced by the discontinuity in the optical properties of the propagating medium at the particle boundary (2D projected contour of the particle), the hologram characteristics are thus independent from the particle material properties. Therefore, the hologram formation can be simply modelled with the scalar diffraction theory and a particle model reduced to a two-dimensional opaque disk (or a pinhole, according to Babinet's principle)[1].

However, in the recent years, several groups have demonstrated that with DIH the refractive index of a spherical particle can be measured, with a reasonable accuracy, from the analysis of its hologram. For micron-sized particles, this measure of the refractive index is obtained using a parametric method fitting the particle hologram intensity profile with those calculated with the Lorenz-Mie Theory (LMT, e.g. [2, 3]). For larger particles, the refractive index can be measured directly from the analysing of the relative position of the photonic jet (PJ, also called the focusing or forward caustic region [4-7]) produced by rays that are single refracted within the particle [8]. These two approaches clearly infirm the aforementioned vision of hologram formation. To go further on, and most notably to extract more accurate or additional data from particle holograms, it is fundamental to better understand how the particle material properties and the various scattering mechanisms influence the formation of a hologram. This is important whether the particle properties are retrieved from the hologram directly, with a back propagation method (e.g. [4, 9, 10]), or with an inverse approach (e.g. [11, 12]).

The goal of the present work is precisely to investigate these relative contributions and more specially the non-diffractive scattering mechanisms. The extended abstract is organized as follows. After this brief introduction, section 2 introduces and discusses the basic equations to calculate rigorously, in the frame of the GLMT, the properties of the holograms formed by a spherical particle that is illuminated by a plane wave or a shaped electromagnetic beam. Afterwards, the principle of the Debye series decomposition and the localization principle (LP) are employed to evaluate the contributions of the different scattering mechanisms. Section 3 briefly summarizes the basic steps of the code developed to perform these calculations as well the backpropagation of holograms. The paper concludes with section 4, where exemplifying numerical results are presented and discussed.

2 Excact calculation of hologram formation

2.1 Generalized Lorenz-Mie theory

A spherical particles, with radius a and refractive index m_p, is located in a continuous medium with refractive index m_0. The particle is centered in the Cartesian coordinate system $(Oxyz)$ and the spherical coordinate system $(Or\theta\phi)$ where, classically, θ is the scattering angle [13]. The observation plane $(O_p xyz_p)$, also referred as the hologram-recording plan (or CCD chip), is parallel to (xy) and distant of z_p from the particle centre. The particle, with relative refractive index $m_r = m_p / m_0$, is illuminated by an incident harmonic beam, with wavelength λ_0 and beam waist ω_0, propagating along z. According to the GLMT [14, 15], the components of the electrical field vector $\mathbf{E}^s(\mathbf{r})$ that is scattered by the particle in the near or far-fields read as:

$$E_r^s = -k_0 E_0 \sum_{n=1}^{+\infty} \sum_{m=-n}^{+n} c_n^{pw} A_n^m \begin{bmatrix} \xi_n''(k_0 r) \\ +\xi_n(k_0 r) \end{bmatrix} P_n^{|m|}(\cos\theta) e^{im\phi}$$

$$E_\theta^s = -\frac{E_0}{r} \sum_{n=1}^{+\infty} \sum_{m=-n}^{+n} c_n^{pw} \begin{bmatrix} A_n^m \xi_n'(k_0 r) \tau_n^{|m|}(\cos\theta) \\ +mB_n^m \xi_n(k_0 r) \pi_n^{|m|}(\cos\theta) \end{bmatrix} e^{im\phi}$$

$$E_\phi^s = -\frac{iE_0}{r} \sum_{n=1}^{+\infty} \sum_{m=-n}^{+n} c_n^{pw} \begin{bmatrix} mA_n^m \xi_n'(k_0 r) \pi_n^{|m|}(\cos\theta) \\ +B_n^m \xi_n(k_0 r) \tau_n^{|m|}(\cos\theta) \end{bmatrix} e^{im\phi} \quad (1)$$

where (ξ_n, ξ_n', ξ_n'') stand for Ricatti-Bessel functions and their derivatives, $k_0 = 2\pi/\lambda_0$ and E_0 for the wave vector and the amplitude of the incident beam at a particular point,

c_n^{pw} is a coefficient specific to the plane wave illumination case with

$$c_n^{pw} = k_0^{-1} i^{n-1} (-1)^n (2n+1) / [n(n+1)] \quad (2)$$

The radial functions $P_n^{|m|}$, and $\tau_n^{|m|}, \pi_n^{|m|}$ are the associated Legendres polynomials and the generalized Legendres functions respectively,

$$P_n^{|m|}(\cos\theta) = (-1)^m (\sin\theta)^m \frac{d^m P_n(\cos\theta)}{(d\cos\theta)^m}$$
$$\tau_n^m(\cos\theta) = \frac{d}{d\theta} P_n^m(\cos\theta);\ \pi_n^m(\cos\theta) = \frac{P_n^m(\cos\theta)}{\sin\theta} \quad (3)$$

where P_n and d stand for the Legendres polynomials of order n and the derivative operator respectively. The coefficients $A_n^m = g_{n,TM}^m a_n$ and $B_n^m = g_{n,TE}^m b_n$, where TM and TE stand for Transversal Magnetic (i.e. parallel polarization component) and Transversal Electric (i.e. perpendicular polarization component), are the generalized external scattering coefficients. They account for the particle shape *via* the external particle scattering coefficients a_n, b_n of the LMT, for homogeneous [13] (or multilayered [14]) spheres. The A_n^m and B_n^m also account for the beam shape through the beam shape coefficients (BSC) $g_{n,TM}^m$, $g_{n,TE}^m$ of the GLMT [15]. The integer numbers n and m stand for the expansion number of the LMT and the beam azimuth number of GLMT respectively. The analysis of the convergence of the infinite series (such as Eq. (1), or more simply a_n, b_n [13]) show that, after a slow oscillating behaviour, they converge rapidly when the value of n exceed the particle size parameter, ka. So that, the infinite series can be truncated and the limit $n \to +\infty$ replaced by a maximum value n_{max} estimated numerically with a fitting procedure. In the case of intermediate sized particles (i.e. $8 < ka < 4200$) [16], one can use:

$$n_{max} = k_0 a + \varepsilon_{max} (k_0 a)^{1/3} + 2 \quad (4)$$

with $\varepsilon_{max} = 4.05$. More details about the magnetic field and internal fields components as well as the different ways to calculate the BSC can be found in Refs. [14, 15].

2.2 Debye series and localization principle

From the expansion series of the LMT and the GLMT, little can be said about the particle scattering mechanisms. Debye series allow clarifying the situation by decomposing the series of the LMT in terms of partial waves that are meaningful in the frame of the more intuitive Geometrical Optics Approximation (GOA). For instance, the external scattering coefficient of a homogeneous spherical particle maybe rearranged as follows:

$$\left.\begin{matrix} a_{n,p} \\ b_{n,p} \end{matrix}\right\} = (1/2)\left[\left(1 - R_{n,\chi}^{(22)}\right) - T_{n,\chi}^{(21)} \left(R_{n,\chi}^{(11)}\right)^{p-1} T_{n,\chi}^{(12)} \right] \quad (5)$$

where $\chi = TE$ for a_n and $\chi = TM$ for b_n, p stands for the partial wave and scattering mechanism order (with $p=1$ for single refraction, $p=2$ for double refraction, etc.). The coefficients $R_{n,\chi}^{(22)}, R_{n,\chi}^{(11)}, T_{n,\chi}^{(21)}$ and $T_{n,,\chi}^{(12)}$, whose expressions can be found in Ref. [17], correspond, respectively, to reflections of partial waves on the outer and the inner surface of the particle, and transmissions into and out of the particle. The external (as well the internal) scattering coefficients of the LMT can be retrieved from Debye series by summing all possible partial waves:

$$\left.\begin{matrix} a_n \\ b_n \end{matrix}\right\} = (1/2)\left[1 - R_{n,\chi}^{(22)} - \sum_{p=1}^{+\infty} T_{n,\chi}^{(21)} \left(R_{n,\chi}^{(11)}\right)^{p-1} T_{n,\chi}^{(12)} \right] \quad (6)$$

Actually, in Eqs. (5) and (6), the last term into the brackets correspond to the different refracting processes ($p = 1,2,3...$, which intensity decrease rapidly for increasing p), while the first two terms, $\left(1 - R_{n,\chi}^{(22)}\right)$, account for three scattering processes that are encompassed in the scattering order $(p=0)$. The unit value is associated to a pure diffractive term [18, 19] since it is totally independent upon the particle material properties. In wave optics, it is this single term that it is generally assumed responsible for holograms formation. The second term, $R_{n,\chi}^{(22)}$ accounts for closely related scattering processes: surface waves, and grazing plus tunnelling rays. It is not possible to properly separate the later contributions in the frame of Debye series. However, this can be partly completed, approximatively, by invoking the localization principle (LP) introduced by Huslt's [8].

According to the LP, the expansion term n is also a partial wave number identifying rays (partial waves indeed) that hits or graze the particle surface at different distances ℓ_n from its centre

$$\ell_n = (n + 1/2)/k_0 \quad (7)$$

For $n + 1/2 = k_0 a$, this distance corresponds exactly to the particle radius a. The LP allows giving some meaning to Eq. (4). The first time ka corresponds to a region (from n=1 to $n \approx k_0 a$) where refracted and specular processes interact directly with the particle surface, while the second term $\varepsilon_{max} (k_0 a)^{1/3}$ corresponds to the width of a corona region surrounding the particle where grazing and tunnelling rays as well as surface wave effects take place [19]. The constant 2 is a fitting value ensuring a good convergence of the LMT series in a large variety of cases (i.e. particle size and refractive index ranges)[16].

3 Numerical calculation of hologram formation and backpropagation

The previous considerations have been implemented in a Matlab code allowing calculating accurately all the properties (amplitude, phase and intensity) of the incident, the internal, the scattered and the total electromagnetic field (incident plus scattered). The total electromagnetic intensity in the hologram-recording plane is simply a particular case. By using Debye series to calculate the external and internal scattering coefficients, the code allows separating the relative contributions (or calculate interference effects) of all refractive terms $(p = 1,2,3...)$ plus the pure diffractive term

(contained in $p=0$). Then, the LP is used to truncate Debye's series in order to separate the grazing-plus-tunnelling contributions from the surface waves contributions. Particular attention has been paid to the numerical stability of the calculations for particles with a large size parameter. For the hologram back-propagation, the Fresnel or Rayleigh-Sommerfeld approximations are used as depicted in Ref. [4].

4 Results and discusion

The numerical results presented herein allows to highlight various features of the "Photonic Jet Method" that was introduced to estimate simultaneously the particle size, refractive index, 3D position and dynamics [4, 5, 7]. Fig. 1 (a) shows, from top to bottom, the direct calculation of the total electromagnetic intensity in the near-field and the (yz) plan, some contour lines of the unwrapped phase of the total electrical field, and the near-field intensity profile along the optical axis of an oil droplet in water. The latter, with radius a=50μm and relative refractive index $m=1.0832$, is illuminated by a non-polarized plane wave with wavelength $\lambda=0.4753\mu m$. While Fig. 1 (a) accounts for all scattering processes (full LMT results), Fig. 1 (b-d) accounts only for (b) pure diffraction, (c) all non-diffractive terms included in the order $(p=0)$, i.e. specular, grazing, tunnelling and surface waves and (d) for the single refraction $(p=1)$. One can notice in Fig. 1 (a) the good agreement between LMT and Debye $(p=0,1,\cdots,100)$ results for the external as well as for the internal field. In Fig. 1 (b), the contribution of the non-diffractive components in the PJ region are clearly noticeable, when Fig. 1 (d) suggests that the structure of the caustic generated by refracted rays may be more complex that the one predicted by a GOA. The latter remarks are important for any attempt to develop a GOA or a Physical Optics Approximation (POA) of the PJ reconstruction.

Looking at the far field, it is again that the non-diffractive terms have a visible influence on the hologram characteristics, see Fig. 2. The parameters used for these simulations are identical to ones of the experimental setup of refs [5] (i.e. 4 megapixels camera located at 10 cm from a water droplet in air with diameter 1 mm, $\lambda=0.633\mu m$). Fig. 3 shows the results obtained when two of these holograms (pure diffraction and single refraction) are back propagated. It is found that the differences are rather small between the axial intensity profiles of the PJ retrieved with the single term $(p=1)$ and with full calculations.

However, the contrast of the reconstructed PJ, regarding the surrounding background, appears rather noisy, suggesting that the single refractive term is not enough to fully describe the forward caustic region.

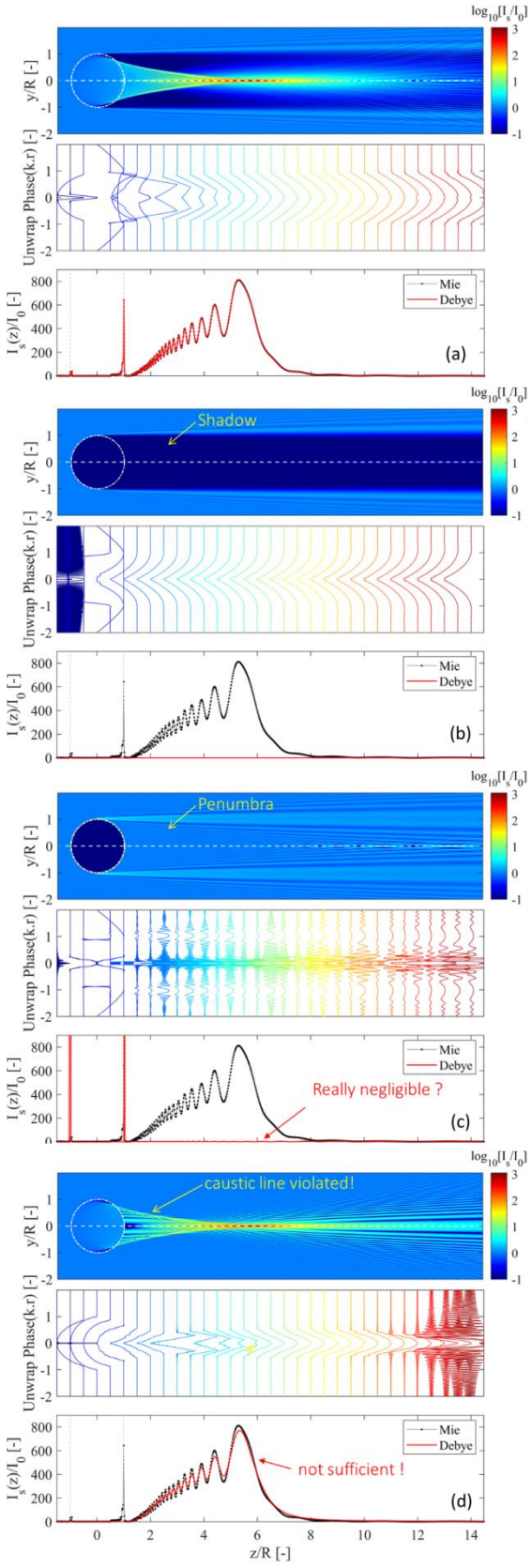

Figure 1 *Near-field intensity map, unwrapped phase and axial-intensity profile when (a) all scattering process are included, (b) only pure diffraction, (c) only edge-wave contributions excluding pure diffraction and (c) only single refraction. Scatterer: oil droplet in water ($k_\omega a$=661).*

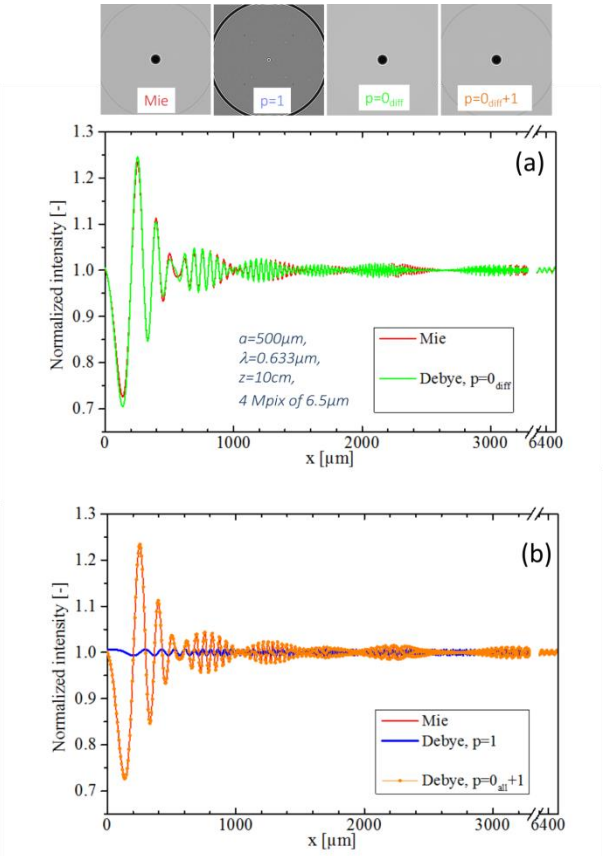

Figure 2 *Holograms (gray images) and their radial intensity profiles when all scattering processes are taken into account (Mie), only pure diffraction (p=0diff), only single refraction (p=1), single refraction and reflections (p=0all+1). Water droplet in air (k0a =4963).*

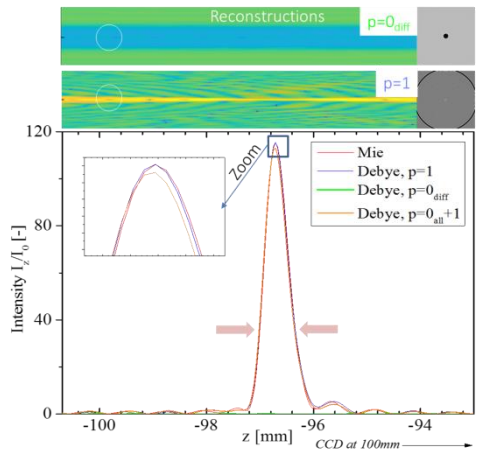

Figure 3 *Backpropagation of holograms of Fig. 2 and corresponding axial intensity profiles in the PJ region.*

5 References

[1] J. W. Goodman, "Introduction to Fourier Optic," Mac. Graw-Hill, New York (1960).

[2] S.-H. Lee, Y. Roichman, G.-R. Yi, S.-H. Kim, S.-M. Yang, A. v. Blaaderen, P. v. Oostrum, and D. G. Grier, "Characterizing and tracking single colloidal particles with video holographic microscopy," Opt. Express **15**, 18275-18282 (2007).

[3] H. Shpaisman, B. J. Krishnatreya, and D. G. Grier, "Holographic microrefractometer," Appl. Phys. Lett. **101**, 091102 (2012).

[4] M. P. L. Sentis, F. R. A. Onofri, and F. Lamadie, "Bubbles, drops, and solid particles recognition from real or virtual photonic jets reconstructed by digital in-line holography," Opt. Lett. **43**, 2945-2948 (2018).

[5] M. P. L. Sentis, F. R. A. Onofri, and F. Lamadie, "Photonic jet reconstruction for particle refractive index measurement by digital in-line holography," Opt. Express **25**, 867-873 (2017).

[6] L. Tian, H. Gao, and G. Barbastathis, "Digital holographic imaging of multi-phase flows," in *Imaging and Applied Optics*, OSA Technical Digest (CD) (Optical Society of America, 2011), CWB5.

[7] M. P. L. Sentis, L. Bruel, S. Charton, F. R. A. Onofri, and F. Lamadie, "Digital in-line holography for the characterization of flowing particles in astigmatic optical systems," Opt. Lasers Eng. **88**, 184-196 (2017).

[8] H. C. van de Hulst, *Light Scattering by Small Particles* (Dover Publications, New-York, 1957).

[9] L. Yao, X. Wu, Y. Wu, J. Yang, X. Gao, L. Chen, G. Gréhan, and K. Cen, "Characterization of atomization and breakup of acoustically levitated drops with digital holography," Appl. Opt. **54**, A23-A31 (2015).

[10] O. Kemppinen, Y. Heinson, and M. Berg, "Quasi-three-dimensional particle imaging with digital holography," Appl. Opt. **56**, F53-F60 (2017).

[11] F. Soulez, L. Denis, É. Thiébaut, C. Fournier, and C. Goepfert, "Inverse problem approach in particle digital holography: out-of-field particle detection made possible," J. Opt. Soc. Am. A **24**, 3708-3716 (2007).

[12] T. Latychevskaia and H.-W. Fink, "Practical algorithms for simulation and reconstruction of digital in-line holograms," Appl. Opt. **54**, 2424-2434 (2015).

[13] C. F. Bohren and D. R. Huffman, *Absorption and scattering of light by small particles* (Wiley & Sons, New york, 1998).

[14] F. Onofri, G. Gréhan, and G. Gouesbet, "Electromagnetic scattering from a multilayered sphere located in an arbitrary beam," Appl. Opt. **34**, 7113-7124 (1995).

[15] G. Gouesbet and G. Gréhan, *Generalized Lorenz-Mie Theories* (Springer, Berlin, 2011).

[16] W. J. Wiscombe, "Improved Mie scattering algorithms," Appl. Opt. **19**, 1505-1509 (1980).

[17] E. A. Hovenac and J. A. Lock, "Assessing the contribution of surface waves and complex rays to far-field scattering by use of the Debye series," J. Opt. Soc. Am. A **9**, 781-795 (1992).

[18] H. M. Nussenzveig, "High-frequency scattering by an impenetrable sphere," Annals of Physics **34**, 23-95 (1965).

[19] J. A. Lock and P. Laven, "Mie scattering in the time domain. Part II. The role of diffraction," J. Opt. Soc. Am. A **28**, 1096-1106 (2011).

13th International Conference Series on
Laser-light and Interactions with Particles
Optical Particle Characterization follow-up !
August 21-26th, 2022, Warsaw, Poland

GLARE POINTS AND NEAR-ZONE SAGITTAL CAUSTIC FOR SCATTERING OF A PLANE WAVE BY ASPHERICAL OR SPHEROIDAL BUBBLE FLOATING IN AIR

James LOCK [1,*] and Markus SELMKE [2]

[1] Physics Department, Cleveland State University, Cleveland, OH 44115, USA
[2] Fraunhofer Institute for Applied Optics and Precision Engineering IOF, Center of Excellence in Photonics, Albert-Einstein Str. 7, 07745 Jena, Germany

*Corresponding author j.lock@csuohio.edu

Abstract

We examine various features of scattering of a plane wave by a spherical or spheroidal bubble floating in air. We interpret the pattern of glare points observed on the far-zone image of the bubble, and the near-zone sagittal caustic of light scattered following one internal reflection. We find the symmetry inherent in these features for a spherical bubble is broken as the bubble is deformed into a shape of lower symmetry.

1 Introduction

We consider a linearly polarized monochromatic plane wave of light of wavelength λ incident on a nonabsorbing spherical bubble floating in air. The bubble has inner radius a and film thickness $d<<a$, with a~O(cm), and d~O(μm). The bubble film has real refractive index n, and both the region exterior to the bubble film and the interior of the bubble have unit refractive index. Rays are transmitted into the bubble, and internally reflect p-1 times from the bubble film before being transmitted out.

When an observer stands in the far-zone at a scattering angle Θ_{scatt} in the backward hemisphere and looks at a floating bubble illuminated by sunlight, he sees a sequence of glare points to each side of center that appear to lie on the image of the bubble. The observed glare points lie in the plane containing the bubble's center, the observer, and the light source. They are progressively closer together and become progressively dimmer as they approach the edge of the image of the bubble. Photographs illustrating this effect and taken by one of the authors (M.S.) are reproduced here as Figs.1,2. The location, intensity, and color of the glare points as viewed by the observer depend on the scattering angle and far-zone intensity of the light scattered by the bubble.

Since a spherical floating bubble is a surface of revolution with respect to the propagation direction of the incident plane wave, the two branches of the near-zone caustic of the scattered rays for each value of p can straightforwardly be determined. The tangential caustic is obtained by finding the locus of the intersection points of adjacent converging rays that are confined to a single plane. The tangential caustic for each value of p lies entirely inside the bubble and is not considered further here. The sagittal caustic is obtained by determining the locus the positions where azimuthal families of rays making p-1 internal reflections cross the z axis. The sagittal caustics on the positive z axis outside the bubble surface decrease very quickly in intensity as a function of z. As a result, in order to view the sagittal caustic, a viewing screen must be placed behind the bubble close to the floating bubble surface. This is also illustrated in Fig.1.

2 Floating Bubble Ray Theory

The floating bubble geometry is a special case of a coated sphere. In the short wavelength limit, $2\pi a/\lambda \sim 10^5$ we use a simplified version of coated sphere ray theory [1]. The usual reflection law is assumed to hold for a ray internally or externally reflected by the thin bubble film. We also assume that rays are transmitted through the thin bubble film without deflection. We model the intensity of the reflected and transmitted parts of the incident broadband spectrum at each interaction with the surface in three stages. First, the intensity Fresnel coefficient for coherent monochromatic light for a single flat interface between the bubble film and the air outside or inside the bubble is denoted by R for either the transverse electric or transverse magnetic polarization.

We are interested in the simplifications that occur for near-grazing rays, where the angle of incidence θ_i^0 is near 90°. We define the small quantity $\sigma<<1$ for these rays by

$$\sigma \equiv \cos(\theta_i^0) . \quad (1)$$

Then for rays with near-grazing incidence,

$$R = 1 - \alpha\sigma + O(\sigma^2) , \quad (2)$$

where α is a polarization-dependent constant of proportionality. Second, one sums the infinite series of successive coherent interactions of a ray with the outer and inner surfaces of the film. The resulting coherent intensity Fresnel coefficient for transmission through the film is T_{film}^{coh} and the resulting coherent intensity Fresnel coefficient for reflection by the film is R_{film}^{coh}. Third, the floating bubble is illuminated by broadband visible sunlight. Thus, the monochromatic intensity Fresnel coefficients must be integrated over both the source spectrum and the sensitivity of the eye of the observer for $0.4\mu m \approx \lambda_{min} \le \lambda \le \lambda_{max} \approx 0.7\mu m$. We make the simplifying assumptions that (i), both the source spectrum and the sensitivity of the eye of the observer are flat between λ_{min} and λ_{max}, and (ii) the film thickness is sufficiently large that the phase ε of the interference between successive paths in the film varies by at least $O(\pi)$ in this wavelength interval. The spectrum-averaged

intensity Fresnel coefficient for internal or external reflection of an incident ray by the thin film is then approximated by

$$(R_{film})^{ave} \approx (1/\pi) \int_0^{\pi} d\varepsilon \; R_{film}^{coh} \;, \quad (3)$$

and the spectrum-averaged intensity coefficient for transmission into the bubble interior and transmission back out following p-1 internal reflections is approximated by

$$(T_{film}\, R_{film}^{p-1}\, T_{film})^{ave} \approx (1/\pi) \int_0^{\pi} d\varepsilon \; T_{film}^{coh} (R_{film}^{coh})^{p-1} T_{coh}^{film} \;. \quad (4)$$

Assuming that the incident wave propagates in the $+z$ direction, we let $\Theta_p(\theta_i^0)$ be the deflection angle of the incident ray whose angle of incidence is θ_i^0 at the outer surface of the bubble film, and that makes p-1 internal reflections before exiting. for p=0 external reflection we have

$$\Theta_0(\theta_i^0) = \pi + 2\theta_i^0 \;, \quad (5)$$

and for $p\geq 2$ we have

$$\Theta_p(\theta_i^0) = (p\text{-}1)(\pi - 2\theta_i^0) \;. \quad (6)$$

We obtain the far-zone intensity of the light scattered by a spherical floating bubble using flux conservation. We assume that successive interactions of a ray with the bubble film at different locations on the floating bubble are incoherent with respect to each other. This assumption is valid because the path length of the ray between these interactions is comparable to the bubble radius, typically ~O(cm) or ~O(mm) for near-grazing incident rays, while the bubble film thickness and the longitudinal coherence length of sunlight are ~O(μm). The far-zone scattered intensity for rays making p-1 internal reflections at the spherical bubble film for $p\geq 2$ is

$$I_p^{scatt}(\Theta_{scatt}) = I_{inc}(a/R_{vs})^2 [1/2(p\text{-}1)][\sin(\theta_i^0)\cos(\theta_i^0)/\sin(\Theta_{scatt})] \times [T_{film}(\theta_i^0)\, R_{film}^{p-1}(\theta_i^0)\, T_{film}(\theta_i^0)]^{ave} \;, \quad (7)$$

where I_{inc} is the intensity of the incoming ray, and R_{vs} is the distance from the center of the floating bubble to the far-zone viewing screen, and the scattering angle Θ_{scatt} associated with the deflection angle Θ_p lies within the interval $0°\leq\Theta_{scatt}\leq 180°$. The polarization of the spectrum-averaged intensity coefficients depends on the plane of incidence of the ray. Similarly, the externally reflected contribution to the scattered intensity is

$$I_0^{scatt}(\Theta_{scatt}) = I_{inc}\,(a/2R_{vs})^2\,[R_{film}(\theta_i^0)]^{ave} \;. \quad (8)$$

Since the directly transmitted light is forward-propagating, it is combined with diffraction to obtain $I_1^{scatt}(\Theta_{scatt})$ in the near-forward direction.

3 Reflection Glare Points of a Spherical Floating Bubble

When the far-zone observer either focuses his eyes on the bubble or photographs it, he records the magnitude-squared of the Fourier transform of the far-zone scattered intensity that is windowed in an interval centered on Θ_{scatt}, whose width is determined by the eye's or camera's aperture [2]. Let the coordinate χ extend from edge to edge, $-L\leq\chi\leq L$, on the equator of the image of the bubble recorded by the observer. The location of the center of the $M\geq 0$ glare spot for p-1 internal reflections of the ray from the bubble film with $p\geq 2$ is then [2,3]

$$\chi_{p,M} = L\cos\{(\Theta_{scatt}+2\pi M)/[2(p\text{-}1)]\} \;, \quad (9)$$

where the range of allowed values of M are

$$0 \leq (\Theta_{scatt} + 2\pi M)/[2(p\text{-}1)] \leq \pi \;. \quad (10)$$

The center of the external reflection glare point for $(p,M)=(0,0)$ occurs at

$$\chi_{0,0} = -L\cos(\Theta_{scatt}/2) \quad (11)$$

corresponding to the angle of incidence $-\theta_i^0$. The center of the one-internal-reflection glare point for $(p,M)=(2,0)$ occurs at

$$\chi_{2,0} = L\cos(\Theta_{scatt}/2) \quad (12)$$

corresponding to the angle of incidence of $+\theta_i^0$. These two glare points are symmetrically located on the equator of the image of the spherical floating bubble, and with Θ_{scatt} in the backward hemisphere, are the brightest glare spots observed. Their intensity ratio is

$$I_{2,0}^{glare} / I_{0,0}^{glare} = (1\text{-}R)(1\text{-}R+R^2)/(1+R^4) \;. \quad (13)$$

If the bubble film has n=1.333, the glare point intensity ratio decreases from 0.886 to zero as the observer moves from Θ_{scatt}=180° where θ_i^0=±0°, to Θ_{scatt}=0° where θ_i^0=±90°.

When the observer is in the backward hemisphere, the sequence of closely-spaced glare points seen near the edge of the bubble, and which are due to rays having near-grazing incidence, become progressively dimmer as $\chi\rightarrow|L|$ because

$$I_{p,M}^{glare} \propto \sigma^2 \;. \quad (14)$$

From top to bottom in Fig.1, the visible glare points are $7\geq p\geq 2, M=0$, then $p=0, M=0$, then $3\leq p\leq 8, M=p\text{-}2$. The scattering angle of the observer is $\Theta_{scatt}\approx 133°$.

4 Sagittal Caustic of a Spherical Floating Bubble

The parametric equation of the sagittal caustic as a function of p and $0\leq|\theta_i^0|\leq 90°$ is

$$z_s = (-1)^p\, a\, \sin(|\theta_i^0|) \,/\, \sin[2(p\text{-}1)|\theta_i^0|] \quad (15a)$$

$$\rho_s = 0 \;. \quad (15b)$$

Each value of p contributes its own sagittal caustic, and all the sagittal caustics lie on top of each other on the z axis. The p=2 sagittal caustic lies inside the bubble for $0°\leq\theta_i^0\leq 60°$, and outside the bubble on the $+z$ axis for $60°<\theta_i^0\leq 90°$. Its location on the z axis as a function of σ in the near-grazing incidence regime is

$$z_s \approx a/2\sigma + O(\sigma^2), \quad (16)$$

and its relative intensity, [4]

$$I_{rel} \approx I_{inc}\,(1/128)\,\alpha a^5/z^4 \;, \quad (17)$$

falls off very rapidly as a function of z.

5 Reflection Glare Points of a Spheroidal Floating Bubble

As a floating bubble is launched, it undergoes transient shape oscillations that quickly damp out to a final spherical shape. The dominant transient shape oscillation is a quadrupole deformation between an oblate and prolate spheroid, given by

$$x_s^2/a^2 + y_s^2/a^2 + z_s^2/b^2 = 1 \quad (18)$$

in the spheroid coordinate system. The spheroidal bubble is arbitrarily orientated with respect to a far-zone observer in the $(\Theta_{scatt},\Phi_{scatt})$ scattering direction whose viewing screen

plane is normal to this direction, and has axes x_{vs} and y_{vs}. The path of the externally reflected ray and the one-internal-reflection ray can be traced through the bubble [5]. It is found that these two reflection glare points continue to be located at equal distances in opposite directions with respect to the center of the elliptical image of the spheroid on the viewing screen. But the line joining the two glare points is now rotated by the angle Ω with respect to the x_{vs} axis. For side-on incidence of the plane wave this angle simplifies to

$$\tan(\Omega) \approx [(a^2/b^2) - 1] \sin(\Phi_{scatt}) \cos(\Phi_{scatt}). \quad (19)$$

The related 4° rotation of the dominant glare points with respect to the higher-order glare points is evident in Fig.2. The semimajor and semi-minor axes of the elliptical image of the spheroid are also rotated by the angle Γ with respect to the x_{vs} and y_{vs} axes. For side-on incidence, this angle simplifies to

$$\tan(2\Gamma) = -\cos(\Theta_{scatt}) \sin(2\Phi_{scatt}) / [\cos(2\Phi_{scatt}) - \sin^2(\Theta_{scatt}) \cos^2(\Phi_{scatt})] . \quad (20)$$

6 Sagittal Caustic of a Spheroidal Floating Bubble

The transient spheroidal shape of the bubble also spoils the point-focusing of the near-zone sagittal caustic observed on a viewing screen behind the bubble in the Θ_{scatt}=0° direction. The formula for the exact shape of the one-internal-reflection sagittal caustic can be determined using the wavefront propagation method [6] since the spheroid still possesses circular symmetry about its axis. For side-on incidence of the plane wave, we are interested in the shape of the sagittal caustic in the vicinity of the positive z axis outside the bubble for one-internal-reflection rays that approach the spheroid with near-grazing incidence. In this limit the shape of the resulting caustic can be expanded in terms of powers of σ. To first order, this gives the four-cusped astroid caustic,

$$(x_{vs})^{2/3} + [(b/a)y_{vs}]^{2/3} = a^{2/3} [1 - (b^2/a^2)]^{2/3} , \quad (21)$$

seen in Fig.2. If a threefold-symmetric harmonic shape distortion of the spheroid shape were present in addition to the dominant twofold-symmetric quadrupole distortion, one of the astroid cusps expands into a three-cusped butterfly caustic [7]. If a fourfold-symmetric hormonic shape distortion was additionally present instead, two opposing cusps of the astroid expand into butterfly caustics. One of the authors (M.S.) has observed and photographed these higher-order near-zone sagittal caustics behind the bubble.

7 References

[1] Princen H.M., Mason S.G., Optical interference in curved soap films, J. Coll. Sci. 20:453-63 (1965).

[2] Lock J.A., Theory of the observations made of high-order rainbows from a single water droplet, Appl. Opt. 26:5291-8 (1987)

[3] Van de Hulst H.C., Wang R.T., Glare points, Appl. Opt. 30:4755-63 (1991)

[4] Burkhard D.G., Shealy D.L., Formula for the density of tangent rays over a caustic surface, Appl. Opt. 21:3299-306 (1982)

[5] Lock J.A., Ray scattering by an arbitrarily oriented spheroid. I. Diffraction and specular reflection, Appl. Opt. 35:500-14 (1996)

[6] Marston P.L., Geometrical and catastrophe methods in scattering, Phys. Acous. 21:1-234 (1992), section 2.8

[7] Berry M.V., Waves and Thom's theorem, Adv. Phys. 25:1-26 (1976)

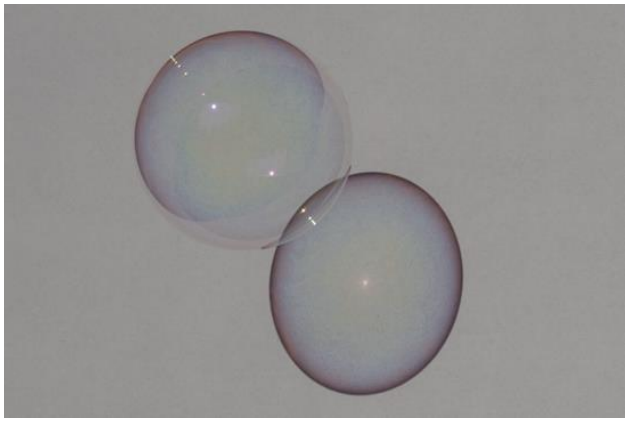

Figure 1 *Glare points on the surface of a spherical floating bubble, and a cross section through the near-zone sagittal axial spike caustic on a viewing screen behind the bubble.*

Figure 2 *Glare points on the surface of a spheroidal floating bubble, and a cross section through the near-zone sagittal astroid caustic on a viewing screen behind the bubble.*

LUNEBRG'S INTERGAL FOR THE DESCRIPTION OF INTERFEROMETRIC PARTICLE IMAGING BEYOND FRESNEL'S APPROXIMATION

Marc BRUNEL[1,*] , Emmanuel PORCHERON [2], Pascal LEMAITRE [2], Jeroen van BEECK [3], Rosaria VETRANO [4], Gérard GREHAN [5] and Sébastien COETMELLEC [1]

[1] UMR CNRS 6614 CORIA, Rouen Normandie Université, Saint-Etienne du Rouvray, 76801, France
[2] Institut de Radioprotection et Sûreté Nucléaire, Gif-sur-Yvette, 91192, France
[3] van Karman Institute, Rhode-Saint-Genese, B-1640, Belgique
[4] KU Leuven, Dpt of Mechanical Engineering, Leuven, B-3001, Belgique
[5] RainbowVision, Déville-lès-Rouen, 76250, France

Corresponding author: marc.brunel@coria.fr

Abstract
Interferometric Particle Imaging is described using a Luneberg's formalism. It can predict and explain the results recorded when Fresnel conditions are not respected.

1 Introduction

ILIDS, and more generally Interferometric Particle Imaging, is an efficient technique to measure the size of droplets or irregular rough particles in a flow when the density of particles remains limited [1-3]. Assimilating particles to an ensemble of coherent emitters (two for a droplet in a classical ILIDS configuration, much more for rough particles), the image formation process can be accurately described using a Fresnel integral [4,5]. Unfortunately, it can happen that Fresnel conditions are not respected (for example with a large aperture combined to a relatively low defocus parameter), inducing some deformations of the interferometric images. This effect is easily identified in the case of droplets: the interference patterns are no more constituted of perfectly parallel fringes on the borders of the images. But it is more difficult to detect the problem in the case of rough particles whose interferometric images are speckle patterns. Without care, the analysis of the pattern could then lead to an erroneous reconstruction of the particle (in size and shape).
In order to understand the modifications that occur, a theoretical description of interferometric Particle Imaging that goes beyond Fresnel conditions is necessary. We propose a description based on the more general Luneberg integral [6]. It is first validated in the case of droplets in an ILIDS configuration, and then applied to rough particles.

2 Results

2.1 Spherical droplets observed with the ALIDS probe

Let us first consider the case of water droplets. The ALIDS probe is a prototype that has been realized within Seventh framework program of the European Community to perform airborne measurements of the size of droplets (EUFAR project: European Facility for Airborne Research). It is been presented in reference [7]. The optical set-up of this probe consists of a frequency-doubled Quantel Ultra 100 laser emitting at 532 nm, a f/0.95 Goyo objective (focus length 25mm) associated to optical windows and deflecting mirrors that ensure a better compactness to the device, and a 8-bit DALSA Genie HM1024 CCD camera. Figure 1(a) shows the interferometric image of a droplet recorded in the highest aperture's configuration.

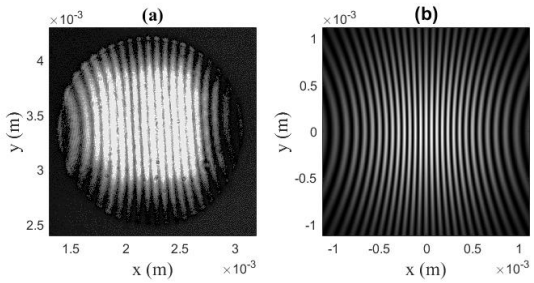

***Figure 1** interferometric image of a droplet recorded with the ALIDS probe under highest aperture (a) and corresponding simulation using Luneberg's formalism and the set of parameters of the probe's (b)*

The interference fringes are not perfectly vertical and parallel. We observe some curvature of the fringes, especially on the borders of the image. It is not possible to describe the geometry of the fringes using a classical simulator based on a Huygens-Fresnel integral [4]. But figure 1(b) shows the interferometric image of a 180 ◎m large droplet using the Luneberg's formalism that has been developed, according to the exact set of parameters of the ALIDS geometry. It appears that it is possible to predict the modifications observed experimentally, which would not be possible with a model based on Fresnel conditions which gives vertical fringes all over the image.

2.2 Irregular rough particles

The interferometric image of irregular rough particles is more complex: it is indeed a speckle pattern [5,8-10]. Assuming that the scattering particle can be assimilated to an ensemble of coherent point emitters located on the envelope of the particle, it is possible to simulate the interferometric image of the particle performing generalized Huygens-Fresnel integrals [5]. In these Fresnel conditions, results show further that the 2D-Fourier transform of the interferometric image gives the 2D-autocorrelation of the envelope of the particle, which could be confirmed in various experiments. Both functions are linked by the scaling factor ◎B_{tot}, where ◎ is the wavelength of the illuminating laser and B_{tot} is the B-parameter of the optical transfer matrix of the imaging set-up (from the particle to the CCD sensor) [8]. In next simulations, ◎=532nm and B_{tot}=2mm. One can wonder what modifications will be observed if Fresnel conditions are not respected, as in previous section with droplets.

To illustrate this, figure 2(a) shows the repartition of 200 coherent point emitters randomly located on a dendrite-like particle. Axes are in meters: the size of the length

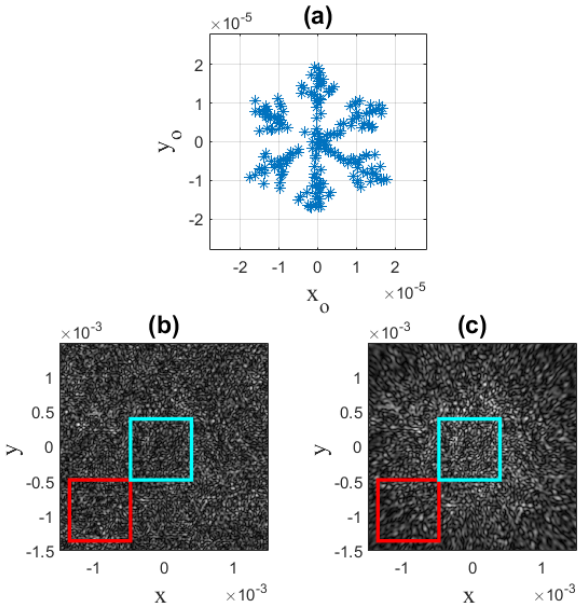

Figure 2 *: dendrite-like particle composed of 200 coherent point emitters (a), its interferometric image using Fresnel model (b), and its interferometric image using Luneberg model (c). Axes are in meters.*

of the particle is thus around 40 ◎m. Figure 2(b) shows its interferometric image predicted using a Fresnel formalism [5], while figure 2(c) shows its image using a Luneberg-based description. All other parameters are identical in both simulations. As for droplets, significant differences are observed on the borders of the two images.

In a second step, figure 3(a) shows the binarized 2D-Fourier transform of the blue box section of the pattern of Fig 2(b) (Fresnel kernel), while figure 3(b) shows the binarized 2D-Fourier transform of the blue box section of the pattern of Fig 2(c) (Luneberg kernel). Both results are very similar. There is no difference between Fresnel and Luneberg models in the centers of the interferograms. However, for comparison, figure 4(a) shows the binarized Fourier transform of the red box section of the pattern of Fig 2(b) (Fresnel kernel), while figure 4(b) shows the binarized Fourier transform of the red box section of the pattern of Fig 2(c) (Luneberg kernel). Both are now very different. If the 2D-Fourier transform of this off-axis section of the interferometric pattern (red box) can still be assimilated to the 2D-autocorrelation of the particle using Fresnel model, Luneberg-based calculations show that this property is not respected if Fresnel conditions are not respected. Using this Fresnel-deduced result, we would deduce erroneously a smaller size and a different shape of the particle, and not the real ones.

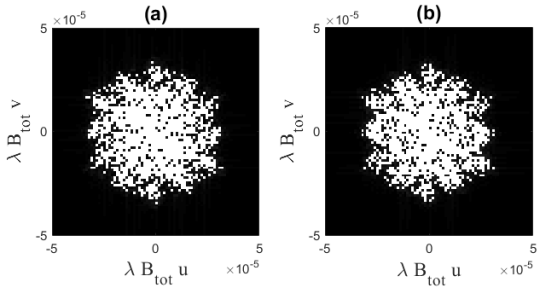

Figure 3 *: binarized 2D-Fourier transform of the blue box section of pattern of Fig 2(b) (Fresnel kernel) (a), and binarized 2D-Fourier transform of the blue box section of pattern of Fig 2(c) (Luneberg kernel) (b). Axes are in meters.*

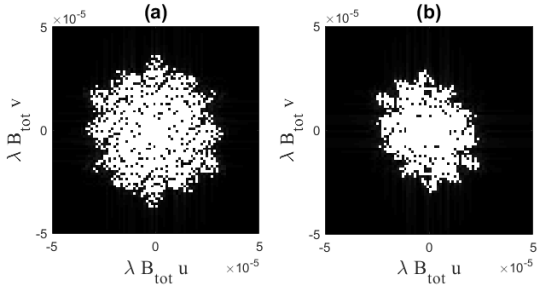

Figure 4 *: binarized 2D-Fourier transform of the red box section of pattern of Fig 2(b) (Fresnel kernel) (a), and binarized 2D-Fourier transform of the red box section of pattern of Fig 2(c) (Luneberg kernel) (b). Axes are in meters.*

In this work, a description of interferometric particle imaging (IPI) based on Luneberg conditions will thus be done and compared to experimental results. The modifications induced on rough particle imaging will be discussed for different shapes of particles. It will be possible to discuss the 3D-tomography of particles [11], combining different angles of view, when Fresnel

conditions are not respected. Finally, as this new formalism gives a vectorial description of the field, this potentiality of the formalism to better understand IPI experiments will be discussed.

3 References

[1] König G., Anders K., Frohn A., A new light-scattering technique to measure the diameter of periodically generated moving droplets, J. Aerosol Sci. 17:157–167 (1986)

[2] Ragucci R., Cavaliere A., Massoli P., Drop sizing by laser light scattering exploiting intensity angular oscillation in the Mie regime, Part. Part. Syst. Charact., 7:221–225 (1990)

[3] Glover A. R., Skippon S. M., Boyle R. D., Interferometric laser imaging for droplet sizing: a method for droplet-size measurement in sparse spray systems, Appl. Opt., 34:8409–8421 (1995)

[4] Brunel M., Shen H., Design of ILIDS configurations for droplet characterization, Particuology, 11:148-157 (2013)

[5] Brunel M., Shen H., Coëtmellec S., Gréhan G., Delobel T., Determination of the size of irregular particles using interferometric out-of-focus imaging, International Journal of Optics, 143904 (2014)

[6] R. K. Luneberg. Mathematical theory of optics. University of California Press, 1964

[7] Porcheron E., Lemaitre P., van Beeck J., Vetrano R., Brunel M., Gréhan G., Guiraud L., Development of a spectrometer for the airborne measurement of droplet in clouds, J. Europ. Opt. Soc.: Rap. Public, 10:15030 (2015).

[8] Brunel M., Gonzalez Ruiz S., Jacquot J., van Beeck J., On the morphology of irregular rough particles from the analysis of speckle-like interferometric out-of-focus images. Opt. Commun., 338:193-198 (2015)

[9] Wu Y., Gong Y., Shi L., Lin Z., Wu X., Gong C., Zhou Z., Zhang Y., Backward interferometric speckle imaging for evaluating size and morphology of irregular coal particles, Opt. Commun. 491:126957 (2021)

[10] González Ruiz S., van Beeck J., Sizing of sand and ash particles using their speckle pattern: influence of particle opacity, Exp. Fluids 58 :100 (2017)

[11] Delestre B., Abad A., Talbi M., Brunel M., Tomography of irregular rough particles using the Error-Reduction algorithm with multiviews interferometric particle imaging, J. Opt. Soc. Am. A, 38:1237-1247 (2021)

SUSPENSIONS

13th International Conference Series on
Laser-light and Interactions with Particles
Optical Particle Characterization follow-up !
August 21-26th, 2022, Warsaw, Poland

CLASSIFICATION OF MILK FAT CONTENT CATEGORIES BASED ON SPECKLE PATTERN USING MACHINE LEARNING

Kwasi NYANDEY[1-2], and Daniel JAKUBCZYK[1,*]

[1]Institute of Physics, Polish Academy of Sciences, Al. Lotników 32/46, 02-668 Warsaw, Poland
[2]Laser and Fibre Optics Centre, Department of Physics, School of Physical Sciences, College of Agriculture and Natural Sciences, University of Cape Coast, Cape Coast, Ghana

Corresponding author: jakub@ifpan.edu.pl

Abstract

Fat globules in milk are known to be secreted as droplets of variable sizes and in different amounts. Hence for industrial, commercial and consumption purposes, there is always the need to accurately and speedily determine fat globule size distribution and classify content into appropriate amounts in each milk batch produced.

We propose a direct approach to classifying speckle images produced by laser light scattering of cow milk with different fat contents using convolutional neural network (CNN). Because the random intensity distribution (speckle) that is observed when coherent light is scattered by a rough surface or transmitted through a scattering medium carries information which can be termed as a fingerprint of the scatterers in question.

We have trained our CNN on four classes of cow milk fat content categories (0.5% 1.5%, 2.0% and 3.2%) with approximately 51,000 images in each class. Our neural network was able to recognize the milk fat content categories from independent as well as mixed dairy plants

1 Introduction

Milk, an important and nutrient-rich liquid food is also a naturally occurring suspension with diverse constituents. Fat globules in milk are known to be secreted as droplets of variable sizes [1] and in different amounts. Hence for industrial, commercial and consumption purposes, there is always the need to accurately and speedily determine fat globule size distribution and classify content into appropriate amounts in each milk batch produced.

In literature, there have been several advancements in tackling these problems [1, 2]. Among these are optical techniques exploiting light scattering phenomena, of which dynamic light scattering is prominent but rarely applied in the industrial setting. Because there is still an inverse problem of particle size determination, concentration and possible contamination during sample preparation.

Recent report of the possibility to directly recognize suspensions with different nanoparticle materials, sizes and concentrations in thin cuvette using speckle technique and machine learning (ML) [3], is promising. Because the technique eliminates the above-mentioned problems. Also speckles are known to carry information which can be termed as a fingerprint of the scatterers [4] in question. In the case of suspension, whose particles are in constant random motion, the movement of speckles is expected to be random but specific. Hence, each recorded speckle image will represent an instance of the fingerprint of these particles, their sizes and/or concentrations. However, the analysis of dynamic speckle with ML still remains a problem mainly due to very high computer resource requirements. With recent GPU capabilities, it is possible to apply ML because it is known to learn rich feature representations of a wide range of images [5].

2 Experiment

A flat thin cuvette was prepared by sticking a 0.05 mm thick adhesive tape on a microscope slide and cutting out a 10 mm circular cross-section from the centre of the tape. The milk sample (10 μL) was loaded into the cuvette and gently covered with a 0.19 mm thick coverslip. As represented in Figure. 1, the sample stage was levelled so that the motion of fat globules will be purely Brownian. The sample was illuminated perpendicularly with a green frequency-doubled Nd:YAG laser at 532 nm, 5 mW and 1.7 mm collimated beam. The illumination was such that the speckle exited through the thin coverslip to minimise lateral shift of speckles. A 14-bit colour camera (Pike F-032C, AVT) was used to record the speckle at 26.9° angle, taking into account the velocity of the speckle movement and camera's available frame rate. Also an IR filter was mounted on the camera to account for the leak of the fundamental and pump frequencies from the laser source in infrared.

The milk was purchased from supermarkets where fresh milk was refrigerated but ultra-high-temperature (UHT) milk was left on the open shelf. The samples were mainly from 3 dairy plants (see Table. 1) and according to the fat content categories produced by such plants.

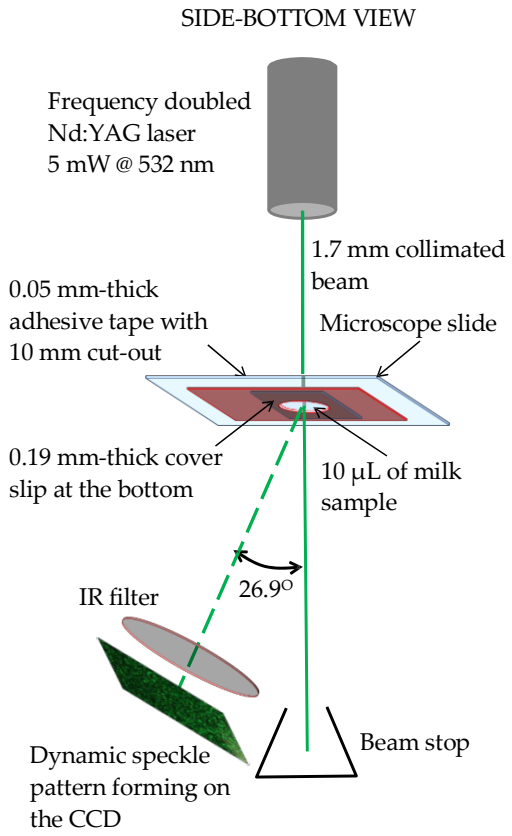

Figure 1 *Experimental setup for recording dynamic speckle movies, adapted from [3]*

Mlekovita with 1.5% fat content was added to bring diversity since we intended to create a separate training sample with mixed dairies. For each fat content category (0.5%, 1.5%, 2.0% and 3.2%), there were 5 replicas of 1 L of milk with different batch/lot numbers. For each lot, 10 movies were recorded at 10 different locations on the sample in the cuvette. Initially, 6.5 s (75 fps) movies were recorded at a single illumination point. Later, 13 s (75 fps) movies were recorded to increase the number of images since the 10-locations on the same sample was exhaustive.

The recorded movies were extracted into frames with the 640 x 480 pixel frames serving as speckle images. During extraction the background (taken to be static speckles resulting from possible glass imperfections or immobile sample particles and averaged over 200 consecutive images) is subtracted from each image. Furthermore, each image was normalised by its highest intensity to within the 0-1 grayscale level. This operation, as reported by [3], is very beneficial since it suppresses intensity variations between raw images and ensures numerical stability of the learning algorithm.

The network used for training is the same as described in [3] and GitHub [6] nicknamed "*t7g24*" since it has produced remarkable classification of speckle images generated by colloidal suspensions. Besides that, this research represents an aspect of a continuous study of suspensions using light scattering and machine learning. The network was trained on all images (640 x 480 pixels) extracted from the movies with a randomised selection of 8:1:1 proportion for training, validation and test sets respectively. All images recorded from the 5 lots of the same fat content category belonged to the same class. The network was first trained to recognise the milk fat content category from the same Dairy plant and then mixed dairies.

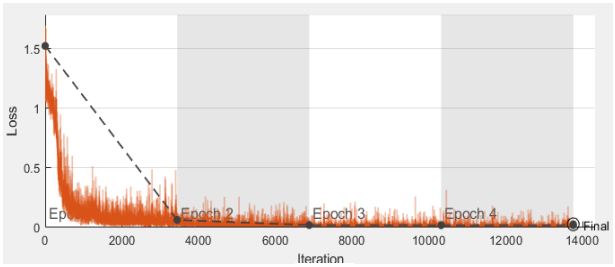

(a)

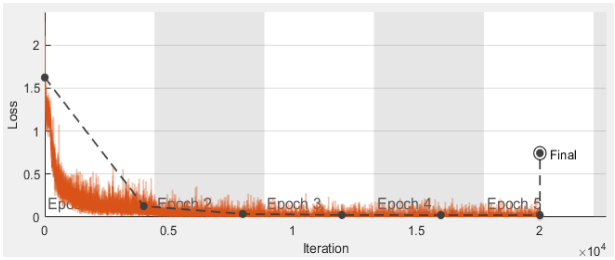

(b)

Figure 2 *The loss function optimisation progress over each epoch for training and validation subsets of (a) Carrefour and (b) mixed dairies*

Market label	Fat content %	Milk type
Carrefour	0.5	UHT
	2.0	UHT
	3.2	UHT
Łaciate	0.5	UHT
	2.0	UHT
	3.2	UHT
Mleczna Dolina	0.5	UHT
	1.5	UHT
	2.0	Fresh
	3.2	UHT
Mlekovita	1.5	UHT

Table 1 *Distribution of cow milk types and fat content categories according to market labels*

2 Results and Discussion

In Figure. 2 (a) and (b) we present the loss function evolution during training of the network on Carrefour and mixed dairies. The loss functions for Mleczna Dolina and Łaciate (not shown) were similar to Carrefour and mixed dairies respectively. The cross entropy loss optimisation during training of network for all data sets progressed

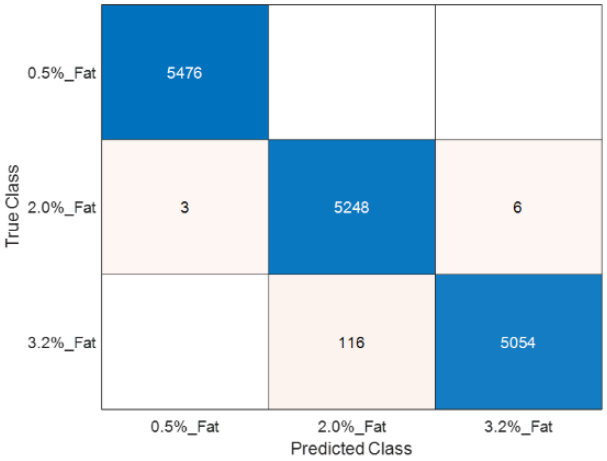

Figure 3 *Classification confusion matrix of speckle images (test set) generated by cow milk with 3 different fat content categories produced by Carrefour*

steadily until the end, where there is a sudden fall of validation accuracies for both Łaciate (not shown) and mixed dairies (Figure. 2 (b)). This sudden jump (sometimes termed as the "variance shift") is a known occurrence in CNNs with batch normalisation layer as explained in [7].

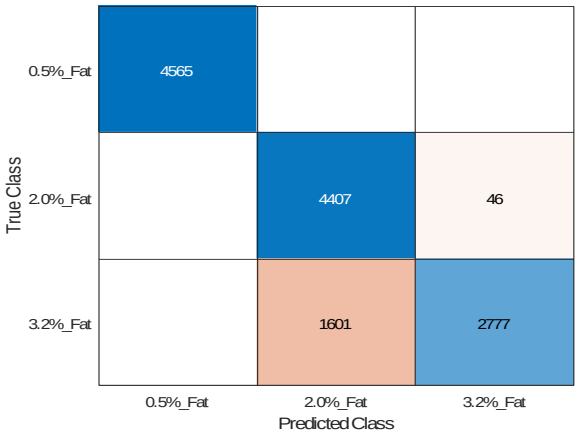

Figure 4 *Classification confusion matrix of speckle images (test set) generated by cow milk with 3 different fat content categories produced by Łaciate*

We obtained accuracies of 99.18%, 95.11%, 87.61% and 84.04% respectively for Carrefour, Mleczna Dolina, Łaciate and mixed dairies.

The classification confusion matrices for test sets of Carrefour and Łaciate are presented in Figure. 3 and 4 respectively, while the classification confusion matrices for test sets of Mleczna Dolina and mixed dairies are presented in Figure. 5 (a) and (b) respectively. For the mixed dairies, we mixed approximately equal proportions of images in the same fat content category from the 3 dairy plants.

These results beat our expectation because we anticipated differences in speckle due to differences in concentration of fat content as well as similarities in speckle due to milk, (which in our case represents the dispersion medium). Because, unlike pure liquids, milk (without fat globules) has its unique particle distribution which also scatters light. Hence, the few misclassifications could be attributed to these similarities due to the influence of other components of milk. While the large misclassifications observed were attributed to the abrupt fall in accuracies at the end of training.

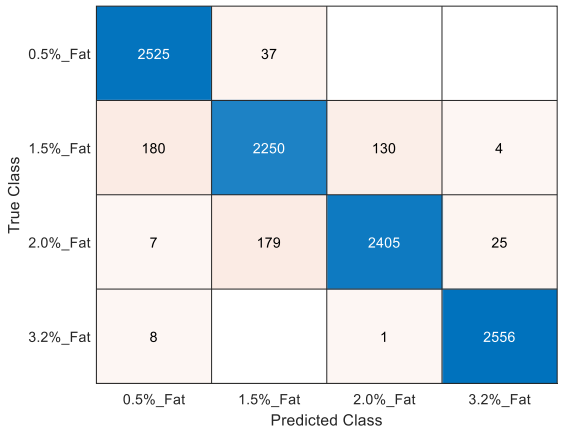

(a)

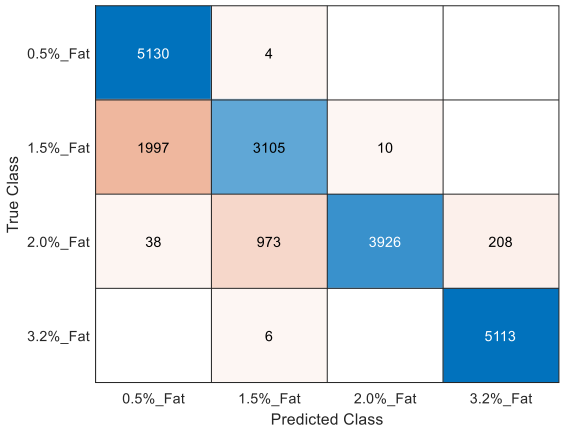

(b)

Figure 5 *Classification confusion matrix of speckle images (test set) generated by cow milk with 4 different fat content categories produced by (a) Mleczna Dolina and (b) mixed dairies. The 1.5% fat content in (b) was created by mixing images from Mleczna Dolina and Mlekovita*

4 Acknowledgement

This research was funded in whole or in part by National Science Centre, Poland, grant number 2021/41/B/ST3/00069. For the purpose of Open Access, the author has applied a CC-BY public copyright licence to any Author Accepted Manuscript (AAM) version arising from this submission.

5 Refferences

[1] El-Loly M. M. Composition, properties and nutritional aspects of milk fat globule membrane-a review. Polish Journal of Food and Nutrition Sciences, 61(1) (2011)

[2] Michalski M. C., Michel F., Geneste C., Appearance of submicronic particles in the milk fat globule size distribution upon mechanical treatments. Le Lait, 82(2): 193-208 (2002)

[3] Jakubczyk, T., Jakubczyk, D., Stachurski, A., Assessing the properties of a colloidal suspension with the aid of deep learning Journal of Quantitative Spectroscopy and Radiative Transfer, 261: 107496 (2021)

[4] Dainty J. C. (Ed.), Laser speckle and related phenomena (Vol. 9) (Springer science & business Media, 2013)

[5] https://www.mathworks.com/help/deeplearning/ug/ train-deep-learning-network-to-classify-new-images.html

[6] Supplementary material for T. Jakubczyk's Masters Thesis n. d. https://github.com/sigrond/MGR

[7] https://www.mathworks.com/matlabcentral/answers/445800-why-do-i-see-a-drop-or-jump-in-my-final-validation-accuracy-when-training-a-deep-learning-networ

13th International Conference Series on
Laser-light and Interactions with Particles
Optical Particle Characterization follow-up !
August 21-26th, 2022, Warsaw, Poland

LASER BASED DETECTION OF MICROPLASTICS IN WATER

Adriana SMARANDACHE[1,*], Ionut-Relu ANDREI[1], Mihai BONI[1], Andra DINACHE[1], Ana-Maria UDREA[1-2], and Angela STAICU[1]

[1] Laser Department, National Institute for Laser, Plasma and Radiation Physics, Magurele, 077125, Romania
[2] University of Bucharest, Research Institute of the University of Bucharest–ICUB, Bucharest, 050095, Romania

Corresponding author: adriana.smarandache@inflpr.ro

Abstract

Finding fast and accurate ways for detection of microplastics in water with a limited number of measurements, easy processing and sampling is a challenging task. In this respect, this work aims to bring new knowledge about the detection of very small particles of plastics in a host fluid droplet, using laser radiation as light source for Raman scattering measurements. The combination of the enhanced sensitivity of Raman spectroscopy obtained using very small samples (microdroplets) with the latest developments in the topics of optofluidics may constitute an advance in the field of real time monitoring of environmental pollutants.

1 Introduction

One major side effect of the abundance of plastic products in modern society is microplastic (MP) pollution, where small size polymer particles of diverse origins and types enter the environment. These particles are only partially removed by the wastewater treatment plants [1].

Plastics are organic polymers, synthesized from the polymerization of monomers extracted from oil or gas, whose global production rose continuously. Approximately 10% end up in marine environment and only a very small fraction is recycled annually [2]. Although initially considered a revolutionary material, it has slowly become a global threat to the environment, with ubiquitous distribution in marine and freshwater ecosystems. The natural environmental conditions of these ecosystems, especially the dynamics of water currents, solar radiation, abrasion and interactions with vessels and organisms, cause plastic products to degrade slowly and to fragment into smaller particles than usual, known as microplastics [3,4].

Regardless of the current disagreements over the definition of MP particles, fragments less than 5 mm in diameter with no lower restriction are considered [5]. The diversity in properties and wide particle size range means that as a group of analytes, they are challenging to efficiently detect and identify in complex environmental matrices, especially when very small (micro-/nanometric) range dimensions are involved [6].

On the other hand, concerns are raising regarding the potential for MP to represent new spreading substrates for microorganisms, especially harmful and pathogenic ones [7]. Also, various organic pollutants, such as polycyclic aromatic hydrocarbons [8], polychlorinated biphenyls [9], and antibiotics [10], can be adsorbed onto MP. This is a research area where many uncertainties exist, with respect to both detection, analysis and identification.

In this connection, we performed Raman spectroscopy measurements on water droplets containing polymethyl methacrylate (PMMA) microparticles. The sampling, control, and acquisition parameters of the experimental set-up have been optimized to better record the Raman scattering spectra. Additional analysis of PMMA microplastic dispersion in water samples were carried out by molecular modelling, as well as UV-Vis absorption and FTIR spectroscopy.

PMMA is also known as acrylic, acrylic glass, or Plexiglas. It is a versatile transparent thermoplastic often used as an alternative to glass, being lighter and resistant to breakage. The recent developments in the applications of PMMA in different areas such as biomedical, optical, solar, sensors, battery electrolytes, nanotechnology can be a potential source of polymer microparticles occurrence in the environment.

2 Experimental Setup

The block scheme of the laboratory-built experimental setup for Raman spectroscopy is shown in Figure 1. Individual droplets with volumes ranging from 1 to 4 μL were optically pumped using a pulsed laser radiation source. We used the 2nd harmonic generation of the Nd:YAG laser (Surelite II, Continuum, Excel Technology, USA) emitted at 532 nm, with frequency of 10 Hz, 9 ns pulse duration (FTWHM), and pulse energies ranging from 2.5 to 24 mJ. For bulk sampling experiments laser beam energies up to 100 mJ were used. The laser beam of 6 mm waist was focused by a lens of 150 mm focal length. The droplet was placed at 122 mm from the lens, so that the collimated beam is equal to or less than the drop diameter.

The droplets were generated by a computer controlled programmable pump (Dual Syringe Dispenser, Mircolab ML560C, Hamilton, USA). The samples were loaded on a capillary circuit from a stock-volume. Droplets were automatically generated, controllable drop by drop, with a resolution of 0.05% of the employed syringe capacity (50μL).

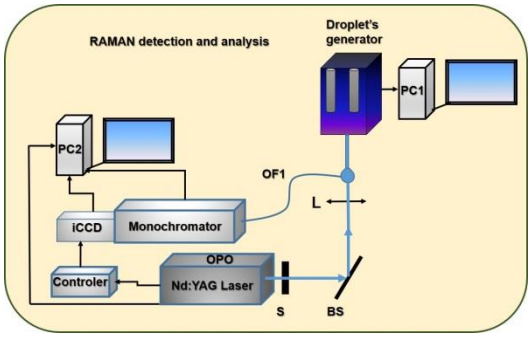

Figure 1 *The Raman spectroscopy set-up*

The capillary tips used had external diameters of 0.51 mm (for volume generation ranging from 1 to 3 µL) and 0.91 mm (for volume greater than 2 µL). The generated droplets had diameters ranging from 1.24 mm to 2 mm, depending on the ratio between the diameter of the drop and the diameter of the capillary tip.

The droplet's Raman scattering radiation was collected at 90° with respect to the pumping laser beam using an optical fiber positioned in the droplet's plane.

For pulse-to-pulse and 5-pulse-series data acquisition, a pulse delay generator (SRS DG535) was used. It generates TTL signals for synchronizing the laser pulse with the data acquisition system (Acton Research/Princeton Instruments) through a mechanical shutter. A spectrograph (SpectraPro SP2750, in Czerny-Turner configuration, with focal length of 750 mm, and 0.8 nm resolution) is coupled with an iCCD-PIMAX Camera detector (Intensifier 25 mm, resolution of 64 lp/mm, 2ns minimum gate opening). The spectrum was acquired using a grating of 2400 grooves with an optical resolution of 0.016 nm for a 10 µm input slot of the spectrograph. The shutter (Digital Shutter Controller 845 HP, Newport) provides a controllable optical pump time window ranging from ms to s.

PMMA was purchased from Sigma Aldrich and MicroParticles (Germany) as microparticle suspensions in water with various standard sizes ranging from 100 nm to 100 µm.

3 Results and Disscussions

We performed Raman spectroscopy measurements on water droplets containing PMMA microparticles. Supplementary analysis of PMMA microplastic dispersion in water were carried out by molecular modelling, as well as UV-Vis absorption and FTIR spectroscopy.

3.1 Vibrational Spectroscopy

The Raman spectra of different concentration of MP-contaminated water droplets were recorded, and the parameters of the experimental configuration were optimized to ensure the best Raman signal. The compared Raman spectra of PMMA microplastic (100µm) dispersed in water in bulk of 1 cm^3 volume, and in droplets of 2 µL volume are plotted in Figure 2.

Among the registered Raman bands, the most prominent one was observed at 2960 cm^{-1}, which corresponds to the stretching vibration of the C–H bonds.

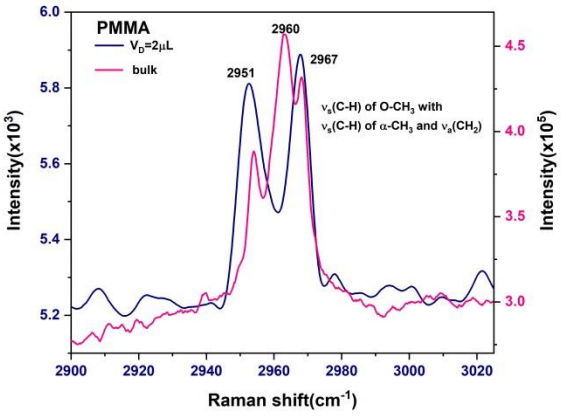

Figure 2 *The Raman spectra of PMMA in bulk vs. droplet*

According to the literature [11], the band centered at 2960 cm^{-1} is due to an overlap of the νCH modes in the CH_2 groups of the skeleton, the α-CH_3 groups and the CH_3 ester groups.

An intensity decrease of the scattering is seen in droplets Raman spectra when compared to PMMA bulk samples probable because the used laser beam energy was limited to a few mJ for droplets sampling.

The FTIR spectra (not shown) were recorded using the Nicolet™ iS™50 spectrometer, in the range 4000-500 cm^{-1} at a resolution of 4 cm^{-1} and a mediation on 32 spectra was made. The samples (20 µL) of MP dispersed in water were dried on a KRS-5 support.

The results are consistent with both the data published in the literature and the calculated spectra, presented below as additional investigations.

3.2 Molecular Modelling

PMMA $(C_5O_2H_8)n$, molecular structures were drawn, 3D protonated, and energy-optimized (using MMFF94X force field at 0.05 gradient with Gasteiger (PEOE) partial charges) using MOE software. After the optimisation protocol we have predicted the 2D and the i3D molecular descriptors. Compounds with a hydrophobic surface area are more likely to be colonized by bacteria [7]. The high predicted number of hydrophobic atoms (21) and the total hydrophobic surface area (730.97) may indicate that PMMA is a hydrophobic compound.

Molecular modelling was performed for PMMA using Gaussian 09 [12] and GaussView 5.0 [13]. Density Functional Theory (DFT) with B3LYP and the 6-311G augmented base set were used for both structural optimization and calculation of the molecules' chemical bonds frequencies. The influence of the dispersive environment (water) on the process of structural

optimization and calculation of FTIR and Raman spectra was implemented in the calculation scheme by selecting the IEFPCM module.

FTIR [cm^{-1}]	RAMAN [cm^{-1}]	Assignment
759	745	ν(C-C) skeleton
894	879	ω(CH_2)
944	921	ω(CH_3)
994	976	ω(O-CH_3)
1096	1058	ν(C-C) skeleton
1189	1176	ν(C-O-C-)
1271	1271	(ν) C O or C—O
1347	1353	δ(C-H) a CH_3
1488	1482	δ(CH_2)
3100	3045	ν(C-H) a O-CH_3

Table 1 *Calculated vibrational modes of the PMMA molecule*

3.3 UV-Vis Absorption Spectroscopy

The absorption spectra of different percent MP dispersion in water were registered by a UV-Vis-NIR Lambda 950 (Perkin-Elmer, USA) spectrophotometer between 175 – 3300 nm. The spectral resolution of device is ⩾ 0.05 nm in UV-Vis spectral range, and ⩾ 0.20 nm in NIR. The intrinsic error of the apparatus is 0.004%.

The absorption spectra of MP in water solutions are represented in Figure 3(a) for samples having percentage concentration from 0.16% to 1.25% and in Figure 3(b) for those with percentage concentration between 2.5% - 10%.

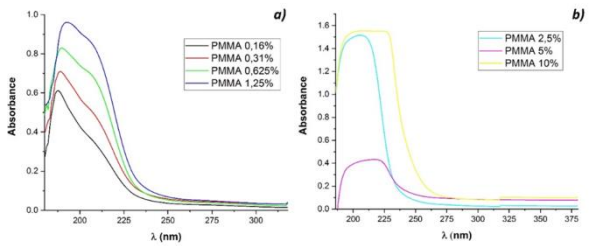

Figure 3 *The UV-Vis absorption spectra of PMMA in water, at concentrations between: a) 0.16% - 1.25% and b) 2.5% - 10%.*

The appearance of the absorption bands in Figure 3(b) and the fact that their absorbance does not increase progressively with increasing concentration of samples may be due to the fact that MP particles do not have the same roughness, so some samples have a higher scattering coefficient, thus influencing the light intensity passing through the sample.

4 Acknowledgement

This work was supported by MCID and UEFISCDI projects PN-III-P2-2.1-PED-2019-1264, and Nucleu Program, ctr. no. 16N /08.02.2019.

5 References

[1] Sun, J., Dai, X., Wang, Q., van Loosdrecht, M. C. M., Ni, B.-J. Microplastics in wastewater treatment plants: Detection, occurrence and removal. Water Research 152, 21–37 (2019).

[2] Coyle, R., Hardiman, G., Driscoll, K. O. Microplastics in the marine environment: A review of their sources, distribution processes, uptake and exchange in ecosystems. Case Studies in Chemical and Environmental Engineering 2, 100010 (2020).

[3] Zeng, E. Y. Microplastic Contamination in Aquatic Environments: An Emerging Matter of Environmental Urgency. (Elsevier, 2018).

[4] Thompson, R. C. Microplastics in the Marine Environment: Sources, Consequences and Solutions. in Marine Anthropogenic Litter (eds. Bergmann, M., Gutow, L., Klages, M.) pp. 185–200 (Springer International Publishing, 2015).

[5] Kershaw, P. J. Ed. Sources, fate and effects of microplastics in the marine environment: a global assessment Rep. Stud. GESAMP No. 90. GESAMP http://www.gesamp.org/publications/reports-and-studies-no-90 (2019).

[6] Wirnkor, V. A., Ebere, E. C., Ngozi, V. E. Microplastics, an Emerging Concern: A Review of Analytical Techniques for Detecting and Quantifying Microplatics. Analytical Methods in Environmental Chemistry Journal 2, 13–30 (2019).

[7] Miao, L., Wang, P., Hou, J., Yao, Y., Liu, Z., Liu, S., et al. Distinct community structure and microbial functions of biofilms colonizing microplastics. Science of The Total Environment 650, 2395–2402 (2019).

[8] Rochman, C. M., Manzano, C., Hentschel, B. T., Simonich, S. L. M., Hoh, E. Polystyrene Plastic: A Source and Sink for Polycyclic Aromatic Hydrocarbons in the Marine Environment. Environ. Sci. Technol. 47, 13976–13984 (2013).

[9] Velzeboer, I., Kwadijk, C. J. A. F., Koelmans, A. A. Strong Sorption of PCBs to Nanoplastics, Microplastics, Carbon Nanotubes, and Fullerenes. Environ. Sci. Technol. 48, 4869–4876 (2014).

[10] Li, J., Zhang, K., Zhang, H. Adsorption of antibiotics on microplastics. Environmental Pollution 237, 460–467 (2018).

[11] Thomas, K. J., Sheeba, M., Nampoori, V. P. N., Vallabhan, C. P. G., Radhakrishnan, P. Raman spectra of polymethyl methacrylate optical fibres excited by a 532 nm diode pumped solid state laser. J. Opt. A: Pure Appl. Opt. 10, 055303 (2008).

[12] M. J. Frisch, G. W. Trucks, H. B. Schlegel, et al. Gaussian 09, Revision E.01. (Gaussian, Inc., 2009).

[13] Roy Dennington, Todd Keith, and John Millam. GaussView. (2009).

13th International Conference Series on
Laser-light and Interactions with Particles
Optical Particle Characterization follow-up !
August 21-26th, 2022, Warsaw, Poland

STATISTICAL INVESTIGATION OF THE ULTRAFAST IMAGE-BASED DYNAMIC LIGHT SCATTERING TO MEASURE BIMODAL GAUSSIAN DISTRIBUTIONS OF NANOPARTICLES

An Ying ZHAO, Jia Jie WANG, Yi Ping HAN and Paul BRIARD*

School of Physics, Xidian University, Xi'an, 710071, P. R. China

Corresponding author: paulbriard@outlook.com

Abstract

In an ultrafast image-based dynamic light scattering (UIDLS) experiment, nanoparticles in Brownian motion in a solvent are illuminated by a focused Gaussian beam and scatter the light toward an ultrafast camera. The cross-correlation coefficients between pairs of pictures recorded by the camera permit to determine a size distribution of "equivalent spherical particles". In this abstract, an iterative UIDLS permit to retrieve characteristic information of a bimodal Gaussian particle size distribution (PSD) in the sample from the distribution of the equivalent spherical particles which has been measured by UIDLS. Satisfying agreements were achieved which indicates the validity of the method.

1 Introduction

In the conventional dynamic light scattering (DLS), nanoparticles are illuminated by a focused Gaussian beam and the scattered light is collected by a photo-detector such as a photomultiplier tube (PMT) [1]. The intensity autocorrelation function (ACF) of the light at the PMT is a multi-exponential function which is then used to extract the PSD by using, for instance a constrained regularization method [2]. The UIDLS is a technique extended from the conventional DLS to measure a PSD using an ultrafast camera [3]. The cross-correlation coefficients between the pairs of pictures recorded at times t and $t+\tau$ determine a PSD of "equivalent spherical particles", which are the monodisperse particles which scatter the same light fluctuations between times t and $t+\tau$ than the polydisperse particles in the measurement volume at time t. Recently, the UIDLS was extended to a polarized-depolarised UIDLS technique to measure characteristic information about size and shape of non-spherical particles [4, 5].

In this abstract, two statistical models are proposed to investigate the UIDLS for bimodal Gaussian distributions of spherical particles. The first model used to describe the direct problem is a statistical UIDLS simulation for a bimodal Gaussian distribution. The second model is a statistical prediction of the UIDLS for a bimodal sample where the variance of the Gaussian modes is $V_1 = V_2 = 0$, and where the Levenberg-Marquardt (LM) algorithm is applied to extract characteristic information of a bimodal Gaussian sample by fitting the PSD of equivalent spherical particles measured by UIDLS.

2 Theoritical treatement

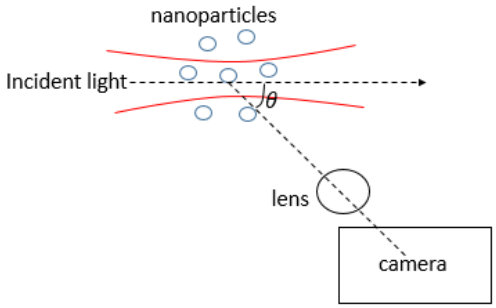

Figure 1 *UIDLS experimental set-up*

In an UIDLS experiment, nanoparticles are illuminated by a focused Gaussian beam. The experimental set-up of the UIDLS is shown in Figure. 1. The scattered light is recorded by a camera located at scattering angle θ. A lens between the sample and the camera permits to control the measurement volume. The cross-correlation coefficients between pairs of pictures are then measured to obtain information about the particles in the sample. To develop a way to measure Gaussian bimodal samples of spherical nanoparticles, two models are chosen to simulate the UIDLS experiment. The first model is the UIDLS simulation for a bimodal Gaussian sample of spherical particles. The second model is the UIDLS simulation for a bimodal sample of nanoparticles where the variance of both Gaussian modes is $V_1 = V_2 = 0$.

In the first model, named BG, the sizes of N particles are randomly generated according to the bimodal Gaussian PSD in the sample. In an UIDLS experiment, particles enter and exit the measurement volume. The cross-correlation coefficients between pair of pictures recorded by the camera at times t and $t+\tau$ are characteristics of the particles in the measurement volume at time t, assumed to be the same particles at time $t+\tau$. Figure. 2 shows an example of a bimodal Gaussian distribution by generating 1000 particles. The characteristic parameters of the bimodal Gaussian distribution are: (i) the average radii of the first Gaussian

mode and that of the second Gaussian mode in the PSD, a_{1G} and a_{2G}, respectively (ii) the mixing proportion between both Gaussian modes described by f_{1G}, the percentage frequency of particles in the first mode (iii) the variance of the first Gaussian mode, and that of the second Gaussian mode, V_1 and V_2, respectively.

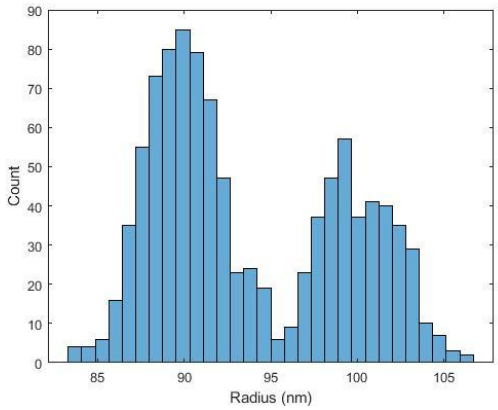

Figure 2 *Example of a bimodal Gaussian distribution where 1000 particles are generated, a_{1G}=90 nm, a_{2G}=100nm, f_{1G}=0.60, $V_1 = V_2 = 5$ nm²*

We describe a distribution of cross-correlation coefficients from the PSDs in the measurement volume which have been randomly simulated. For a total of N_G cross-correlation coefficients N*N_G random radii are determined. The cross-correlation coefficient G(τ) between a pair of pictures recorded at times t and t + τ is [3]:

$$G(\tau) = g^{(2)}(\tau) - 1 = \beta\left[g^{(1)}(\tau)\right]^2, \quad (1)$$

where $g^{(2)}(\tau)$ is the normalized ACF of the intensity scattered by the particles in the measurement volume, $g^{(1)}(\tau)$ is the normalized ACF of the electric field, τ is the time interval, β is an instrumental constant [3]. From the N*N_G random radii, N_G values of cross-correlation coefficients are determined. From a PSD in the measurement volume randomly determined, the normalized ACF of the electric field [2] is:

$$g^{(1)}(\tau) = \sum_{i=1}^{N} h(a_i)\exp\left(-q^2 D_t(a_i)\tau\right) \quad (2)$$

where **q** is the scattering vector which depends on the scattering angle θ and the wavelength λ of the incident light in the surrounding medium [1]. $D_t(a_i)$ is the translational diffusion coefficient [1] of the i-th particle. The coefficient $h(a_i)$ is the fraction of the light intensity scattered by the i-th particle in the measurement volume.

In summary, from a randomly determined PSD in the measurement volume, a normalized electric field ACF can be obtained, from which the cross-correlation coefficient is determined. The distribution of cross-correlation coefficients is then used to determine a PSD of equivalent spherical particles.

In the present abstract, a way is proposed to get characteristic information about the bimodal Gaussian PSD in the sample by using UIDLS simulations for bimodal samples where the variances are $V_1 = V_2 = 0$, associated with the LM algorithm.

The second model of UIDLS simulation, named "BV0" model, is based on the statistical prediction of the cross-correlation coefficients corresponding to a bimodal sample where the variance of the Gaussian modes are $V_1 = V_2 = 0$ (the parameters which describe the PSD are the radii a_1 and a_2, and f_1 the percentage frequency of particles of radius a_1 in the sample). In this model, the particle size is the radius a_1 or the radius a_2. The number of cross-correlation coefficients N_k corresponding to a PSD in the measurement volume with k particles of radius a_1 and N-k particles of radius a_2 among N particles is described as:

$$N_k = N_G \frac{N!}{k!(N-k)!} f_1^{\,N}\left(1-f_1\right)^{N-k}, \quad (4)$$

where all the coefficients N_k from k=0 to k=N are described from the probability $P(k)=N_k/N_G$. As in the BG model, the values of the cross-correlation coefficients are described from the PSDs in the measurement volume, and the PSD of equivalent spherical particles is determined from the distribution of the cross-correlation coefficients.

3 Numerical results and disscussion

The direct problem is simulated using the BG model, for a given bimodal Gaussian distribution. The corresponding cross-correlation coefficients are computed and then the PSD of equivalent spherical particles is obtained. Figure. 3. shows an example of PSD of equivalent spherical particles simulated using the BG model.

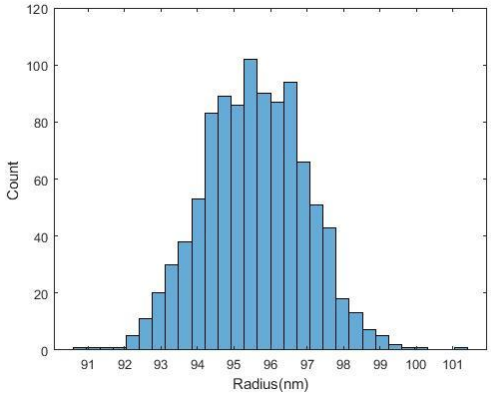

Figure 3 *Example of a PSD of equivalent spherical particles measured for a bimodal Gaussian distribution in the sample (simulation using the BG model)*

The particles are immerged in water at temperature 298 K. The number of particles in the measurement volume is N=1000. The number of cross-correlation coefficients is N_G=1000. The time interval is the same for all the cross-correlation coefficients: $\tau = 10^{-3}$s . The wavelength of the incident beam is 532 nm. The scattering angle θ is $\pi/4$ rad. The instrumental constant β equals 1. The parameters of the

bimodal Gaussian PSD are: same variance $V_1 = V_2 = 5$ nm^2 for both Gaussian modes, and average radii a_{1G}=90 nm and a_{2G}=100 nm. A white noise $\delta G = 10^{-3} \times R$, where $R \in [-1,1]$ is a uniform random number, has been added to the cross-correlation coefficients. From the PSD of equivalent spherical particles, the LM algorithm associated with the BV0 model is used to get characteristic information of the bimodal Gaussian PSD. It determines two radii a_1 and a_2, and the percentage frequency f_1. Table. 1. shows a comparison of the bimodal Gaussian PSD set in the simulation and the bimodal PSD of variances $V_1 = V_2 = 0$ obtained by fitting the PSD of equivalent spherical particles using the LM algorithm associated with the BV0 model.

	Bimodal Gaussian PSD in the sample	Fit of the PSD of equivalent spherical particles (using BV0 model and LM algorithm)
Example 1	a_{1G}=90.0 nm	a_1=91.2 nm
	a_{2G}=100.0 nm	a_2=101.3 nm
	f_{1G}=60%	f_1=65.5 %
Example 2	a_{1G}=80.0 nm	a_1=88.8 nm
	a_{2G}=100.0 nm	a_2=98.4 nm
	f_{1G}=60%	f_1=55.5%

Table 1 *A comparison of the bimodal Gaussian PSD set in the simulation (BG model) and the result of the fit of the PSD of the equivalent spherical particles based on simulations for bimodal samples of variances $V_1 = V_2 = 0$ (BV0 model associated with LM algorithm)*

In Table. 1, we can see that for the first example, both radii a_{1G} and a_{2G} agree with the radii of the bimodal sample of variance $V_1 = V_2 = 0$ that fit the PSD of equivalent spherical particles, but for the second example, $a_{1G} = 80.0$ nm has been overestimated, which is due to the Rayleigh scattering of the particles: the intensity scattered by a particle is proportional with the 6th power of its size. Our numerical results show that the LM algorithm associated with the BV0 model has the potential to measure characteristic information about the bimodal Gaussian PSD, and our next step is to validate it in the UIDLS experiment with bimodal Gaussian PSDs in the sample. However, the BV0 model cannot permit to measure the variances V_1 and V_2 of the Gaussian modes in the sample. Thus, one of our purposes is to extend our model of iterative UIDLS in order to measure information about the variances. The LM algorithm associated with UIDLS simulations could also permit to measure the distributions of characteristic parameters of the size and the shape of non-spherical particles.

4 Conclusion and perspectives

Two different models of simulation of the UIDLS experiment and an iterative UIDLS to measure characteristic information of a bimodal Gaussian PSD of spherical nanoparticles have been proposed. The following work are in the tray: (i) To develop a new model of UIDLS simulation where the Brownian motion and the light scattered by the particles are computed to describe the cross-correlation coefficients, which will permit us to investigate the influence of the characteristics of the camera and the measurement volume on the measurement of the PSD in the sample (ii) the experimental validation of our numerical simulations by the measurement of bimodal Gaussian samples of spherical nanoparticles (iii) to investigate the measurement of the variances of the Gaussian modes in the bimodal sample, which is not possible to determine with the BV0 model described in the present abstract, and extend the measurement of bimodal distributions to other kinds of polydisperse PSDs in the sample (iv) to extend our models of simulation to measure the distributions in the sample of characteristic parameters of the size and the shape of non-spherical particles.

5 Acknowledgement

The authors acknowledge the support by the Innovation Capability Support Program of Shaanxi (Grant no. 2021JZY-006); Fundamental Research Funds for the Central Universities (Grant no. XJS190507); Foreigner Young Talent Program (Grant no. QN20200027010)

6 References

[1] B. J. Berne and R. Pecora, Dynamic light scattering with applications to chemistry, biology, and physics (Dover, New-York, 2000)

[2] Xu M., Shen J., Thomas J. C., Huang Y., Zhu X., Clementi L. A., Vega J. R.. Information-weighted constrained regularization for particle size distribution recovery in multi-angle dynamic light scattering, Optics Express 26(1): 15-31 (2018)

[3] Zhou W., Zhang J., Liu L., Cai X. Ultrafast image-based dynamic light scattering for nanoparticle sizing, Review of Scientific Instruments 86(11): 115107 (2015)

[4] Briard P., Liu Z., Cai X., Measurement of the mean aspect ratio and two characteristic dimensions of polydisperse arbitrary shaped nanoparticles, using translational-rotational ultrafast image-based dynamic light scattering, Nanotechnology 31: 395709 (2020)

[5] Liu Z., Briard P, Cai X., Dimension measurement of nanorods based on depolarized-polarized image-based dynamic light scattering, Acta Sinica Optica 41(21): 2129001 (2021)

Forces & Properties

13th International Conference Series on
Laser-light and Interactions with Particles
Optical Particle Characterization follow-up !
August 21-26th, 2022, Warsaw, Poland

PHOTOPHORETIC FORCE ON AN ABSORBING SPHERE ILLUMINATED BY A GAUSSIAN BEAM

Lei LIU[1], Jiajie WANG[1,*], Paul BRIARD[1], Leonardo André AMBROSIO[2], Gérard GOUESBET[3]

[1] School of Physics, Xidian University, Xi'an, 710071, P. R. China.
[2] Department of Electrical and Computer Engineering. São Carlos School of Engineering, University of São Paulo. 400 Trabalhador são-carlense Ave. 13566-590, São Carlos, SP, Brazil.
[3] CORIA-UMR 6614 - Normandie Université. CNRS-Université et INSA de Rouen. Campus Universitaire du Madrillet. 76800, Saint-Etienne du Rouvray, France.

Corresponding author: wangjiajie@xidian.edu.cn

Abstract

Photophoretic force exerted on an absorbing sphere in air by a focused Gaussian beam is analysed theoretically using the generalized Lorenz-Mie theory. The influence of parameters of Gaussian beam (size of beam waist and location of beam waist centre) and that of particle parameters on the photophoretic force are investigated in detail. The results show that the photophoretic force can be larger than the radiation pressure force by an order of 4~5, which makes the radiation force to be negligible in practical experiments in certain conditions.

1 Introduction

Compared to the extensive studies on the radiation pressure force of optical tweezers, the photophoretic force is a "forgotten force" in the field of optical manipulation technique. This is partially because most of the previous studies of photophoretic force were motived by the applications in atmospheric science and astrophysics. Until recent years, breakthroughs have been made in the experimental line that photophoresis-based optical manipulation of small particles provides a significant way to investigate the characteristics of physical and chemical properties of aerosol particles, in a combination of other techniques, such as imaging, light scattering, Raman spectroscopy and others. The application of trapped particle in realizing three-dimensional displays in space named as optical trap displays also attracted a lot of attention.

Compared to the rapid developments in the experiments, theoretical analysis of photophoretic forces is less developed, which is partially because it is an interdisciplinary problem of thermal dynamics, electromagnetic scattering and fluid mechanics that requires corresponding development in each field. The underlying mechanisms of photophoretic force exerted by a structured laser beam are not fully understood. In this abstract, photophoretic force exerted on an absorbing sphere in air by a focused Gaussian beam is analysed using the generalized Lorenz-Mie theory [1].

2 Theoritical treatements

For a homogeneous non-volatile sphere in the gaseous medium, analytical solutions have been obtained in different conditions depending on the Knudsen number $Kn = l / a$, where l and a are the mean free path of the gas molecules and the particle size, respectively. In the slip-flow or continuous regime, where the size of the particle is much larger the mean free path of the gas molecules, we have $Kn < 1$ or $Kn << 1$. The photophoretic force is mainly due to the thermal creep around the particle. By applying the boundary conditions, the photophoretic force for a non-volatile sphere in the slip-flow regime is given by Mackowski [2]:

$$F_p = -\frac{4\pi c_s \eta_g^2 I_\lambda a}{\rho_g k_s T_0} \frac{1}{(1+3c_m l/a)(1+2c_t l/a + 2k_g/k_s)} J_1 \quad .(8)$$

where c_s, c_m and c_t are the momentum exchange coefficient, the thermal slip coefficient and the jump coefficient, respectively. T_0 is the temperature at infinity, which is assumed to be the ambient gas temperature. ρ_g and η_g is the density and viscosity of the surrounding gaseous medium, respectively. I_λ is the intensity of the incident wave. k_g and k_s are the thermal conductivity of the gas and that of the particle, respectively. For the special case $Kn << 1$, Eq. (1) can be approximated by:

$$F_p = -\frac{4\pi c_s \eta_g^2 I_\lambda a}{\rho_g k_s T_0} \frac{1}{(k_s + 2k_g)} J_1 . \quad (9)$$

which are the same as those given by Yalamov [3]. For a strong absorbing particle where radiation is absorbed entirely on the illuminated surface, the asymmetry factor $J_1 = 0.5$, and Eq. (1) reduced to that given by Reed [4].

On the other hand, if the size of the particle is much smaller than the mean free path of the gas molecules, we have $Kn >> 1$. Then the kinetic theory of gases is applied to give an analytical solution to the photophoretic force for a non-volatile sphere:

$$F_p = -\frac{\pi^2 \alpha \eta_g^2 I_\lambda a}{6\rho_g k_s T_0} \frac{(a/l)^2}{1+H_m} J_1 . \quad (10)$$

where

$$H_m = \frac{4\alpha}{15}\frac{k_g}{k_s}\frac{a}{l}. \tag{11}$$

where α is the thermal accommodation coefficient defined as the ratio of the net molecular kinetic energy transfer to the particle to that if all reflected molecules were characterized by a Maxwellian distribution evaluated at the actual local surface temperature. Considering:

$$l = 2\eta\left(\frac{\pi M}{8RT_0}\right)^{1/2}\frac{1}{\rho_g},\quad k_s = \frac{15}{4}\eta\frac{R}{M}, \tag{12}$$

Eq. (3) can be written as:

$$F_p = -\frac{\pi a^3 \alpha p I_\lambda}{3(ha+k_s)T_0}J_1. \tag{13}$$

which is the same as those given by Zulehner and Rohatschek [5], and Yalamov et al [6]. For radiation absorbed entirely on the particle surface, where $J_1 = -0.5$, then Eq. (6) is exactly the same as that given by Hidy and Brock [7] with $h = \alpha p\bar{v}/(2T_0)$.

As shown in Eqs. (1)-(6), in both the slip-flow and the free molecule limit cases, expressions for the photophoretic forces have the same dependency upon radiative absorption, which is embodied in the photophoretic asymmetry factor J_1. The asymmetry factor J_1 represents a weighted integration of the source function over the particle volume and depends on the intensity of radiative heating, which makes the knowledge of internal field distribution a key issue [8,9]. In the case of a structured laser beam illumination, the asymmetric factor is extended to a vector, and the photophoretic force can be expressed as:

$$\mathbf{F}_{\text{ph}} = -C_{Kn}\mathbf{v}_{\text{as}}. \tag{14}$$

where C_{Kn} is a constant value in certain conditions and $\mathbf{v}_{\text{as}}$ is the asymmetric vector

$$\mathbf{v}_{\text{as}} = I_\lambda(J_x\hat{x} + J_y\hat{y} + J_z\hat{z}). \tag{15}$$

$$J_{\begin{Bmatrix}x\\y\end{Bmatrix}} = \frac{6nk}{|M|^2 x^3}\begin{Bmatrix}\text{Im}\\ \text{Re}\end{Bmatrix}\sum_{n=1}^{\infty}[A_n^m(S_n^* + \frac{n+1}{M}R_{n+1}) + B_n^m(-S_n + \frac{n+1}{M}R_n) + iC_n^m S_n]. \tag{16}$$

$$J_z = -\frac{12nk}{|M|^2 x^3}\text{Im}\sum_{n=1}^{\infty}\sum_{m=-n}^{n}[D_n^m(S_n^* + \frac{n+1}{M}R_{n+1}) + E_n^m(-S_n + \frac{n+1}{M}R_n) + iF_n^m S_n]. \tag{17}$$

$$A_n^m = \frac{1}{(n+1)^2}\{\sum_{m=0}^{n-1} d_n d_{n+1}^* g_{n+1,TM}^{m,*} g_{n,TM}^{m+1}\frac{(n+|m|+1)!}{(n-|m|-1)!} + \sum_{m=0}^{n} d_n^* d_{n+1} g_{n,TM}^{m,*} g_{n+1,TM}^{m+1}\frac{(n+|m|+2)!}{(n-|m|)!} - \sum_{m=-n}^{-1} d_n d_{n+1}^* g_{n+1,TM}^{m,*} g_{n,TM}^{m+1}\frac{(n+|m|+1)!}{(n-|m|+1)!} - \sum_{m=-n}^{-1} d_n^* d_{n+1} g_{n,TM}^{m,*} g_{n+1,TM}^{m+1}\frac{(n+|m|)!}{(n-|m|)!}\} \tag{18}$$

$$B_n^m = \frac{1}{(n+1)^2}\{\sum_{m=0}^{n-1} c_n c_{n+1}^* g_{n+1,TE}^{m,*} g_{n,TE}^{m+1}\frac{(n+|m|+1)!}{(n-|m|-1)!} + \sum_{m=0}^{n} c_n^* c_{n+1} g_{n,TE}^{m,*} g_{n+1,TE}^{m+1}\frac{(n+|m|+2)!}{(n-|m|)!} - \sum_{m=-n}^{-1} c_n c_{n+1}^* g_{n+1,TE}^{m,*} g_{n,TE}^{m+1}\frac{(n+|m|+1)!}{(n-|m|+1)!} - \sum_{m=-n}^{-1} c_n^* c_{n+1} g_{n,TE}^{m,*} g_{n+1,TE}^{m+1}\frac{(n+|m|)!}{(n-|m|)!}\} \tag{19}$$

$$C_n^m = \frac{2n+1}{[n(n+1)]^2}d_n c_n^* \times\{\sum_{m=0}^{n}(g_{n,TM}^{m+1} g_{n,TE}^{m,*} \pm g_{n,TM}^{m} g_{n,TE}^{m+1,*})\frac{(n+|m|+1)!}{(n-|m|-1)!} - \sum_{m=-n}^{-1}(g_{n,TM}^{m+1} g_{n,TE}^{m,*} \pm g_{n,TM}^{m} g_{n,TE}^{m+1,*})\frac{(n+|m|)!}{(n-|m|)!}\} \tag{20}$$

$$D_n^m = \frac{1}{(n+1)^2}d_n^* d_{n+1} g_{n,TM}^{m,*} g_{n+1,TM}^{m}\frac{(n+|m|+1)!}{(n-|m|)!} \tag{21}$$

$$E_n^m = \frac{1}{(n+1)^2}c_n^* c_{n+1} g_{n,TE}^{m,*} g_{n+1,TE}^{m}\frac{(n+|m|+1)!}{(n-|m|)!} \tag{22}$$

$$F_n^m = m\frac{2n+1}{[n(n+1)]^2}c_n^* d_n g_{n,TE}^{m,*} g_{n,TM}^{m}\frac{(n+|m|)!}{(n-|m|)!} \tag{23}$$

where $x = 2\pi a/\lambda$ is the size parameter, λ is the wavelength, $g_{n,TE}^m$ and $g_{n,TM}^m$ are the beam shape coefficients. c_n, d_n are the scattering coefficients.

3 Numerical results and disscussions

Parameters	Values
Particle density ρ_s	1.2613×10^3 kg / m^3
Gas Viscosity η_g	1.82×10^{-5} Pa·s
Thermal conduction coefficient k_s	0.28W / (m·K)
Temperature T_0	300K
Light Intensity I_λ	3.8×10^3 W / m^2
Pressure p	30Torr
Mass of Gas	28.952 kg/mol
Gas constant R	8.31

Table 1 *Parameters of the ambient atmosphere conditions and those of particle used in the simulations.*

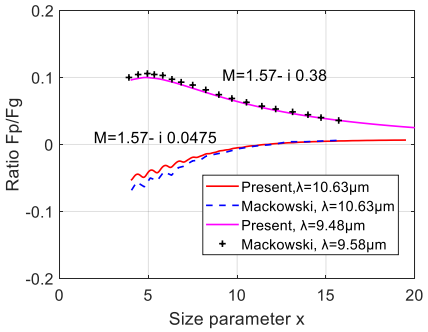

Fig.1 *Ratio of photophoretic force to gravity force of a glyceryl particle illuminated by a plane wave. Complex refractive indices of the particle are* $M=1.57-i0.0475$ *and* $M=1.57-i0.38$ *which correspond to the wavelength of* λ=10.63μm *and* λ=9.58μm，*respectively.*

To validate the correctness of the theoretical derivation, ratio of photophoretic force to gravity force of a glyceryl particle was calculated and displayed in Fig. 1 for a plane wave illumination. The parameters in the simulation concerning the ambient atmosphere conditions those of particle used in the simulations are listed in Table 1, which are the same as those given in the experiment implemented by Arnold and Lewitters [10]. As shown in Fig. 1. Satisfactory agreements have been achieved between the results obtained by Mackowski [2] and those calculated by our method in the case of plane wave case.

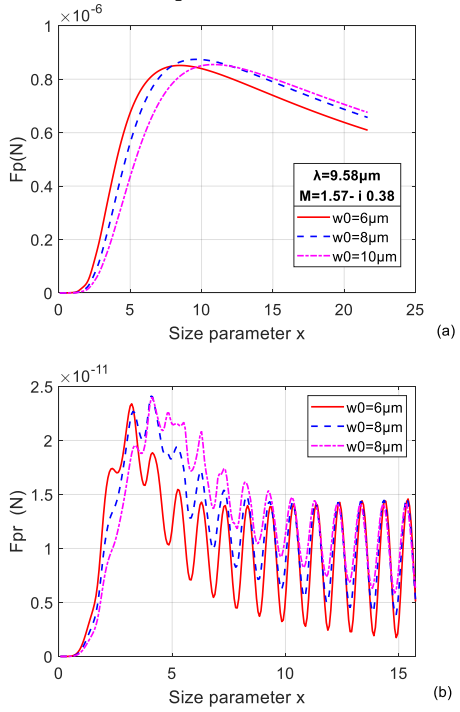

Fig. 2 *Variations of (a) photophoretic force; and (b) radiation pressure force of a glyceryl particle with size parameter. The parameters used are the same as those in Fig.1. Wavelength* λ=9.58μm，$M=1.57-i0.38$.

Variations of photophoretic force and radiation pressure force exerted on a glyceryl particle illuminated by a tightly focused Gaussian beam have been studied and the results for the case of λ=9.58μm and $M=1.57-i0.38$ are displayed in Fig. 2. The parameters used are the same as those in Fig. 1. The particle is assumed to be in the center of beam waist, e.g. $x_0=y_0=z_0=0$. The power of the laser beam is 300mW. As shown in Fig. 2, the photophoretic force is much larger than the radiation pressure force by an order of 4~5. Concerning the density of glyceryl, the gravity force of the particle is less than the photophoretic force by 2 orders. Thus, the glyceryl will be pushed away from the beam waist centre and then find an equilibrium position where the illumination density is much less than the beam waist centre.

4 Conclusion and perspectives

With the framework of GLMT, photophoretic force and radiation force exerted on an absorbing sphere by a focused Gaussian beam are studied. The influence of parameters of Gaussian beam and of parameters of particle on the photophoretic force are investigated. More detailed results will be presented in the coming conference.

5 Acknowledgement

The authors acknowledge the support by the Innovation Capability Support Program of Shaanxi (Grant no. 2021JZY-006); Fundamental Research Funds for the Central Universities (Grant no. XJS190507); Foreigner Young Talent Program (Grant no. QN20200027010)

6 References

[1] Gouesbet G, Gréhan G, Generalized Lorenz-Mie Theories Second Edition, Berlin, Springer (2011)

[2] Mackowski D W, Photophoresis of aerosol particles in the free molecular and slip-flow regimes, International Journal of Heat and Mass Transfer 32(5):843-854 (1989)

[3] Yalamov Y I, Kutukov V B, Shchukin E R., Theory of the photophoretic motion of the large-size volatile aerosol particle, Journal of Colloid and Interface Science 57(3): 564-571 (1976)

[4] Reed L D., Low Knudsen number photophoresis, Journal of Aerosol Science 8(2): 123-131 (1977)

[5] Zulehner W, Rohatschek H., Representation and calculation of photophoretic forces and tor-ques, Journal of Aerosol Science 26(2):201-210 (1995)

[6] Yalamov Y I, Kutukov V B, Shchukin E R. Motion of small aerosol particle in a light field, Journal of Engineering Physics 30(6):648-652 (1976)

[7] Hidy G M, Brock J R., Photophoresis and the descent of particles into the lower stratosphere, Journal of Geophysical Research 72(2): 455-460 (1967)

[8] Ambrosio L A., Towards photophoretic forces in the generalized Lorenz-Mie theory. Journal of Quantitative Spectroscopy & Radiative Transfer. To be published (2022).

[9] Ambrosio L A., Generalized Lorenz-Mie theory in the analysis of longitudinal photophoresis of arbitrary-index particles: On-axis axisymmetric beams of the first kind. Journal of Quantitative Spectroscopy & Radiative Transfer 275, 107889 (2021).

[10] Arnold S, Lewittes M., Size dependence of the photophoretic force, Journal of Applied Physics 53(7): 5314-5319 (1982)

13th International Conference Series on
Laser-light and Interactions with Particles
Optical Particle Characterization follow-up !
August 21-26th, 2022, Warsaw, Poland

PARTICLE MANIPULATION USING EVANESCENT LIGHT FIELDS OF OPTICAL NANOFIBRES

Georgiy TKACHENKO[1-2], Viet Giang TRUONG[1] and Síle NIC CHORMAIC[1,*]

[1] Light-Matter Interactions for Quantum Technologies Unit, OIST Graduate University, Onna, Okinawa 904-0495, Japan

[2] Tokyo University of Science, Shinjuku, Tokyo 162-8601, Japan

Corresponding author: sile.nicchormaic@oist.jp

Abstract

We discuss microparticle manipulation in the evanescent field of an optical nanofibre. Due to the nonparaxial nature of the tightly confined field, observation of the transverse spin of light becomes possible. We also note that inhomogeneous particles, such as gold-silica Janus particles, can be trapped using the evanescent field, with the gold cap acting as an optical sail. Some of the subtleties of the nature of the evanescent light field will be explored.

1 Particle Manipulation using Optical Nanofibres

In recent years, optical nanofibres are being used as alternatives to optical tweezers for micro- and nanoparticle trapping, manipulation, and sorting [1-4]. The intense evanescent field with a steep field gradient provides a strong trapping force consisting of gradient and scattering force components. Using counterpropagating beams in the nanofibre can localise the particles at specific positions allowing us to observe coupling of the spin component of light to orbital motion of the particle [5]. Recently, methods to control the polarisation of light in the evanescent field [6-8] have dramatically improved the functionality of optical nanofibres as particle trapping devices, allowing us to observe the transverse spin angular momentum of light and to exploit inhomogeneities in the particle's composition to emphasise some of the features of the light field.

1.1 Observation of the transverse spin of light using anisotropic particles in an evanescent field

In contrast to paraxial light, tightly confined light carries an appreciable amount of transverse spin angular momentum, $\mathbf{S}_\perp$. We have detected $\mathbf{S}_\perp$ in the evanescent field near the waist of an optical nanofibre by observing the rotation of an anisotropic microparticle held near the fibre and rotated using an optical tweezers, see Figure 1. By setting the optical tweezer's driving spin angular momentum to be parallel or antiparallel with respect to the transverse spin near the nanofibre, we can change the rate of the particle's rotation compared to the case where there is no light propagating in the fibre [9].

1.2 Janus particle manipulation in an evanescent field

Janus particles are composite particles that have gained interest in the research community recently, primarily in relation to biomedical applications. Such particles can act as micro- or nanoactuators, carriers, or imaging agents. One major challenge is the manipulation of Janus particles as they can be difficult to trap in standard optical tweezers. We demonstrate that the optical forces in the evanescent field of an optical nanofibre can be used to efficiently manipulate Janus particles consisting of silica microspheres half-coated with gold. We find that the Janus particles exhibit stronger transverse localisation and faster propulsion compared to silica particles of comparable size [10].

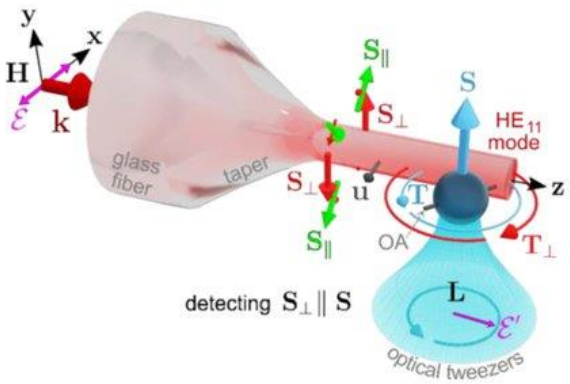

Figure 1 *Schematic of the experiment for a demonstration of the transverse spin of light. An anisotropic particle is trapped using an optical tweezers and placed in the evanescent field of an optical nanofibre. An optical torque* $\mathbf{T}_\perp$ *is produced via the transverse spin of light* $\mathbf{S}_\perp$ *and this contributes to the total torque* $\mathbf{T}$ *on the particle [9].*

2 Conclusion

We have presented several optical manipulation examples using nanofibre waveguides to control the motion of microparticles in the evanescent light field. The highly confined electromagnetic field allows us to demonstrate effects that are not easily observed using paraxial light fields, such as the transverse spin of light. By careful choice of the particle, we have been able to observe spin-orbit coupling, whereby the polarisation of the light influences the orbital motion of the particle around the optical nanofibre, and the transverse spin angular momentum of light. In future, we will focus our work on nonspherical particles.

3 Acknowledgement

The authors acknowledge I. Sanskriti for fabrication and imaging of some of the particles used, C. Esporlas for early

contributions to this research topic, I. Toftul and M. Petrov for theoretical contributions, and K. Karlsson M. Ozer and the Engineering Support Section of OIST for technical assistance. This work was funded by OIST and the Japan Society for the Promotion of Science (JSPS) KAKENHI (Grant-in-Aid for JSPS Fellows) 18F18367. G. T. was supported by a JSPS International Research Fellowship (Standard) P18367.

4 References

[1] Maimaiti A., Holzmann D., Truong V.G., Ritsch H., Nic Chormaic S., Nonlinear force dependence on optically bound micro-particle arrays in the evanescent fields of fundamental and higher order microfibre modes, Scientific Reports 6:30131 (2016)

[2] Xin H., Li B., Fiber-based optical trapping and manipulation, Frontiers of Optoelectronics 12:97-110 (2019)

[3] Yoshino T., Yamaura D., Komiya M., Sugawara M., Mitsumori Y., Niwano M., Hirano-Iwata A., Edamatsu K., Sadgrove M., Optical transport of sub-micron lipid vesicles along a nanofiber, Optics Express 28(26):38527-38538 (2020)

[4] Sadgrove, M., Yoshino T., Sugawara M., Mitsumori Y., Edamatsu K., Optically induced sieve effect for nanoparticles near a nanofiber taper, Physical Review Applied 16:044034 (2021)

[5] Tkachenko G., Toftul I., Esporlas C., Maimaiti A., Le Kien, F., Truong V.G., Nic Chormaic S., Light-induced rotation of dielectric microparticle around an optical nanofiber, Optica 7(1):59-62 (2020)

[6] Lei F., Tkachenko G., Ward J.M., Nic Chormaic S., Complete polarization control for a nanofiber waveguide using directional coupling, Physical Review Applied 11(6):064041 (2019)

[7] Joos M., Bramati A., Glorieux Q., Complete polarization control for a nanofiber waveguide using the scattering properties, Optics Express 27(13):18818-18830 (2019)

[8] Tkachenko G., Lei F., Nic Chormaic S., Polarisation control for optical nanofibres by imaging through a single lens, Journal of Optics 21(12):125604 (2019)

[9] Tkachenko G., Toftul I., Vylegzhanin A., Truong V.G., Petrov M., Nic Chormaic S., Detection of the transverse spin of light by twisting anisotropic particles near an optical nanofiber waveguide, Proceedings Volume 11926, Optical Manipulation and Structured Materials Conference 2021; 119260R (2021)

[10] Esporlas C.L., Tkachenko, G., Sanskriti I., Truong V.G., Nic Chormaic, S., Efficient optical manipulation of Janus particles by optical nanofibers, arXiv:2108.00748 [physics.optics] (2021)

13th International Conference Series on
Laser-light and Interactions with Particles
Optical Particle Characterization follow-up !
August 21-26th, 2022, Warsaw, Poland

OPTICAL PROPERTIES OF MONOLAYER OF SPHERICAL PARTICLES IN ABSORBING HOST MEDIUM UNDER NORMAL ILLUMINATION

Valery LOIKO*, Alexander MISKEVICH, Natalia LOIKO

[1] Institute of Physics, National Academy of Sciences of Belarus, Minsk, 220072, Belarus

Corresponding author: loiko@ifanbel.bas-net.by

Abstract

The method is developed to describe optical properties of a normally illuminated monolayer (2D array) of spherical particles embedded in a homogeneous absorbing host medium (matrix). It is based on multipole expansion of electromagnetic (EM) fields and dyadic Green's function in terms of vector spherical waves functions and takes into account multiple scattering of waves in the quasicrystalline approximation. The method is applied to describe the scattering and absorbing properties of partially ordered monolayers of spherical voids in silver (Ag) matrix.

1 Introduction

The particulate layers are object of intensive investigations in the last decades. The interest is caused by unique possibilities which are opened by usage of these layers in optics, optoelectronics, photonics and nanophotonics, medical applications, etc. The majority of work devoted to these structures imply that absorbing or nonabsorbing particles are located in a nonabsorbing host medium. However, some applications require consideration of particulate layers in absorbing environment, e.g. solar cells, photonic crystals, ocean optics, etc. There are publications where optical properties of single particles [1] or sparse ensembles of particles [2,3] in absorbing host medium are considered. But we are not aware of publications in which densely packed monolayers of particles in an absorbing medium would be studied.

We present a brief summary of the method we are developing for determining the optical properties of a monolayer of spherical homogeneous particles in an absorbing host medium (matrix). This method is used to describe the optical characteristics of a monolayer of identical densely packed partially ordered spherical voids in a silver plate.

2 Theory

We consider the monolayer of N identical spherical particles centered at the points $\mathbf{R}_1$, $\mathbf{R}_2$, …, $\mathbf{R}_N$ in the monolayer plane (x,y). The coordinate origin O is in the center of arbitrarily chosen particle (Figure. 1). The monolayer stands in an absorbing matrix and is normally illuminated by the plane EM wave with electric vector $\mathbf{E}_0$ and unit polarization vector $\hat{\boldsymbol{\varepsilon}}_0 = \varepsilon_x\hat{\mathbf{x}} + \varepsilon_y\hat{\mathbf{y}}$:

$$\mathbf{E}_0 = \hat{\boldsymbol{\varepsilon}}_0 E_0 e^{ik_h z}, \qquad (1)$$

where $k_h=2\pi m_h/\lambda$ is complex wavenumber, $m_h=n_h+i\kappa_h$, n_h and κ_h are refractive and absorption indices of host medium, λ is the wavelength of incident wave in vacuum, E_0 is the amplitude of incident wave in the monolayer plane (z=0).

The field $\mathbf{E}(\mathbf{r})$ in some point $\mathbf{r}$ is the sum of fields of incident wave and waves scattered by the given configuration of particulate ensemble:

$$\mathbf{E}(\mathbf{r}) = \mathbf{E}_0(\mathbf{r}) + \sum_{j=1}^{N} \mathbf{F}_j(\mathbf{r}, \mathbf{R}_j). \qquad (2)$$

Here

$$\mathbf{F}_j(\mathbf{r}, \mathbf{R}_j) = \frac{(k_p^{\,2} - k_h^{\,2})}{4\pi} \int_{V_p} d\mathbf{r}' \ddot{\mathrm{G}}(\mathbf{r}, \mathbf{R}_j + \mathbf{r}') \cdot \mathbf{E}(\mathbf{R}_j + \mathbf{r}') \qquad (3)$$

is the field created in point $\mathbf{r}$ by the particle centred at point $\mathbf{R}_j$, $k_p=2\pi m_p/\lambda$ is complex wavenumber, $m_p=n_p+i\kappa_p$, n_p and κ_p are refractive and absorption indices of particle, V_p is the particle volume, $0\le|\mathbf{r}'|\le D/2$, D is the particle diameter, $\mathbf{E}(\mathbf{R}_j+\mathbf{r}')$ is the field in point $\mathbf{R}_j+\mathbf{r}'$ within the particle (internal field), $\ddot{\mathrm{G}}$ is the dyadic (tensor) Green's function:

$$\ddot{\mathrm{G}}(\mathbf{r}, \mathbf{r}_0) = \left[\ddot{\mathrm{I}} + \frac{1}{k_h^2}\nabla\otimes\nabla\right] \frac{e^{ik_h|\mathbf{r}-\mathbf{r}_0|}}{|\mathbf{r}-\mathbf{r}_0|}, \qquad (4)$$

$\ddot{\mathrm{I}}$ is identity dyadic.

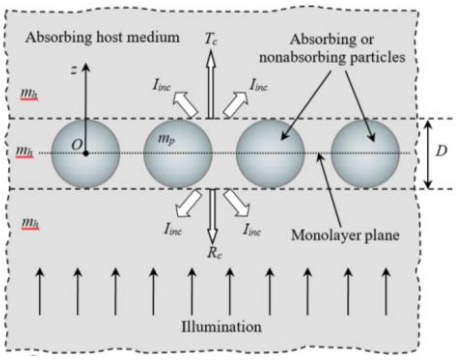

Figure 1 *Schematic view (along the monolayer plane) of normally illuminated monolayer of spherical particles embedded in absorbing host medium (matrix). T_c and R_c are coherent transmission and reflection coefficients of the system consisting of the monolayer of particles with diameter D and matrix layer with thickness D. I_{inc} is the intensity of the incoherent light.*

Averaging the Eqs. (2) and (3) over all possible ensemble configurations results in the following equations [4]:

$$\langle \mathbf{E}(\mathbf{r})\rangle = \mathbf{E}_0(\mathbf{r}) + \sum_{j=1}^{N}\langle \mathbf{F}_j(\mathbf{r},\mathbf{R})\rangle = \mathbf{E}_0(\mathbf{r}) + \\ + \frac{(k_p{}^2 - k_h^2)}{4\pi}\rho_0 \int \mathrm{d}\mathbf{R}\int_{V_p}\mathrm{d}\mathbf{r}'\ddot{\mathrm{G}}(\mathbf{r},\mathbf{R}+\mathbf{r}')\cdot\langle \mathbf{E}(\mathbf{r}')\rangle_1 , \quad (5)$$

$$\langle \mathbf{E}(\mathbf{r}')\rangle_1 = \mathbf{E}_0(\mathbf{r}') + \frac{(k_p{}^2 - k_h^2)}{4\pi}\int_{V_p}\mathrm{d}\mathbf{r}''\ddot{\mathrm{G}}(\mathbf{r}',\mathbf{r}'')\cdot\langle \mathbf{E}(\mathbf{r}'')\rangle_1 + \\ + \frac{(k_p{}^2 - k_h^2)}{4\pi}\rho_0 \int \mathrm{d}\mathbf{R}\mathrm{g}(R)\int_{V_p}\mathrm{d}\mathbf{r}''\ddot{\mathrm{G}}(\mathbf{r}',\mathbf{R}+\mathbf{r}'')\cdot\langle \mathbf{E}(\mathbf{r}'')\rangle_1 . \quad (6)$$

Here ρ_0 is averaged number density (concentration) of particles, g(R) is the radial distribution function (RDF) [4,5] characterizing the probability to find the particle centred at distance R relative the particle centred at the coordinate origin, $R=|\mathbf{R}|$, $\langle \mathbf{E}(\mathbf{r}')\rangle_1$ is the field in the particle centred at the coordinate origin, averaged over the positions of all other particles (averaged internal field). It determined by Eq. (6) with applying the quasicrystalline approximation (QCA) [6].

The field in the far zone in the direction $\hat{\mathbf{r}}$ for the single monolayer particle is determined via the amplitude scattering function:

$$\mathbf{f}(\hat{\mathbf{r}}) = \frac{(k_p{}^2 - k_h^2)k_h}{4\pi}\int_{V_p}\mathrm{d}\mathbf{r}'\left(\ddot{\mathrm{I}} - \hat{\mathbf{r}}\otimes\hat{\mathbf{r}}\right)e^{-ik_h\hat{\mathbf{r}}\cdot\mathbf{r}'}\cdot\langle \mathbf{E}(\mathbf{r}')\rangle_1 . \quad (7)$$

It takes into account the multiple scattering of waves. To determine $\mathbf{f}(\hat{\mathbf{r}})$ we expand the functions entered in (6), (7) in terms of vector spherical wave functions [4]. As a result, we obtain:

$$\mathbf{f}(\hat{\mathbf{r}}) = E_0[\mathrm{f}_\theta(\hat{\mathbf{r}})\hat{\boldsymbol{\theta}} + \mathrm{f}_\varphi(\hat{\mathbf{r}})\hat{\boldsymbol{\varphi}}], \quad (8)$$

where

$$\mathrm{f}_\theta(\hat{\mathbf{r}}) = i\sum_{l=1}^{\infty}\frac{(2l+1)}{l(l+1)}\left[\begin{matrix}\pi_l^{(1)}(\mu)\cdot\left(b_{lM}^{(o)}\cos\varphi + ib_{lM}^{(e)}\sin\varphi\right)+\\ +\tau_l^{(1)}(\mu)\cdot\left(b_{lE}^{(e)}\cos\varphi + ib_{lE}^{(o)}\sin\varphi\right)\end{matrix}\right], \quad (9)$$

$$\mathrm{f}_\varphi(\hat{\mathbf{r}}) = -\sum_{l=1}^{\infty}\frac{(2l+1)}{l(l+1)}\left[\begin{matrix}\tau_l^{(1)}(\mu)\cdot\left(b_{lM}^{(e)}\cos\varphi + ib_{lM}^{(o)}\sin\varphi\right)+\\ +\pi_l^{(1)}(\mu)\cdot\left(b_{lE}^{(o)}\cos\varphi + ib_{lE}^{(e)}\sin\varphi\right)\end{matrix}\right]. \quad (10)$$

Angular functions $\pi_l^{(1)}(\mu)=\mathrm{P}_l^{(1)}(\cos\theta)/\sin\theta$, $\tau_l^{(1)}(\mu)=\mathrm{d}\mathrm{P}_l^{(1)}(\cos\theta)/\mathrm{d}\theta$, where $\mu=\cos\theta$, $\mathrm{P}_l^{(1)}(\cos\theta)$ are associated Legendre function, $\hat{\boldsymbol{\theta}}$ and $\hat{\boldsymbol{\varphi}}$ are unit vectors in the directions determined by polar θ and azimuthal φ scattering angles.

The expansion coefficients $b_{lM}^{(o,e)}$ и $b_{lE}^{(o,e)}$ take into account multiple scattering of waves and determine the contribution of multipoles of different orders into the total scattering field. They are calculated by analogy with the technique described in [4]. Using these coefficients, we can write the equations for coherent transmission T_c and coherent reflection R_c coefficients:

$$T_c = e^{-4x\beta_h}\left[\begin{matrix}\left|\varepsilon_x - \frac{\eta}{x^2(1+i\beta_h)^2}\sum_{l=1}^{\infty}(2l+1)\left(b_{lM}^{(o)} + b_{lE}^{(e)}\right)\right|^2 + \\ +\left|\varepsilon_y - i\frac{\eta}{x^2(1+i\beta_h)^2}\sum_{l=1}^{\infty}(2l+1)\left(b_{lM}^{(e)} + b_{lE}^{(o)}\right)\right|^2\end{matrix}\right], \quad (11)$$

$$R_c = e^{-4x\beta_h}\left(\frac{\eta}{x^2(1+i\beta_h)^2}\right)^2\left[\begin{matrix}\left|\sum_{l=1}^{\infty}(-1)^l(2l+1)\left(b_{lM}^{(o)} - b_{lE}^{(e)}\right)\right|^2 + \\ +\left|\sum_{l=1}^{\infty}(-1)^l(2l+1)\left(b_{lM}^{(e)} - b_{lE}^{(o)}\right)\right|^2\end{matrix}\right], \quad (12)$$

where $x=\pi D n_h/\lambda$ is the particle size parameter in the host medium, $\beta_h=\kappa_h/n_h$, η is the monolayer filling factor describing the ratio of the area of all particle projections into the monolayer plane to the area where the particles are distributed.

The incoherent scattering coefficient F_{inc} of a monolayer is determined as follows:

$$F_{inc} = \int_0^{2\pi}\mathrm{d}\varphi\int_0^{\pi} I_{inc}^{rd}(\theta,\varphi)e^{-2x\beta_h[1+1/|\cos\theta|]}\sin\theta\,\mathrm{d}\theta . \quad (13)$$

Here I_{inc}^{rd} is the reduced intensity [4] of incoherently scattered light:

$$I_{inc}^{rd}(\theta,\varphi) = \frac{\eta\,\mathrm{S}_2(\sin\theta)}{\pi x^2(1+\beta_h^2)}\times \\ \times\left\{\begin{matrix}\left|\sum_{l=1}^{\infty}\frac{(2l+1)}{l(l+1)}\left[\begin{matrix}\pi_l^{(1)}(\mu)\cdot\left(b_{lM}^{(o)}\cos\varphi + ib_{lM}^{(e)}\sin\varphi\right)+\\ +\tau_l^{(1)}(\mu)\cdot\left(b_{lE}^{(e)}\cos\varphi + ib_{lE}^{(o)}\sin\varphi\right)\end{matrix}\right]\right|^2 + \\ +\left|\sum_{l=1}^{\infty}\frac{(2l+1)}{l(l+1)}\left[\begin{matrix}\tau_l^{(1)}(\mu)\cdot\left(b_{lM}^{(e)}\cos\varphi + ib_{lM}^{(o)}\sin\varphi\right)+\\ +\pi_l^{(1)}(\mu)\cdot\left(b_{lE}^{(o)}\cos\varphi + ib_{lE}^{(e)}\sin\varphi\right)\end{matrix}\right]\right|^2\end{matrix}\right\}, \quad (14)$$

were $\mathrm{S}_2(\sin\theta)$ is the structure factor of a monolayer [4,7]:

$$\mathrm{S}_2(\sin\theta) = 1 + 8\eta\int_0^{\infty}[\mathrm{g}(u)-1]\mathrm{J}_0(2xu\sin\theta)u\,\mathrm{d}u , \quad (16)$$

$u=R/D$ is the dimensionless distance in the monolayer plane expressed in the particle diameters D.

The absorption coefficient A of a monolayer is defined using the (11)-(13) as follows:

$$A = 1 - T_c - R_c - F_{inc}. \quad (15)$$

These coefficients characterize only the system consisting of the layer of host medium of thickness D (bounded by dashed lines in Figure 1) containing the monolayer of spheres with diameter D. They do not take into account absorption of host medium outside the monolayer.

3 Results of Calculations

We applied the developed method to consider the optical properties of the system consisting of the partially ordered submicron spherical voids in a homogeneous silver plate.

Figure 2 shows the spectral dependences of T_c, R_c, F_{inc} and A coefficients of such system at different diameters D of voids. One can see that in the spectral region of plasmonic resonance (λ=0.3 - 0.4 μm) the coherent transmittance, as a whole, grows with decreasing the void diameter (Figure 2a). For small voids, $D\leq$0.05 μm, the "extraordinary transmittance" is observed. Less pronounced peaks occur outside this region for larger voids.

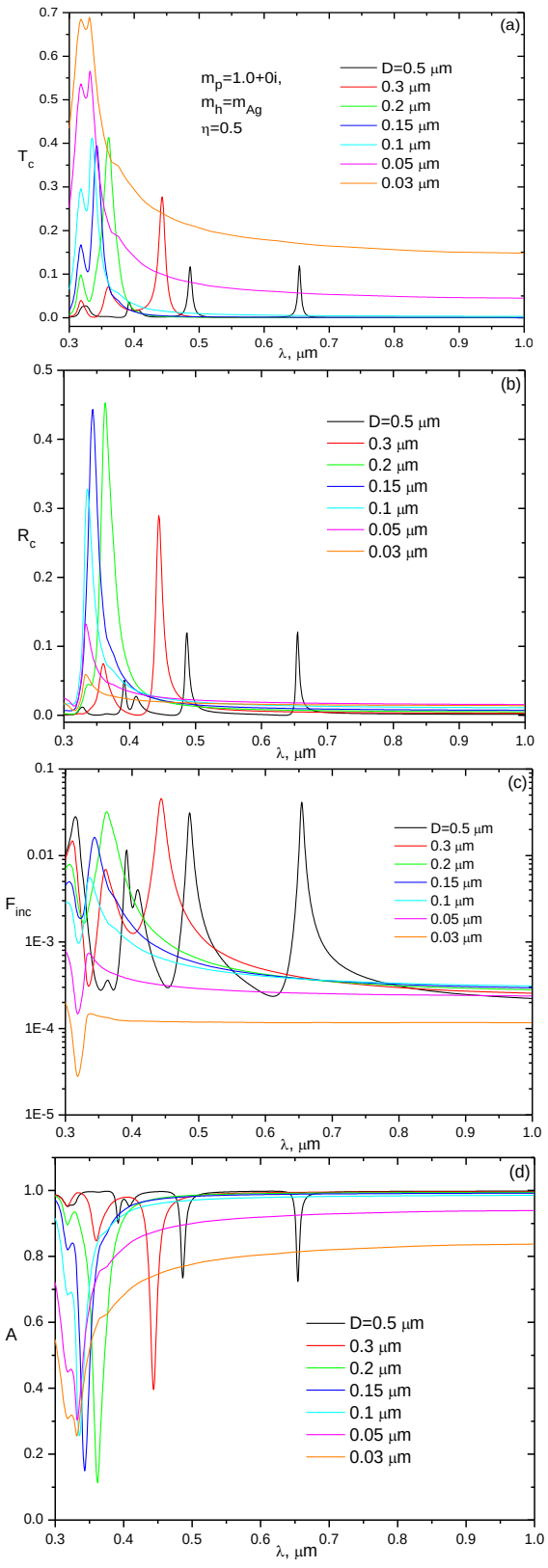

Figure 2 *Spectral dependences of T_c, R_c, F_{inc} and A coefficients of the partially ordered monolayer of spherical voids in silver (Ag) plate at different diameters D of voids. η=0.5*

From Figure 2 it follows that for larger voids, the strong correlation takes place between T_c, R_c, F_{inc} and A spectra, especially in the wavelength range outside the plasmonic resonance region. In contrast to the monolayer of silver particles in air [8] where dips in the transmission and peaks in the absorption coefficients spectra take place, here the peaks in $T_c(\lambda)$ and dips in $A(\lambda)$ are observed. Also, the low amount of incoherently scattered (Figure 2c) and large amount of absorbed (Figure 2d) light take place.

4 Conclusions

The method to describe optical properties of a normally illuminated monolayer of homogeneous identical spherical particles in an absorbing host medium is developed. It is based on multipole expansion of electromagnetic (EM) fields and dyadic Green's function in terms of vector spherical waves functions and takes into account multiple scattering of waves in the quasicrystalline approximation.

The method is applied to describe scattering and absorbing properties of the system consisting of the monolayer of voids of various diameters D in the silver matrix. The effect of "extraordinary transmittance" is observed for the monolayer of nanosized (D≤0.05 μm) voids.

The method and obtained results can be used to investigate and optimize various optical, optoelectronic, and photonic devices, such as solar cells, light emitting diodes, optical filters, etc.

5 References

[1] Sudiarta W., Chylek P., Mie-scattering formalism for spherical particles embedded in an absorbing medium, JOSA A 18:1275–8 (2001).

[2] Mishchenko M.I., Dlugach J.M., Multiple scattering of polarized light by particles in an absorbing medium, Appl. Opt. 58:4871–7 (2019).

[3] Zhai J., Ma L., Xu W., Liu L., Effect of host medium absorption on the radiative properties of dispersed media consisting of optically soft particles, JQSRT 254:108206, 9 pp. (2020).

[4] Loiko N.A., Miskevich A.A., Loiko V.A., Incoherent component of light scattered by a monolayer of spherical particles: analysis of angular distribution and absorption of light, JOSA A 35(1):108-118 (2018).

[5] J.M. Ziman, *Models of disorder* (Univ. Press, Cambridge, 1979).

[6] Lax M., Multiple Scattering of Waves. II. The Effective Field in Dense Systems, Physical Review 85(4):621-629 (1952).

[7] A.P. Ivanov, V.A. Loiko, V.P. Dick, *Propagation of light in close-packed disperse media* (Nauka i Tekhnika, Minsk, 1988) (in Russian).

[8] Loiko N.A., Miskevich A.A., Loiko V.A., Light scattering and absorption by two-dimensional arrays of nano and micrometer monodisperse spherical silver particles, JQSRT 266:107571, 20pp. (2021).

13th International Conference Series on
Laser-light and Interactions with Particles
Optical Particle Characterization follow-up !
August 21-26th, 2022, Warsaw, Poland

RADIATION FORCE ON A PEMC SPHERE ILLUMINATED BY ARBITRARY-SHAPED BEAM

Huan TANG[1,*], Renxian LI[1-2], Liu YANG[1], Bing WEI[1], Shuhong GONG[1]

[1] School of Physics and Optoelectronic Engineering, Xidian University, Xi'an 710071, China
[2] Collaborative Innovation Center of Information Sensing and Understanding, Xidian University, Xi'an 710071, China
Corresponding author: htang_1@stu.xidian.edu.cn

Abstract

The radiation force generated by the interaction between the arbitrary-shaped optical polarized beams and the PEMC (perfect electromagnetic conductor) sphere is discussed in this paper. The generalized Lorenz-Mie theory (GLMT) for a laser beam of arbitrary shape illuminating a perfect electromagnetic conductor (PEMC) sphere is presented. The precise expressions of arbitrary-shaped optical polarized beams are attained based on the vector spherical wave functions (VSWFs) and beam shape coefficients (BSCs). The scattering beams are composed of the VSWFs and scattering coefficients which are gotten considering the special boundary conditions at the surface of the PEMC sphere. According to the Maxwell stress tensor, the exact expression of the radiation force in the GLMT frame is attained, which is divided into three parts: co-polarization, cross-polarization, and interference components. Taking the Bessel beam as incident, the effects of size parameters, admittance coefficient, and the beam parameters of the Bessel beam on the radiation force are calculated. The radiation force effect between the structural beam and the meta-material has promising application prospects, such as in biology, medicine, and particle manipulation.

1 Introduction

As a type of electric-magneto metamaterial [1, 2], the perfect electromagnetic conductor (PEMC) [3, 4] aroused more interest for its special characteristics. Different from the dielectric conductors, the electromagnetic field disappears in the internal of PEMC [5]. Besides, the "optical rotation" effect [6, 7] is presented when a PEMC is illuminated by some kind of polarized beam. Just as its name implies, the polarization states change when the electromagnetic field illuminates to a PEMC, which induces other cross-polarized scattering waves except for conventional co-polarized scattering waves. This "optical rotation" (It is also named circular dichroism.) effect has been discovered in chiral material [8, 9] (quartz and tartrate), liquid crystals [10, 11], and ice crystal [12] .etc. Besides, it has been applied to the pharmaceutical and biological fields [13].

The PEMC usually is considered as an extension of the perfect electrical conductor (PEC) [14] and perfect magnetic conductor (PMC) [15]. The characteristics both of PEC and PMC are united by the PEMC using admittance coefficient M. The PEMC degenerates into PEC (limit $M \to \infty$) or PMC ($M = 0$) only depending on the M . Since the concept of PEMC was put forward, there are plenty of researches on the PEMC because of its promising prospect.

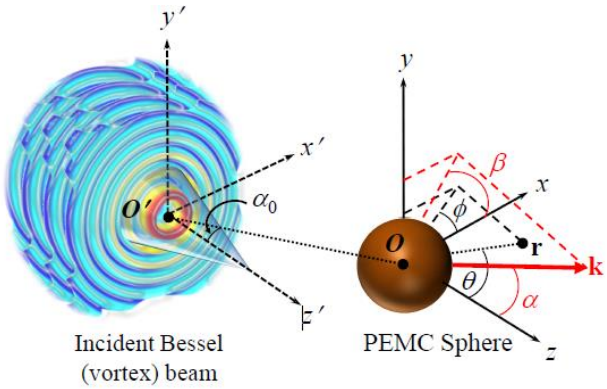

Figure 1 *Demonstration diagram that a PEMC sphere is illuminated by an arbitrarily shaped beam (The Bessel beam with half-cone angle α_0 as the incident beam in this Fig). The radial vector* $\mathbf{r}$ *and the wave vector* $\mathbf{k}$ *are shown in* $O-xyz$ *coordinate. The included angle* α *and* β *express the relation between the wave vector* $\mathbf{k}$ *and the* $O-xyz$ *coordinate.*

The PEMC is seen as a perfect reflector to the beam and the electromagnetic field. Therefore, the reflection, scattering, and absorption of PEMC to electromagnetic waves always is a key research area [16]. Over the past few years, the interaction when a plane - wave illuminates to the PEMC is a critical research direction. A research studied the scattering of two-dimensional PEMC and PEMC strips to the plane - wave [17]. Another research also studied the scattering that a plane - wave illuminates to a PEMC strip which buried in non-integer dimensional dielectric half-space is using Kobayashi potential method [18]. Some scholars made some researches that the electromagnetic radiation scattering by PEMC circular cylinder [19], sphere [20] and arbitrarily oriented dipole field [21] in free space. Another scholar studied the electromagnetic scattering by a PEMC plate in a lossy medium [22]. Besides, some studies considered the scattering effect [23] and polarizabilities when the electromagnetic wave illuminates a PEMC sphere located in chiral media. The scattering characteristics that the plane - wave illuminates to a PEMC cylinder covered by a homogeneous plasma anisotropic material also has been

studied [24]. What's more, the interference and diffraction effects also attract others' attention [25]. In recent years, a study focused on the diffraction when a plane - wave illuminates to a PEMC half-screen [26].

Recently, the research contents also extent to the radiation force and the torque effects, not just the scattering effect. The electromagnetic radiation force was studied when a plane - wave illuminates to a PEMC circular cylinder[28,29]. Later, the more complex model to research the electromagnetic radiation force was built that PEMC sphere is illuminated by a linear polarization plane - wave [30]. Besides, the radiation force and torque were explored when a circular polarized plane - wave illuminates to a PEMC sphere placed in a lossy space [31]. More physical characteristics have been discovered based on these relatively new researches.

Improvement based on the PEMC theory and combined the well-known characteristics of arbitrary-shaped optical polarized beams, this manuscript highlights the interaction between the PEMC sphere and the arbitrary-shaped optical polarized beams. The main formulas that arbitrary-shaped optical polarized beams illuminate to a PEMC are derived. At first, the beam shape coefficients (BSCs) of arbitrary-shaped beams are derived using the angular spectrum decomposition method (ASDM). By substituting the expressions of the vector spherical wave functions (VSWF), the exact expressions of arbitrary-shaped optical beams under different polarization states are attained. Later, the precise formulas for scattering fields are attained based on the generalized Lorenz-Mie theory (GLMT). Based on the correlation expressions of the incident and the scattering fields, both the longitudinal and the transverse radiation forces are determined. The scattering coefficients are gotten after solving the boundary conditions. Different from traditional scattering coefficients gotten when electromagnetic wave illuminates to a dielectric sphere, the scattering coefficients are divided into co-polarized and cross-polarized components. In order to better explain the physical phenomenon, this paper uses the Bessel beam as the incident illuminating to a PEMC sphere. The optical radiation force and its various polarization components are highlighted in this paper.

2 Method

The incident electromagnetic field are expressed as Eqs. (1 – 2) according to the VSWFs and BSCs.

$$\mathbf{E}_{inc} = -\sum_{n=1}^{\infty}\sum_{m=-n}^{n} iE_{mn}\left[p_{mn}\mathbf{N}_{mn}^{(1)}(k,\mathbf{r}) + q_{mn}\mathbf{M}_{mn}^{(1)}(k,\mathbf{r})\right] \quad (24)$$

$$\mathbf{H}_{inc} = -\frac{k}{\omega\mu_0}\sum_{n=1}^{\infty}\sum_{m=-n}^{n} E_{mn}\left[q_{mn}\mathbf{N}_{mn}^{(1)}(k,\mathbf{r}) + p_{mn}\mathbf{M}_{mn}^{(1)}(k,\mathbf{r})\right] \quad (25)$$

Where, the $\mathbf{N}_{mn}^{(1)}$ and $\mathbf{M}_{mn}^{(1)}$ are the VSWFs and the BSCs (p_{mn} and q_{mn}) are attained based the ASDM.the scattering electric field and magnetic field are expressed using VSWFs as

$$\mathbf{E}_{sca} = \sum_{n=1}^{\infty}\sum_{m=-n}^{n} iE_{mn}\left[a_{mn}\mathbf{N}_{mn}^{(3)}(k\mathbf{r}) + b_{mn}\mathbf{M}_{mn}^{(3)}(k\mathbf{r})\right] \quad (26)$$

$$\mathbf{H}_{inc} = -\frac{k}{\omega\mu_0}\sum_{n=1}^{\infty}\sum_{m=-n}^{n} E_{mn}\left[q_{mn}\mathbf{N}_{mn}^{(1)}(k,\mathbf{r}) + p_{mn}\mathbf{M}_{mn}^{(1)}(k,\mathbf{r})\right] \quad (27)$$

Where the a_{mn} and b_{mn} are the scattering coefficient. with

$$E_{mn} = i^n E_0\sqrt{\frac{2n+1}{n(n+1)}\frac{(n-m)!}{(n+m)!}} \quad (28)$$

Because of the boundary condition of PEMC sphere surface:

$$\mathbf{n}\times(\mathbf{H}+M\mathbf{E}) = \mathbf{0} \quad (29)$$

The scattering coefficients can be attained:

$$\begin{aligned} a_{mn} &= a_{mn}^{TE\to TM} + a_{mn}^{TM\to TM} \\ b_{mn} &= b_{mn}^{TE\to TE} + b_{mn}^{TM\to TE} \\ a_{mn}^{TM\to TM} &= p_{mn}a_n^{TM\to TM} \\ a_{mn}^{TE\to TM} &= q_{mn}a_n^{TE\to TM} \\ b_{mn}^{TE\to TE} &= q_{mn}b_n^{TE\to TE} \\ b_{mn}^{TM\to TE} &= p_{mn}b_n^{TM\to TE} \end{aligned} \quad (30)$$

$$a_n^{TM\to TM} = \frac{\left\{M^2\eta^2 h_n^{(1)}(ka)\left[kaj_n(ka)\right]' + j_n(ka)\left[kah_n^{(1)}(ka)\right]'\right\}}{\left(1+M^2\eta^2\right)h_n^{(1)}(ka)\left[kah_n^{(1)}(ka)\right]'}$$

$$a_n^{TE\to TM} = \frac{iM\eta\left\{j_n(ka)\left[kah_n^{(1)}(ka)\right]' - h_n^{(1)}(ka)\left[kaj_n(ka)\right]'\right\}}{\left(1+M^2\eta^2\right)h_n^{(1)}(ka)\left[kah_n^{(1)}(ka)\right]'}$$

$$b_n^{TE\to TE} = \frac{\left\{M^2\eta^2 j_n(ka)\left[kah_n^{(1)}(ka)\right]' + h_n^{(1)}(ka)\left[kaj_n(ka)\right]'\right\}}{\left(1+M^2\eta^2\right)h_n^{(1)}(ka)\left[kah_n^{(1)}(ka)\right]'}$$

$$b_n^{TM\to TE} = -a_n^{TE\to TM} \quad (31)$$

Where the $a_{mn}^{TM\to TM}$ and $b_{mn}^{TE\to TE}$ are the scattering co-polarization components, and the $a_{mn}^{TE\to TM}$ and $b_{mn}^{TM\to TE}$ are the scattering cross–polarization components.

Because the time - averaged Maxwell's stress tensor is

$$\overset{\mathrm{t}}{\boldsymbol{\sigma}} = \left(\varepsilon_0\mathbf{E}\otimes\mathbf{E} + \mathbf{H}\otimes\mathbf{H} - \frac{1}{2}\left(\varepsilon_0\mathbf{E}\cdot\mathbf{E} + \mathbf{H}\cdot\mathbf{H}\right)\overset{\mathrm{t}}{\mathbf{I}}\right) \quad (32)$$

The expression of radiation force is shown as follows

$$\langle\mathbf{F}\rangle = \iint_{\Omega}\langle\overset{\mathrm{t}}{\boldsymbol{\sigma}}\rangle\cdot\mathbf{n}d\Omega \quad (33)$$

Therefore, the precise expressions of radiation force in x, y, and z directions and their components can be rewritten as the combinations of BSCs and scattering coefficients. Due to space limitation, the derivation will not be carried out here.

3 Discussion and conclusion

In this work, the radiation force generated because of the interaction between the PEMC sphere and arbitrary-shaped optical polarized beams is discussed. The size parameter ka and admittance coefficient M have been proved they take effect on the radiation force and its co-polarization, cross-polarization and interference components. Besides, the effect from order l and half cone angle α_0 of the Bessel beam has been verified. Limited to space, we can't discuss

it here. This work is of great significance in the research of optical tweezers, particle manipulation, and metamaterials.

4 Acknowledgement

The authors acknowledge the support from the National Natural Science Foundation of China [61901324 , 62001345], China Research Institute of Radiowave Propagation [61971385], and the China Postdoctoral Science Foundation [2019M653548 , 2019M663928XB].

5 References

[1] David Schurig, Jack J Mock, BJ Justice, Steven A Cummer, John B Pendry, Anthony F Starr, and David R Smith. Metamaterial electromagnetic

[2] Ari Sihvola. Metamaterials in electromagnetics. Metamaterials, 1(1):2–11, 2007.

[3] Ismo V Lindell and Ari H Sihvola. Perfect electromagnetic conductor. Journal of Electromagnetic Waves and Applications, 19(7):861–869,2005.

[4] Ismo V Lindell and Ari H Sihvola. Losses in the pemc boundary. IEEE transactions on antennas and propagation, 54(9):2553–2558, 2006.

[5] Ismo V Lindell and Ari H Sihvola. Electromagnetic boundary conditions defined in terms of normal field components. IEEE Transactions on Antennas and Propagation, 58(4):1128–1135, 2010.

[6] Nina Berova, Koji Nakanishi, and Robert W Woody. Circular dichroism: principles and applications. John Wiley & Sons, 2000.

[7] Gerald D Fasman. Circular dichroism and the conformational analysis of biomolecules. Springer Science & Business Media, 2013.

[8] Mario Hentschel, Vivian E Ferry, and A Paul Alivisatos. Optical rotation reversal in the optical response of chiral plasmonic nanosystems: the role of plasmon hybridization. Acs Photonics, 2(9):1253–1259, 2015.

[9] RJM v Nolte, AJM Van Beijnen, andWDrenth. Chirality in polyisocyanides. Journal of the American Chemical Society, 96(18):5932–5933,1974.

[10] Julian Cheng and Robert B Meyer. Pretransitional optical rotation in the isotropic phase of cholesteric liquid crystals. Physical Review A,9(6):2744, 1974.

[11] Hendrik J Gerritsen and Richard T Yamaguchi. A microwave analog of optical rotation in cholesteric liquid crystals. American Journal of Physics, 39(8):920–923, 1971.

[12] Louis J Ippolito. Radiowave propagation in satellite communications. Springer Science & Business Media, 2012.

[13] Stephen R Martin and Maria J Schilstra. Circular dichroism and its application to the study of biomolecules. Methods in cell biology, 84:263–293, 2008.

[14] Patrik Persson and Roberto G Rojas. High-frequency approximation for mutual coupling calculations between apertures on a perfect electric conductor circular cylinder covered with a dielectric layer: Nonparaxial region. Radio Science, 38(4):18–1, 2003

[15] Ryuji Kuse, Toshikazu Hori, and Mitoshi Fujimoto. Pmc and ebg characteristics of cross type artificial magnetic conductor. In 2012 International Symposium on Antennas and Propagation (ISAP), pages 1526–1529. IEEE, 2012.

[16] Ari Sihvola and Ismo V Lindell. Perfect electromagnetic conductor medium. Annalen der Physik, 17(9-10):787–802, 2008.

[17] Shakeel Ahmed and QA Naqvi. Electromagnetic scattering from a two dimensional perfect electromagnetic conductor (pemc) strip and pemc strip grating simulated by circular cylinders. Optics Communications, 281(17):4211–4218, 2008.

[18] Qaisar Abbas Naqvi. Scattering from a perfect electromagnetic conducting (pemc) strip buried in non-integer dimensional dielectric halfspace using kobayashi potential method. Optik, 149:132–143, 2017

[19] Shakeel Ahmed and Qaisar Naqvi. Directive em radiation of a line source in the presence of a coated pemc circular cylinder. Progress In

[20] R Ruppin. Scattering of electromagnetic radiation by a perfect electromagnetic conductor sphere. Journal of Electromagnetic Waves andApplications, 20(12):1569–1576, 2006.

[21] Ahsan Illahi and Qaisar Abbas Naqvi. Scattering of an arbitrarily oriented dipole field by an infinite and a finite length pemc circular cylinder.Central European Journal of Physics, 7(4):829–853, 2009..

[22] Saeed Ahmed, Muhammad Khalid Khan, and Atta Ur Rehman. Scattering by a perfect electromagnetic conductor (pemc) plate embedded in lossy medium. International Journal of Electronics, 103(7):1228–1235, 2016.

[23] Abdul Ghaffar, SI Ahmad, R Fazal, S Shukrullah, and QA Naqvi. Scattering of electromagnetic wave by perfect electromagnetic conductor (pemc) sphere placed in chiral media. Optik, 124(21):4947–4951, 2013

[24] Electromagnetic scattering from anisotropic plasma-coated perfect electromagnetic conductor cylinders. AEU - International Journal of

[25] Amjad Imran, QA Naqvi, and K Hongo. Di raction of electromagnetic plane wave from a pemc strip. International Journal of Applied Electromagnetics and Mechanics, 34(3):181–193, 2010.

[26] Yusuf Ziya Umul. Scattering of electromagnetic waves by a perfect electromagnetic conductor half-screen. Optik, 181:383–388, 2019.

[27] Shakeel Ahmed and QA Naqvi. Electromagnetic scattering from a two dimensional perfect electromagnetic conductor (pemc) strip and pemc strip grating simulated by circular cylinders. Optics Communications, 281(17):4211–4218, 2008.

[28] FG Mitri. Electromagnetic radiation force on a perfect electromagnetic conductor (pemc) circular cylinder. Journal of Quantitative Spectroscopy and Radiative Transfer, 233:21–28, 2019.

[29] FG Mitri. Optical radiation force expression for a cylinder exhibiting rotary polarization in plane quasi-standing, standing, or progressive waves. JOSA A, 36(5):768–774, 2019.

[30] FG Mitri, RX Li, and H Sun. Optical radiation force on a perfect electromagnetic conductor (pemc) sphere. Journal of Quantitative Spectroscopy and Radiative Transfer, 256:107280, 2020..

[31] FG Mitri, Huan Tang, Renxian Li, and Shuhong Gong. Interaction of circularly polarized light with an absorptive electromagnetic conductor sphere–radiation force and spin torque. Results in Optics, 5:100128, 2021.

FORCES & TRAPPING

13th International Conference Series on
Laser-light and Interactions with Particles
Optical Particle Characterization follow-up !
August 21-26th, 2022, Warsaw, Poland

A THREE-ANGLE LIGHT SCATTERING DETECTION SCHEME FOR PROBING ORIENTATIONAL DYNAMICS OF OPTICALLY TRAPPED MICROSPHERE DIMERS

Praveen PARTHASARATHI[1], Daniel MACIVER[1], Leo LUE[1], Jan SEFCIK[1], and Mark HAW[1*]

[1] Chemical and Process Engineering, James Weir Building, 75 Montrose Street, University of Strathclyde, Glasgow, UNITED KINGDOM

Corresponding author: praveen.parthasarathi@strath.ac.uk

Abstract

Obtaining Static Light Scattering profiles from optically trapped entities poses considerable engineering challenge due to space constraints in a typical Optical Trap setup. We propose here a three-angle light scattering technique that can not only help characterize the structure but also be useful in understanding the dynamics of microscopic objects that are trapped optically. In this work, we demonstrate the use of such a measurement scheme in determining the optimal angles for light scattering measurements and probing the orientational dynamics of a microsphere dimer.

1 Introduction

Since their invention in the late 1980's by Arthur Ashkin [1], Optical Tweezers have found application in experiments ranging from single-molecule Biophysics [2] to those that test fundamental assumptions of Quantum Mechanics [3]. Perhaps the most common use of the Optical Tweezer is in force transduction and sensing [4]. While Raman Scattering is used to characterize the trapped particles [5], this technique cannot shed light on the dynamics of the trapped microparticles. In contrast, light scattering can be used to both characterize the trapped micro-structure and also obtain information on dynamics. However, adapting Light Scattering measurements in an Optical Tweezer Setup, typically involving an inverted microscope arrangement, is a significant engineering challenge as the oil-immersion objective used for trapping makes physical contact with the coverslip of the sample holder and thus rules out the possibility of introducing a second scattering wavelength from the bottom of the sample holder. A further complexity is the collection of scattered light at precise angles with a reasonably small angular range. Both these concerns were addressed by Saffran and co-workers [6] where they measured light scattering from a trapped microbead using an optical fibre placed precisely at 75-degree with respect to the direction of incidence of the scattering light which was also the trapping light. Since they collect scattered light at one angle only, they were reliant on autocorrelation estimates for characterizing the trapped bead.

We propose a three-angle light scattering detection scheme and explore its suitability to characterize trapped microstructures. We further discuss the usefulness of this scheme in inverting the light scattering problem to determine the orientation of the microsphere dimer from a light scattering measurement at only 3 angles.

We hope to extend this technique to study the orientations and dynamics of more complex shapes trapped in an optical tweezer in a subsequent full-length paper.

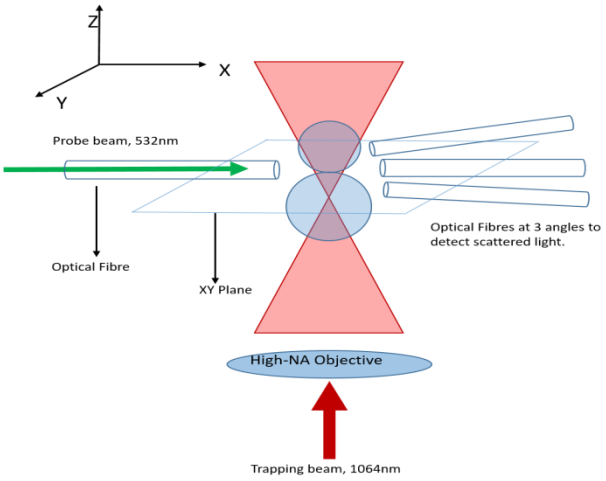

Figure 1: *Schematic of Light scattering detection from an optically trapped asymmetric microsphere doublet. The optical fibre carrying the probe beam and the 3 fibres used to detect scattered light are all in the XY plane. The reference frame is assumed to be coincident with the trap-centre and the z-axis is assumed to be along the propagation direction of the trapping beam*

2 Methodology

2.1 Optimization Protocols for solving the Inverse light scattering problem

In this section, we formulate a method to determine the optimal angles at which one may collect scattered light in order to deduce the orientation of the pair of particles. The orientation of the particles is labelled by the unit vector $\hat{n}$ which points from the centre of particle 1 to the centre of particle 2 (Fig 1) and its components along X, Y, and Z directions are indicated as nx, ny, and nz respectively. Shining a plane wave on these particles will produce a scattering pattern $I(\theta, \hat{n})$ which will depend on the orientation $\hat{n}$. The angle dependent scattering from the particles is calculated at several different orientations $\hat{n}$

using the T-Matrix based, package MSTM v3.0 [7] which is capable of computing scattered light from microsphere clusters.

The intensity of scattered light can vary by orders of magnitude at different angles. Instead of using these measurements directly, the values are scaled so that the response y_k at each angle k is normalized as

$$y_k(\hat{n}) = \frac{I(\theta_k,\hat{n}) - \langle I(\theta_k)\rangle}{\langle I^2(\theta_k)\rangle - \langle I(\theta_k)\rangle^2} \quad (34)$$

Where $\langle I(\theta_k)\rangle = \int d\hat{n} I(\theta_k,\hat{n})$ and $\langle I^2(\theta_k)\rangle = \int d\hat{n} I^2(\theta_k,\hat{n})$ The intensity of the scattered light is only collected at three angles θ_1, θ_2, and θ_3. When the particle is in orientation $\hat{n}$, we denote the measurement as the three dimensional vector $\bar{y}_q(\hat{n})$; the subscript q denotes the particular choice of angles at which the measurements were performed (i.e., the specific values θ_1, θ_2, and θ_3), and different sets of angles correspond to different values of q.

The Scattering simulations give us the expected measurement values $\bar{y}_q(\hat{n})$ when the particles are at a particular orientation $\hat{n}$. In practice, there are uncertainties associated with a measurement. We assume that these are Gaussian, with a standard deviation σ. The scattering simulations give us the conditional probabilities $p(y|\hat{n})$, which is the probability that a particle in orientation $\hat{n}$ will yield a light-scattering measurement y as:

$$p_q(y|\hat{n}) = (2\pi\sigma^2)^{-d/2} e^{-|y-\overline{y_q(\hat{n})}|^2/2\sigma^2} \quad (35)$$

(2)

We are interested in determining the orientation of the particle given a light scattering measurement. This can be formulated as the conditional probability $p_q(\hat{n}|y)$, the probability that the particles are in orientation $\hat{n}$ given the measurement y. This probability can be determined from Bayes' theorem

$$p_q(\hat{n}|y) = \frac{p_q(y|\hat{n})p(\hat{n})}{p_q(y)} \quad (3)$$

Where $p(\hat{n})$ is the prior estimate that the particles are in orientation $\hat{n}$ and $p_q(y)$ is the prior probability that a measurement y will be obtained $p_q(y) = \int d\hat{n} p(\hat{n}) p_q(y|\hat{n})$. Without any prior evidence, we assume that the orientation of the particles is distributed as $p(\hat{n})$, which can be uniformly oriented or oriented with respect to some Boltzmann distribution. Knowledge from previous measurements (e.g., immediately before the current measurement) can also be used to inform the estimate for $p(\hat{n})$.This gives us an estimate of the orientation of the particle, given a particular value of the measurement. In principle, this solves the inversion problem; however, if the probability distribution $p_q(\hat{n}|y)$ is broad or has multiple peaks, then we will have a poor estimate of the particles' orientation. A probability distribution with more than one peak points at the fact that there are multiple sets of orientations possible for a given scattering measurement. This problem can then be mitigated by changing the angles at which we perform the measurements. Such a choice of measurement angles can help optimize $p_q(\hat{n}|y)$.

From the probabilities, it may be possible to write down the information content 'H' as $H = -\int d\hat{n} p(\hat{n}) \ln p(\hat{n})$ while the information content for a prior measurement may be written as $H_q(y) = -\int d\hat{n} p_q(\hat{n}|y) \ln p_q(\hat{n}|y)$ which is $H_q = -\int dy H_q(y) p_q(y)$. The expected information gain from obtaining measurements is $H_q - H$.

$$H_q - H = \frac{1}{2} + \frac{3}{2}\ln(2\pi\sigma^2) + \int dy p_q(y) \ln p_q(y) \quad (4)$$

A maximization of the parameter above should help determine the best possible choice of 3 angles at which to measure the light scattering, given the dynamics of the dimers and also the noise expected in a typical photodetector based measurement.

2.2 Orientational Brownian Motion simulation for dimers

To test the ability of the method to invert the light scattering measurements and determine the particle orientation, we simulate the Brownian motion of a dimer of rigidly connected polystyrene spheres in water at 25°C that is optically trapped. The stochastic dynamics of the trapped dimer was simulated using the software package in [7] which outputs positions of the centre-of-mass of the dimer and it's orientation along the 3 axes of a laboratory-frame centred on the trap-centre. The diffusion coefficient for the dimer was adopted from [9].

In Fig [2], we show a typical time evolution of the orientation of microsphere dimers made of polystyrene spheres of radii 1 micron and 0.5 micron in (a), 1 micron and 0.2 micron in (b), and 1-micron each in (c). The orientations along the three axes of a reference frame centred on the trap-centre with the z-axis pointing along the propagation direction of the trapping laser are indicated as nx, ny, and nz.

The dimers are suspended in water at a temperature of 25°C and are trapped in an Optical Trap generated using an objective of numerical aperture 1.2 and with 1064nm laser light whose power was assumed to be 5mW. The scattering laser is assumed to be a plane wave, linearly polarized along x-axis, and propagating along the x-direction as shown in Figure (1).

In Figure (3) we show the time evolution of the position of the centre of mass of the three dimers.

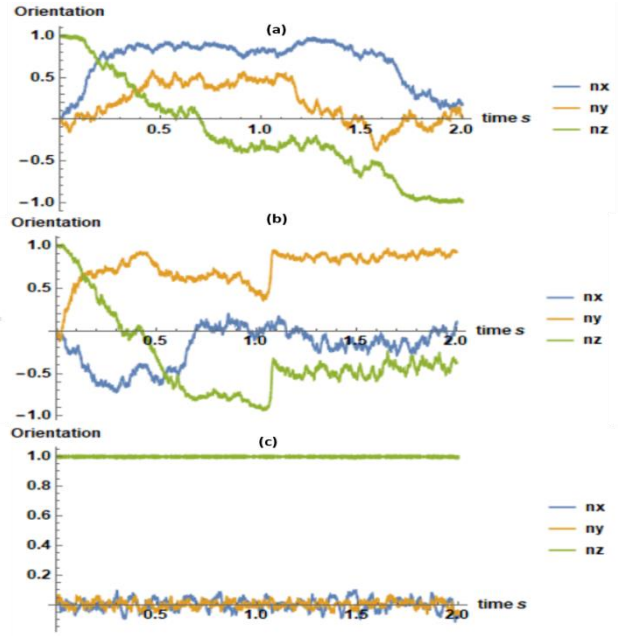

Figure 2 *Time evolution of orientation of dimers of radii (a)1:0.5-micron (b) 1:0.2-micron and (c) 1:1-micron. Dimers are suspended in water at 25˚C and are being trapped in an Optical Trap of NA 1.2.*

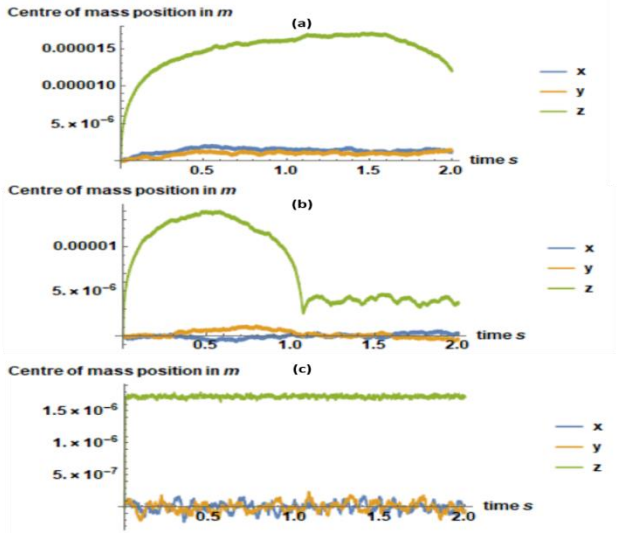

I

Figure 3 *Time evolution of the position of the centre of mass of dimers of radii (a)1:0.5-micron (b) 1:0.2-micron and (c) 1:1-micron. These positions are being reported with respect to the centre of the laser-trap*

As seen in Figures (2) and (3), the dynamics of the dimers are dependent sensitively on size and one may expect the proposed light scattering detection scheme to detect signatures of the dimers' orientation and position.

Our computer programs are presently capable of generating light scattering for each position and orientation of the dimers and we are working towards implementing the inverse light-scattering protocols. We expect to benchmark these protocols against light scattering signals obtained from dimers of known size in an actual experiment and also from MSTM based calculations so that they may be useful in characterizing trapped dimers of unknown size ratios. This, we hope will open up the possibilities of extending this technique to characterize more complex shapes.

3 Conclusions and future work

We assess the feasibility of characterizing trapped entities in an optical trap by use of a 3-angle light scattering detection technique and propose a protocol to optimize the detection angles therein. We have setup Brownian motion and light scattering computations and are presently working on the computations aimed at optimizing the choice of measurement angles given a realistic estimate for measurement noise.

We hope to write up these results in a subsequent full-length paper.

4 Acknowledgement

Praveen Parthasarathi and Dan Maciver acknowledge the Leverhulme Trust for a Postdoctoral fellowship and a PhD fellowship respectively.

5 References

[1] Ashkin A., Dzeidzic J.M., Bjorkholm J.E., and Chu S., Observation of a single beam gradient force optical trap for dielectric particles, Optics Letters 11(5): 288-290 (1986)

[2] Bustamante C.J., Chemla Y.R., Liu S., and Wang M.D., Optical tweezers in single-molecule biophysics, Nature Reviews Methods Primers 1 (25) (2021).

[3] Yin Z, Li T., Zhang X., and Duan L.M., Large quantum superpositions of a levitated nanodiamond through spin-optomechanical coupling, Physical Review A, 88, 033614 (2013)

[4] Neuman K.C., and Block S.M., Optical Trapping, Review of Scientific Instruments, 75, 2787 (2004)

[5] Ahlawat S., Chowdhury A., Uppal A., Kumar N., and Gupta P.K., Use of raman optical tweezers for cell cycle analysis, Analyst, 141, 1339 (2016)

[6] Bar-Ziv R et al., Localized dynamic light scattering: Probing single particle dynamics at the nanoscale, Physical Review Letters, 78, 154 (1997)

[7] Vigilante W., Lopez O., Fung J., Brownian dynamics simulations of sphere clusters in optical tweezers, Optics Express, 28(24):36131-36146 (2020)

[8] Mishchenko M.I., Scattering, Absorption, and Emission of light by small particles (Cambridge University Press, Cambridge, 2002)

[9] Nir A., and Acrivos A., On the creeping motion of two arbitrary-sized touching spheres in a linear shear field, Journal of Fluid Mechanics, 59(2):209-223 (1973)

13th International Conference Series on
Laser-light and Interactions with Particles
Optical Particle Characterization follow-up !
August 21-26th, 2022, Warsaw, Poland

OPTICAL TRAPPING WITH FEMTOSECOND PULSES: EXCITEMENTS, CHALLENGES AND OPPORTUNITIES

Arijit DE*

Condensed Phase Dynamics Group, Indian Institute of Science Education and Research Mohali, SAS Nagar, 140 306, India.

*Corresponding author: akde@iisermohali.ac.in

Abstract

Theories and experiments on optical trapping under femtosecond pulsed excitation demonstrated that the force/potential acting on, and hence the ensuing dynamics of, the particles is quite different from that under continuous-wave excitation, owing to optical and thermal nonlinearities. In this paper, we revisit the progress in this field, elucidating the key concepts and potential applications through exploiting optical nonlinearity.

1 Introduction

Recent theoretical and experimental works from our group [1-9] showed that the nature of optical trapping force/potential under continuous-wave (CW) excitation and femtosecond pulsed excitation (at the same time-averaged power) is distinctly different. Under pulsed excitation, optical and thermal nonlinearities can dramatically modulate the force/potential acting on the particles, and hence the course of particles' trapping dynamics. In this paper, we elucidate the concept of 'escape potential', arising from nonlinear optical force under femtosecond pulsed excitation, which was first theoretically envisaged for particles of varying sizes [1-7]; subsequently, it was validated through meticulous experiments [7-9] which also revealed the critical role played by thermal nonlinearity manifested by observation of an 'adjustment dynamics'. We further elaborate how we can harness optical nonlinearity to have far-reaching applications in facile and controlled optical manipulation.

2 Results and discussion

Refraction of light through a translucent non-absorbing particle gives rise to a three-dimensional *gradient force* that would try to restore the particle to the geometric focus whenever it moves away from the focus; on the other hand, reflection of light imparts a one-dimensional *scattering force* that tries to push the particle forward, i.e. along the beam propagation direction. Therefore, the net force acting on the particle along the direction transverse to the beam propagation is always restoring in nature; however, the net force along the beam propagation direction results from a balance between scattering force and axial component of gradient force and the overall stability of the trap relies on this delicate balance.

Now, under femtosecond pulsed excitation, optical nonlinearity sets in which renders part of the refractive index dependent on intensity of light. Due to dependence of gradient and scattering force on light intensity to different extent, the trapping force/potential on the particle is dramatically modulated which can be controlled by excitation parameters (for example, power/intensity, pulse-width, etc) as well as by material properties (nonlinear refractive index, particle-size, etc).

Let us now compare the theoretical results simulating the nature of axial force/potential under CW and femtosecond pulsed excitation. In Figure 1, the force and potential are plotted for 100 mW CW excitation. The resulting potential along axial direction is asymmetric (and has a minimum slightly ahead of geometric focus) due to addition of (conservative) gradient force and (non-conservative) scattering force.

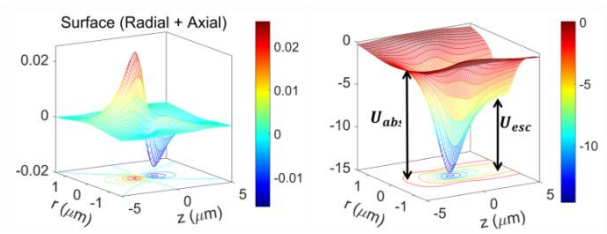

Figure 1 *Force (left panel) and potential (right panel) on an 80 nm diameter polystyrene bead under CW excitation at 100 mW time-averaged power.*

The asymmetry is more for femtosecond pulsed excitation at the same time-averaged power, which is evident from Figure 2.

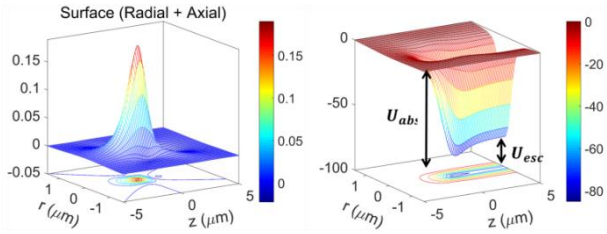

Figure 2 *Force (left panel) and potential (right panel) on an 80 nm diameter polystyrene bead under femtosecond pulsed excitation at 100 mW time-averaged power.*

While escaping the trap, the particle is most likely to overcome the lower-side of the potential barrier and be

ejected in the forward direction. Therefore, it is imperative to investigate the behaviour of this potential barrier to escape the trap, termed as escape potential (U_{esc}) [1], with laser power.

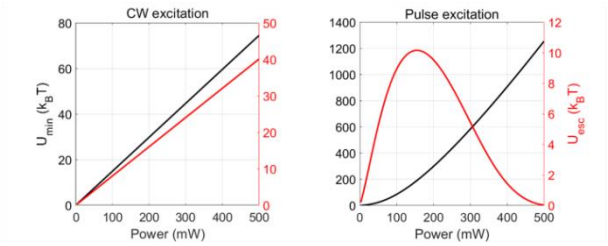

Figure 3 *Variation of absolute potential (black curves) and escape potential (red curves) with increasing time-averaged power for CW excitation (left panel) and femtosecond pulsed excitation.*

As shown in Figure 3, while the absolute well depth, termed as absolute potential (U_{abs}), monotonically increases under both excitations, under femtosecond pulsed excitation the escape potential maximizes at a particular average power before falling off to zero. Therefore, for such excitation, there exists an optimal power corresponding to most stable trap which refutes the widely accepted rule-of-thumb that a higher power would lead to more stable trapping.

Although the results shown here are based on dipole approximation calculation (in the Rayleigh scattering limit) [1, 5], the same were shown to hold using different theories [3, 6] and for different particle-size limits [2, 4, 6].

One crucial observation in the experiment on micron-sized particles [7] was that, following a steep rise (due to initial dragging of the particle toward trap centre), the backscatter signal drops from its peak value by certain amount and remain constant as long as the particle resides inside the trap; by changing the viscosity of the medium, this drop in signal was attributed to the movement of the trapped particle to a new equilibrium position contributed by the delayed action of thermal nonlinearity.

As theoretically envisaged, optical nonlinearity can be harnessed for facile optical manipulation involving reversal of force on hollow-core dielectric nanoparticles [10-11], multi-particle trapping (due to trap-splitting) [12] and force reversal (due to Fano resonance) for metallic nanoparticles [13], enhanced force on layered (core/shell type) dielectric and hybrid nanoparticles [14], and so on.

On a final note, despite these stimulating results, a rigorous theoretical description for thermal nonlinearities incorporating hydrodynamic effects (for example, laser induced convection) in the medium and thermal nonlinearity due to presence of the particle is yet to be formulated. From, experimental point-of-view, synchronization among variation detection modalities, to have simultaneous spatial and temporal resolution, is yet to be explored. These new horizons are presently being pursued in the author's lab.

3 Conclusion

To conclude, the salient features of optical trapping under femtosecond pulsed excitation are elucidated and its potential applications are summarized.

4 Acknowledgements

The authors thank IISER Mohali and SERB, DST (Grant No: ECR/2016/000467) for funding. AD and SY thank IISER Mohali and UGC for graduate fellowship.

5 References

[1] Devi A., De A. K., Theoretical investigation on nonlinear optical effects in laser trapping of dielectric nanoparticles with ultrafast pulsed excitation, Optics Express 34(9):21485-21496 (2016)

[2] Devi A., De A. K., Theoretical investigation on optical Kerr effect in femtosecond laser trapping of dielectric microspheres, Journal of Optics (IOP Publishing) 19(6):065504 (1-6) (2017)

[3] Devi A., De A. K., Theoretical estimation of nonlinear optical force on dielectric spherical particles of arbitrary size under femtosecond pulsed excitation, Physical Review A 96 (2):023856 (1-9) (2017)

[4] Devi A., De A. K., An alternate analytic formulation of optical force on a dielectric sphere in the ray optics limit, Journal of the Optical Society of America B 35(2):244-250 (2018)

[5] Devi A., De A. K., Generalized description of the nonlinear optical force in laser trapping of dielectric nanoparticles, Physical Review Research 2(4):043378 (1-5) (2020)

[6] Devi A., De A. K., A unified treatment of nonlinear optical force in laser trapping of dielectric particles of varying sizes, Physical Review Research 3(3):033074 (1-21) (2021)

[7] Devi A., Yadav S., De A. K., Dynamics of a dielectric microsphere inside a nonlinear laser trap, Applied Physics Letters 117(16):161102 (1-6) (2020)

[8] Devi A., De A. K., A table-top compact multimodal nonlinear laser tweezer, Optics Communications 482:126440 (1-12) (2021)

[9] Devi A., De A. K., Simultaneous detection of two-photon fluorescence and back-scattered signal of optical trapping of dielectric nanoparticles under femtosecond pulsed excitation, JNP Letters (Journal of Nanophotonics) 13(2):020501 (1-8) (2019)

[10] Devi A., De A. K., Harnessing optical nonlinearity to control reversal of trapping force: A theoretical investigation, Journal of Optics (IOP Publishing) 21:065502 (1-8) (2019)

[11] Devi A., De A. K., Investigating the reversal nature of optical forces in a nonlinear laser trap using a generalized Lorenz-Mie theory, Physical Review A 102:023509 (1-9) (2020)

[12] Devi A., Nair S.S., De A. K., Disappearance and reappearance of optical trap for silver nanoparticles under femtosecond pulsed excitation: A theoretical investigation, EPL (Europhysics Letters) 126:28002 (1-7) (2019)

[13] Yadav S., Devi A., De A. K., Synergistic effect of Fano-resonance and optical nonlinearity in laser trapping of silver nanoparticles, Physical Review A 102(4):043511 (1-7) (2020)

[14] Devi A., Nair S.S., Yadav S., De A. K., Controlling optical trapping of metal–dielectric hybrid nanoparticles under ultrafast pulsed excitation: a theoretical investigation, Nanoscale Advances 3(11):3288-3297 (2021)

BEAMS & SURFACES

13th International Conference Series on
Laser-light and Interactions with Particles
Optical Particle Characterization follow-up !
August 21-26th, 2022, Warsaw, Poland

BEAM SHAPE COEFFICIENTS OF ELECTROMAGNETIC ZERO-ORDER ON-AXIS CONTINUOUS FROZEN WAVES IN THE GENERALIZED LORENZ-MIE THEORY

Leonardo André AMBROSIO

[1] Department of Electrical and Computer Engineering. São Carlos School of Engineering, University of São Paulo. 400 Trabalhador são-carlense Ave. 13566-590, São Carlos, SP, Brazil.

leo@sc.usp.br

Abstract

Extending a recent theoretical work from the author, it is shown here that it is indeed possible to analytically describe the beam shape coefficients (BSCs) of an interesting and promising type of optical field known as zero-order *continuous frozen wave* (CFW), at least under an on-axis configuration. This represents a first step towards a full analytical incorporation of CFWs in the framework of the generalized Lorenz-Mie theory (GLMT). As will be seen, such a construction demands several intermediate steps which might also be useful for describing azimuthally-symmetric beams, whenever its spectrum – in terms of the longitudinal wave number – is known *a priori*.

1 Brief Introduction and Theoretical Aspects

An optical CFW is a continuous sum of propagating (non-evanescent) Bessel beams. Omitting a time-harmonic convention $\exp(+i\omega t)$, where ω is the angular frequency, and assuming +z free space propagation, its scalar version (which serves as a building block for the construction of vector beams) is written as [1-3]:

$$\psi(\rho,z)=\psi_0\int_{-k}^{k}S(k_z)J_0(k_\rho\rho)e^{-ik_z z}dk_z \qquad (1)$$

In Eq. (1), $k=2\pi/\lambda$ is the wave number, with λ being the wavelength, k_z and k_r are the longitudinal and transverse wave number, respectively and $J_0(.)$ is the zero-order Bessel function. Cylindrical coordinates (ρ,ϕ,z) are assumed attached to both a Cartesian (x,y,z) and a spherical (r,θ,ϕ) coordinate system. In the GLMT, the origin O of the (x,y,z) system coincides with the centre of a spherical scatterer [4].

A zero-order CFW is therefore a continuous superposition of Bessel beams. It is, however, a superposition of a very special kind, since its spectrum $S(k_z)$ is made attached to its pre-defined longitudinal intensity pattern $|F(z)|^2$ which, in turn, is defined within $-L/2\le z\le L/2$. Indeed, by expanding $S(k_z)$ into a truncated Fourier series, $S(k_z)=\sum_{l=-l_{\max}}^{l_{\max}}A_l\exp\left(i\pi l k_z/k\right)$, the expansion coefficients A_l are given by [1,2]:

$$A_l=\frac{1}{2k}F\left(\frac{\pi l}{k}\right) \qquad (2)$$

that is, the expansion coefficients are sampled values of the reference function $F(z)$, which is a very convenient property.

In a recent work [3], the authors have shown that a full analytical description of the BSCs of vector versions of Eq. (1), with different polarizations and for arbitrary off-axis configuration, would be possible if: (i) certain special functions, viz.,

$$\begin{aligned}b^{1,2}(k_z)&=m\frac{k_z}{k}\pi_n^m\left(\frac{k_z}{k}\right)\pm\tau_n^m\left(\frac{k_z}{k}\right)\\ b^{3,4}(k_z)&=m\pi_n^m\left(\frac{k_z}{k}\right)\pm\frac{k_z}{k}\tau_n^m\left(\frac{k_z}{k}\right)\\ b^{5}(k_z)&=\frac{k_z}{k}\tau_n^m\left(\frac{k_z}{k}\right)\end{aligned} \qquad (3)$$

can be Fourier expanded, and (ii) integrals of the form

$$\begin{aligned}I_{k_z}^{j}&=\int_{-k}^{k}dk_z\frac{S(k_z)}{k_z/k}e^{ik_z z_0}b^{j}(k_z)J_{m\mp1}\left(\rho_0\sqrt{k^2-k_z^2}\right)e^{-i(m\mp1)\phi_0}\\ I_{k_z}^{5}&=\int_{-k}^{k}dk_z\frac{S(k_z)}{k_z/k}e^{ik_z z_0}b^{5}(k_z)J_{m}\left(\rho_0\sqrt{k^2-k_z^2}\right)e^{-im\phi_0}\end{aligned} \qquad (4)$$

can be analytically evaluated. Both problems have been left open in [3].

In Eq. (3), the upper and lower signs in the l.h.s. refer to the first or the second of the upper indices in the r.h.s, respectively. Besides, $n\ge1$ and $-n\le m\le n$, with n and m integers, and $\tau_n^m(x)=-(1-x^2)^{1/2}\,dP_n^m(x)/dx$ and $\pi_n^m(x)=P_n^m(x)/(1-x^2)^{1/2}$ are generalized Legendre functions [4], with $P_n^m(x)$ being the associated Legendre polynomials according to Hobson's definition [5]. In Eq. (4), $j=1$ to 4, and one considers that the original scalar beam in Eq. (1), after being taken as one of the transverse electric field components depending on the chosen polarization, is subsequently and arbitrarily displaced by (ρ_0,ϕ_0,z_0) from the origin O.

The TM (Transverse Magnetic) and TE (Transverse Electric) BSCs, $g_{n,TM}^m$ and $g_{n,TE}^m$, are then written in terms of Eq. (4). As an example, for x-polarized CFWs, it can be shown that [3]:

$$g_{n,TM}^m=\frac{i^{m+1}}{2}(-1)^{(m-|m|)/2}\frac{(n-m)!}{(n+|m|)!}\left(I_{k_z}^1+I_{k_z}^2\right), \qquad (5)$$

$$g_{n,TE}^m=-i\frac{i^{m+1}}{2}(-1)^{(m-|m|)/2}\frac{(n-m)!}{(n+|m|)!}\left(I_{k_z}^3-I_{k_z}^4\right), \qquad (6)$$

with similar expressions for y-, circular, azimuth and radial polarizations.

If, at one hand, it might be challenging to find explicit analytical solutions to Eq. (4) for off-axis CFWs, the situation becomes tractable for $\rho_0 = 0$, that is, for on-axis beams. Under this configuration, the Bessel functions appearing in Eq. (4) are either 1 (when $m = \pm 1$, for $j = 1$ to 4, or when $m = 0$, for $I_{k_z}^5$) or 0. Under such conditions, the exponentials containing ϕ_0 disappear, and the integrals can be readily evaluated, thus allowing one to write, with the aid of Fourier expansions for $S(k_z)$ and $b^j(k_z)$, explicit analytical expressions to Eqs. (5) and (6):

$$g_{n,TM}^{m} = -\frac{i^m}{2}(-1)^{(m-|m|)/2}\frac{(n-m)!}{(n+|m|)!}\sum_{l=-l_{\max}}^{l_{\max}}\sum_{p=-\infty}^{\infty} 2kA_l \times\left(B_p^1\delta_{m,1} + B_p^2\delta_{m,-1}\right)\mathrm{Si}\left[\pi(l+p)+kz_0\right], \quad (7)$$

$$g_{n,TE}^{m} = -\frac{i^{m+1}}{2}(-1)^{(m-|m|)/2}\frac{(n-m)!}{(n+|m|)!}\sum_{l=-l_{\max}}^{l_{\max}}\sum_{p=-\infty}^{\infty} 2kA_l \times\left(B_p^3\delta_{m,1} + B_p^4\delta_{m,-1}\right)\mathrm{Si}\left[\pi(l+p)+kz_0\right]. \quad (8)$$

In Eqs. (7) and (8), Si[.] is the sine integral function and $\delta_{i,j}$ is the Kronecker delta. In addition, B_p^j (j = 1 to 4) are the Fourier coefficients of the functions defined according to Eq. (3), and they read as:

$$B_p^1 = \frac{n(n+1)}{2}\sum_{q=0}^{Q(n,0)} a_q^{n,0} \times\begin{cases} -B(\mu_1,\nu_1)\,{}_1F_2\left(\nu_1;\frac{1}{2},\mu_i+\nu_1;-\frac{\pi^2p^2}{4}\right), & n \text{ even} \\ i\pi pB(\mu_1,\nu_1+\frac{1}{2})\,{}_1F_2\left(\nu_1+\frac{1}{2};\frac{3}{2},\mu_1+\nu_1+\frac{1}{2};-\frac{\pi^2p^2}{4}\right), & n \text{ odd}\end{cases} \quad (9)$$

$$B_p^2 = \frac{1}{n(n+1)}B_p^1, \qquad B_p^3 = B_p^{31} + B_p^{32}, \qquad B_p^4 = \frac{1}{n(n+1)}B_p^3, \quad (10)$$

$$B_p^{3j} = -\frac{1}{2}\sum_{q=0}^{Q(n,j)} a_q^{n,j} \times\begin{cases} -B(\mu_{3j},\nu_{3j})\,{}_1F_2\left(\nu_{3j};\frac{1}{2},\mu_{3j}+\nu_{3j};-\frac{\pi^2p^2}{4}\right), & n \text{ odd} \\ i\pi pB(\mu_{3j},\nu_{3j}+\frac{1}{2})\,{}_1F_2\left(\nu_{3j}+\frac{1}{2};\frac{3}{2},\mu_{3j}+\nu_{3j}+\frac{1}{2};-\frac{\pi^2p^2}{4}\right), & n \text{ even}\end{cases} \quad (11)$$

$$B_p^5 = -\frac{1}{2}\sum_{q=0}^{Q(n,1)} a_q^{n,1} \times\begin{cases} -B(\mu_5,\nu_5)\,{}_1F_2\left(\nu_5;\frac{1}{2},\mu_5+\nu_5;-\frac{\pi^2p^2}{4}\right), & n \text{ even} \\ i\pi pB(\mu_5,\nu_5+\frac{1}{2})\,{}_1F_2\left(\nu_5+\frac{1}{2};\frac{3}{2},\mu_5+\nu_5+\frac{1}{2};-\frac{\pi^2p^2}{4}\right), & n \text{ odd}\end{cases} \quad (12)$$

In Eqs. (9)-(12), $Q(n,j)$ is the integer part of $(n-j)/2$, $B(\mu,\nu)$ is the Beta function and ${}_1F_2(\alpha;\beta_1,\beta_2;x)$ is the generalized hypergeometric function. In addition, $\mu_1 = \mu_{32} = q+1$, $\mu_{31} = q+2$, $\mu_5 = (2q+3)/2$, $\nu_1 = \nu_5 = (n-2q+1)/2$, $\nu_{31} = (n-q)/2$ and $\nu_{32} = (n-q+2)/2$. Finally, $a_q^{n,j}$ are coefficients which depend on the values of q, n and j, see Eq. (3) of [6].

2 Computational Examples

As an example of computation of CFWs in the GLMT, we consider a x-polarized field with a reference function $F(z) = \exp[-8(2z/L)^2]\cos(8\pi z/L)\exp(-iQz)$, where L = 44 μm. Here, $Q = 0.75k$ determines the degree of paraxiality of the beam, its transverse field concentration and the central position of $S(k_z)$. For the simulations, λ = 1064 nm, free space propagation is assumed and we have truncated the sum over p in Eqs. (7) and (8) at $p = p_{\max} = 100$. Field reconstructions in the GLMT are in accordance with Wiscombe's criterion [7], with expressions for the electromagnetic field components in terms of partial wave expansions available elsewhere, see Eqs. (3.39)-(3.50) of [4].

Figure 1(a) shows $S(k_z)$ for the chosen reference function $F(z)$, while Figure 1(b) illustrates $|\psi(0,z)|^2$ and $|F(z)^2|$. In Eqs. (7) and (8), $l_{\max}$ = ceil[L/λ], with ceil[.] denoting the ceiling function, see [1] for details. It is seen that, for the chosen parameters, Eq. (1) adequately reproduce the intended $F(z)$. Density plots of the expected

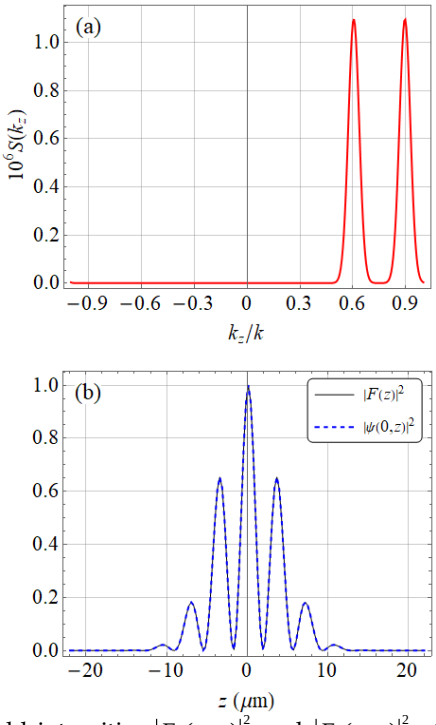

electric field intensities $|E_x(\rho,z)|^2$ and $|E_z(\rho,z)|^2$ at the xz plane are shown in Figure 2.

Figure 1 *(a) $S(k_z)$ as a function of k_z for the given reference function $F(z)$. (b) $|\psi(0,z)|^2$ and $|F(z)^2|$, the former being calculated from Eq. (1)*

The electric field components reconstructed from the GLMT expressions, along $\rho = 0$, can be appreciated in Figure 3(a). The curve for $|\psi(0,z)|^2$ is again shown for reference purposes. As observed from Figure 3(b) from the logarithmic error $\ln\left[\left(|\psi(0,z)|^2 - |E_x(0,z)|^2\right)/|\psi(0,z)|^2\right]$, an excellent field reconstruction is achieved, at least along $\rho = 0$, which is the region of most interest for practical applications. It can be shown, by plotting $|\psi(\rho, z = z')|^2$ for

distinct z', that an excellent agreement is also observed in the transverse direction.

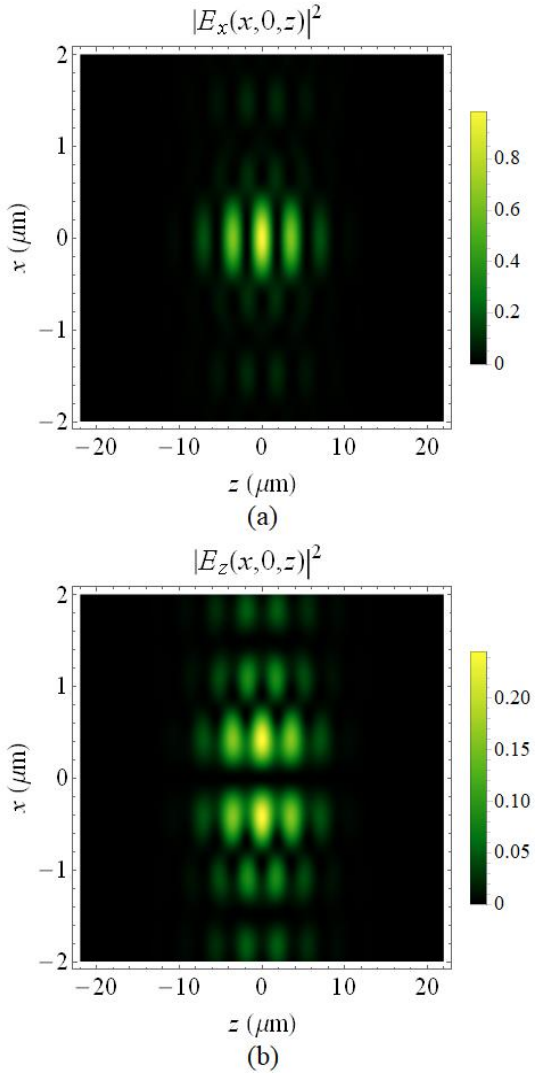

Figure 2 *Density plot of (a) and (b) at the xz plane, corresponding to the reference function of Figure 1(b)*

3 Conclusions

An analytical method for the evaluation of the beam shape coefficients of zero-order continuous frozen waves has been presented under an on-axis configuration. This is a first step towards a full incorporation of such beams in the generalized Lorenz-Mie theory envisioning light scattering applications. Interestingly enough, the method here presented is also suitable for describing on-axis azimuthally-symmetric arbitrary-shaped beams. In this case, however, there is no direct relation between the Fourier coefficients of their spectra and a pre-chosen reference function as expressed here in Eq. (2). This means that their spectra must be known a priori for each particular shaped beam, which might not always be in terms of as shown by the coefficients in Eq. (2). Continuous frozen waves, being a class of micrometer-structured non-diffracting beams, can be of interest in applications ranging from optical tweezers and bistouries, 2D and 3D imaging and printing, holography and so on, and an extension of the present work for arbitrary-order beams under off-axis configuration is certainly deserved. This is current in progress

4 Acknowledgement

The author thanks M. Zamboni-Rached and G. Gouesbet for kind discussions. He also thanks the National Council for Scientific and Technological Development (CNPq) (426990/2018-8, 309201/2021-7) for supporting this work.

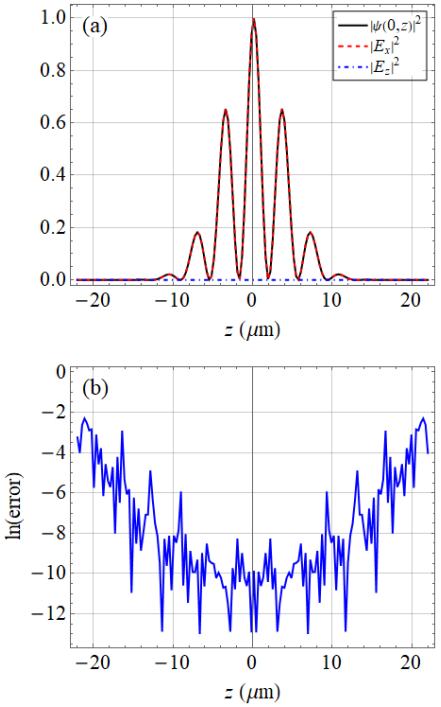

Figure 3 *(a) Electric field components along the z axis, reconstructed using the GLMT [4]. (b) Corresponding logarithmic error* $\ln\left[\left|\left(|\psi(0,z)|^2-|E_x(0,z)|^2\right)\Big/|\psi(0,z)|^2\right|\right]$

5 References

[1] Zamboni-Rached M., Recami E., Subluminal wave bullets: Exact localized subluminal solutions to the wave equations, Phys. Rev. A 77:033824 (2008)

[2] Zamboni-Rached M., Ambrosio L.A., Dorrah A.H., Mojahedi M., Structuring light under different polarization states within micrometer domains: exact analysis from the Maxwell equations, Opt. Express 25(9):10051-10056 (2017)

[3] Ambrosio L.A., Zamboni-Rached M., Gouesbet G., Zeroth-order continuous vector frozen waves for light scattering: exact multipole expansion in the generalized Lorenz-Mie theory, J. Opt. Soc. Am. B 36(1):81-89 (2019)

[4] G. Gouesbet, and G. Gréhan, Generalized Lorenz-Mie Theories (Springer, 2nd. Ed., 2017).

[5] L. Robin, Fonctions sphériques de Legendre et fonctions sphéroidales (Gauthier-Villars, Paris, Volumes 1, 2, 3, 1957).

[6] Wong B.R., On the overlap integral of associated Legendre polynomials, J. Phys. A: Math. Gen. 31:1101-1103 (1998)

[7] Wiscombe W.J., Improved Mie scattering algorithms, Appl. Opt. 19(9):1505-1509 (1980)

13th International Conference Series on
Laser-light and Interactions with Particles
Optical Particle Characterization follow-up !
August 21-26th, 2022, Warsaw, Poland

ELLIPSOMETRIC CONTROL OF PLASMONIC EVOLUTION AFTER HIGH-TEMPERATURE ANNEALING OF THIN GOLD FILM

Tetiana MISHAKOVA[1*], Eugene BORTCHAGOVSKY[2] and Victor STEPKIN[3]

[1] Institute of High Technologies of Taras Shevchenko Kyiv National University, ave.Glushkov 4g, Kyiv 03022, Ukraine

[2] V. Lashkarev Institute of Semiconductor Physics of NAS of Ukraine, pr.Nauki 41, Kyiv 03028, Ukraine

[3] Institute of Physics of NAS of Ukraine, pr.Nauki 46, Kyiv 03028, Ukraine

Corresponding author: sku4auptica@gmail.com

Abstract

Annealing of thin metallic films is well-known to influence parameters of resulting nanoparticles. Metal of the film coalescences into nanoparticles, which size and shape strongly depend on the temperature and time of the annealing as well as materials of the film and substrate, which in turn define the diffusion length, so the number and size of seeds on which nanoparticles grow. High temperature can results in recrystallization of nanoparticles creating faceted monocrystals.

In such a way annealing manages plasmonic properties of the resulting layer of nanoparticles via their size [1] and concentration on the surface [2].

Ellipsometry has demonstrated its ability to record plasmonic properties of system of interests [3] providing both amplitude and phase information. So, the aim of this work is to control by ellipsometry plasmonic properties of layers of nanoparticles created by high-temperature annealing of thin gold films.

1 Experimental

Gold films were thermally evaporated in vacuum of $5x10^{-6}$ torr on glass with gradient thickness due to the corresponding deposition of substrates in vacuum chamber according to the vapour source. Resulting thicknesses were in the range 7-3nm.

Annealing was made by the next protocol: samples were put for 5 minutes into the chamber heated to 190^{0}C and pumped out to 50 torr. After that the chamber was heated with the speed 80^0/min for 7 minutes till 750^{0}C. One portion of samples was kept at that temperature for 1 minutes and the chamber was opened to the air after that. The second similar samples were exposed to the air immediately after reaching of 750^{0}C temperature.

Ellipsometry used for the control of annealed samples measures two so-called ellipsometric angles Ψ and Δ bearing amplitude and phase information [4]. As by definition $tg\Psi=|r_p|/|r_s|$ where r_i are Fresnel reflection coefficients, behaviour of the angle Ψ reflects the excitation of localized plasmons by extremums due to the energy transfer to modes of the system of interest.

2 Results and Discussion

Results for the sample with the thickest film kept for one minute at 750^{0}C are shown in Figure 1. Mass thickness of the film in the shown areas is about 7, 6.7 and 6.2 nm correspondingly. Spectra of Ψ measured at angles of incidences 60^0, 70^0 and 75^0 are shown under the pictures. The arrow indicate evolution of spectra at the change of the initial thickness from 7 to 6.2 nm.

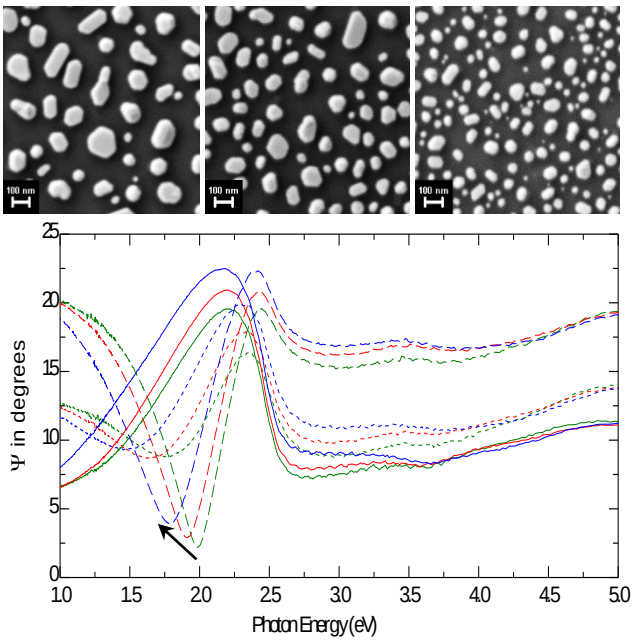

Figure 1 *Pictures of areas with the thickest film and corresponding spectra of Ψ angle.*

It is seen that keeping of annealed film at high temperature results in faceting of nanoparticles, e.i. recrystallisation happens. For thickest film resulted nanoparticles have the size of about 100nm, as for the thinnest area of this sample it is practically twice smaller with noticeably bigger concentration what decreases the separation of particles and correspondingly enhances their interactions. As the result it overcompensates the blue shift of the resonance for smaller particles and the final shift of localised plasmon is red.

Such a behaviour can be proven by simple consideration of the material balance. Total volume of the initial film coincides with the sum volume of resulted nanoparticles. So it can be shown that for the same amount of material the average interparticle distance $a \sim R^{3/2}$ where R is the average size of particles. At the same time there is scaling in nanoplasmonics. Particles polarizability is proportional to R^3 as the near-field of a plasmon is proportional to R^{-3}. It means that if everything is measured in the size of particles, no interaction changes at the system scaling. As in our case at decreasing of the size in two times the interparticle distance decreased in almost three times we have final red shift of the resonance.

Similar results are for the sample without keeping at high temperature, however the size of nanoparticles is about twice smaller and there is no faceting as there was no time for atomic diffusion at high temperature.

The opposite situation is for the sample with the thinnest film. Results for two areas with the mass thickness of about 4.3 and 4 nm are shown in Figure 2.

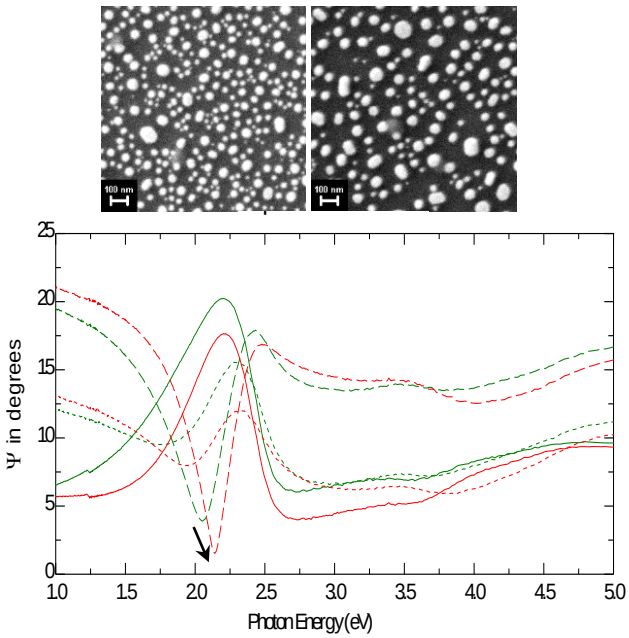

Figure 2 *Pictures of areas with the thinnest film and corresponding spectra of Ψ angle.*

In this case noticeable increasing of the interparticle distances decreases their interactions and we have relative blue shift.

It is worth to note that samples with the mass thickness in the range 5.7-5.3nm give after annealing localized plasmons independent on the initial thickness. The position of those resonances depend on the used annealing protocol. Annealing without keeping the sample at 750^0C produces particles of 30-50nm in size with the localized resonance about 2.4eV. Keeping the sample at 750^0C increases the size of nanoparticles to 100-150nm with much bigger spreading. So the resonance is much wider with the energy about 2.1eV as it should be for bigger particles.

3 Conclusions

Ellipsometry demonstrates that plasmonic properties of annealed films strongly depend on the initial mass thickness of the film. It is interesting to note that general dependence of the resonance with the change of the initial thickness does not depend on the annealing protocol.

4 References

[1] C.F. Bohren, and D.R. Huffman, Absorption and scattering of light by small particles (Wiley, New-York, 1983).

[2] Persson B.N.J., Lateral interactions in small particle system, J. de Physique Colloque 44(C10):C10-409-419 (1983).

[3] Bortchagovsky E.G., Mishakova T.O. and Hingerl K., Ellipsometry of layers of nanoparticles with the account of depolarization, Thin Solid Films 571:625-630 (2014).

[4] R.M.A. Azzam and N.M. Bashara, Ellipsometry and polarized light (North-Holland, Amsterdam, 1977).

13th International Conference Series on
Laser-light and Interactions with Particles
Optical Particle Characterization follow-up !
August 21-26th, 2022, Warsaw, Poland

CLASSICAL AND STIMULATED DOPPLER EFFECTS AND THE RECOIL EFFECT ON A MOVING MEDIA INTERFACE

Valentyn LYMAR[1,*], Yevhen MAKOVETSKYI[1], Roman OVSIANNIKOV[2] and Tetyana SARII[3]

[1] Physical Optics Department, School of Physics, Karazin Kharkiv National University, Kharkiv, 61022, Ukraine
[2] School of Physics and Technology, Karazin Kharkiv National University, Kharkiv, 61022, Ukraine
[3] Kharkiv Lyceum No 89, Kharkiv, 61103, Ukraine

Corresponding author: valentinelymar@gmail.com

Abstract

Light refraction on moving surface of an increasing gas bubble is examined in the case of laser-trapping in an absorbing liquid solution. The treatment involves Doppler effect on moving walls of the bubble. At different stages of the bubble growth both classical (CDE) and stimulated Doppler effects (SDE) take place. It may be treated the former, CDE, as a recoilless limit of the energy-momentum conservation laws while the latter, SDE, is considered to be manifestation of the disbalance in the quantities of up and down stimulated transitions in some resonance two-level surface quantum system. Such disbalance is caused by the spontaneous transitions in this system. The recoil effect on a moving media surface is possible also as a result of a mass transfer process through the interface; its probability is bound to increase with the velocity of the surface movement.

1 Introduction

1.1 Light Pressure and Recoil Effect

Light or radiation pressure phenomenon is caused by the feature of momentum of running electromagnetic wave (in electrodynamics) or photon (in quantum mechanics). It is studied theoretically and experimentally over a century, but some questions are to be answered yet, the choice between Minkowski and Abraham definitions for photon momentum in a medium being among them [1]. In the case of normal incidence from vacuum on an immobile surface of an absorbing medium, the pressure of the light flux creates momentum $\hbar\cdot\omega_0\cdot(1+R)/c$ on average per photon, and the momentum direction coincides with the light beam wave vector, here $\hbar\cdot\omega_0$ being the energy of the incident photon. The same applies to a specularly reflecting interface at reflection coefficient $R=1$ and modification Δp_r of photon momentum is derived in the process:

$$\Delta p_r = \frac{2\cdot\hbar\cdot\omega_0}{c}\,. \qquad (1)$$

But single-photon momentum modification Δp_t and its sign is not determined uniquely for a photon transmitted through the free-space surface of transparent dielectric [2]. Let a plane monochromatic wave falls on a coated immobile smooth interface of the transparent semi-infinite medium. As far as law of refraction takes place, a tangential component of the light particle momentum is preserved in its passage through the interface while the normal component is increased (under natural assumption of medium refractive index being $n>1$). Then, according to the momentum conservation law, surface and medium together have to be forced outwards. It is a recoil effect of a sort because of its opposite trend to the case of radiation pressure on a specular or absorbing surface. Evidently, most of manifestations of so-called "negative optical forces" [3, 4] are connected with this recoil effect. However, in the limit of a large medium mass $M\to\infty$ the refraction process gets recoilless. It is obvious, our treatment is consistent only with Minkowski definition of photon momentum, i. e. $p_t = n\cdot\hbar\cdot\omega_0/c$. Therefore it results in transmitted photon momentum modification Δp_t at normal incidence on the free-space surface of the transparent dielectric:

$$\Delta p_t = \frac{\hbar\cdot\omega_0}{c}\cdot(n-1)\,. \qquad (2)$$

Let us note that changing $n\to -1$ [5] in Eq. (2) gives the value of Δp_r from Eq. (1) and minus sign corresponds to different directions of $\Delta\mathbf{p}_r$ and $\Delta\mathbf{p}_t$.

Formally, the ratio of Eqs. (1) and (2) is

$$\frac{\Delta p_r}{\Delta p_t} = \frac{2}{n-1}\,, \qquad (3)$$

and it is the value that is important for our following presentation.

1.2 Classical Doppler Effect on a Moving Interface: Wave Approach

Let us briefly consider the question concerning the Doppler effect in refraction-reflection processes on a moving surface of a transparent medium. At normal incidence of electromagnetic wave, electric and magnetic field components of a composite incident-reflected-refracted field have to be continuous on the moving interface [6]. If v is a velocity of the interface movement in the normal direction ($\mathrm{v}<<c$), then the Doppler frequency shifts (DFSh) $\delta\omega_r$ or $\delta\omega_t$ take place for the reflected or transmitted-refracted wave accordingly. In doing so:

$$\delta\omega_t = \omega_t - \omega_0 = \pm\frac{\mathrm{v}}{c}\cdot(n-1)\cdot\omega_0 \qquad (4)$$

where plus corresponds to the increase of the frequency when the interface moves in the same direction as light does while movement in the opposite direction results in reduction of the frequency of the transmitted wave.

As earlier, changing $n \to -1$ in Eq. (4) results in the DFSh value $\delta\omega_r = \omega_r - \omega_0$ of the reflected wave. It is easy to define the ratio of DFSh values $\delta\omega_r$ and $\delta\omega_t$:

$$\left|\frac{\delta\omega_r}{\delta\omega_t}\right| = \frac{2}{n-1}, \qquad (5)$$

the latter coinciding with the value from Eq. (3).

To conclude the introduction, let us note that the experimental measurement of the DFSh ratio gives not only the refractive index n of the moving dielectric medium but also the recoilless ratio of the photon impacts (in the limit of the medium mass $M \to \infty$) during its reflection-refraction processes on the free-space interface of the transparent dielectric. Deviations of the DFSh ratio from the proper value from Eq. (5) may indicate the deviation of nature of the reflection-refraction processes from the classical one.

2 Classical and Stimulated Doppler Effects and the Recoil effect on a Moving Interface: Quantum Approach

It is possible to consider the Doppler effect on a moving interface from the quantum point of view. The photon-based refraction process is illustrated schematically in Figure 1.

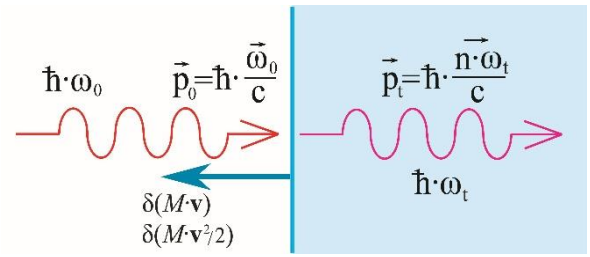

Figure 1 *The principal scheme of the photon refraction on a moving interface. Momentum-energy conservation laws must be fulfilled. A collinear geometry is not obligatory.*

If $\mathbf{v}$ is a velocity vector of the moving medium of the mass M then $\delta(M \cdot \mathbf{v})$ and $\delta(M \cdot \mathbf{v}^2/2)$ are correspondingly the recoil impact and energy originated at the photon transition through the interface. The following momentum-energy conservation laws must be fulfilled:

$$\mathbf{p}_0 = \mathbf{p}_t + \delta(M \cdot \mathbf{v}); \qquad (6)$$

$$\hbar \cdot \omega_0 = \hbar \cdot \omega_t + \delta(M \cdot \mathbf{v}^2/2) \qquad (7)$$

where $\mathbf{p}_0$ and $\mathbf{p}_t$ are momentums of the incident and refracted photon, $\hbar \cdot \omega_0$ and $\hbar \cdot \omega_t$ are corresponding energies. It is naturally to assume:

$$\delta(M \cdot \mathbf{v}) = M \cdot \delta\mathbf{v} + \mathbf{v} \cdot \delta M; \qquad (8)$$

$$\delta(M \cdot \mathbf{v}^2/2) = M \cdot \mathbf{v} \cdot \delta\mathbf{v} + \frac{\mathbf{v}^2}{2} \cdot \delta M. \qquad (9)$$

As photons are indivisible light particles, the plus signs perform rather disjunctive function in Eqs. (8) and (9). At $M = \text{const}$ only first summands are kept there and it results from Eqs. (6) and (7) that

$$\delta\omega_t = \omega_t - \omega_0 = \mathbf{v} \cdot \delta\mathbf{k}_t \qquad (10)$$

where $\delta\mathbf{k}_t = \mathbf{k}_t - \mathbf{k}_0$ is the wave vector alteration at the photon transition through the interface. In the recoilless limit $M \to \infty$ Eq. (8) provides $\delta\mathbf{v} \to 0$ and Eq. (10) describes CDE at refraction on a moving transparent interface. In the case of normal incidence it is easy to derive Eq. (4) from Eq. (10).

In experiments on laser thermocapillary gas bubble trapping some resonant absorption is inherent in the liquid medium [7]. Then the principal scheme in Figure 1 should be modified to the scheme in Figure 2. Separating two

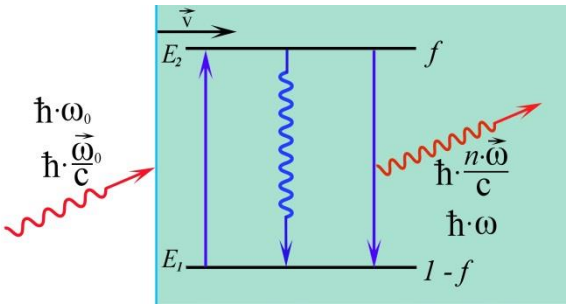

Figure 2 *The principal scheme of the photon refraction on a moving interface with resonant absorption. Straight blue arrows correspond to stimulated transitions, while waving blue – to spontaneous one: **f** and **1-f** are the level populations (in fractions of a unit) of upper and lower levels*

infinite media moving interface is treated as a quantum two-level surface system. Spontaneous and stimulated radiative processes are possible here. If $\delta\mathbf{k}_t^{st} = \hbar^{-1} \cdot \delta\mathbf{p}_t^{st}$ is the wave vector alteration at the stimulated photon transition through the interface then, as it easy to show by analogy with [8], the DFSh takes the "stimulated" value

$$\delta\omega_t^{st} = \hbar^{-1} \cdot \mathbf{v} \cdot \delta\mathbf{p}_t^{st} \cdot (1-f) = \mathbf{v} \cdot \delta\mathbf{k}_t^{st} \cdot (1-f) \qquad (11)$$

where $1-f$ has assumed the sense of the fraction of time the system spends in the lower state [8]. It is the name "stimulated Doppler effect" (SDE) that is proposed to describe the DFSh at the presence of stimulated emission and in accordance with Eq. (11).

Let us return to Eqs. (6)-(9). At $\mathbf{v} = \text{const}$ only second summands are kept in Eqs. (8) and (9). Having substituted them into Eqs. (7) and (6) we get

$$-\frac{\mathbf{v}^2}{2} \cdot \delta M = \hbar \cdot \delta\omega_t; \qquad (12)$$

$$\delta\omega_t = \omega_t - \omega_0 = \frac{1}{2} \cdot \mathbf{v} \cdot \delta\mathbf{k}_t. \qquad (13)$$

In the process a "mass defect" δM becomes a host of the recoil impact and energy per photon. That is why the term "recoil effect" (RE) will be used to present the process outlined by Eqs. (12)-(13).

Quantitatively, the distinctions between the Doppler and the recoil effects, CDE, SDE and RE, are characterised completely by Eq. (10), Eq. (11) and Eqs. (12), (13). But in a qualitative sense an analogy with certain classical mechanical model seems to be appropriate. Let some traveller to be jumping from a railroad bridge down onto a moving railway platform of a large mass M. If friction on the platform is large enough then the traveller successfully becomes a stowaway. Such transformation is realized at the expense of the recoilless transmission of momentum $M \cdot \delta \mathbf{v}$ from the platform to the passenger ($\delta \mathbf{v} \to 0$ is an infinitesimal reduction of the platform velocity, but $\mathbf{v} \neq \text{const}$). To some extent, the described model is analogous to CDE at photon refraction process on a moving interface. But if there is no friction on the platform then the only way for the traveller to become a passenger is dumping some cargo mass δM from the platform, "Bolivar cannot carry double". In this case the velocity $\mathbf{v}$ of the platform remains the same due to lack of interaction force between the platform and the passenger. Evidently, such process is analogous to RE.

Generally, all of Eqs. (6-10, 12-13) could be repeated concerning the photon reflection on a moving interface. In doing so the only required modification is the replacement of the lower index *"t"* (transmitted-refracted) by the lower index *"r"* (reflected) in Eqs. (6-7, 10, 12-13). The question remains opened concerning a possibility of SDE (Eq. (11)) in reflection.

3 Experimental Observations of Doppler Effects on Moving Surface of a Gas Bubble Thermocapillary Trapped by a Laser Beam

Our foregoing discussion results from the experiments on laser thermocapillary trapping of a gas bubble in an absorbing liquid [9]. The He-Ne laser of power about 10 mW was used to trap a gas bubble in an ethanol solution coloured by brilliant green dye. The simple principal experimental scheme of the trap was presented in [7, 9]. It is possible to manage the size of the trapped gas bubble until it is too large. Movement of reflected and transmitted interference patterns observed may be treated as a manifestation of the Doppler effect because of the moving bubble walls.

The DFSh may be determined at any observation angle including both near-zero one and specular one by measuring the time dependences of intensities both in transmitted and reflected light. Therefore DFSh ratio defined by Eq. (5) is measurable. The examples of ordinary intensity dependencies are presented in Figure 3 at initial, intermediate and final stages of the bubble growth.

Evidently, at the initial stage (Figure 2 (a)) the proper DFSh ratio value of approximately 6 is observed. The table value of the refractive index of ethanol is $n = 1.360$. CDE takes place at this stage and refraction process is recoilless.

At the final stage of the bubble growth (Figure 2 (c)) the

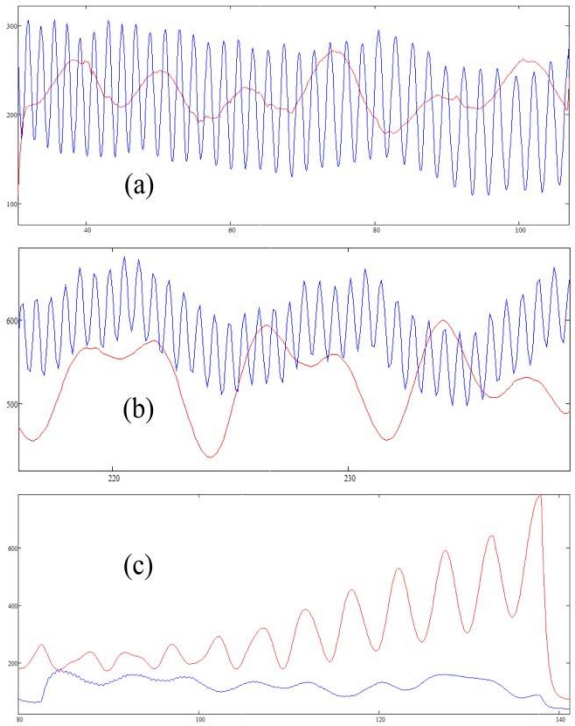

Figure 3 *The typical time dependences of the intensities (in arbitrary units) of the light transmitted through an increasing laser trapped gas bubble at near-zero observation angle (red curve) and of the light specularly reflected from it (blue curve): (a) at the initial trapping stage (initial bubble diameter $D \approx 15 \div 20\ \mu m$); (b) at the intermediate stage ($D \approx 50 \div 150\ \mu m$); (c) at the final stage (bubble escapes the trap at $D \geq 200\ \mu m$). Time axis numbers are in seconds.*

value of DFSh ratio is approximately two times more than the proper value from Eq. (5) [7, 9, 10], although the ripples of the reflected signal are not distinguishable enough in the Figure 2(c). Probably, it indicates a deviation from the classical recoilless limit, and SDE (at the state of saturated absorption $f \to 1/2$, see Eq. (11)) occurs in the photon refraction process on the moving bubble walls. There is a distinctive amplification of the scope of the transmitted signal oscillations at this stage, and this indicates contribution of stimulated radiation to the signal. The input of RE (see Eq. (13)) is possible also at this stage, but more likely its probability is essentially lower than the same of SDE.

The intermediate stage of the bubble growth is characterized by the specific form of a "cowboy hats" in the time dependence of the transmitted signal. The intermediate character of the stage provides non-zero probabilities for both CDE and SDE in photon refraction. Progressing from the initial stage to the final one increases SDE probability while diminishing probability of CDE.

4 References

[5] Kemp B.A., Resolution of the Abraham-Minkowski debate: Implications for the electromagnetic wave theory of light in matter, J. Appl. Phys. **109**, 111101 (2011).

[6] Loudon R., Theory of the radiation pressure on dielectric surfaces, Journal of Modern Optics 49(5-6): 821-838 (2002).

[7] Kajorndejnukul V., Ding W., Suhov S., Qiu C.-W., Dogariu A., Linear momentum increase and negative optical forces at dielectric interface, Nature Photon. 7: 787-790 (October 2013).

[8] Dogariu A., Suhov S., Saenz J.J., Optically induced "negative forces", Nature Photon. 7: 24-27 (January 2013).

[9] R.P.Feynman, R.B. Leighton, and M. Sands, *The Feynman lectures on physics* (Addisson-Wesley Pub. Co., Reading-London, 1963).

[10] I. Ye. Tamm, *Foundations of electricity theory* (Nauka, Moscow, 1989) (in Russian).

[11] Lymar V.I., Kazachkova N.A., Kofman O.I., and Slabunova N.V., Stimulated Doppler effect on the surface of a gas bubble thermocapillary trapped by a laser in an absorbing liquid, *2016 IEEE 7th Int. Conf. on Advanced Optoelectronics and Lasers (CAOL)*, paper caol2016_110, 12-15 September, Odessa, Ukraine, 2016.

[12] Ashkin A., Atomic-Beam Deflection by Resonance-Radiation Pressure, Phys. Rev. Lett. 25 (19):1321-24 (1970).

[13] Lymar V.I., Kazachkova N.A., Kofman O.I., Slabunova N.V., and Luzan N.A., Stimulated Doppler effect on the surface of a gas bubble thermocapillary trapped by a laser in an absorbing liquid, Visnyk KhNU, Ser. "Physics"25: 26-29 (2016).

[14] Butenko A.D., Kazachkova N.A., Kofman O.I., and Lymar V.I., "Optical gas bubble management" at its laser thermo-capillary trapping in an absorbing liquid, *10th Int. Conf. on Laser-light and Interactions with Particles (LIP2014)*, paper ME-21, 25-29 August, Marseille, France, 2014.

13th International Conference Series on
Laser-light and Interactions with Particles
Optical Particle Characterization follow-up !
August 21-26th, 2022, Warsaw, Poland

INVERSE DESIGN OF METASURFACE BASED ON NEURAL NETWORK

Liu YANG [1,*], Renxian LI [1-2] and Huan TANG [1]

[1] School of Physics and Optoelectronic Engineering, Xidian University, Xi'an 710071, China
[2] Collaborative Innovation Center of Information Sensing and Understanding, Xidian University, Xi'an 710071, China

Corresponding author: lyang_6@stu.xidian.edu.cn

Abstract

As a kind of artificial electromagnetic interface, optical metasurface performs well in the manipulation and control of the beam. The inverse design of the characteristic parameters based on the objective can be applied to the design of the metasurface structure through the combination of artificial intelligence algorithm and numerical simulation. It presets the structure shape of the metasurface according to the optimization target, determines the parameter to be optimized and its value range, and then selects the appropriate optimization algorithm for optimization, including genetic algorithm, gradient descent algorithm, and density penalty algorithm, etc. According to the objective of optimization, the objective function is written, and the required parameters are optimized.

1 Introduction

As a kind of artificial material, metasurface has attracted much attention due to its flexible optical operation over subwavelength propagation distance [1-3]. It consists of a series of planar artificial units arranged and combined in a specific order. Based on Huygens principle, the artificial units in different areas of the plane are precisely designed to obtain the metasurface with various electromagnetic wave reflection or transmission phase distribution, which can realize the high efficient control of electromagnetic wave[4,5].

The traditional design is to accurately predict the spectral properties and functions of the metasurface by applying iterative calculation scheme combined with FEM [6,7] or FDTD[8,9], and then prepare the metasurface nanostructures according to the model. A set of discrete elements is obtained by calculating the phase amplitude variation of the radiation field in the whole parameter space. For FDTD, the process of TDTD is as follows: the differential expression in Maxwell's domain field curl equation is replaced by the finite difference expression, so as to obtain the finite difference expression of the field components. For the object under study, we can use the same grid of electrical parameters for simulation, select a reasonable initial value of the field and the boundary conditions of the calculation space for calculating, obtain the numerical solution of Maxwell's equations with time factor, and obtain the frequency domain solution in the three-dimensional space through Fourier transform. The motion law and process of electromagnetic wave in electromagnetic field are simulated by computer [10]. However, the calculation and design process of traditional design methods are complicated and time-consuming. Moreover, the shape of the designed metasurface is relatively regular, and the ability to control the beam is also limited.

The main work is to realize the inverse design of the metasurface by training a deep neural network and realize beamforming. Unlike most works, which relying on the training set of known devices, the core idea of this paper is directly learning the physical relationship between device geometry and response through electromagnetic simulations. Then, the trained network will promptly calculate the requirements of the target and output a metasurface structure that matches the expected target.

2 Method

In the one-dimensional case, the EM wave propagates along the z-axis, and the medium parameters and field quantities are independent of x, y, $\partial/\partial x = 0$, $\partial/\partial y = 0$, so Maxwell's equation[11] is

$$-\frac{\partial H_y}{\partial z} = \varepsilon \frac{\partial E_x}{\partial t} + \sigma E_x \tag{36}$$

$$\frac{\partial E_x}{\partial z} = -\mu \frac{\partial H_y}{\partial t} - \sigma_m H_y \tag{37}$$

Sampling of E and H component space nodes in one-dimensional case is shown in the figure.

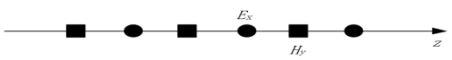

***Figure 1** Sampling of E and H component space nodes in one-dimensional case.*

The FDTD dispersion of equation (1-2) are

$$\begin{aligned} E_x^{n+1}(k) &= CA(m)\,E_x^n(k) \\ &\quad -CB(m)\left[\frac{H_y^{n+\frac{1}{2}}\left(k+\frac{1}{2}\right)-H_y^{n+\frac{1}{2}}\left(k-\frac{1}{2}\right)}{\Delta z}\right] \end{aligned} \tag{38}$$

$$\begin{aligned} H_y^{n+\frac{1}{2}}\left(k+\frac{1}{2}\right) &= CP(m)\,H_y^{n-\frac{1}{2}}\left(k+\frac{1}{2}\right) \\ &\quad -CQ(m)\left[\frac{E_x^n(k+1)-E_x^n(k)}{\Delta z}\right] \end{aligned} \tag{4}$$

Among them, CA, CB, CP, CQ are respectively

$$E_{mn} = i^n E_0 \sqrt{\frac{2n+1}{n(n+1)}\frac{(n-m)!}{(n+m)!}} \tag{39}$$

$$\begin{aligned}
CA(m) &= \frac{\frac{\varepsilon(m)}{\Delta t} - \frac{\sigma(m)}{2}}{\frac{\varepsilon(m)}{\Delta t} + \frac{\sigma(m)}{2}} = \frac{1 - \frac{\sigma(m)\Delta t}{2\varepsilon(m)}}{1 + \frac{\sigma(m)\Delta t}{2\varepsilon(m)}} \\
CB(m) &= \frac{1}{\frac{\varepsilon(m)}{\Delta t} + \frac{\sigma(m)}{2}} = \frac{\frac{\Delta t}{\varepsilon(m)}}{1 + \frac{\sigma(m)\Delta t}{2\varepsilon(m)}} \\
CP(m) &= \frac{\frac{\mu(m)}{\Delta t} - \frac{\sigma_m(m)}{2}}{\frac{\mu(m)}{\Delta t} + \frac{\sigma_m(m)}{2}} = \frac{1 - \frac{\sigma_m(m)\Delta t}{2\mu(m)}}{1 + \frac{\sigma_m(m)\Delta t}{2\mu(m)}} \\
CQ(m) &= \frac{1}{\frac{\mu(m)}{\Delta t} + \frac{\sigma_m(m)}{2}} = \frac{\frac{\Delta t}{\mu(m)}}{1 + \frac{\sigma_m(m)\Delta t}{2\mu(m)}}
\end{aligned} \tag{5}$$

where m represents a set of integers or half-integers at the observation point (x, y, z).

For functions defined in the discrete domain, convolution is defined as

$$(f * g)[m] = \sum_n f[n]g[m-n] \tag{40}$$

In a convolutional neural network[12-15], if the input size is set as (N, C_{in}, H, W), the output size is $(N, C_{out}, H_{out}, W_{out})$, then the mathematical expression of the convolutional layer is

$$\begin{aligned}
out(N_i, C_{out_j}) &= bias(C_{out_j}) \\
&+ \sum_{k=0}^{C_{in}-1} weight(C_{out_j}, k) * input(N_i, k)
\end{aligned} \tag{41}$$

where input and out represent the input and output data of the current convolutional layer respectively. Weight and bias represent the current volume respectively the weight parameters and bias parameters of the layer.

Ignore the bias, the padding is 1, the size of the convolution kernel is 3×3, and the calculation formula of the output coordinate point (i, j) of the convolution layer is

$$out_{i,j} = \sum_{m=i-1}^{i+1} \sum_{n=j-1}^{j+1} weight_{m-i+1,n-j+1} input_{m,n} \tag{42}$$

In the one-dimensional case,

$$out_i = \sum_{m=i-1}^{i+1} weight_{m-i+1} input_m \tag{43}$$

We can change the value of W to achieve forward or backward differentiation. In the one-dimensional case, when the corresponding parameters of the convolution kernel are the same as the difference, the difference can be regarded as a special convolution, and the mathematical equivalence relationship makes it possible to use the convolution instead of the difference to implement the FDTD method. This also provides a theoretical basis for the neural network to directly learn the physical relationship between device geometry and response through electromagnetic simulation during the design of metasurface.

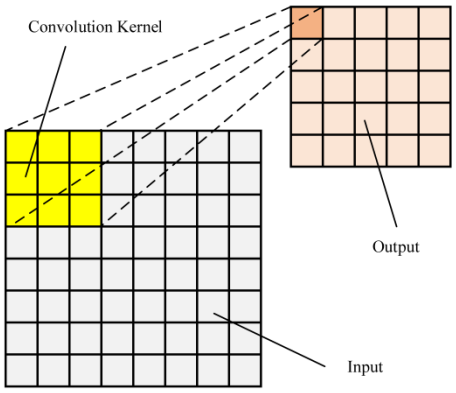

Figure 2 *Convolution operation.*

3 Discussion and conclusion

In this work, in the design process of using neural network to realize metasurface, we realize the inverse design of metasurface by directly learning the physical relationship between device geometry and response by combining electromagnetic simulation, in order to avoid the preparation of large data sets, to realize the purpose of beamforming.

4 Acknowledgement

The authors acknowledge the support from CETC Key Labora- tory of Data Link Technology (No: CLDL-20182418), the National Natural Science Foundation of China [61901324 , 62001345], China Research Institute of Radiowave Propagation [61971385], and the China Postdoctoral Science Foundation [2019M653548 , 2019M663928XB].

5 References

[1] Yu, Nanfang, Capasso, et al. Flat optics with designer metasurfaces.[J]. Nature Materials, 2014.

[2] Yu N , Aieta F , Genevet P , et al. A broadband, background-free quarter-wave plate based on plasmonic metasurfaces.[J]. Nano Letters, 2012, 12(12):6328-6333.

[3] Zhao Y , Alu A . Tailoring the dispersion of plasmonic nanorods to realize broadband optical meta-waveplates.[J]. Nano Letters, 2013, 13(3):1086-1091.

[4] Kildishev A V , Boltasseva A , Shalaev V M . Planar Photonics with Metasurfaces[J]. Science, 2013, 339(6125):1232009.

[5] Light Propagation with Phase Discontinuities: Generalized Laws of Reflection and Refraction.[J]. Science, 2011.

[6] Noguchi S , Matsutomo S , Cingoski V . An Adaptive FEM Based on Magnetic Field Conservation Applying to Ferromagnetic Problems[J]. IEEE Transactions on Magnetics, 2018, PP(3):1-4.

[7] Zhang R , Jia P , Hu L , et al. FEM-DDM-BEM for a 3-D Electromagnetic Scattering Analysis of Metal Dieletric Composite Structure[C]// International Conference on Computational Electromagnetics. 0.

[8] Yee K S . Numerical solution of initial boundary value problems involving maxwell's equations in isotropic media[J]. IEEE Transactions on Antennas & Propagation, 1966, 14(5):302-307.

[9] Ohtani T , Kanai Y , Kantartzis N V . Wide-angle elimination of TF/SF-generated spurious waves in the nonstandard-FDTD technique[C]// Electromagnetic Field Computation. IEEE, 2016.

[10] Kasher J C, Yee K S. A numerical example of a two-dimensional scattering problem using a subgrid[J]. Applied Compzrtational Electromagnetics Society Journal and Newsletter, 2, 1987, 2: 75-102.

[11] TAFLOVE A, HAGNESS S. Computational electrodynamics: the finite-difference time-domain method[J]. Optical Technology, 2005, 5(15):629-670.

[12] KRIZHEVSKY, ALEX, SUTSKEVER, ILYA, HINTON, GEOFFREY E.. ImageNet Classification with Deep Convolutional Neural Networks[J]. Communications of the ACM,2017,60(6):84-90. DOI:10.1145/3065386.

[13] He M Y , Li J J . Machine Learning Based Neural Network Solving Methods for the FDTD Method[C]// 2018 IEEE International Symposium on Antennas and Propagation & USNC/URSI National Radio Science Meeting. IEEE, 2018.

[14] Massa A , Marcantonio D , X Chen, et al. DNNs as Applied to Electromagnetics, Antennas, and Propagation - A Review[J]. IEEE Antennas and Wireless Propagation Letters, 2019, PP(99):1-1.

[15] Ren Y, Dang X, Wang C, et al. Fast RCS Data Generation Based on InfoGAN[C]//2021 Photonics & Electromagnetics Research Symposium (PIERS). IEEE, 2021: 331-336.

MISCELLANEOUS

13th International Conference Series on
Laser-light and Interactions with Particles
Optical Particle Characterization follow-up !
August 21-26th, 2022, Warsaw, Poland

OPTICAL MODEL TO DESCRIBE COHERENT TRANSMITTANCE AND ABSORPTANCE OF POLYMER DISPERSED LIQUID CRYSTAL FILM DOPED WITH CARBON NANOTUBES AT NORMAL INTERFACE ANCHORING

V. A. LOIKO[1*], A.V. KONKOLOVICH[1], A. A. MISKEVICH[1], D. E. NESTSEROVICH[1], D. MANAILA-MAXIMEAN[2], O. DANILA[2], V. CÎRCU[3], A. BĂRAR[2].

[1]Stepanov Institute of Physics, National Academy of Sciences of Belarus, Minsk, 220072, Belarus
[2]University Politehnica of Bucharest, Department of Physics, Bucharest, R-060042, Romania
[3]University of Bucharest, Department of Inorganic Chemistry, 23 Dumbrava Rosie St., Bucharest, Sector 2, 020484, Romania

Corresponding author: loiko@ifanbel.bas-net.by

Abstract

An optical model has been developed for analyzing the coherent transmittance and absorptance of a polymer dispersed liquid crystal films doped with carbon nanotubes (CNTs) at uniform normal droplet-polymer interface anchoring. It is based on the Foldy–Twersky and anomalous diffraction approximations, Maxwell-Garnett equations, and the order parameters concept. The model allows one to analyze the electro-optical response of films depending on the film thickness, the refractive indices of the liquid crystal (LC) and the polymer matrix, the size and concentration of the LC droplets, the concentration of nanotubes, the conductivities and permittivities of the CNTs, LC and the polymer. Experimental verification of the model is performed.

1 Introduction

The polymer-dispersed liquid crystal (PDLC) films [1] consist of a polymer matrix containing liquid crystal (LC) droplets, in which the orientation of the LC molecules can be changed under the electric or magnetic fields. This allows one to control the optical response of the films. They are used in displays, optoelectronic, microelectronic, and telecommunication systems, laser devices, etc. Electrically or magnetically controlled optical response of PDLC films is based on light scattering. It does not require the use of additional polaroids in comparison with the ordinary (bulk) LC layers.

In recent years, there is an increasing interest in studying the dielectric and optical properties of composite materials based on bulk LC and PDLC films doped with carbon nanotubes (CNTs) [2-5]. This is due to additional opportunities provided by nanotubes (NTs) to form and control electro-optical response.

Currently, studies of the electro-optical response of composite PDLC-CNTs films are mainly experimental [4,5]. As far as we know, there are no theoretical optical models that allow one to describe and predict electro-optical response of the PDLC-CNTs films as function of the component parameters (LC, polymer, NTs).

In this paper, we suggest an electro-optical model for analyzing the coefficients of coherent (directional, regular) transmission (coherent transmittance) and absorption (absorptance) of a PDLC-CNTs film with a homogeneous normal interface anchoring. To determine the coherent transmittance of the film, the Foldy–Twersky approximation is used [6,7]. The optical characteristics of a single droplet of nematic LC are determined in the framework of the anomalous diffraction approximation [1,7] using the effective refractive indices of the droplet [6]. Based on the Maxwell–Garnett equations [8], a method has been developed to determine the refractive index of the polymer matrix, the effective refractive index of the LC droplets, and the threshold field of the reorientation of the director structure of LC droplets upon doping the PDLC film with NTs.

A technique has been developed for determining the volume filling factor of the film with LC droplets, volume filling factors of the LC droplets and polymer matrix doped with NTs, depending on the mass fractions of the components in the PDLC-CNTs composite. The technique is applicable to singlewall (SWCNTs) and multiwall (MWCNTs) carbon nanotubes. Experimental verification of the developed model was carried out.

2 Theory

Let us consider a PDLC film containing a polydisperse ensemble of spheroidal LC droplets with rotation symmetry relatively to small axis directed along the normal to the film. The anisometry parameter ε_a, defined as the ratio of the major axis of the droplet in the film plane to the minor axis along the normal to the film, is the same for all droplets. In the framework of the Foldy-Twersky approximation, it is possible to write the following expressions for the coherent transmittance T_c and albedo Λ of a film:

$$T_c = \exp\left(-\gamma_{ext} l\right), \qquad (1)$$

$$\Lambda = Q_{scat} / Q_{ext} = Q_{scat} / (Q_{scat} + Q_{abs}), \quad (2)$$

$$\gamma_{ext} = \frac{3c_d}{4a_{ef}} Q_{ext}, \quad (3)$$

where γ_{ext} is the extinction coefficient of the PDLC film; l is the film thickness; Q_{scat}, Q_{ext} and Q_{abs} are the scattering, extinction and absorption efficiency factors for single droplet; c_d is the volume filling factor of the film with LC droplets (ratio of the volume of all droplets to the volume of film where they are distributed); a_{ef} is the effective [7] length of the minor droplet semiaxis a along the normal to the film.

Using the anomalous diffraction and effective medium approximations and based on the results of [6,7], we obtained:

$$Q_{ext} = 4 \operatorname{Re} K_h(v_{ext}), \quad (4)$$

$$v_{ext} = i2ka_{ef}(m-1), \quad (5)$$

$$Q_{abs} = 2K_h(v_{abs}), \quad (6)$$

$$v_{abs} = 2 \operatorname{Re} v_{ext}, \quad (7)$$

$$k = 2\pi / (\lambda m_{p+CNTs}), \quad (8)$$

$$m = m_{d+CNTs} / m_{p+CNTs}, \quad (9)$$

where K_h is the Hulst function [1],

$$K(v) = \frac{1}{2} - \frac{\exp(-v)}{v} + \frac{\exp(-v)-1}{v^2}, \quad (10)$$

m is the complex refractive index of LC droplet relative to the refractive index of polymer matrix; λ is the wavelength of the incident light in vacuum; m_{d+CNTs} and m_{p+CNTs} are the effective refractive indices of the LC droplet and polymer matrix doped with nanotubes. They are determined as follows:

$$m_{d+CNTs} = \sqrt{\varepsilon_{d+CNTs}}, \quad (11)$$

$$\varepsilon_{d+CNTs} = \varepsilon_{m+CNTs} - \frac{1}{3} \Delta\varepsilon_{LC+CNTs} S S_{d+CNTs}(E), \quad (12)$$

$$\varepsilon_{m+CNTs} = \frac{2\varepsilon_{LC+CNT,\perp} + \varepsilon_{LC+CNT,\parallel}}{3}, \quad (13)$$

$$\Delta\varepsilon_{LC+CNTs} = \varepsilon_{LC+CNT,\parallel} - \varepsilon_{LC+CNT,\perp}, \quad (14)$$

$$m_{p+CNTs} = \sqrt{\varepsilon_{p+CNTs}}. \quad (15)$$

In Eqs. (11)-(15), ε_{d+CNTs} and ε_{p+CNTs} are the complex effective permittivities droplet and polymer with CNTs; ε_{m+CNTs} and $\Delta\varepsilon_{LC+CNTs}$ are the average value permittivity and dielectric anisotropy of liquid crystal; $\varepsilon_{LC+CNTs,\parallel}$ and $\varepsilon_{LC+CNTs,\perp}$ are permittivities parallel and orthogonal to director of LC; S is the molecular order parameter of LC [1]; $S_{d+CNTs}(E)$ is the order parameter of LC droplets with nanotubes, depending on the control electric field E.

To find of $\varepsilon_{LC+CNTs,\parallel}$, $\varepsilon_{LC+CNTs,\perp}$ and ε_{p+CNTs} we used the Maxwell-Garnett approximation:

$$\varepsilon_{LC+CNTs,\parallel} = \varepsilon_{LC,\parallel}\left(1 + c^d_{CNTs}\left(R_{LC+CNTs,\parallel} - 1\right)\right), \quad (16)$$

$$R_{LC+CNTs,\parallel} = \varepsilon_{CNTs,\parallel} / \varepsilon_{LC,\parallel}, \quad (17)$$

$$\varepsilon_{LC+CNTs,\perp} = \varepsilon_{LC,\perp} \frac{1 + 0.5(1 + c^d_{CNTs})\left(R_{LC+CNTs,\perp} - 1\right)}{1 + 0.5(1 - c^d_{CNTs})\left(R_{LC+CNTs,\perp} - 1\right)}, \quad (18)$$

$$R_{LC+CNTs,\perp} = \varepsilon_{CNTs,\perp} / \varepsilon_{LC,\perp}, \quad (19)$$

$$\varepsilon_{p+CNTs} = \varepsilon_p \left\{ 1 + \frac{c^p_{CNTs}}{3} \frac{R_{p+CNTs,\parallel} - 1 + 4\dfrac{R_{p+CNTs,\perp} - 1}{R_{p+CNTs,\perp} + 1}}{1 - (2/3) c^p_{CNTs} \dfrac{R_{p+CNss,\perp} - 1}{R_{p+CNTs,\perp} + 1}} \right\}, \quad (20)$$

$$R_{p+CNTs,\parallel} = \varepsilon_{CNTs,\parallel} / \varepsilon_p, \quad R_{p+CNTs,\perp} = \varepsilon_{CNTs,\perp} / \varepsilon_p, \quad (21)$$

where $\varepsilon_{LC,\parallel}$ and $\varepsilon_{LC,\perp}$ are the permittivities of LC; ε_p is the permittivity of polymer; $\varepsilon_{CNTs,\parallel}$ and $\varepsilon_{CNTs,\perp}$ are the permittivities of nanotubes; c^d_{CNTs} and c^p_{CNTs} are the volume filling factors of the LC droplets and the polymer matrix with CNTs (characterizing the part of droplets and polymer matrix volume occupied by CNTs).

For droplets with normal interface anchoring, when a control field is applied along the normal to the film, using the results of [8], it is possible to write the following expression for the droplet order parameter in Eq.(12):

$$S_{d+CNTs}(E) = 1 - \exp(-e). \quad (22)$$

Here $e = E/E_c$ is the dimensionless normalized value of the control field: E_c is the critical value of the control field [9-11].

3 Results

To compare the results obtained in the framework of the developed model with the measurement data, we used the experimental dependences of the normalized transmittance $T_c^{norm} = T_c / T_c^{max}$ (T_c^{max} is maximum transmittance) on the control field E.

The measurements were carried out for PDLC films based on E7 LC and PMMA polymer without NTs and upon doping with NTs. The samples were illuminated along the normal to the film surface by a He-Ne laser at the wavelength λ=0.6328 μm. In the absence of NTs, ordinary $n_\perp$ and extraordinary $n_\parallel$ refractive indices of the LC are equal to: $n_\perp$=1.52, and $n_\parallel$=1.745, the refractive index of the polymer n_p=1.503. The filling factor of the PDLC film c_d=0.435. Films thickness l=50 μm. The average radius of droplets in the plane of the samples is $\langle a \rangle$=1.07 μm; effective droplet size a_{ef}=2.34 μm. The experimental and theoretical dependences of $T_c^{norm}(E)$ are presented in Figure 1. The following parameters were used in the calculation: the volume filling factor of the film with nanotubes c_{CNT}=0.03 (c^d_{CNT}=0.011, c^p_{CNT}=0.019); the electrical conductivities of LC $\sigma_\parallel = 5.7 \times 10^{-8}$ S/m and $\sigma_\perp = 2.6 \times 10^{-8}$ S/m. The calculations were carried out for different values of the electrical conductivities σ_p of the polymer matrix with and without nanotubes. One can see a good agreement of the theoretical and experimental results at variation of the model parameters in both cases.

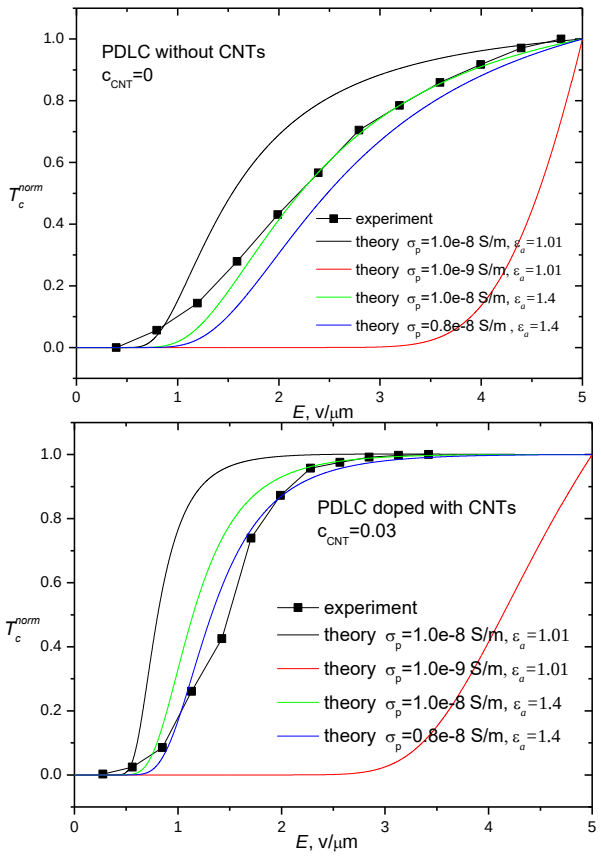

Figure 1 *Theoretical and experimental dependences of the normalized transmittance $T_c^{norm}(E)$ for the PDLC film (top) and PDLC-CNTs film (bottom) at different values of the electrical conductivities σ_p of the polymer matrix*

4 Conclusions

In the present work a model for describing the electro-optical response of PDLC-CNT films is developed. The model is validated by comparison with experiment.

Pay attention that the theory is developed for the films with a uniform normal interface anchoring. Such films are characterized by a polarization-independent coherent transmittance at normal illumination, when the control electric field is directed normally to the film. They are promising for applications in optoelectronic devices where modulation of light is required without changing its polarization state and to modulate the unpolarized light. The model can be extended to PDLC-CNT films with polarization-dependent tangential interface anchoring and the PDLC films doped with other nanoparticles: gold, ferroelectric, silica, etc.

5 References

[16] P. S. Drzaic, Liquid Crystal Dispersions (World Scientific, 1995).

[17] Rahman M., Lee W., Scientific duo of carbon nanotubes and nematic liquid crystals, J. Phys. D: Appl. Phys. 5: 063001 (2009).

[18] Yadav S.P., Singh S., Carbon nanotube dispersion in nematic liquid crystals: An overview, Progress in Mater. Sci. 80:38 (2016).

[19] Shriyan S.K., Fontecchio A.K., Improved Electro-Optic Response of Polymer Dispersed Liquid Crystals Doped with Oxidized Multiwalled Carbon Nanotubes, Mol. Cryst. Liq. Cryst. 525:158 (2010).

[20] Wu Y., Cao H., Duan M. et al., Effects of a chemically modified multiwall carbon nanotubes on electro-optical properties of PDLC films, Liquid Crystals 45:1023 (2017).

[21] V.A. Loiko, Polymer Films with Nanosized Liquid-Crystal Droplets: Extinction, Polarization, Phase, and Light Focusing, In Nanodroplets, Zh. M.Wang, ed. Springer Series Lecture Notes on Nanoscale Science and Technology, Chapter 9, P. 195-235. New York, Heidelberg, Dordrecht, London (Springer ,2013).

[22] Loiko V.A., Konkolovich A.V., Zyryanov V.Ya., Miskevich A.A., Polarization of light by a polymer Film Containing Elongated Drops of Liquid Crystal with Inhomogeneous Interfacial Anchoring, Opt. and Spectr. 122::984 (2017).

[23] Bloisi F., Ruocchio C., Terrecuso P., and Vicari L.., Angular dependence of light transmittance in polymer dispersed liquid crystals, Phys. Rev. E 54:5242 (1996).

13th International Conference Series on
Laser-light and Interactions with Particles
Optical Particle Characterization follow-up !
August 21-26th, 2022, Warsaw, Poland

HIGH-RESOLUTION VOLUMETRIC LITHOGRAPHIC RECORDING OF 3D STRUCTURES BY ACTIVATING UP-CONVERSION LUMINESCENCE IN Yb^{3+} AND Tm^{3+} NANOPARTICLES DOPED INTO A NEGATIVE SU8 PHOTORESIST

Julija PERVENECKA[1*], Jurgis GRUBE [1], Ernests TROPINS[1], Kaspars VITOLS[1], Viesturs-Tenis VIKSNA[1], Janis TETEROVSKIS[1], Aivars VEMBRIS[1], Jelena BUTIKOVA[1], Guna KRIEKE[1] and Maris SPRINGIS[1]

[1] Laboratory of Organic Materials, Institute of Solid State Physics, University of Latvia, Riga, LV-1063, Latvia

Corresponding author: julija.pervenecka@cfi.lu.lv

Abstract

In this work we demonstrate success of an innovative approach to lithographic recording of high-resolution 3D structures from the volume of hybrid inorganic/photoresist systems by activating up-conversion luminescence in Yb^{3+} and Tm^{3+} nanoparticles doped into a negative photoresist SU8. That is highly perspective for the fabrication of various types of microstructures from such hybrid systems as organic-chromophores/UCNPs/SU8, without damaging light sensitive organic compound, demanded in photonic applications.

Keywords: lithography, SU-8 photoresist, hybrid systems, guest-host system, UCNP, luminescence, up-conversion, microstructures.

1 Introduction

In nowadays, great attention has been attracted to the up-conversion nano-particles (UCNPs). One of the greatest advantages and at the same time unique properties of UCNPs are anti-Stokes's shift luminescence, meanwhile all conventional luminescent materials have down-conversion luminescence. Another important advantage of them is well controlled solution chemical synthesis process where through several modifications can be designed and changed core/shell structured UCNP's active light emitting core or comparably passive - shell dopant ions or they concentration, as well as size and form of all UCNP's.

At the present time perspective, but not as widely investigated application for up-conversion luminescence emitting nanoparticles is photolithography. In traditional photolithography exposure are made through the surface, mostly, by i-line UV radiation, which is limited by the thickness of photo sensitive layer. In thick samples most of the radiation is absorbed in the upper layers, which results in unexposed deeper layers, turning to strong distortion (partial) or fully washing off all recorded structures upon development process. More over, traditional i-line photolithography is not the effectivnes for negative tone photoresists as SU8, since appropriates to the range of its absorption spectrum decay (~20-30%). This problem can be solved in case when light emitting sources are placed into photoresist thus ensures uniform absorption of required blue or UV-light in all volume of exposed structure. It can be achieved by doping the photoresist with light sources, such as inorganic nanoparticles [1], which emitts light (luminescence) in appropriate spectral region after excitation with external energy source (laser).

Here luminescence is excited with the wavelength at which the photoresist is transparent, meanwhile, by nano-particles emitted light will be absorbed by photoresist and behaves in similar as blue or UV light. In practis, it can be done by mixing photoresist with nanoparticles activated with rare-earth ions, in which up-conversion luminescence occurs. Up-conversion luminescence is one of the Anti-Stokes process, which can be excited in inorganic nanoparticles prepared in a special way. It occures when UV and visible luminescence is excited with the absorption of multiple infrared (IR) photons [2].

The photoresist and organic compounds are transparent for infrared light; therefore, it is possible to guide the excitation light into the volume of the photoresist. It means, that in perspective similarly, up-conversion luminescence could be used to expose a photoresist mixed with organic chromophores. Overcoming the biggest problem, total degradation of organic chromophores upon traditional i-line UV radiation due to high absorption of it. That allows to create systems containing organic chromophores for possible application in medicine, telecommunications and other technologies demanded light emitting micro-structure creation.

In this work system of SU8 photoresist mixed with up-converting nanoparticles were created. Our made method demonstrates an innovative approach for recording high-resoluted three-dimensional structures in a negative photoresists as SU8 by tunable through the synthesis process up-conversion luminescence of the Yb3+ and Tm3+ activated in incorporated core/shell (C/S)-structured nanoparticle as an alternative of an traditional optical lithography. We show that it is possible to create optical writing in systems volume, by exciting nanoparticles with a 975 nm laser diode, by achieving high resolution, uniformly thick 100x500 µm microstructures with a good appropriance to the focused structure dimensions, at less

then 5 min longed exposure in samples with 20-15%wt of UCNPs in SU8.

1.1 Synthesis and characterization of Yb^{3+} and Tm^{3+} core/shell structured nanoparticle)

The investigated nanoparticles with a hexagonal (d = 30-50 nm) core/shell structure were synthesized by thermolysis method in two-day long process. To perform the work, the nanoparticle synthesis setup was created: a three-necked flask, which is placed in a magnetic heater. For the synthesis process to be successful, most of the synthesis must take place under an argon atmosphere (three vacuum and argon aeration cycles are performed). The shell and core nanocrystals are made at the same time in different flasks and have the same synthesis procedures. From Yttrium oxide is made shell nanocrystals while core nanocrystals are made from Yttrium (Y), Ytterbium (Yb) and Thulium (Tm) oxides (concentration: Y – 74.7%, Yb – 25%, Tm – 0.3%). At the last stage is added 40 ml of Chloroform and centrifuged for 10 minutes, then prepared solution is poured in storage containers:

1.2 Sample preparation

All samples were made as host-guest systems, by adding guests – UC nano-particles - consisting $CHCl_3$ solution into photoactive host - 400 - 500 nm thin film layer providing solution of dissolved in chloroform SU-8 GM1075 epoxy-based negative type photoresist matrix. Photoactive thin film samples were made from solution by spin-coating method on BK7 glass substrates, precleand with oxigen plasma by Plasma Asher Tepla setup. Keeping constant volume ratio of system compounds to solvent, varying concentration ratios of UCPN in SU8 were made series of the samples with UCPN concentration 10, 15, 20, 25, 30, 40, 50 wt%.

1.3 Up-conversion luminescence based lithographic record

Up-conversion luminescence based lithographic recording were made by the self-made system see Figure 1.

Figure 1 *Self-made optical system for up-conversion luminescence based lithographic recording*

UC luminescence excitation were made at 975 nm by Thorlabs L975P1WJ CW laser diode mounted on TCLDM9 - TE-Cooled Mount from Thorlabs was used (LD). Laser diode beam was focused on the sample surface 100x500 µm area using anamorphic prism pairs (Thorlabs N-SF11 Mounted Prism Pair, ARC: 650 - 1050 nm, Mag: 4.0) and objective lens (OL) (Thorlabs High-Power MicroSpot Focusing Objective, 5X, 980 - 1130 nm, NA = 0.13). Laser power was set to 700 mW. Exposition times were set to 5, 10, 15 and 25 minutes. As the beam passes through a pair of prisms (APP), it changes from an ellipse to a rectangular-circular profile.

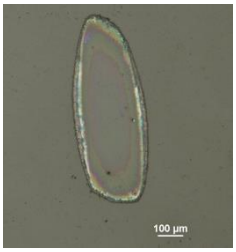

Figure 2 *Optical image of recorded structures in sample with 15wt% of nanoparticles in SU8 (exposed ~10 min , ~ 450 nm thickness). Obtained by high-resolution optical microscope Nikon ECLIPSE L150 at x50 zoom.*

2 Conclusions

Our made method is an alternative of an traditionnal optical litography. It is an innovative approach for recording high-resoluted three-dimensional structures in a negative photoresists SU8 by up-conversion luminescence of the Yb3+ and Tm3+ activated in incorporated core/shell (C/S)-structured nanoparticle.

We proved that it is possible to create optical writing in systems volume, by exciting nanoparticles with a 975 nm laser diode, by achieving high resolution, uniformly thick 100x500 µm microstructures with a close apropriance to the focused structure dimensions, at 5-10 min longed exposure in samples with 20-15%wt of UCNPs in SU8 see Figure. 2.

3 Acknowledgement

This research is funded by the Latvian Council of Science, project "Up-conversion luminescence photolithography in organic compounds using nanoparticles/photoresist composition", project No. lzp-2019/1-0422.

Institute of Solid State Physics, University of Latvia as the Center of Excellence has received funding from the European Union's Horizon 2020 Framework Programme H2020-WIDESPREAD-01- 2016-2017-TeamingPhase2 under grant agreement No. 739508, project CAMART².

4 References

[1] A. Wickberg, J.B. Mueller, Y.J. Mange, J. Fischer, T. Nann, M. Wegener, Appl. Phys. Lett., 106 (13) (2015), p. 13310

[2] F. Auzel, Upconversion and Anti-Stokes Processes with f and d Ions in Solids, Chem. Rev. 104, (2004), p. 139 – 173.

AEROSOLS

13th International Conference Series on
Laser-light and Interactions with Particles
Optical Particle Characterization follow-up !
August 21-26th, 2022, Warsaw, Poland

REMOTE SENSING OF BIOMASS BURNING AEROSOL BY THE MEANS OF MULTIWAVELENGTH LIDAR MEASUREMENTS IN WARSAW

Lucja JANICKA [1*], Iwona S. STACHLEWSKA [1], Christine BOECKMANN [2], Steigvile BYCENKIENE [3], Wojciech KUMALA [1], Holger BAARS [4] and Ronny ENGELMANN [4]

[1] Remote Sensing Laboratory, Faculty of Physics, University of Warsaw, ul. Pasteura 5, 02-093 Warsaw, Poland
[2] Institute of Mathematics, University of Potsdam, Karl-Liebknecht-Str. 24-25, D-14476 Potsdam, Germany
[3] Center for Physical Sciences and Tehnology (FTMC), Saulėtekio av. 3, LT-10257 Vilnius, Lithuania
[4] Leibniz Institute for Tropospheric Research (TROPOS), Permoserstraße 15, 04318 Leipzig, Germany
Corresponding author: lucja.janicka@fuw.edu.pl

Abstract

Long-term remote sensing of the atmospheric aerosol is crucial for climate studies. Biomass burning aerosol is of special importance, as it scatters and absorbs solar radiation, whereby the latter leads to local warming of the atmosphere. In this study, a comparative analyses of particle optical properties of biomass burning aerosol, as derived from the vertical lidar profiles within the troposphere, is discussed. The profiling was done with the multi-wavelength, double field-of-view, Raman-Mie, polarization, and water vapor Lidar. The selected cases represent different-origin episodes of biomass burning aerosol advection over Warsaw.

1 Introduction

Small particles suspended in the atmosphere, called atmospheric aerosol, play an important role in the Earth's climate system due to their interactions with the solar radiation: aerosol particles scatter and/or absorb solar light, dependent on its wavelength. Scattering leads to the cooling of the atmosphere, whereas absorption causes heating of the atmosphere at a layer at which absorbing aerosol are present. Therefore, studies of absorbing aerosol are so important for the climate change modelling [1].

The crucial aerosol component that is absorbing solar radiation constitute black carbon. It can be released into the atmosphere by the combustion processes of fossil and bio fuels, that among others, can originate from wildfires of natural ecosystems or agriculture areas. Additionally to the black carbon, biomass burning aerosol (BBA) consist of organic carbon and inorganic particles [2]. Emission of the BBA during the episodes of forest or grassland fires is huge, can last long-time, and results in release of large amounts of heat. The released heat causes deep convection, which can uplift the aerosol (even up to the stratosphere) and redistribute over long-distances from the place of BBA origin [3]. After the emission, the BBA is subject to the intense ageing processes, which causes changes of its optical and microphysical properties. Consequently, that makes the BBA influence on the Earth's radiation budget significant.

In this study a few particular events of long-range BBA transport over the Warsaw are analysed, whereby the episodes represent different places of aerosol origin and different aerosol age.

2 Methodology

Advanced lidar systems are very convenient tools for atmospheric aerosol studies, as they can provide vertical profiles of optical properties of the atmosphere. Advanced lidars can detect the laser light scattered elastically backwards on the aerosol particles, but also using the Raman scattering on the atmospheric nitrogen molecules. Thus, they can provide independent profiles of the aerosol particle extinction and backscattering coefficients. Information of the particles shape (spherical or aspherical) is provided by the detection channels measuring the cross- and parallel-polarization of the emitted linearly polarized laser light changed by aerosol particle. Using the data-products derived from lidar at several wavelengths, lidar provides the data set sufficient to be used as an input for the mathematical inversion algorithms [4], which allow to obtain microphysical aerosol properties such as: particle effective radius, particle refractive index, number, surface, and volume concentrations, and single scattering albedo. The latter can be directly used for the estimation of the radiative forcing due to aerosol [5].

2.1 Instrument

The modern 12-wavelength PollyXT lidar system [6] operates in the Remote Sensing Laboratory (RS-Lab) at the Institute of Geophysics, Faculty of Physics, University of Warsaw since July 2013. The system was build with the scientific cooperation with the Leibniz Institute for Tropospheric Research (TROPOS). The system provides the quasi-continuous vertical lidar measurements with the emitted Nd:Yag laser light at 355, 532, and 1064 nm. Backscattered light is collected by two Newtonian-type telescopes (narrow and wide field of view) and is divided

into 8 detection channels for the far-range (0.6 -15 km) and into 4 detection channels for the near-range (0.12 – 3.5 km), respectively. Combination of two telescopes minimizes the effect of incomplete overlap of the laser beam and the narrow telescope field of view. The far-range channels are 355, 532, 1064 nm elastic; 355, 532 nm cross-polarized; 387, 607 nm Raman-shifted on N_2 and 407 nm Raman-shifted on H_2O to provide profiles of water vapour mixing ratio. The near-range channels are 355, 532, 387, and 607 nm. Signals are detected with photomultipliers (in photon counting mode) with raw resolution of 30 s and 7.5 m.

The lidar operates within the European Aerosol Lidar Network *EARLINET* [7], the worldwide network of PollyXT lidars - *PollyNET* [8] and the Polish Aerosol Research Network *PolandAOD* [9].

2.2 Data evaluation

The particle optical properties profiles: particle backscatter coefficients (β) at 3 wavelengths and particle extinction coefficients (α) at 2 wavelengths were derived using the classical Raman approach, according to the evaluation scheme given in [10]. The profiles of linear depolarization ratios (δ) at 2 wavelengths were derived with the ±45° calibration method [6]. The water vapour mixing ratio (wv) was calculated as given in [11].

The lidar ratio was calculated as $LR_\lambda = \alpha_\lambda/\beta_\lambda$ at particular wavelength; this parameter is useful for aerosol type identification. Ångström exponent (related to extinction) was calculated as $AE_{355/532} = -\ln(\alpha_{355}/\alpha_{532})/\ln(355/532)$.

The analysis was supported by the data products of the MODIS measurements onboard satellite and the model output backward trajectories runs with HYSPLIT [12] to assess and better specify the aerosol place of origin (Figure 1).

3 Results

Four episodes of BBA advection over Warsaw were chosen for comparative study (Figure 1):

a) long-range transport of the smoke from Canadian forest fires on 9th July 2013 [13];

b) fast transport of the BBA from wildfires in Ukraine driven by the clean Arctic air-mass on 19th March 2015;

c) advection during the heat wave on 10th August 2015 from the southern Ukraine through Southern and Central Europe;

d) advection of the aged BBA from the Iberian Peninsula through southern edge of Western Europe on 1st September 2018.

The lidar ratios for analyzed cases are in the range of 35-100 sr, whereby the lowest and the highest one was for 355 nm (Table 1). In the cases of Ukrainian BBA sources, the LRs are high (68-100 sr) and the values for 355 nm are higher than the ones for 532 nm. The relation of $LR_{355}>LR_{532}$ indicates stronger absorption of short waves. The opposite relation was observed for the case of long-range transport of smoke from Canadian forest fires and from the Iberian Peninsula with lower LR values (35 sr at 355 and 67 sr at 532 nm). The relation of $LR_{355}<LR_{532}$ is often observed for the aged BBA [14], as the ageing processes lead to the increase of the particles size.

The extinction related Ångström exponent had the lowest value of 0.64 for the Iberian fires, higher of 0.97 for the Canadian fires and the highest of 1.62-1.71 in the Ukrainian cases. This values confirm hypothesis of larger particles in the aged BBA, as low values of AE indicate larger particles size.

The particle linear depolarization ratio was in the range of 1.2-8.3 %. Higher values were obtained at 532 nm for all cases. The values of 5.4 % (355 nm) and 8.3 % (532 nm) (the highest ones) were observed for the case of the fast aerosol transport in the Arctic air-mass. Such high depolarization can be related to the very dry condition of the Arctic air (relative humidity data not shown here for brevity) and to the short time after aerosol emission. Small values up to 3 % were observed on 10th August 2015 and 1st September 2018 and can be attributed to high relative humidity. For the Canadian fires, the depolarization was relatively low of 3.3-3.5 % and almost equal for both wavelengths.

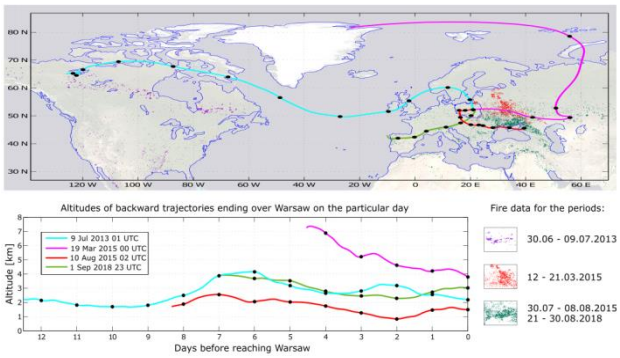

Figure 1 *The HYSPLIT backward trajectories on episodes of BBA advection to Warsaw chosen for comparative study and corresponding active fire data from the MODIS satellite sensor.*

	9 Jul 2013 blue	19 Mar 2015 pink	10 Aug 2015 red	1 Sep 2018 green
LR_{355} [sr]	43	100	86	35
LR_{532} [sr]	61	71	68	67
$AE_{355/532}$ [-]	0.97	1.71	1.62	0.64
$\delta_{part355}$ [%]	3.3	5.4	1.4	1.2
$\delta_{part532}$ [%]	3.5	8.3	3	1.7

Table 1 *Mean lidar-derived properties of BBA in four episodes of advection to Warsaw.*

4 Conclusion

Quasi-continuous lidar measurements of atmospheric aerosol performed in the RS-Lab allow to observe episodes of biomass burning aerosol advection of different origin and

time of transport in the atmosphere. The presented comparative study of four cases show, that the aged aerosol originating from Canada and the Iberian Peninsula differ significantly from the ones from Ukrainian sources: the lidar ratios were lower and the relation of LRs was reversed, Ångström exponent and the depolarization ratios were relatively low for the aged aerosols.

The data obtained in the analysis of biomass burning aerosol over Warsaw will be used for the inversion of microphysical aerosol parameters for selected cases.

5 Acknowledgement

The PollyXT-UW lidar was developed within R&D collaboration of the University of Warsaw and the Leibniz Institute of Tropospheric Research (TROPOS), in the PollyXT development group of Dietrich Althausen. This development was financed by the Polish Foundation of Science and Technology (519/FNITP/115/2010).

The algorithms used for lidar data evaluation were developed in the frame of ESA-ESTEC Contract 4000112373/14/NL/CT (MULTIPLY).

The EARLINET lidar observations in Warsaw were/are supported by the European Union Research Infrastructure Actions under the H2020 Grant Agreements No. 654109, No. 739530, and No. 871115.

The current measurements of biomass burning aerosol including measurement campaigns in Warsaw (FUW) and Vilnius (FTMC) are financed by NCN DAINA-2 grant (2020/38/L/ST10/00480) "Importance of long range transport of BIOmass burning emissions to local Smog events in Urban Environments (BIOSURE)".

6 References

[1] Stocker T., Qin D., Plattner G., Tignor M. et al., IPCC, 2013: Climate Change 2013: The Physical Science Basis. Contribution of Working Group I to the Fifth Assessment Report of 5 the Intergovernmental Panel on Climate Change (Cambridge Univ. Press, Cambridge, UK, and New York, 1535 pp., 2013).

[2] Reid J.S., Koppmann R., Eck T.F., Eleuterio D.P., A review of biomass burning emissions part II: intensive physical properties of biomass burning particles, Atmos. Chem. Phys. 5:799-825 (2005).

[3] Ortiz-Amezcua P., Guerrero-Rascado J. L., Granados-Muñoz M. J., Benavent-Oltra J. A. et al., Microphysical characterization of long-range transported biomass burning particles from North America at three EARLINET stations, Atmos. Chem. Phys. 17:5931-5946 (2017).

[4] Böckmann C., Hybrid regularization method for the ill-posed inversion of multiwavelenght lidar data to determine aerosol size distributions, Appl. Optics 40:1329-1342 (2001).

[5] Markowicz K., Chilinski M.T., Lisok J., Zawadzka O. et al., Study of aerosol optical properties during long-range transport of biomass burning from Canada to Central Europe in July 2013, Journal of Aerosol Science 101:156-173 (2016).

[6] Engelmann R., Kanitz T., Baars H., Heese B. et al., The automated multiwavelength Raman polarization and water-vapor lidar PollyXT: The next generation, Atmos. Meas. Tech. 9:1767-1784 (2016).

[7] Pappalardo G., Amodeo A., Apituley A., Comeron A. et al., EARLINET: Towards an advanced sustainable European aerosol lidar network, Atmos. Meas. Tech. 7:2389-2409 (2014).

[8] Baars H., Kanitz T., Engelmann R., Althausen D. et al., An overview of the first decade of Polly NET: An emerging network of automated Raman-polarization lidars for continuous aerosol profiling, Atmos. Chem. Phys. 16:5111-5137 (2016).

[9] Markowicz K.M., Stachlewska I.S., Zawadzka-Manko O., Wang D. et al., A decade of the Poland-AOD aerosol research network observations, Atmosphere 12 :1583 (2021).

[10] Wang D., Szczepanik D., Stachlewska I.S., Interrelations between surface, boundarylayer, and columnar aerosol properties derived in summer and early autumn over a continental urban site in Warsaw, Poland, Atmos. Chem. Phys. 19:13097–13128 (2019).

[11] Stachlewska I.S., Costa-Surós M., Althausen D., Raman lidar water vapour profiling over Warsaw, Poland, Atmos. Res. 194:258-267 (2017).

[12] Stein A.F., Draxler R.R., Rolph G.D., Stunder B.J.B. et al., NOAA's HYSPLIT atmospheric transport and dispersion modeling system, Bull. Amer. Meteor. Soc. 96:2059-2077 (2015).

[13] Janicka L., Stachlewska I.S., Veselovskii I., Baars H., Temporal variations in optical and microphysical properties of mineral dust and biomass burning aerosol derived from daytime Raman lidar observations over Warsaw, Poland, Atmos. Env. 169:162–174 (2017).

[14] Nicolae D., Nemuc A., Müller D., Talianu C. et al., Characterization of fresh and aged biomass burning events using multiwavelength Raman lidar and mass spectrometry, Journal of Geophysical Research: Atmospheres 118:2956–2965 (2013).

13th International Conference Series on
Laser-light and Interactions with Particles
Optical Particle Characterization follow-up !
August 21-26th, 2022, Warsaw, Poland

ON THE IMPACT OF THE INTERNAL COUPLING ON FRACTAL AGGREGATES STRUCTURE FACTORS

Clément ARGENTIN[1,*], Marek MAZUR[1], Romain CEOLATO[2], Matthew J BERG[3] and Jérôme YON[1]

[1] Normandie Université, INSA Rouen, UNIROUEN, CNRS, CORIA, 76000, Rouen, France.
[2] ONERA, The French Aerospace Lab, University of Toulouse, Toulouse, 31055, France
[3] Kansas State University, Department of Physics, 1228 N. 17th St., Manhattan, KS 66506-2601, USA

Corresponding author: yon@coria.fr

Abstract

Angular light scattering by aerosol particles, including complex particles such as fractal aggregates, can give access to the size and morphology through an *in-situ* approach. For this purpose, the angular scattering signal must be processed by a theory that provides a structure factor, which takes into account particle shape. Such a function is accurately determined for X-rays or for transparent objects in the visible range since the assumption of no internal coupling is fairly well respected. However, for some materials such as fractal soot aggregates, the internal coupling is suspected to modify the morphological and size dependence of the structure factor. The objective of this work is to understand and quantify such a deviation from the internal electric field analysis using a phasor approach.

1 Context and motivations

Aerosols such as soot become a matter of concern in our daily life. Due to their impact on human health but also on global warming, their characterization is of extremely high relevance. Angular light scattering is a technique that enables the *in-situ* characterization of such particles in terms of size (radius of gyration R_g) as well as in terms of morphology (fractal dimension D_f) for fractal aggregates. For nano-aerosols, the Rayleigh-Debye-Gans (RDG) approximation for fractal aggregates (FA) is frequently used essentially due to its simplicity since it provides a simple analytical expression of the angular scattering pattern (called structure factor). However, this approximation implies two strong assumptions. First, the monomers composing the aggregate behave as Rayleigh spheres, i.e., they are small enough compared to the wavelength and transparent enough to make the phase shift negligible. Second, it is supposed that there is no electromagnetic coupling between the monomers, i.e., each one sees only the incident light and not the light scattered by its neighbors. As explained by Sorensen [1] when internal coupling is neglected, it is possible to link mathematically the structure factor to the particle pair-correlation by a simple Fourier transform.

Nevertheless, as shown by Yon *et al.* [2], in certain cases, as for Diesel soot particles, this approach can lead to errors up to 45% on the predicted forward scattering by RDG-FA and could alter the determination of the fractal dimension by a factor up to 10% since the slope in the power-law regime (large qR_g) can be affected (see Fig. 1). Conversely, the same authors concluded that the impact on the optical determination of radius of gyration is limited.

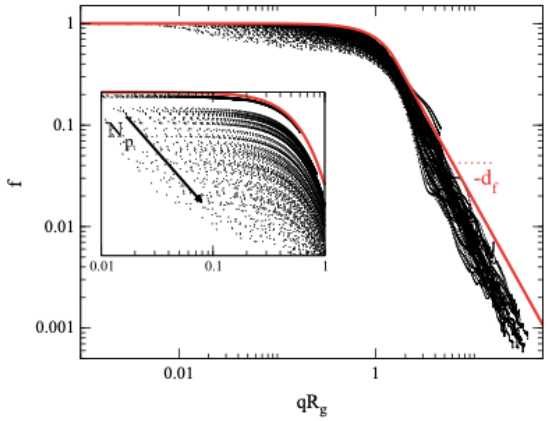

Figure 3: *Comparison between rigorous calculations (DDSCAT, black dots) of aggregate structure factor f and prediction by RDG-FA theory (solid red lines) at λ=266 nm.*

In a recent study [3], we have shown how the non-uniformity of the internal electric field affects the forward scattering using a phasor approach. The aim of the present study is to extend the phasor approach to understand how internal coupling affects the structure factor, in particular at large angles and especially at 180° as a better evaluation of the backscattering using the RDGFA is essential for lidar applications measuring smoke and soot plumes.

2 Phasor approach of the structure factor

According to [1], in respect of the RDG hypothesis, the scattered light at angle θ is proportional to the structure factor defined as

$$f = \frac{\sum_i^N \sum_j^N \exp\left[i\mathbf{q}.(\mathbf{r}_i - \mathbf{r}_j)\right]}{N^2} \qquad (1)$$

where i denotes all the volume elements composing the aggregate and $\mathbf{q} = \mathbf{k}_i - \mathbf{k}_s$ is the scattered wave vector which depends on θ and on the wavelength λ. This expression is valid if the internal electric field is uniform. The non-uniformity generated by internal coupling can be quantified by a complex number called phasor which is proportional to the local internal electric field [4]:

$$z_{y,i}(\hat{\mathbf{x}}) = \frac{m^2+2}{3E_0} E_{y,i}^{\text{int}}(\mathbf{r}_i)\exp(-ikx_i) \quad (2)$$

In this equation, $E_{y,i}^{\text{int}}$ is the y-component of the local internal electric field and $\hat{\mathbf{x}}$ is the direction of propagation of the light, m is the complex refractive index, E_0 the amplitude of the incoming electric field and k the wavenumber. The phasor can be seen as the wavelet scattered by a volume element to the detector for a vertical polarization (along $\boldsymbol{y}$) of the incident and the scattered light "vv".

By developing the Volume Integral Equation based on the phasor formalism, one can express the structure factor according to the spatial distribution of the phasor (Ceolato and Berg [5] did it for backscattering). Here we retain the Eulerian expression of the phasor $z_y = \Lambda\exp(\Phi)$ to show that the classical expression of the structure factor Eq.(1) is finally decomposed into two terms when internal coupling is considered Eq.(2):

$$f_{\text{IC}} = f_r - f_i \text{ with}$$

$$f_r = \frac{\sum_i^N\sum_j^N \Lambda_i\Lambda_j\cos(\Phi_i-\Phi_j)\cos[\mathbf{q}.(\mathbf{r}_i-\mathbf{r}_j)]}{\sum_i^N\sum_j^N \Lambda_i\Lambda_j\cos(\Phi_i-\Phi_j)} \quad (3)$$

$$f_i = \frac{\sum_i^N\sum_j^N \Lambda_i\Lambda_j\sin(\Phi_i-\Phi_j)\sin[\mathbf{q}.(\mathbf{r}_i-\mathbf{r}_j)]}{\sum_i^N\sum_i^N \Lambda_i\Lambda_i\cos(\Phi_i-\Phi_i)}$$

Without internal coupling ($\Lambda = 1$ and $\Phi = 0$), the first term corresponds to Eq.(1) and becomes purely morphology-dependent. This term is noted f_r because it remains when phasors are purely real. In turns, without internal coupling, the second term is null. It becomes non-null only if $\Phi \neq 0$ and varies in space, justifying the subscript "i" for "imaginary". It is therefore interesting to observe that the contribution tends to reduce the amplitude of the structure factor.

3 Numerical setup

All the presented results correspond to monodisperse DLCA aggregates composed of $N_m = 284$ monomers with a radius $R_m = 15$ nm, a fractal dimension $D_f = 1.78$ and a fractal prefactor $k_f = 1.44$. DDSCAT is used to compute the internal electric field over 500 orientations of the aggregates relatively to the incoming light source. While Figs. 5 and 6 correspond to a fixed random orientation of the aggregate, the remaining figures correspond to cases where the phasors are averaged over the considered orientations. The wavelength is set to $\lambda = 266$ nm because lower wavelengths favor multiple scattering effects. The impact of the refractive index is evaluated by considering $m = 1.1 + i0.01$, $m = 1.1 + i0.4$, $m = 1.1 + i0.8$ to study the effect of increasing $Im\{m\}$ and $m = 1.1 + i0.8$, $m = 1.5 + i0.8$, $m = 1.9 + i0.8$ to study the effect of increasing $Re\{m\}$.

4 Results

4.1 Structure factor contributions

Fig. 2 first validates the proposed methodology by comparing the structure factor directly provided by DDSCAT with the one reprocessed by the phasor approach f_{IC}. Indeed, both curves are perfectly superimposed.

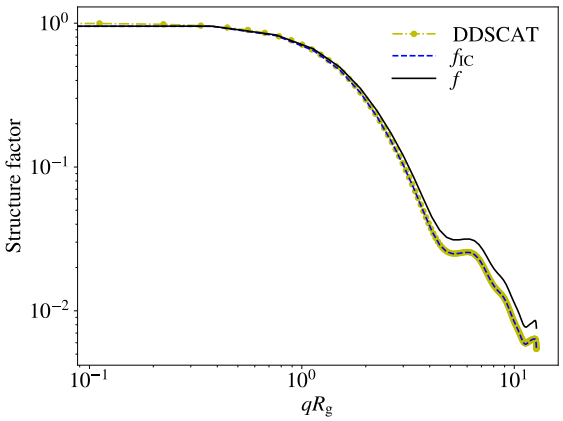

Figure 4: *Comparison between DDSCAT calculation (circle marker) of aggregate structure factor and Eqs. (1) (solid line) and (3) (dashed line) for* $m = 1.1 + i0.8$

This figure also reports the purely morphologically dependent structure factor f obtained by imposing the phasor to be 1 ($\Lambda = 1$ and $\Phi = 0$ in Eq.(2)). It appears that the inclusion of an internal coupling globally decreases the angular scattering amplitude, in particular at large scattering angles (large q). Moreover, since the fractal dimension is evaluated as the opposite of the slope in the power-law regime, it seems that internal coupling can provoke an over-estimation of the optically determined fractal dimension as previously suggested [2].

To better understand this phenomenon, let's study the relative departure of f_r and f_i to f. Fig. 3 shows the ratio f_r/f in the upper plot and f_i/f in the bottom plot for three different indices, $m = 1.1 + i0.01$ (in green dash dot line), $m = 1.1 + i0.4$ (in orange dot line) and $m = 1.1 + i0.8$ (in blue dashed line).

First, we observe that f_i/f $(qR_g = 0) = 0$. This explained by the term $\sin[\mathbf{q}.(\mathbf{r}_i - \mathbf{r}_j)]$ which tends toward zero at small angles (see Eq.(3)). This term never exceeds 5% of deviation for the range of investigated qR_g and optical indices. At small scattering angles (Guinier Regime) f_r/f is close to 1. It is the reason why the gyration radius measurement is not so affected by internal coupling as already observed [2].

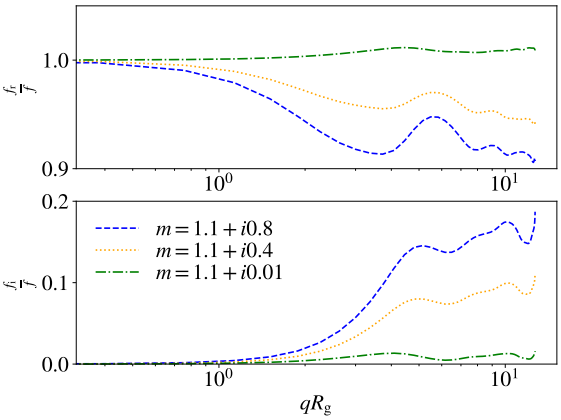

Figure 3: *Deviation of f_r and f_i with respect to f for m=1.1+i0.01 (in green dash dot line), m=1.1+i0.4 (in orange dot line) and m=1.1+i0.8 (in blue dashed line).*

Still, both terms play a role in the deviations at larger scattering angles. Indeed, f_r can reach 10% of deviation whereas f_i/f can be twice. Because $f_{IC} = f_r - f_i$, the maximum deviation for this aggregate can reach almost 30% at 180° showing the importance of internal multiple scattering for backward measurements as used for LIDAR. Note that, depending on the morphology of the aggregate the maximum deviation is not necessarily at 180°.

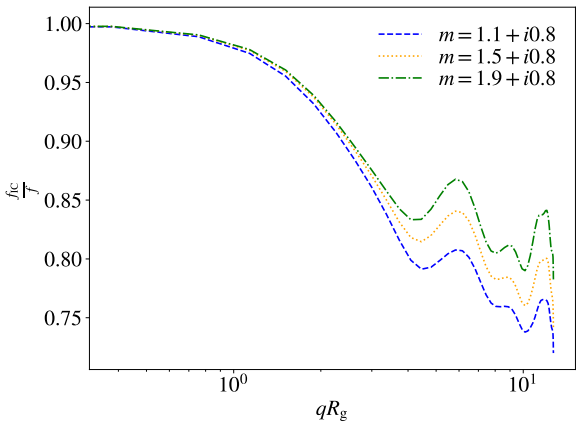

Figure 4: *Deviation of f_IC with respect to f for m=1.9+i0.8 (in green dash dot line), m=1.5+i0.8 (in orange dot line) and m=1.1+i0.8 (in blue dashed line).*

We also observe the role played by the imaginary part of the optical index. Indeed, the higher $Im\{m\}$ is, the more the deviation is important. In comparison, Fig. 4 shows the impact of the real part of the optical index ($m = 1.1 + i0.8$, $m = 1.5 + i0.8$ and $m = 1.9 + i0.8$).

It seems that the impact of the real part of the optical index is less important than the one induced by changing $Im\{m\}$ as the three curves are similar. From this observation, we conclude that $Im\{m\}$ have a predominant impact on the structure factor

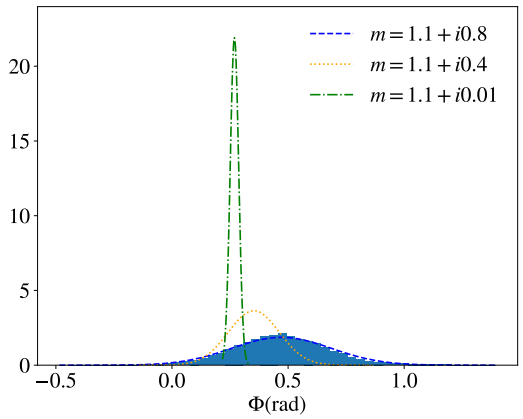

Figure 5: *Probability density of the phase of the phasors for a fixed orientation of the aggregate for m=1.1+i0.01 (in green dash dot line), m=1.1+i0.4 (in orange dot line) and m=1.1+i0.8 (in blue dashed line).*

4.2 Physical interpretation

According to Eq.(3) f_r and f_i are driven by the phasor amplitude Λ and its phase Φ. Fig. 5 reports the probability density of the phasors's phase Φ for a fixed orientation of the aggregate.

Indeed, this figure highlights an increase of the phase dispersion when $Im\{m\}$ is increased. Therefore, the more the phase dispersion is important the more $cos(\Phi_i - \Phi_j)$ will be weak, and inversely, the more $sin(\Phi_i - \Phi_j)$ will increase.

This explains the relative deviations of f_r and f_i. Absorbing materials favor internal trapping which increases the phase shift as the light propagates through the particle [3]. This provokes a dispersion of the phase at the origin of the deviation of the structure factor to the purely morphologically predicted one.

Similarly, Fig. 6 shows the probability density of the phasor amplitudes. It can be seen that the product $\Lambda_i\Lambda_j$ will decrease with $Im\{m\}$ as the average of Λ decreases due to absorption phenomena. As the amplitude decreases and the phase shift increases f_r will weaken with $Im\{m\}$, whereas f_i will increase. Nevertheless, as f_i varies in $sin(\Phi_i - \Phi_j)$ we can possibly encounter a case where the phase dispersion grows faster than the amplitude decreases, therefore, in such case f_i will not be necessary higher with $Im\{m\}$.

Without phase dispersion, f_i would be equal to zero whatever the amplitude value is and f_r will almost overlap with f. Therefore, we can imagine cases where the indices created strong local amplitudes of the internal electric field, called "hot spots" without causing important trapping (decrease in amplitude and increase in phase along the direction of light propagation). In that case, forward scattering would be moderately affected but structure factor. Still, strongly absorbing material will promote internal trapping which alter significantly the structure factor, especially at large scattering angles.

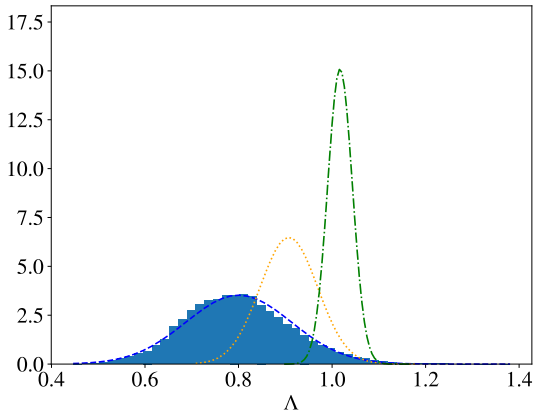

Figure 6: *Probability density of the amplitude of the phasors for a fixed orientation of the aggregate for m=1.1+i0.01 (in green dash dot line), m=1.1+i0.4 (in orange dot line) and m=1.1+i0.8 (in blue dashed line).*

5 Perspectives

The phasor analysis of the structure factor enables a decomposition of the structure factor into two distinct terms driven by the amplitude and phase dispersion of the internal electric field. This decomposition allows for the understanding of the impact of the internal multiple scattering on the angular light scattering pattern. This work has to be pursued in order to investigate the role played by fractal dimension and more complex morphologies (primary spheres polydispersion, overlapping, necking, coating…).

6 References

[1] Sorensen CM. Light scattering by fractal aggregates: a review. Aerosol Science and Technology 2001;35(2):648-87.

[2] Yon J, Liu F, Bescond A, Caumont-Prim C, Rozé C, Ouf F-X. Effects of multiple scattering on radiative properties of soot fractal aggregates. Journal of Quantitative Spectroscopy and Radiative Transfer. 2014;133:374-81.

[3] Argentin C, Berg MJ, Mazur M, Ceolato C, Poux A, Yon J. A semi-empirical correction for the Rayleigh-Debye-Gans approximation for fractal aggregates based on phasor analysis: Application to soot particles. Journal of Quantitative Spectroscopy and Radiative Transfer. 2022;283:108143.

[4] Berg MJ. Power-law patterns in electromagnetic scattering: A selected review and recent progress. Journal of Quantitative Spectroscopy and Radiative Transfer. 2012;113(18):2292-309.

[5] Ceolato R, Berg M.J. Aerosol light extinction and backscattering: A review with a lidar paerspective. Journal of Quantitative Spectroscopy and Radiative Transfer. 2021;262:107492.

13th International Conference Series on
Laser-light and Interactions with Particles
Optical Particle Characterization follow-up !
August 21-26th, 2022, Warsaw, Poland

MODELING ATMOSPHERIC DUST PARTICLE OPTICAL PROPERTIES USING IRREGULAR TRIANGULAR BIPYRAMID PARTICLES

Nancy OKEUDO[1,*], Jiachen DING[1], Ping YANG[1-3] and R. SARAVANAN[1-2]

[1] Department of Atmospheric Sciences, Texas A&M University, College Station, TX, 77843, USA
[2] Department of Oceanography, Texas A&M University, College Station, TX, 77843, USA
[3] Department of Physics and Astronomy, Texas A&M University, College Station, TX, 77843, USA

Corresponding author: nnokeudo@tamu.edu

Abstract

Dust particles are a major type of aerosol in the Earth's atmosphere. Accurate modelling of dust particle optical properties can reduce the uncertainties in inferring dust particle radiative and microphysical properties from remote sensing observations. It is critical to use suitable nonspherical shapes to represent all dust particles. In this study, we introduce a possible surrogate dust shape called the first-generation fractal triangular bipyramid. In particular, we compare the optical properties of the first-generation fractal triangular bipyramid ensemble with those based on the original triangular bipyramid ensemble.

1 Introduction

We calculate the single-scattering properties of the original triangular bipyramid shaped dust ensemble displayed in Figure. 1.

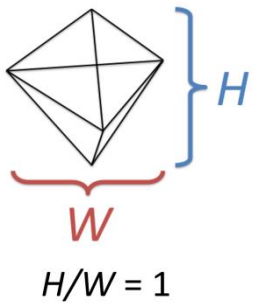

Figure 1 *The original triangular bipyramid – shaped dust particle with an aspect ratio of 1.*

The motiviation of the present simulation is to explore if the original triangular bipyramid-shaped dust particle is a possible surrogate for dust particles in the atmosphere.

1.1 Methodology

In this study, we used a combination of the invariant imbedding T-matrix method (IITM) for small–sized particles and the physical geometric optics method (PGOM) for moderate to large-sized particles. A previous study has shown that a combination of IITM and PGOM is useful in calculating the optical properties of nonspherical particles [1]. Then, we compare our results with laboratory measurements obtained by the Granada-Amsterdam Light Scattering Database, sphere ensemble, and prolate spheroid ensemble with an aspect ratio of 1.7.

1.2 Experimental Setup

For our preliminary study, we are interested in computing the phase matrix elements $\mathbf{P_{11}}$, $-\mathbf{P_{12}/P_{11}}$ and $\mathbf{P_{22}/P_{11}}$. Note that $\mathbf{P_{11}}$, and $-\mathbf{P_{12}/P_{11}}$ describe the angular variations of the scattered intensity and the degree of linear polarization, whereas $\mathbf{P_{22}/P_{11}}$ is an indicator of degree of particle nonsphericity. Another note to consider is the accuracy of the degree of linear polarization and scattered intensity is very important in radiative transfer simulations. We will use Feldspar measurement data as our reference. Feldspar measurement data has the following parameters listed in Table. 1.

Refractive Index*	$1.5 + 0.001i$
Wavelength	0.6328 microns
Effective Particle Size	1.0 microns
Variance	1.0
Particle Size Range	0.075858 – 12.882 microns

Table 1 *Feldspar size distribution information from the Granada-Amsterdam Light Scattering Database*

Note that the refractive index is based on the optimal value, not reference values because the reference values does not consider spectral dependence [3]. The size distribution is assumed to be the lognormal distribution based on [4]. The particle size parameter of the measurements, diamond, spheroid, and sphere ensembles is determined based on the equivalent projected-area sphere. Note that, for the Feldspar measurement data, we do not know the scattered intensity in the near forward and backward scattering directions. As a result, we must calculate the relative phase matrix element $\mathbf{P_{11}/P_{11}}(30°)$ instead of $\mathbf{P_{11}}$.

2 Preliminary Results and Discussions

Based on Figure. 2, the original triangular bipyramid denoted as diamond ensemble and spheroid ensembles are more accurate than spheres in capturing the features of $\mathbf{P_{11}/P_{11}}(30°)$, $-\mathbf{P_{12}/P_{11}}$, and $\mathbf{P_{22}/P_{11}}$. In particular, the backscattering direction of the sphere ensemble. Compared

to the sphere and spheroid ensembles, the original triangular bipyramid ensemble in the side scattering direction best estimates the degree of linear polarization. As for $\mathbf{P_{22}/P_{11}}$, the spheroid and triangular bipyramid ensemble and measurements have the same pattern even though they overestimate $\mathbf{P_{22}/P_{11}}$. This indicates that the sphericity index might be higher than measurements.

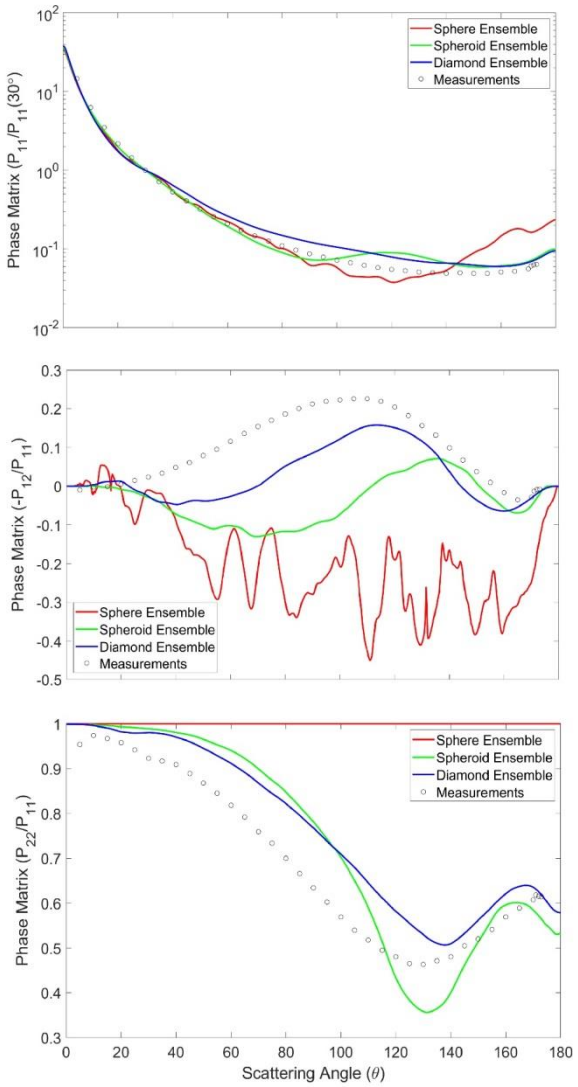

Figure 2 *This figure illustrates* $\mathbf{P_{11}/P_{11}}(30°)$, $\mathbf{-P_{12}/P_{11}}$, *and* $\mathbf{P_{22}/P_{11}}$ *phase matrix elements of the sphere, spheroid, original triangular bipyramid ensembles, and Feldspar measurements.*

Based on the preliminary results, we will consider modifying the original triangular bipyramid by adding in first generation fractals to make the triangular bipyramid shape more irregular using the technique described in [5]. Furthermore, we will test the modified triangular bipyramid shape with the fractals added to see if it will batter match the phase matrix elements of the measured data. Our hope is that the adding in first–generation fractal to the original triangular bipyramid shape will better match the measurement data.

3 Acknowledgements

The authors acknowledge the use of the Amsterdam-Granada Light Scattering Database for the measured data. We also like to thank the Texas A&M High Performance Computing Center for the carrying out the IITM and PGOM simulations. This research is funded by NASA (grant no. 80NSSC20K1608).

4 References

[1] Yang, P., Ding, J., Panetta, R. L., Liou, K. N., Kattawar, G. W., & Mishchenko, M. (2019). On the convergence of numerical computations for both exact and approximate solutions for electromagnetic scattering by nonspherical dielectric particles. Electromagnetic waves (Cambridge, Mass.), 164, 27.

[2] Jin, C., Liu, C., Yin, Y., Bi, L., & Nousiainen, T. (2016). Modeling the scattering phase matrix of red clays. Optics Letters, 41(21), 4879-4882.

[3] Saito, M., Yang, P., Ding, J., & Liu, X. (2021). A comprehensive database of the optical properties of irregular aerosol particles for radiative transfer simulations. Journal of the Atmospheric Sciences, 78(7), 2089-2111.

[4] Hansen, J. E., & Travis, L. D. (1974). Light scattering in planetary atmospheres. Space science reviews, 16(4), 527-610.

[5] Liu, C., Panetta, R. L., Yang, P., Macke, A., & Baran, A. J. (2013). Modeling the scattering properties of mineral aerosols using concave fractal polyhedra. Applied optics, 52(4), 640-652.

13th International Conference Series on
Laser-light and Interactions with Particles
Optical Particle Characterization follow-up !
August 21-26th, 2022, Warsaw, Poland

IMPROVING ICE CLOUD BACKSCATTERING AND DETERMINING AN OPTIMAL ICE PARTICLE OPTICAL PROPERTY DATABASE FOR LIDAR-BASED APPLICATIONS

James COY[1,*], Masanori SAITO[1], Jiachen DING[1], Ping YANG[1]

[1] Department of Atmospheric Sciences, Texas A&M University, College Station, Texas, United States
*Corresponding author: jcoy93@tamu.edu

Abstract

A new ice particle single-scattering database based on a Two Habit Model (THM) is developed to accurately retrieve ice cloud properties using lidar-based radiative transfer simulations. For moderate and large particle sizes, the approximate computational method known as the Improved Geometric Optics Method (IGOM) is used. A more accurate (particularly for backscattering computation) method known as the Physical Geometric Optics Method (PGOM) is used to calculate the phase matrix in backscattering directions. The backscattering properties of the single-scattering database are paramount for the accurate retrieval of ice cloud properties using lidar-based methods. Lidar ratio (LR) values are calculated using the bulk properties of the database. The integrated attenuated backscatter (IAB) values are calculated analytically from the LRs and various ice cloud optical thicknesses (ICOTs) that represent theoretical ice clouds. The calculated LRs and IABs of the new THM and a previous THM are compared to Cloud-Aerosol Lidar with Orthogonal Polarization (CALIOP) LRs and IABs and CloudSat ice cloud optical depths (ICOTs). The results show that the LR and IAB values of the new THM database are significantly more consistent with observational data due to the PGOM-enhanced phase function backscattering which will lead to more accurate lidar-based retrievals if the new database is used. In addition, a smooth, hexagonal column is added to the new THM as a fraction of the "simple" habit to further improve consistency with the CALIOP data.

1 Introduction

Ice clouds cover about 20% of the Earth and thus influence both the climate system radiation budget and large-scale atmospheric circulations [1,2,3]. Ice clouds, however, are also the one of the least understood atmospheric parameters in remote sensing and radiative transfer calculations due to uncertainties in their microphysical and optical properties such as ice particle effective radius (R_{eff}s) and ice cloud optical thickness (ICOT). Accurate estimation of R_{eff} and ICOT are important in understanding of the radiative effects that ice clouds have on the atmosphere [4,5] as they could even switch between having a net cooling or warming radiative effect on the atmosphere [2]. These properties can even be used to infer other microphysical and optical properties. For example, the product of R_{eff} and ICOT is proportional to the ice water path (IWP).

Observations from remote sensing satellites are commonly used to infer ice cloud properties. Active-sensor, lidar observations provide ample information for retrieving ice cloud microphysical and optical properties [6,7]. Lidar signals for cloudy scenes are determined by the bulk backscattering properties of cloud particles. Commonly used lidar measurements are the lidar ratio (LR) and integrated attenuated backscatter (IAB). LR is physically defined as the ratio of the volume extinction coefficient to the volume backscatter coefficient, and is inversely proportional to the ice particle bulk phase function 180° backscattering direction. IAB is the integration of backscattered light after attenuation through a cloud layer, and is inversely proportional to LR. IAB is also closely related to ICOT which allows for the derivation of ICOT from IAB measurements [7,8] if the ice cloud is optically thin (ICOT < 4).

Since the LR is dependent on the 180° backscattering phase function of the ice particles comprising the ice clouds, developing an accurate ice particle optical property database is paramount in retrieving accurate ice cloud properties from lidar-based radiative transfer simulators. Ice particle optical property databases help to describe the microphysical and optical properties of ice clouds. Currently, most ice particle optical property databases are developed using the Invariant Imbedding T-Matrix Method (IITM) and/or IGOM [3,5,9]. The IITM is an exact method primarily used for small size parameters [10,11] and IGOM is an approximate method used for moderate and large size parameters [12,13]. Despite IGOM being a fairly accurate numerical method and computationally efficient, it has been shown to underestimate phase function backscattering [14] which is critical for accurate lidar-based retrievals of ice cloud properties. A more sophisticated geometric optics method known as the PGOM has been developed that provides accurate backscattering calculations [15]. Ice particle optical property databases comprised of backscattering calculations from PGOM can significantly improve active lidar-based retrievals.

2 Methodology

2.1 The Lidar Two Habit Model

The newly-developed ice particle optical property database used for this study is known as a THM. It is based on the concept that atmospheric ice particles can be

separated into two categories in terms of geometrical complexity (i.e., simple and complex) that are dependent on particle size [16]. The simple particle geometry dominates small particle sizes and as the size increases, the complex geometry eventually becomes the dominate habit.

***Figure** 1 The THM-new habit fraction distribution diagram*

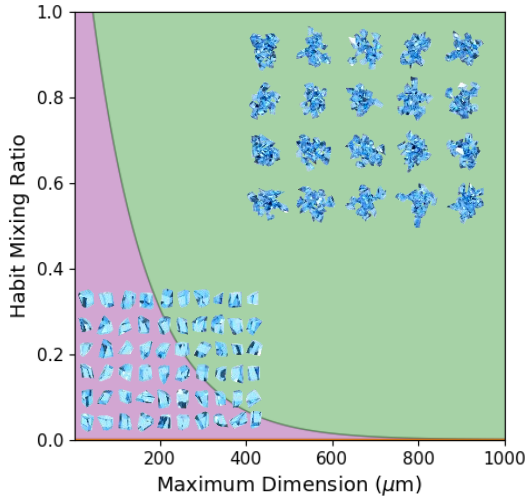

show two ensembles of different ice crystals and their mixing ratios. The 60-particle ensemble in the purple region irregularly-shaped single columns and the 20-particle ensemble in the green-shaded region are irregularly-shaped 20-column aggregates. The maxing ratios of the two habits add up to one.

$$f_{single} = \begin{cases} e^{-0.0076\left(D_{max}-45\right)} & D_{max} \geq 45\mu m \\ 1 & D_{max} < 45\mu m \end{cases} \quad (1)$$

$$f_{aggregate} = 1 - f_{single} \quad (2)$$

The THM used for this study (THM-new) is shown in Fig. (1) and the equations describing the habit fractions are shown in Eqs. (1) and (2). THM-new contains the three lidar wavelengths of 355, 532, and 1064nm, and 189 maximum dimension (D_{max}) size bins ranging from 2.206 – 11031.337μm. In addition to using IITM and IGOM calculations to develop the database, PGOM is used for moderate and large size parameters ($kD > 35$) to obtain more accurate backscattering. The PGOM scattering phase matrix calculations in the backscattering region are merged with IGOM's using a continuous weighting function that transitions the IGOM-based calculations to the PGOM calculations from 160° to 170° scattering angles. This THM is considered to be an update to the THM (THM-prev) that is composed of a roughened hexagonal column and 20-particle irregularly-shaped 20-column aggregates and only have IITM and IGOM calculations [5].

2.2 Lidar Ratio and Integrated Attenuated Backscatter

The LR us in unit of steradians (sr) and is defined as the ratio of the volume extinction coefficient to the volume backscatter coefficient. LR (S) can be given in terms of the backscatter phase function value defined as:

$$S = \frac{4\pi}{P_{11}(180^\circ)\,\tilde{\omega}} \quad (3)$$

where $P_{11}(180°)$ is the phase function in the 180° backscattering direction and $\tilde{\omega}$ is the single-scattering albedo. Ice particles are non-absorbing at 355, 532, and 1064nm wavelengths and thus have $\tilde{\omega}$ nearly equal to 1. Eq. (3) can be simplified to being inversely proportional to the normalized phase function in the 180° backscattering direction.

IAB is defined [6] as:

$$IAB = \frac{1 - e^{-2\eta\tau}}{2\eta S} \quad (4)$$

Where S is the LR, τ is the ICOT, and η is the multiple scattering coefficient. η is implicitly assumed to be independent of optical thickness for a uniform particle size distribution in ice clouds [6] and has a value of 0.7. Eq. (4) demonstrates than an IAB-ICOT relationship exists and that LR, Eq. (2), is inversely proportional to IAB. Based on Eq. (4), IAB becomes asymptotic and approaches a constant value of $1/2\eta S$ when optical thickness is large. This means that IABs derived from lidar observations are sensitive to optically thin clouds. For this study, ICOT values less than 4 are considered for the analytical calculations using THM-new and THM-prev as well as the observational data.

2.3 Satellite Data

For this study, the CALIOP Level-2 5km Cloud Layer Product [17] and the CloudSat 1 km ancillary Collection 6 Moderate Resolution Imaging Spectroradiometer (MODIS) cloud property product (MOD06-AUX) [18] from the year 2009 are collocated to compare observed IAB and ICOT with the analytical results. The CALIOP product is also used to compare observed LR with those inferred from the bulk scattering properties of the new lidar database.

The associated parameters used to find collocated thin ice clouds include time, latitude and longitude from both products, number of cloud layers and feature classification flags from the CALIOP lidar product. During 2009, both the Cloud-Aerosol Lidar and Infrared Pathfinder Satellite Observations (CALIPSO) carrying the CALIOP sensor, and CloudSat satellites orbit the same orbital plane along with 3 other satellites known as the A-train. CloudSat leads CALIPSO by about 15 seconds and thus feasible to collocate the data of both products. As the products are in different resolutions, the nearest-neighbour estimation method is used to collocate ice cloud cases of CALIOP 5km pixels with those of CloudSat 1km pixels.

The CALIOP Cloud Layer product provides cloud mid-layer temperature as well as LR and IAB at 532 nm. MOD06-AUX provides ICOT from a MODIS two-channel retrieval method using band 7 (2.1 μm) and either band 1 (0.65 μm), 2 (0.86 μm), or 5 (1.2 μm). To ensure that the highest quality of the collocated data is obtained, CALIOP pixels that have a single layer, transparent ice cloud classification with a

mid-layer temperature of -40°C are considered for this study. From the MOD06-AUX product, MODIS-retrieved ICOTs are limited to be less than 4 since IAB is expected to reach an asymptotic, maximum value beyond this value.

3 Preliminary Results

3.1 Phase Function Backscattering and Lidar Ratio

Incorporating PGOM backscattering calculations to existing IGOM calculations of the scattering phase matrix of THM-new is shown to have significant differences from THM-prev. Fig. (2) shows that the THM-new 532nm phase function (P11) in the backscattering region now has a pronounced peak at 180° scattering angle for both small and moderate particle sizes.

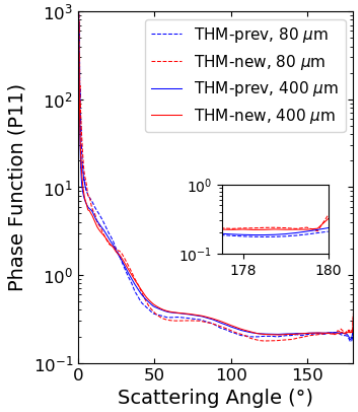

Figure 2 *532nm wavelength P11 of the THM-prev (blue) and THM-new (red) databases at D_{max}s of 80 (dashed) and 400μm (solid). The backscattering region (177.5° - 180°) is enhanced to show differences between the databases and particle sizes.*

The LR values calculated using the bulk P11 values at the 180° scattering angle for THM-prev and THM-new are shown in Fig. (3). At wavelengths 355 and 532 nm, the LRs for THM-new are significantly less than those of THM-prev throughout the effective radii range. Since Eq. (3) shows the P11 value at 180° scattering angle being inversely proportional to LR, the higher P11 backscattering values of THM-new due to the PGOM calculations correspond to lower LRs. For 1064nm, the LRs of THM-new are only slightly less than the LRs of THM-prev. This is due to 1064nm belonging to the near-infrared regime where backscattering is dampened.

Figure 3 *LR values of THM-prev (blue) and THM-new (red) with respect to effective radii from 2 to 320μm for 355 (dashed), 532 (solid), and 1064 nm (dotted) wavelengths.*

3.2 Integrated Attenuated Backscatter and Ice Cloud Optical Thickness Relationship

The calculated 532nm LRs at specified R_{eff}s of the THM-new and THM-prev databases are used to calculate their corresponding IABs over a range of ICOTs. The analytical IAB-ICOT relationship is plotted over a 2-dminsional frequency distribution of collocated CALIOP IAB/CloudSat ICOT data shown in Fig. (4). The THM-new IAB-ICOT relationship for all chosen R_{eff}s are significantly more

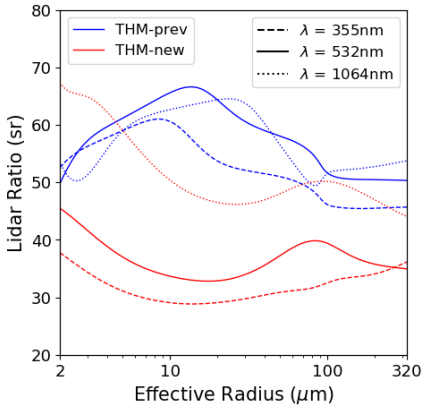

consistent to the collocated observational data than THM-prev, especially for ICOTs from 0.25 to 1. Unfortunately, THM-new appears to still slightly underestimate IAB for optically thicker ice clouds (ICOT > 1). This improvement in IAB-ICOT relationship consistency between the analytical and observational data will likely lead to improved lidar-based retrievals when using the THM-new database.

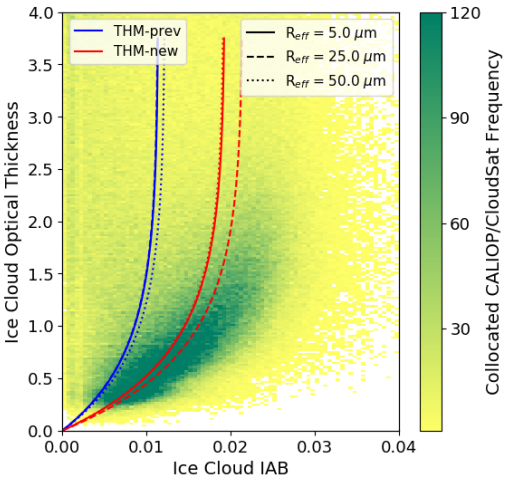

Figure 4 *Comparison of ice cloud IAB-ICOT relationship of analytical calculations using THM-prev (blue) and THM-new (red) and collocated CALIOP/CloudSat 2009 data frequency. The analytical IAB-ICOT relationships have effective radii of 5 (solid), 25 (dashed), and 50μm (dotted).*

3.3 Adding Smooth Hexagonal Column to the New Database

As a preliminary test, another version of the new THM is developed with the inclusion of 8% smooth hexagonal column single-scattering properties in the "simple" particle habit (THM-hex). Fig. (5) shows that the inclusion of a smooth hexagonal column, even a small habit fraction, noticeably further decreases the LRs of the THM for all three wavelengths. The decrease in LRs is concentrated between

the R_{eff} range of 10 to 200μm. Since IAB is inversely proportional to LR, THM-hex is expected to have higher IABs than THM-new and will likely lead to further improved consistency with the collocated observational data. Further analyses will be done to determine the optimal smooth hexagonal column habit fraction to be included in the new THM.

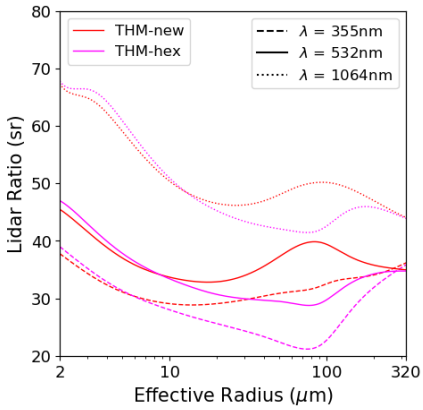

Figure 5 *LR values of THM-new (red) and THM-hex (purple) with respect to effective radii from 2 to 320μm for 355 (dashed), 532 (solid), and 1064 nm (dotted) wavelengths.*

4 References

[1] Liou K. N., Influence of cirrus clouds on weather and climate processes: a global perspective, Monthly Weather Review, 114(6):1167-1199 (1986).

[2] Stephens G. L., Tsay S. C., Stackhouse P. W., and Flatau P. J., The relevance of the microphysical and radiative properties of cirrus clouds to climate and climatic feedback, Journal of Atmospheric Sciences., 47(14):1742-1754 (1990).

[3] Liu C., Yang P., Minnis P., Loeb N., Kato S., Heymsfield A., and Schmitt C., A two-habit model for the microphysical and optical properties of ice clouds, Atmospheric Chemistry and Physics., 14:13719-13737 (2014).

[4] K. N. Liou and P. Yang, Light Scattering by Ice Crystals: Fundamentals and Applications (Cambridge University Press, Cambridge, United Kingdom, 2016).

[5] Loeb N. G., Yang P., Rose F. G., Hong G., Sun-Mack S., Minnis P., Kato S., Ham S., Smith W. L., Hioki S., and Tang G., Impact of ice cloud microphysics on satellite cloud retrievals and broadband flux radiative transfer model calculations, Journal of Climate, 31:1851-1864 (2018).

[6] Platt C. M. R., Lidar and radiometric observations of cirrus clouds, Journal of Atmospheric Sciences., 30(6):1191-1204 (1973).

[7] Seifart P., Ansmann A., Muller D., Wandinger U., Althausen D., Heymsfield A. J., Massie S. T., and Schmitt C., Cirrus optical properties observed with lidar, radiosonde, and satellite over the tropical Indian Ocean during the aerosol-polluted northeast and clean maritime southwest monsoon, Journal of Geophysical Research: Atmospheres, 112(D17):D17205 (2007).

[8] Ding J., Yang P., Holz R. E., Platnick S., Meyer K. G., Vaughan M. A., Hu Y., and King M. D., Ice cloud backscatter study and comparison with CALIPSO and MODIS satellite data, Optics Express, 24(1):620-636 (2016).

[9] Yang P., Bei L., Baum B. A., Liou K. N., Kattawar G. W., Mishchenko M. I., and Cole B., Spectrally consistent scattering, absorption, and polarization properties of atmospheric ice crystals at wavelengths from 0.2 to 100 μm, Journal of Atmospheric Sciences, 70:330-347 (2013).

[10] Johnson B. R., Invariant imbedding T matrix approach to electromagnetic scattering, Applied Optics, 27(23):4861-4873 (1988).

[11] Yang P., Ding J., Panetta R. L., Liou K. N., Kattawar G., and Mishchenko M. I., On the convergence of numerical computations for both exact and approximate solutions for electromagnetic scattering by nonspherical dielectric particles, Progress in Electromagnetics Research, 164:27-61 (2019).

[12] Cai Q. and Liou K. N., Polarized light scattering by hexagonal ice crystals: theory, Applied Optics, 21:3589-3580 (1982).

[13] Takano Y and Liou K. N., Solar radiative transfer in cirrus clouds. Part I: Single-scattering and optical properties of hexagonal ice crystals, Journal Atmospheric Sciences, 46:3-19 (1989).

[14] Saito M., Iwabuchi H., Yang P., Tang G., King M. D., and Sekiguchi M., Ice particle morphology and microphysical properties of cirrus clouds inferred from combined CALIOP-IIR measurements, Journal of Geophysical Research: Atmospheres, 122:4440-4462 (2017).

[15] Yang P. and Liou K. N., Geometric-optics-integral-equation method for light scattering by non-spherical particles, Applied Optics, 35:6568-6584 (1996).

[16] Schmitt C. G. and Heymsfield A. J., Observational quantification of the separation of simple and complex atmospheric ice particles, Geophysical Research Letter., 41:1301-1307 (2014).

[17] Vaughan M. A., Young S. A., Winker D. M., Powell K. A., Omar A. H., Liu Z., Hu Y., and Hostetler C. A., Fully automated analysis of space-based lidar data: an overview of the CALIPSO retrieval algorithms and data products, Laser Radar Techniques for Atmospheric Sensing, 5575 (2004).

[18] H. Cronk and P. Partain, CloudSat MOD06-AUX auxiliary data process description and interface control document (National Aeronautics and Space Administration Earth System Science Pathfinder Mission, 2018)

BIOMEDIA

13th International Conference Series on
Laser-light and Interactions with Particles
Optical Particle Characterization follow-up !
August 21-26th, 2022, Warsaw, Poland

HIGH THROUGHPUT LIGHT SCATTER IMAGING OF MICROPARTICLES IN FLOW CYTOMETRY

Jonas GIENGER*, Christian GOERKE, Alexander HOPPE, Alexander PUTZ, Dirk GROSENICK, Martin HUSSELS

Physikalisch-Technische Bundesanstalt (PTB), Abbestr. 2-12, 10587 Berlin, Germany

**Corresponding author: jonas.gienger@ptb.de*

Abstract

We equipped a flow cytometer with two low-cost industrial CMOS cameras to image the scattered intensity distributions of single microparticles and cells at throughputs of several hundred events per second. These images are compared to the far-field scattered intensity distributions computed with various computational methods, which yields information about particle size, shape and orientation in the fluid flow.

1 Introduction

In a flow cytometer, microscopic objects of interest (e. g., biological cells or artificial micro- and nanoparticles) pass through a laser focus one by one in a fluid flow. In most standard devices the scattered light is collected with detectors in the forward and sideward directions, without any angular resolution. Depending on the device, the objects flow at velocities of a few metres per second and throughput may exceed 10,000 events/s. This means that interaction times with the laser are in the microsecond range. Fluorescent labelling is often used for the differentiation of cells on a biomolecular basis.

Imaging flow cytometry combines the high information content of microscopic images with the high throughput of flow cytometry. This can be particularly useful in applications where very small populations of target cells must be identified and quantified within huge numbers of other cells, coincidences and agglomerates. Minor errors in counting those populations can have a major impact on the diagnosis. As differentiation between single cells, coincidences, and cell agglomerates is challenging for common flow cytometers, we developed a flow cytometer with integrated multi-dimensional imaging.

Our instrument combines the high signal detection rates of photomultiplier tubes (PMTs) with the ability to capture images of particles or cells of interest. Here we present data for differently shaped polystyrene and silica particles in the forward direction. Compared with light scattering simulations, this reveals the potential of the comprehensive analysis of agglomerates and coincidences by imaging for improving particle or cell counting accuracy and for label-free differentiation.

2 Experiment

A schematic of the measurement setup is shown in Figure 1. We operate a continuous wave laser at 488 nm and a gated laser at 406 nm focused into the flow cell with a small offset along the flow direction. Images are captured by two low-cost industrial CMOS cameras (no side scatter images are shown in this extended abstract). Triggering of the cameras and gating of the 406 nm laser emission are

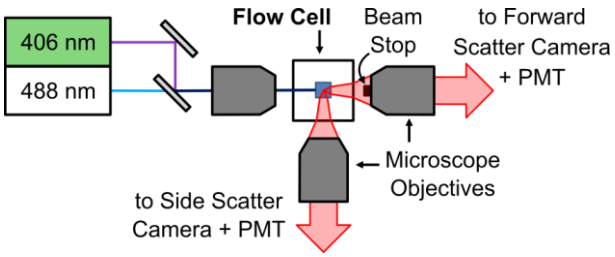

Figure 1 *Cytometer flow cell with lasers and objectives. The flow direction is into the image plane.*

controlled by an FPGA. As the same FPGA processes all data of the PMTs, this enables to set camera trigger conditions for each conventional detector channel of the setup.

When an object passes the 488 nm laser focus, the data of the PMTs is analysed by the FPGA and compared to the trigger conditions. In case all conditions are fulfilled, the cameras are triggered instantaneously, and the laser gate is shortly opened when the object will be in the focus of the 406 nm laser. This results in a short laser flash (0.1 µs to 1 µs) on the object being much shorter than the minimum exposure time (>59 µs) of the cameras to prevent motion blur. This way, we can benefit from low-cost industrial cameras to capture sharp images at high flow velocities (~2 m/s). Currently, we can set a trigger window for each PMT detector channel, but more complex trigger conditions are possible.

3 Simulations

To aid the interpretation of the scattered light intensity distributions, we perform light scattering simulations for different classes of particle shapes. Lorenz-Mie Theory (LMT) can be used for single spherical particles. For

coincidences of two (or more) spherical particles passing the laser simultaneously, we use the T-matrix method, specifically the multiple sphere T-matrix (MSTM) code [1]. For general aspherical particles we use the discrete dipole approximation (DDA) framework and employ the ADDA code [2].

Using the amplitude scattering matrices or Mueller matrices from these numerical simulations we can compute far-field intensity distributions $I(\theta,\phi)$ over the angles in the medium inside the flow cell (here water) for a given laser polarization (along the flow direction). The images in the experiment are recorded with a microscope objective and subsequent additional optics outside of the flow cell and surrounded by air (see Figure 1). To compare the simulated patterns with measured ones, we need to take into account the refraction of light rays at the interfaces of the flow cell (water-quartz and quartz-air) to find the mapping $\rho = g(\theta)$ from angles inside to flow cell to positions in the forward principal plane of the microscope objective. For the forward scatter direction this would be $\rho = z\tan\theta$ with $z = f$(focal length of the objective) in the absence of interfaces. With two plane-parallel interfaces, a relation $\rho = g(\theta)$ can be found based on Snell's law and basic geometry. To display the simulated intensity pattern like the measured images, this mapping needs to be applied and the far-field intensity values $I(\theta,\phi)$ then need to be scaled according to the element of area of the mapping g according to conservation of energy/power. This accounts for oblique incidence and yields

$$\tilde{I}(\rho,\phi) = I(\theta,\phi)\,\frac{\sin(\theta)}{g(\theta)}\,\frac{1}{g'(\theta)}. \qquad (1)$$

The inverse relation can be used to extract far-field intensity distributions $I(\theta,\phi)$ from the measured images $\tilde{I}(\rho,\phi)$.

4 Particles and Simulation Parameters

We show here results for particles made from a hybrid silica material with an estimated refractive index of 1.41 at 406nm. Figure 2 shows a microscope image of a "dumbbell" shaped particle (microparticles GmbH, Berlin. Germany)

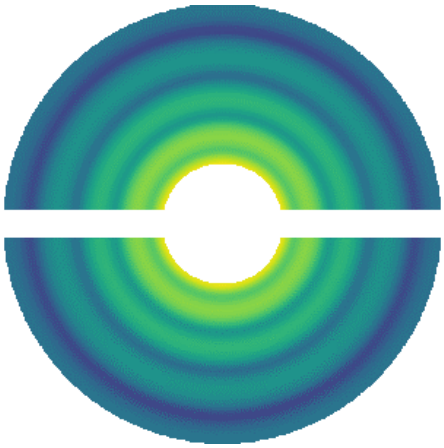

Figure 2 *Simulated forward scatter image for a single hybrid silica sphere.*

which consists of two fused spheres. For light scattering simulations these particles are modelled using the bi-sphere model in ADDA with a centre-to-centre distance smaller than the sphere diameter ($R_{cc}/d \approx 0.6$) to have the spheres overlapping in the centre of the particle and match the size of 5.7µm by 3.4µm as specified by the manufacturer.

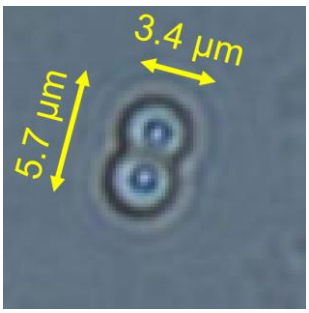

Figure 3 *Microscope image of a hybrid silica "dumbbell" particle.*

The spot size of the laser in the cytometer is sufficiently large compared to the particle size (>10µm along the narrow direction) such that we assume plane-wave illumination in all the simulations. The surrounding medium is pure water with an RI of 1.343 [3].

5 Results

Even though the particle suspension was manufactured to contain dumbbell-shaped particles, it also contains a significant percentage of single spheres. The measured scattering pattern from such a spherical particle is shown in Figure 3, which can be compared to the simulation result in Figure 4. Logarithmic intensity scales are used in all images

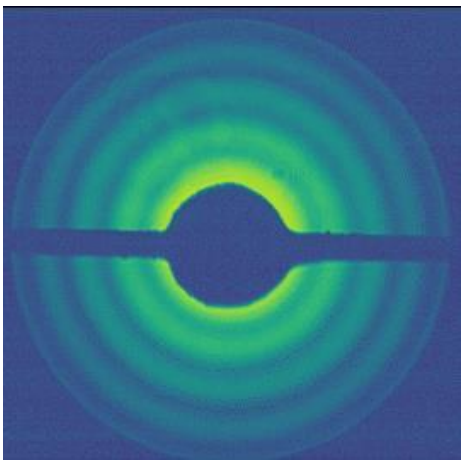

Figure 4 *Measured forward scatter image of a single hybrid silica sphere (presumably 3.4µm diameter) in water at 406nm wavelength. Logarithmic intensity scale.*

shown here. In the measurements, the direct laser beam is blocked before the microscope objective (see Figure 1) to avoid over-exposure of the camera. The beamstop has the shape of a circular disc on a strip (for mounting) and can be clearly seen as a dark region in the measurements. This area

was also removed in the simulated images. Figures 5 and 6 show measurement and simulation results for a dumbbell particle oriented along the flow direction (vertical axis in the images). In addition to the spherical pattern from a single sphere, horizontal stripes are visible, that correspond to the length of the particle.

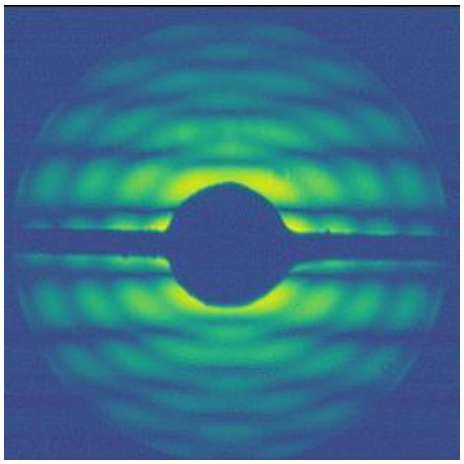

Figure 5 *Measured forward scatter image of a single hybrid silica dumbbell (3.4µm wide, 5.7µm long).*

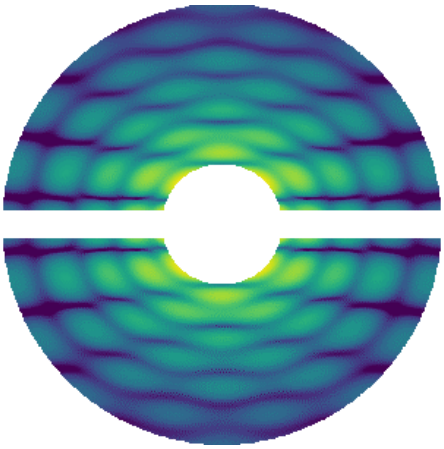

Figure 6 *Simulated forward scatter image for a single hybrid silica dumbbell.*

6 Conclusion

Our setup can capture images of the intensity distribution of the light scattered by single microparticles in flow at a high throughput. These can be compared to numerical simulations from various light-scattering frameworks for different particles. In this presentation we discuss how these data can be used to obtain information about the individual particles. For example, for spherical particles, fitting the parameters of the LMT (diameter and refractive index) can allow for accurate particle characterization. For non-spherical particles or coincidences/aggregates of spheres, the scattered intensity pattern carries information about shape and orientation in flow. Combining imaging in the forward and side directions is particularly useful in this case. The measurements can readily be extended to biological cells. This could, for example yield information about their deformation in flow or simply to distinguish coincidences. However, finding accurate simulation models might be more challenging for these more complex biological objects than for artificial particles.

7 References

[1] Mackowski D.W., Mishchenko M.I., A multiple sphere T-matrix Fortran code for use on parallel computer clusters, Journal of Quantitative Spectroscopy and Radiative Transfer, 112(13):2182–92 (2011)

[2] Yurkin M.A., Hoekstra A.G., The discrete-dipole-approximation code ADDA: Capabilities and known limitations, Journal of Quantitative Spectroscopy and Radiative Transfer, 112(13):2234–47 (2011)

[3] Daimon M., Masumura A., Measurement of the refractive index of distilled water from the near-infrared region to the ultraviolet region, Applied Optics 46(18):3811–20 (2007)

13th International Conference Series on
Laser-light and Interactions with Particles
Optical Particle Characterization follow-up !
August 21-26th, 2022, Warsaw, Poland

SCANNING DLS-OCT FLOW IMAGING

Konstantine CHEISHVILI[1,*] and Jeroen KALKMAN[1]

[1] Department of Imaging Physics, Delft University of Technology, Delft, 2628 CJ, The Netherlands

Corresponding author: k.cheishvili@tudelft.nl

Abstract

We show scanning dynamic light scattering optical coherence tomography (OCT) omnidirectional flow measurements. Our method improves the velocity measurement limit over conventional correlation-based or phase-resolved Doppler OCT by more than a factor of 2. Our technique is applicable without a-priori knowledge of the flow geometry as our method works both for non-zero Doppler angle and non-ideal scan alignment..

1 Introduction

Dynamic light scattering optical coherence tomography (DLS-OCT) relies on the measurement of fluctuations of scattered light and coherence gating to obtain simultaneous depth-resolved information about diffusive and translational motion of particles. This information is extracted from the temporal autocorrelation of the OCT signal for every voxel in depth. Initially, DLS-OCT was used for particle sizing [1] where the particle size is determined from the estimated diffusion coefficient using the Stokes-Einstein relation.

Flow measurements with OCT have been performed using phase-resolved Doppler OCT, lateral resonant Doppler OCT [2], and M-scan correlation-based DLS-OCT [3,4,5]. The axial velocity of Doppler OCT is limited by phase wrapping. In the correlation-based measurements, the maximum transverse velocity is limited by the decorrelation rate, which depends on the spatial resolution of the system [6]. The axial velocity range is limited by interference fringe washout [7] and the coherence length of the source. When measuring the diffusion of particles under flow, the decorrelation in the flow causes uncertainty in the estimated diffusion coefficient [8], which, in case of high flows, cannot be measured at all.

In this work we apply beam scanning in DLS-OCT to improve the maximum measurable velocity limit for omnidirectional flows. We extend the existing theoretical models [3,9] for the OCT signal autocorrelation and incorporate the motion of the beam into it. We show that when scanning the OCT beam in the direction of the flow, the dynamic velocity range is significantly increased. We demonstrate that the B-scan correlation-based DLS-OCT method is capable of measuring a far higher range of velocities then standard Doppler OCT, lateral resonant Doppler OCT [2] or conventional correlation analysis (M-scan) with stationary beam.

2 Methods

Flow was generated inside the rectangular flow cell by a syringe pump. We used Intralipid with dilution 1:40 as scattering medium. The experiments were performed using a Thorlabs GANYMEDE II HR series spectral domain OCT System, with a bandwidth centered around 900 nm with an axial resolution of 3 μm in air. The OCT system was operated both in M-scan and B-scan modes. For scanning the beam along any arbitrary flow direction, lateral and axial scanning schemes were implemented. Fig. (1) shows the experimental geometry with the flow and OCT beam motion. Lateral beam scanning (B-scan), perpendicular to the beam direction, is executed by moving galvo mirrors. Axial scanning is performed numerically. Since DLS-OCT provides simultaneous information for all depths, it is possible to numerically align the beam scan vector along any arbitrary direction in 3D using a spatial shift of the OCT signal in the depth domain obtained after the inverse Fourier transformation of the spectrum, or, equivalently, by using a phase multiplication in the frequency domain before the inverse Fourier transform. Fig. (2) shows a typical B-scan flow cell image at a nonzero tilt angle before and after the numerical alignment.

3 Results

We performed experiments at three different flow cell tilt angles and at ten different pump discharge rates. Fig. (3-4) show the comparison of results obtained using the conventional and our method for a tilt angle of 0.94 degrees. Parabolic dashed curves represent the theoretical velocity profiles based on the pump discharge rate. Results that significantly deviate from the expected values are omitted in the plot. Horizontal dashed lines show the maximum velocities that can be measured using every method. Only the suggested B-scan correlation analysis method is capable of correctly measuring depth-resolved velocities up to 250 mm/s. Clearly, with the B-scan method demonstrated here we can measure much higher flows. We obtain similar results for other tilt angles, indicating that there is no explicit dependence of the method accuracy on the Doppler angle. Furthermore, we found that when performing multiple scans at different speeds, then no calibration measurement, a-priori flow knowledge or perfect scan alignment is required. This is demonstrated by scanning the beam at a non-zero in-plane angle with respect to the flow direction at five several different scan speeds, performing the numerical alignment, and obtaining the velocity profiles.

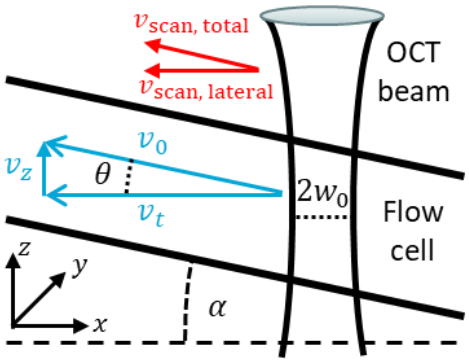

Figure 1 *– Flow geometry and OCT setup*

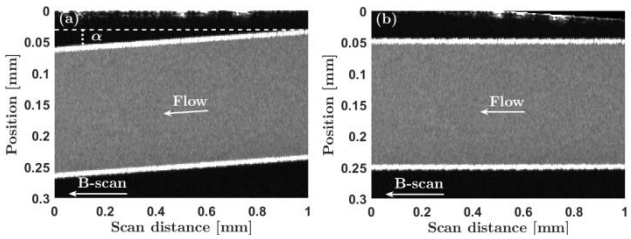

Figure 2 *– Original depth-resolved B-scan image (a) and numerically aligned OCT image (b)*

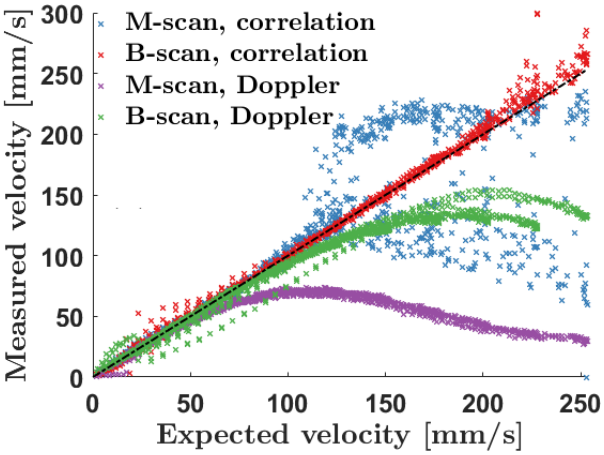

Figure 3 *– Measured versus expected flow velocities for all methods with tilt angle 0.94 degrees*

4 Conclusion

We have implemented the B-scan correlation-based DLS-OCT method for measuring omnidirectional flows. Our method extends the maximum measurable velocity limit by at least a factor of 2 compared to the standard M-scan DLS-OCT or Doppler OCT techniques. We have shown that our method can be applied to flow geometries where a proper scan alignment is not possible. In addition, we have demonstrated that the suggested method can be used to estimate a diffusion coefficient more accurately under flow conditions.

5 References

[1] J. Kalkman, R. Sprik, and T. G. van Leeuwen, Path-length-resolved diffusive particle dynamics in spectral-domain, Phys. Rev. Lett. 105 (2010)

[2] J. Walther and E. Koch, Flow Measurement by Lateral Resonant Doppler Optical Coherence Tomography in the Spectral Domain, Applied Sciences 7 (2017)

[3] N. Weiss, T. G. van Leeuwen and J. Kalkman, Localized measurement of longitudinal and transverse flow velocities in colloidal suspensions using optical coherence tomography, Physical Review E 88 (2013)

[4] J. Lee, W. Wu, J. Y. Jiang, B. Zhu and D. A. Boas, Dynamic light scattering optical coherence tomography, Optics Express 20 (2012)

[5] B. K. Huang and M. A. Choma, Resolving directional ambiguity in dynamic light scattering-based transverse motion velocimetry in optical coherence tomography, Optics Letters 39 (2014)

[6] X. Liu, Y. Huang, J. C. Ramella-Roman, S. A. Mathews and J. U. Kang, Quantitative transverse flow measurement using OCT speckle decorrelation analysis, Optics Letters 38 (2013)

[7] H. C. Hendargo, R. P. McNabb, A. Dhalla, N. Shepherd and J. A. Izatt, Doppler velocity detection limitations in spectrometer-based versus swept-source optical coherence tomography, Biomedical Optics Express 2 (2011)

[8] N. Weiss, T. G. van Leeuwen and J. Kalkman, Simultaneous and localized measurement of diffusion and flow using optical coherence tomography, Optics Express 23 (2015)

[9] N. Uribe-Patarroyo, M. Villiger and B. E. Bouma, Quantitative technique for robust and noise-tolerant speed measurements based on speckle decorrelation in optical coherence tomography, Optics Express 22 (2014)

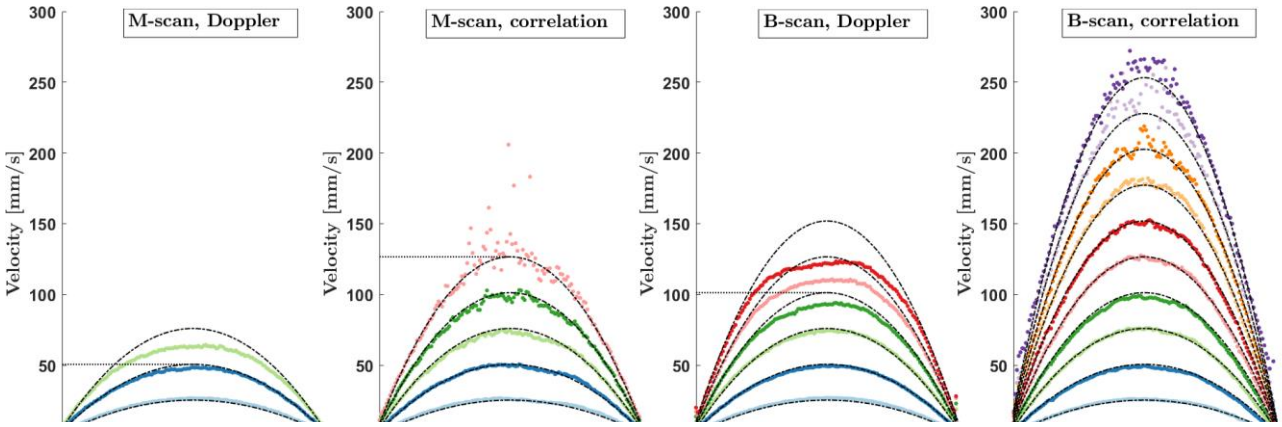

Figure 4 *– Flow profiles obtained using different OCT methods with tilt angle 0.94 degrees*

13th International Conference Series on
Laser-light and Interactions with Particles
Optical Particle Characterization follow-up !
August 21-26th, 2022, Warsaw, Poland

MODELLING OF ANGLE-RESOLVED NEAR-FORWARD LIGHT-SCATTER PULSES IN FLOW CYTOMETRY USING GENERALIZED LORENZ-MIE THEORY

Jonas GIENGER [1,*], Daniel KAGE [2], and Toralf KAISER [2]

[1] Physikalisch-Technische Bundesanstalt (PTB), Abbestraße 2–12, 10587 Berlin, Germany
[2] German Rheumatism Research Centre Berlin (DRFZ) – Flow Cytometry Core Facility, Charitéplatz 1 (Virchowweg 12), 10117 Berlin, Germany

Corresponding author: jonas.gienger@ptb.de

Abstract

Particles passing through a laser focus in a flow cytometer cause time-dependent angular intensity distributions of the scattered light which can be detected as signal pulses. If no beamstop is used, effects of interference of the incident beam and the scattered light near the forward direction. We present angle-resolved measurements of such pulses for polymer microparticles using an optical fibre array and compare with simulation results based on Generalized Lorenz-Mie Theory.

1 Introduction

In a flow cytometer, microscopic objects of interest (e. g., cells or bacteria) pass through a laser focus, scatter light and thus create time-dependent angular intensity distributions. Here we discuss a novel detection principle where (i) time-dependent signals are measured with (ii) an array of optical fibres instead of a single forward-scatter detector resulting in both, angular and temporal resolution of the scattered light. Extinction effects are observed in the pulses of near-forward fibres due to interference between the incident beam and the scattered light. This leads to a variety of non-trivial pulse shapes even for spherical particles ("beads"), which are used as "cell dummies". For cells, this additional information about their light scattering properties can allow for a classification without the need for fluorescent labelling. We discuss how this measurement principle can be mathematically modelled and simulated using Generalized Lorenz-Mie Theory (GLMT) for the scattering of off-axis elliptical Gaussian beams by spherical particles and compare the simulation results with measurement data for polystyrene beads.

2 Experiment

The measurement setup was recently presented in [1]. In short, a commercial flow cytometer was equipped with custom-made signal acquisition electronics, modified optics, and a fiber array to combine the angle- and time-resolved forward scatter detection. The cytometer features a 488 nm laser for light scattering measurements, which is shaped to an elliptical focus with aspect ratio 1:6 and then focused into the flow cell. The short axis of the ellipse is oriented along the flow direction (x direction). A schematic view is shown in Figure 1. The light coming from the flow

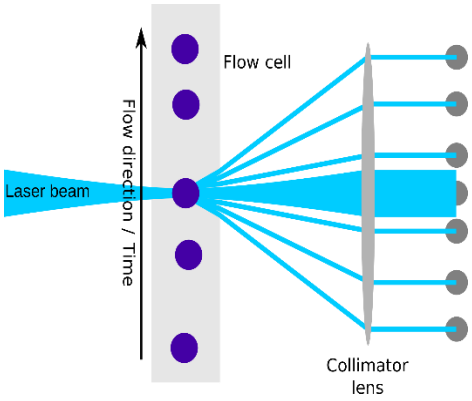

Figure 1 *Illustration of the flow-cytometric detection system discussed here (not to scale). Instead of a single detector, an array of optical fibres is positioned in the detection plane of the forward-scatter channel. The fibres collect light scattered by a single particle (dark blue disk) in different angles (indicated by the cyan rays).*

cell is collimated and detected using an array of fibers (Figure 2), connected to photomultiplier tubes. Most of the fibers only detect light when a particle passes the laser and scattering occurs. Several of the innermost fibers, however, are directly illuminated by the laser beam due to its finite divergence, such that their intensity can both increase or decrease when a particle passes.

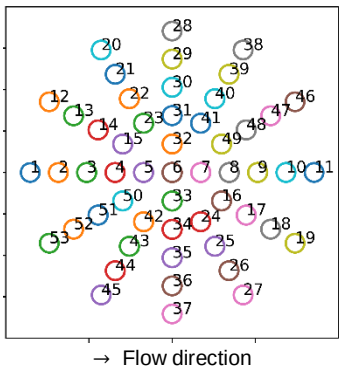

Figure 2 *Fibre layout and numbering. Note the flow direction.*

3 Theory

3.1 Elliptical Gaussian beams

A $e^{i\omega t}$ time dependence is assumed for all time-harmonic fields. We model the focused laser beam of the cytometer as an elliptical Gaussian beam (EGB) or "laser-sheet" focused at the point $\mathbf{r}_0 = (x_0, y_0, z_0)$. We define beam-centered coordinates $(u, v, w) := \mathbf{r} - \mathbf{r}_0 = (x, y, z) - (x_0, y_0, z_0)$. The beam propagates along the w (or z) direction (left to right in Figure 1, out of the image plane in Figure 2) and is polarized in the uw (or xz) plane (image plane in Figure 1). The field of an EGB with waist semiaxes w_{0x}, w_{0y} along the x and y directions, respectively, reads

$$\mathbf{E}^{\text{inc}} = (E_u, E_v, E_w) = \left(1, 0, -\frac{2\, s_x\, Q_x\, u}{w_{0x}}\right) E_0 \Psi_0 e^{-ikw}, \quad (1)$$

where the wavevector is given by $k = 2\pi/\lambda$ and λ is the wavelength in the respective host medium (here water) and the two waist parameters are given by $s_x = 1/(k\, w_{0x}), s_y = 1/(k\, w_{0y})$ [2]. The envelope function reads

$$\Psi_0 = i\sqrt{Q_x\, Q_y}\; e^{-iQ_x \frac{u^2}{w_{0x}^2} - iQ_y \frac{v^2}{w_{0y}^2}}$$
$$\text{with} \quad Q_j = \frac{1}{1 + 2\, s_j \frac{w}{w_{0j}}}, \quad j = x, y. \quad (2)$$

The above expression represents the so-called "order L of approximation" and holds for sufficiently small values of $s = \max(s_x, s_y)$.

3.2 Far-field limit of elliptical Gaussian beams

The detection optics are assumed to be in the far-field, i. e., $r \to \infty$. Here, the scattered field is asymptotically equivalent to an outgoing spherical wave with a direction-dependent amplitude:

$$\mathbf{E}^{\text{sca}}(r, \vartheta, \varphi) \sim \boldsymbol{\mathcal{E}}^{\text{sca}}(\vartheta, \varphi)\, \frac{e^{-ikr}}{kr} \quad \text{at } r \to \infty. \quad (3)$$

In order to describe the interference of $\mathbf{E}^{\text{sca}}$ and $\mathbf{E}^{\text{inc}}$, we also take the far-field limit of the latter. I. e., in beam-centered spherical coordinates q, θ, ϕ that correspond to the Cartesian coordinates u, v, w, we let $q \to \infty$ (i. e., much larger than the length scales of the beam). The EGB then takes the shape of an elliptical cone. The corresponding envelope function will exponentially suppress the field for large $\tan\theta/s$, such that $\tan\theta = \mathcal{O}(s)$. I. e., we must neglect any terms of non-leading order in $\tan\theta$ or $\sin\theta$, because the order L of approximation already neglected higher order terms in s. Otherwise, unphysical phase errors can occur. This leads to

$$\mathbf{E}^{\text{inc}}(q, \theta, \phi) \sim \boldsymbol{\mathcal{E}}^{\text{inc}}(\theta, \phi) \begin{cases} \frac{e^{-ikq}}{k\, q} & \text{for } \cos\theta > 0 \\ \frac{e^{+ikq}}{k\, q} & \text{for } \cos\theta < 0 \end{cases} \quad (4)$$

at $q \to \infty$ with the vector components in spherical coordinates

$$\boldsymbol{\mathcal{E}}^{\text{inc}} = (E_q, E_\theta, E_\phi) = \frac{i}{2\, s_x s_y}\, e^{-\frac{\tan\theta^2}{4}\left(\frac{\cos\phi^2}{s_x^2} + \frac{\sin\phi^2}{s_y^2}\right)} \cdot (0, \cos\phi, -\text{sgn}(\cos\theta)\sin\phi). \quad (5)$$

I. e., the Gaussian beam behaves like a transverse spherical wave with an angle-dependent envelope. Because the beam itself is not radiating from any sources at finite positions and propagates from $w = -\infty$ to $w = +\infty$, it behaves like an *incoming* spherical wave in the backward direction ($\cos\theta < 0, w < 0$) and like an *outgoing* spherical wave in the forward direction ($\cos\theta > 0, w > 0$), which agrees with physical intuition.

3.3 Generalized Lorenz-Mie Theory

GLMT [3] describes the scattering of a focused beam by a (typically homogeneous) spherical particle. In GLMT, the particle is located at the origin of the coordinate system x, y, z. The corresponding spherical coordinates are r, ϑ, φ. All fields are expressed in eigenfunctions of the Helmholtz operator – (vector) spherical wavefunctions. For example, the ϑ component of the scattered field reads:

$$E_\vartheta^{\text{sca}} = \frac{-E_0}{kr} \sum_{n=1}^{\infty} \sum_{m=-n}^{n} (-i)^{n+1} \frac{2n+1}{n(n+1)} \cdot \{a_n\, g_{n,\text{TM}}^m\, \xi_n'(kr)\, \frac{d}{d\vartheta} P_n^{|m|}(\cos\vartheta) + m\, b_n\, g_{n,\text{TE}}^m\, \xi_n(kr) \frac{P_n^{|m|}(\cos\vartheta)}{\sin\vartheta}\}\, e^{im\varphi} \quad (6)$$

with the Riccati-Bessel function $\xi_n(x) := x\, h_n^{(2)}(x)$ corresponding to outgoing waves. P_n^m are the associated Legendre functions.

The scattering coefficients a_n, b_n of the spherical particle are those of standard (i. e., plane wave) Lorenz-Mie Theory. Furthermore, the GLMT contains *beam shape coefficients* (BSCs) $g_{n,}^m$ that describe the focused beam. The BSCs can generally not be computed in closed form. Here, we use the so-called integral localized approximation (ILA) [4] to compute the BSCs. For EGBs, the ILA has favorable numerical stability and complexity compared to the (non-integral) localized approximation [5].

3.4 Computations

As a basis for our far-field GLMT computations we use the Fortran code provided with the textbook by Gouesbet and Gréhan [3], for which a Python wrapper was written. This was complemented with a Python implementation of EGBs, i. e., BSCs computation with ILA and the far-field expressions in Eq. (4). This allows us to compute the "outgoing spherical wave" part of both, incident and scattered field that determine the intensity in the forward direction.

To transform from the particle-centered GLMT to the beam-centered laboratory system in the far-field picture,

i. e., to account for the shifted origin $\mathbf{r} = \mathbf{q} + \mathbf{r}_0$, the phase relation between $\boldsymbol{\mathcal{E}}^{\mathrm{inc}}$ and $\boldsymbol{\mathcal{E}}^{\mathrm{sca}}$ is obtained by inserting

$$\frac{1}{kr}\mathrm{e}^{-\mathrm{i}kr} = \frac{1}{kq}\,\mathrm{e}^{-\mathrm{i}kq}\mathrm{e}^{-\mathrm{i}k(\mathbf{r}\cdot\mathbf{r}_0)/r} \quad \text{as } q, r \gg |\mathbf{r}_0| \tag{7}$$

in Eq. (3) and identifying $\vartheta \leftrightarrow \theta, \varphi \leftrightarrow \phi$. This allows us to compute $\boldsymbol{\mathcal{E}}^{\mathrm{tot}} = \boldsymbol{\mathcal{E}}^{\mathrm{inc}} + \boldsymbol{\mathcal{E}}^{\mathrm{sca}}$ [Eq. (3) and (4)] for a set of directions θ, ϕ and determine the intensity $\mathcal{I}^{\mathrm{tot}} = |\boldsymbol{\mathcal{E}}^{\mathrm{tot}}|^2$.

4 Results and discussion

Figure 3 shows simulated intensity patterns for a single polystyrene bead ($d = 6.11\ \mu\mathrm{m}, n_{\mathrm{PS}} = 1.6054 - 0\mathrm{i}$ [6]) in water ($n_{\mathrm{m}} = 1.3374$ [7]) at $\lambda = 488\ \mathrm{nm}/n_{\mathrm{m}}$. They exhibit the typical circular pattern of spherical scatterers, interference near the edges of the EGB as well as a significant dependence on the particle position. To account for the fact that the scattering takes place in water and the detector is placed in air (Fig. 1), we applied Snell's law to transform the scattering angle θ from water to air. The intensity pattern $\mathcal{I}^{\mathrm{tot}}(\theta^{(\mathrm{air})}, \phi)$ can now be integrated over the solid angle of the individual fibres (coloured circles in Figure 3). Repeating this for a range of beam/particle positions $\mathbf{r}_0 = -\mathbf{r}_{\mathrm{p}}$ simulates the intensity variations during particle transit and yields a set of intensity pulses that can be compared with measurements. Figure 4 shows measurement and simulation results for the corresponding pulses. The estimated flow speed in the cytometer is $v = (3.5 \pm 0.4)$ m/s, such that the 28 µm length interval shown for x_{p} in the simulations corresponds to the 8 µs time interval $[v\,\Delta t = (28 \pm 3)\ \mu\mathrm{m}]$ in the measurements. As can be seen, both, the complex shape of the pulses as well as their length is well described by the simulations.

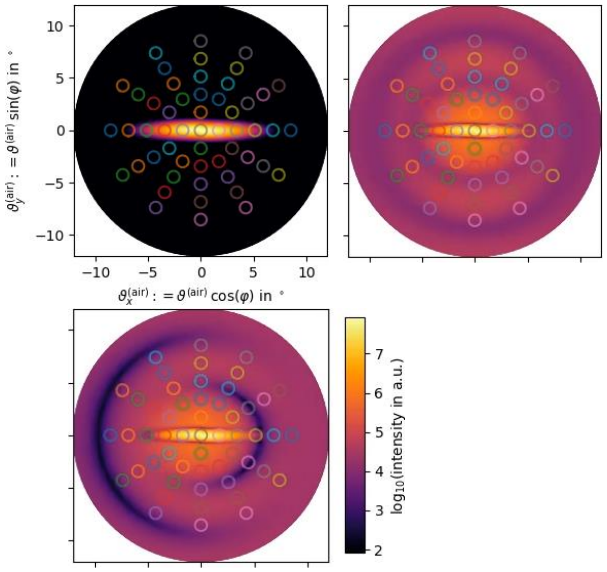

Figure 3 *Simulated far-field intensity patterns of the total field* $\boldsymbol{\mathcal{E}}^{tot} = \boldsymbol{\mathcal{E}}^{inc} + \boldsymbol{\mathcal{E}}^{sca}$

The concept presented here to model interference of $\mathbf{E}^{\mathrm{inc}}$ and $\mathbf{E}^{\mathrm{sca}}$ in the far-field is not limited to GLMT, but can be extended to other (numerical) frameworks for light-scattering that allow for off-axis scattering with focused beams, such as the discrete dipole approximation or T-matrix methods. Perspectively, this allows to simulate such interference for non-spherical particles of suitable size parameters, too.

5 References

[1] Kage D., Heinrich K., von Volkmann K., Kirsch J., Feher K., Giesecke-Thiel C., Kaiser T., Multi-angle pulse shape detection of scattered light in flow cytometry for label-free cell cycle classification, Communications Biology 4(1):1–11 (2021)

[2] Ren K.F., Gréhan G., Gouesbet G, Electromagnetic field expression of a laser sheet and the order of approximation, Journal of Optics 25(4):165–76 (1994)

[3] G. Gouesbet, and G. Gréhan, Generalized Lorenz-Mie theories (Springer, 2017), 2nd ed.

[4] Ren K.F., Gouesbet G., Gréhan G., Integral localized approximation in generalized Lorenz–Mie theory, Applied Optics 37(19):4218–25 (1998)

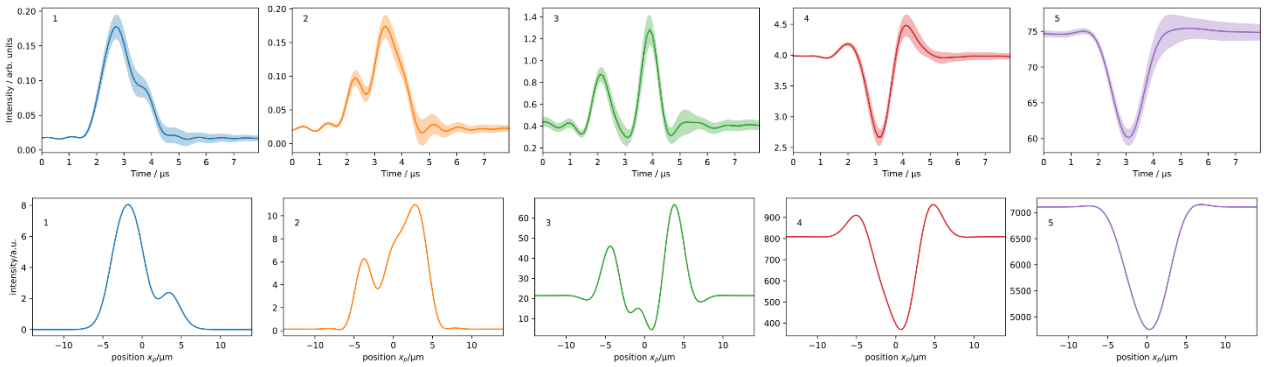

Figure 4 *Intensity pulse shapes for 6.11 µm polystyrene particles on fibres 1–5 (along the flow direction, see Figure 2).* ***Top****: Measurement results for ca.* 10^4 *events (mean ± standard deviation).* ***Bottom:*** *Simulation results.*

[5] Ren K.F., Gréhan G., Gouesbet G., Evaluation of laser-sheet beam shape coefficients in generalized Lorenz–Mie theory by use of a localized approximation, Journal of the Optical Society of America A 11(7):2072–9 (1994)

[6] Nikolov I.D., Ivanov C.D., Optical plastic refractive measurements in the visible and the near-infrared regions, Applied Optics 39(13):2067–70 (2000)

[7] Daimon M., Masumura A., Measurement of the refractive index of distilled water from the near-infrared region to the ultraviolet region, Applied Optics 46(18):3811–20 (2007).

PLASMONICS & NANOPARTICLES

13th International Conference Series on
Laser-light and Interactions with Particles
Optical Particle Characterization follow-up !
August 21-26th, 2022, Warsaw, Poland

A New Method for Measurement of Surface Plasmon Polaritons Propagation Losses in a Laser-Cut Single Silver Nanowire

M. ĆWIERZONA[1], M. ŻEBROWSKI[1], M. A. ANTONIAK[2], K. SULOWSKA[1], M. NYK[2], S. MAĆKOWSKI[1], D. PIĄTKOWSKI[1,*]

[1]Institute of Physics, Faculty of Physics, Astronomy and Informatics, Nicolaus Copernicus University in Toruń, ul. Grudziądzka 5, 87-100 Toruń, Poland

[2]Advanced Materials Engineering and Modelling Group, Faculty of Chemistry, Wrocław University of Science and Technology, Wybrzeże Wyspiańskiego 27, 50-370 Wrocław, Poland

Corresponding author: dapi@umk.pl

Abstract

In this work, we propose a new experimental approach to directly measure propagation losses of surface plasmon polaritons (SPPs) in a single silver nanowire (AgNW). Using a precise microinjector, a femtoliter droplet with up-converting nanocrystals (NCs) is deposited at one end of the nanowire. When illuminated with a laser, NCs provide a stable source of SPPs, which then propagate through the nanowire to its other end. The intensity of radiation measured at that end provides information about propagation losses. By gradually reducing the length of the nanowire through a precisely controlled laser-cutting technique, it is possible to measure the intensity of scattered polaritons versus the effective length of the nanowire. Interestingly, the experimental techniques presented in this work prove to be beneficial as an characterization tool due to their relatively low cost and ease implementation in an already built measurement setup.

1 Measurement setup

The experiment was carried out using a confocal microscope (Ti2, Nikon) equipped with two microscope objectives (Figure 1): a high numerical aperture (NA) oil immersion objective (Apo TIRF 60x, NA = 1.49, Nikon) operating in an inverted configuration, and a low numerical aperture air objective (LU Plan 50x, NA = 0.55, Nikon) mounted on a tripod-holder, placed directly above the sample and attached to sample stage.

The bottom objective was used to both collect photoluminescence (PL) signal from NC and cut the nanowire. The top objective was solely used to provide a stable excitation source for locally deposited nanocrystals. Raster scanning for luminescence image reconstruction is possible due to a piezoelectric sample holder (P-545, Physik Instrumente). As a light source, a single-mode fiber-coupled infrared laser diode operating at 980 nm (LP980-SA100, Thorlabs) was used. A photon counting module (COUNT-100C, Lasaer Components) was used to detect the signal acquired by the bottom objective.

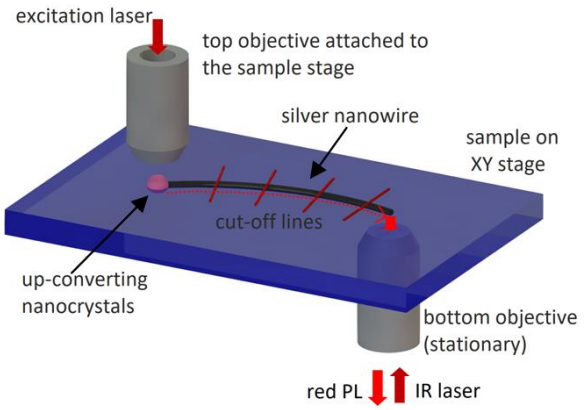

Figure 1 *Sketch of the experimental configuration.*

2 Sample preparation

As a sample base, regular coverslips (No 1, Roth) were chosen since glass does not introduce an additional attenuation of polaritons. Next, about 20 µL of colloidal silver nanowires in water were spin-coated on the coverslip for 30 s at 2500 rpm. One silver nanowire, isolated from other particles, was selected from the resulting random distribution of nanowires on the glass surface. By using a femtolitre capillary tip, a small NCs droplet of about 500 nm in diameter was deposited exactly at one end of the selected nanowire (Figure 2).

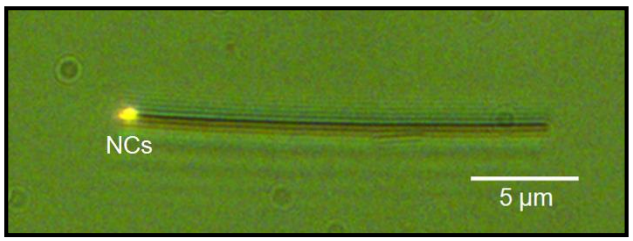

Figure 2 *Single, silver nanowire with nanocrystals deposited at one end, observed in transmitted light.*

3 Sample characterization

Initial dimensions of the nanowire were estimated using fully optical techniques. The length of the nanowire was about 23 μm and was measured using scattering imaging with an accuracy of about 0.5 μm (Figure 3).

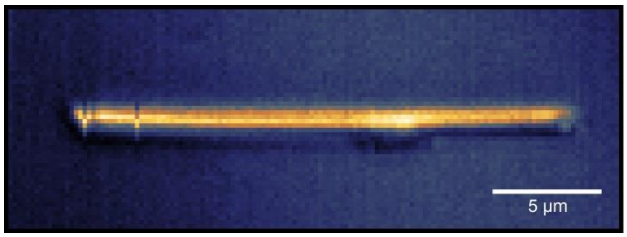

Figure 3 *Single, silver nanowire imagined using backscattered laser light.*

Due to the diffraction limit, nanowire diameter cannot be estimated using classical imaging techniques. One can, however, use an indirect method based on complex interactions between the silver nanowire and Gaussian beam [1]. A laser beam focused on the free end of the nanowire by an objective with a high numerical aperture launches $SPPs_L$, which transports energy along x-direction to the nanocrystals deposited at the other end of the nanowire [2]. Excited nanocrystals launch $SPPs_{PL}$ propagating back to the excitation/detection point (bottom objective). The shape and intensity of this emission strongly depends on the laser polarization and nanowire diameter which can be used to determine nanowire thickness [1]. It has been shown that in the case of thin nanowires (d<100 nm) and linearly polarized laser oriented perpendicular to nanowire long axis, only E_{0x} and E_{0z} laser field components are visible [1]. A four-lobe PL pattern observed for the investigated nanowire indicates that its diameter is below 100 nm (Figure 4).

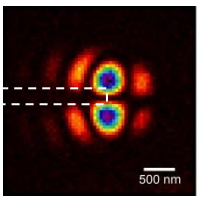

Figure 4 *PL distribution observed at the free end, excited by laser light polarized perpendicular to the nanowire.*

4 Experiment

The SPPs propagation losses measurement was realized using the configuration presented in Figure 1. The top objective is used to position the excitation laser spot on the NCs droplet, which then becomes a source of polaritons. Using low numerical aperture objective guarantees lower power densities, reducing the possibility of accidental damages of the nanowire. Eventually, $SPPs_{PL}$ launched by NCs reach the opposite end of the nanowire and are collected by the bottom objective in the form of out-scattered radiation (PL). This radiation is then integrated and plotted versus nanowire length. After PL measurement, the laser was redirected to the bottom objective and polarized alongside the nanowire to ensure the most efficient absorption. Next, the laser power was increased to provide enough energy to melt the thin nanowire. After each melting step, the laser power was reduced and redirected back to the top objective to excite NCs again and collect PL image. This procedure was repeated for 11 different lengths of the nanowire. The first and last step of this process is presented in Figure 5. The distribution of integrated intensities plotted versus the temporary length of the nanowire (Figure 6) can be accurately described by the exponential function.

a) b)

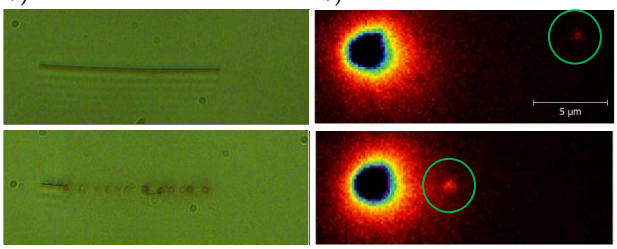

Figure 5 *First (upper images) and last (lower images) step of SPPs propagation losses measurements: (a) transmission and (b) PL images.*

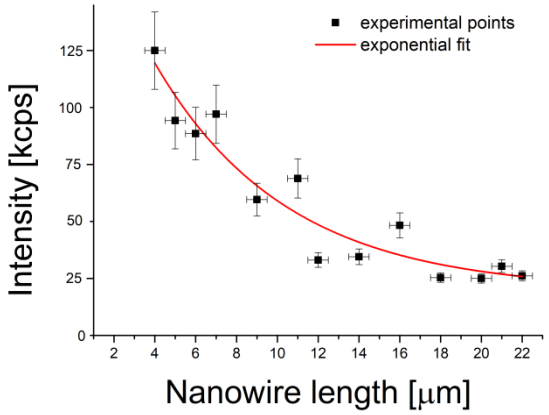

Figure 6 *The integrated intensities of PL signal, measured at the free end of the nanowire for different lengths of the nanowire.*

5 References

[1] Song M., Dellinger J., Demichel O., Buret M., Francs G.C.D., Zhang D., Dujardin E., Bouhelier, Selective excitation of surface plasmon modes propagating in Ag nanowires, A. Opt. Express, OE 25, 9138 (2017).

[2] Prymaczek A., Cwierzona M., Grzelak J., Kowalska D., Nyk M., Mackowski S., and Piatkowski D., Remote activation and detection of up-converted luminescence via surface plasmon polaritons propagating in a silver nanowire, Nanoscale 10, 12841 (2018).

13th International Conference Series on
Laser-light and Interactions with Particles
Optical Particle Characterization follow-up !
August 21-26th, 2022, Warsaw, Poland

ELLIPSOMETRIC REGISTRATION OF COUPLING OF SURFACE AND LOCALIZED PLASMONS

Eugene BORTCHAGOVSKY[1,*], Tetiana MISHAKOVA[2] and Alla BOGOSLOVSKA[1]

[1] V. Lashkarev Institute of Semiconductor Physics of NAS of Ukraine, pr.Nauki 41, Kyiv 03028, Ukraine
[2] Institute of High Technologies of Taras Shevchenko Kyiv National University, ave.Glushkov 4g, Kyiv 03022, Ukraine
Corresponding author: bortch@yahoo.com

Abstract

Ellipsometry was used to register coupling of surface and localized plasmons in the system with gold nanoparticles deposited on a gold film. It is known that coupling of modes results in their hybridization and splitting of dispersion relations of separated modes, which crosses without coupling. Dispersion relations were obtained from ellipsometric measurements made as in standard configuration with external reflection as in Kretschmann configuration with internal reflection and direct excitation of surface plasmon. Those dispersions demonstrate expected splitting and allow to speak about strong coupling and Rabi splitting.

1 Experimental

Spherical gold nanoparticles of 50nm diameter from "Nanopartz" were deposited by absorption on a gold layer of about 40nm thickness. Gold layer was evaporated directly on BK7 glass slide and, for more uniform adsorption of nanoparticles, monolayer of dithiol ($C_{10}S_2H_{22}$) was preliminary adsorbed on gold surface. Result of the adsorption is shown in Figure 1.

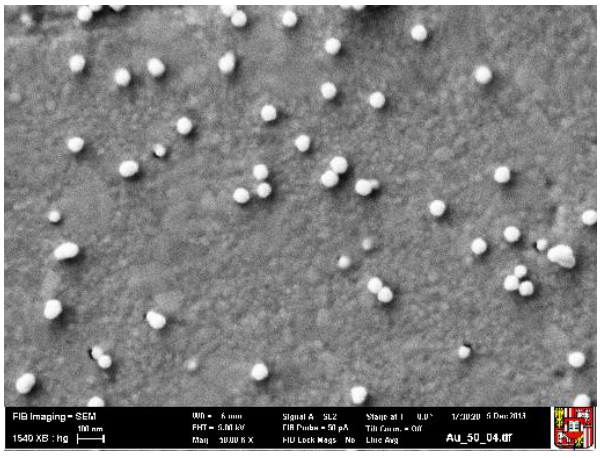

Figure 1 *Nanoparticles on the gold surface.*

In addition to the standard measurement configuration with external reflection ellipsometric measurements were made in Kretschmann configuration with internal reflection too. For such measurements additional 90^0 prism from BK7 glass was optically contacted to the glass slide by spectrally matched immersion liquid from Cargille Co.

Ellipsometry provides two so-called ellipsometric angles Ψ and Δ bearing amplitude and phase information [1]. As by definition $tg\Psi=|r_p|/|r_s|$ where r_i are Fresnel reflection coefficients, behaviour of the angle Ψ reflects extremums of reflection coefficients allowing to follow conditions of the energy transfer to modes of the system of interest.

2 Results and Discussion

Spectra of the angle Ψ for different angles of incidence measured for the system with nanoparticles independently on the measurement mode demonstrate two additional minima in comparison to the results for the clean gold film. Those minima correspond to the conditions of the excitation of additional modes created in the system after deposition of nanoparticles. Dispersion relations for those modes restored from the position of all recorded minima are shown in Figure 2.

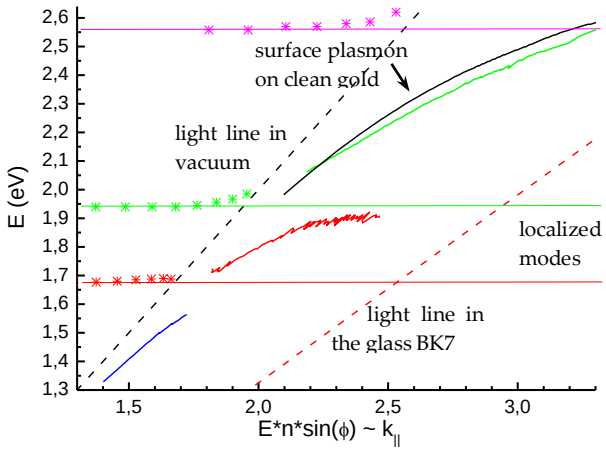

Figure 2 *Dispersion relations.*

A number of lines are presented in Figure 2. Two inclined dashed lines correspond to plane wave in air or BK7 glass. They separate the whole space into three areas where the area left to the light line in air is accessible by standard measurements with external reflection, the area between two light lines is accessible by internal reflection in Kretschmann geometry, any the last area is not accessible in our experiement. Horizontal lines are eye guides for the position of dispersionless localized modes of deposited nanoparticles. It is worth to note that deposition of spherical

nanoparticles on a substrate lifts the degeneration of the localized plasmon of a spherical metallic nanoparticle and shifts it to lower energy. Black line corresponds to the recorded surface plasmon for clean gold film. It is seen that the visibility of this mode is restricted but it continues in both sides.

Three different branches created by the hybridisation of localized and surface plasmons are well seen and shown by colours. Lines correspond to the dispersion recorded by internal reflection as stars to the dispersion recorded by external reflection. It is interesting to notice that hybridisation increases the range of visibility of modes to low energies.

At least two other interesting results are visible in Figure 2. Dispersion recorded in both measurement modes well coincide and the mode recorded by external reflection is dispersive in contrary to the case of nanoparticles on a glass [2]. It happens because of the hybridization and reflects the existence of the surface plasmon felt in this way even at external reflection. The second worth result is the splitting about 0.2eV between modes coded by red and green what allows to speak about possible strong coupling of two plasmons and Rabi splitting between them.

The origin of the third mode at ~2.55eV is questionable. From one side it looks like the third mode also split with surface plasmon what is visible as deviation of the green mode from surface plasmon for clean gold. From other side this deviation may be explained by standard reaction of surface plasmon on material deposited on the surface. Also there should be no dipole mode of spherical gold nanoparticles at that energy. So, this question demands additional investigations.

3 Conclusions

Ellipsometry demonstrates good ability in the investigation of plasmonic systems and coupling of different plasmonic modes. Obtained results demonstrate splitting of coupled modes and allow to speak about strong coupling of localized and surface plasmons in the investigated system. Additionally results demonstrate that in such a system surface plasmon is exhibited even at external reflection at grazing incidence due to the noticed hybridisation.

4 References

[1] R.M.A. Azzam and N.M. Bashara, Ellipsometry and polarized light (North-Holland, Amsterdam, 1977).

[2] Bortchagovsky E.G., Dejneka A., Jastrabik L., Lozovski V.Z., Mishakova T.O., Deficiency of standard effective medium approximation models for ellipsometry of layers of nanoparticles, J. Nanomater. 2015:602848-1-8 (2015)

13th International Conference Series on
Laser-light and Interactions with Particles
Optical Particle Characterization follow-up !
August 21-26th, 2022, Warsaw, Poland

DEPENDENCE OF PLASMONIC PROPERTIES OF LATTICES OF NANOPARTICLES ON THEIR ORIENTATION. MICROELLIPSOMETRIC INVESTIGATIONS.

Eugene BORTCHAGOVSKY[1,*], Yuri DEMYDENKO[1], Alla BOGOSLOVSKA[1], Tetiana MISHAKOVA[2], Jia TANG[3], Monika FLEISCHER[3], Ilya MILEKHIN[4], and Dietrich R. T. ZAHN[4]

[1] V. Lashkarev Institute of Semiconductor Physics of NAS of Ukraine, pr.Nauki 41, Kyiv 03028, Ukraine
[2] Institute of High Technologies of Taras Shevchenko Kyiv National University, ave.Glushkov 4g, Kyiv 03022, Ukraine
[3] Institute for Applied Physics and Center LISA+, Eberhard Karls Universität Tübingen, Auf der Morgenstelle 10, D 72076 Tübingen, Germany
[4] Semiconductor Physics, Chemnitz University of Technology, Reichenhainer Straße 70, D-09107 Chemnitz, Germany

*Corresponding author: bortch@yahoo.com

Abstract

Microellipsometry was used to reveal plasmonic properties of an ordered lattices of nanoparticles depending on the mutual orientation of the plane of incidence of exciting light and own vectors of the lattice. Although Rayleigh anomalies for differently oriented lattice are different, they are reflected at energies beside of experimental range. In spite of this fact, registered positions of plasmonic resonances are different and obtained behaviour is not standard birefringence.

1 Experimental

Plasmonic structures of gold nanodiscs ordered in square lattices were prepared by electron-beam lithography [1]. Electron-microscopic image of one of the structures with the period of 150 nm is shown in Figure 1.

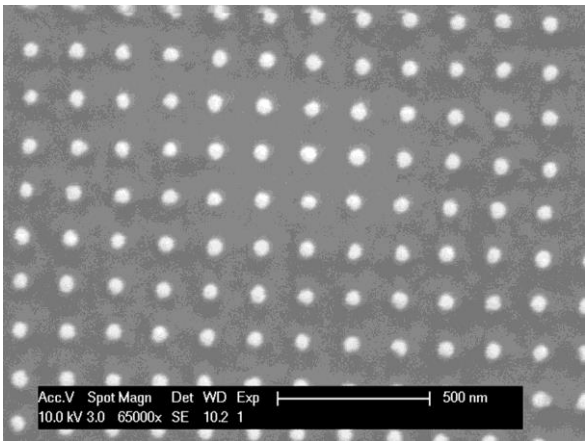

Figure 1 *Image of the lattice of nanodiscs.*

Imaging ellipsometer nanofilm_ep4 from Accurion GmbH with spatial resolution on the micrometer range was used for the investigation of these structures. Measurements were made with the plane of incidence oriented either along the side of squares of the lattice or along the diagonal of squares.

2 Results and Discussion

It was shown [1] that interparticle interactions in lattices result in effective birefringence of a layer of nanoparticles depending on the angle of incidence. The optical axes of this birefringence are fixed by the geometry – along (X) and perpendicular (Y) to the plane of incidence in the surface plane and perpendicular to the surface (Z). Independence of the X- and Y- effective components of the birefringence can be proven by simple symmetrical considerations [1]. However, this effective birefringence behaves contrary to the standard crystal birefringence. Another symmetrical consideration demonstrates that the rotation of the plane of incidence relative to the lattice and its arrangement along the diagonal of the square lattice leads to the planar optical axes again directed along and perpendicular to the plane of incidence and their components of the birefringence are independent again. In the case of crystal birefringence, the optical axes would be fixed by the lattice, not by the plane of incidence, and by rotation of the plane of incidence by 45° the Jones matrix [19] of the reflection would be nondiagonal and components of the dielectric functions along planar axes are mixed in the strongest way in such a geometry.

Ellipsometry provides two so-called ellipsometric angles Ψ and Δ bearing amplitude and phase information [2]. It is demonstrated [3] that the spectral behaviour of the angle Ψ of a system with a layer with resonances in relation to the spectrum of the angle Y of the system without this layer reflects resonances by the extremums allowing easily assign separated extremums to resonances of different components of the fielectric function of the birefringent layer.

Spectra of the angle Ψ for different angles of incidence measured for two noticed mutual orientations of the plane of incidence and the lattice are shown in Figure 2.

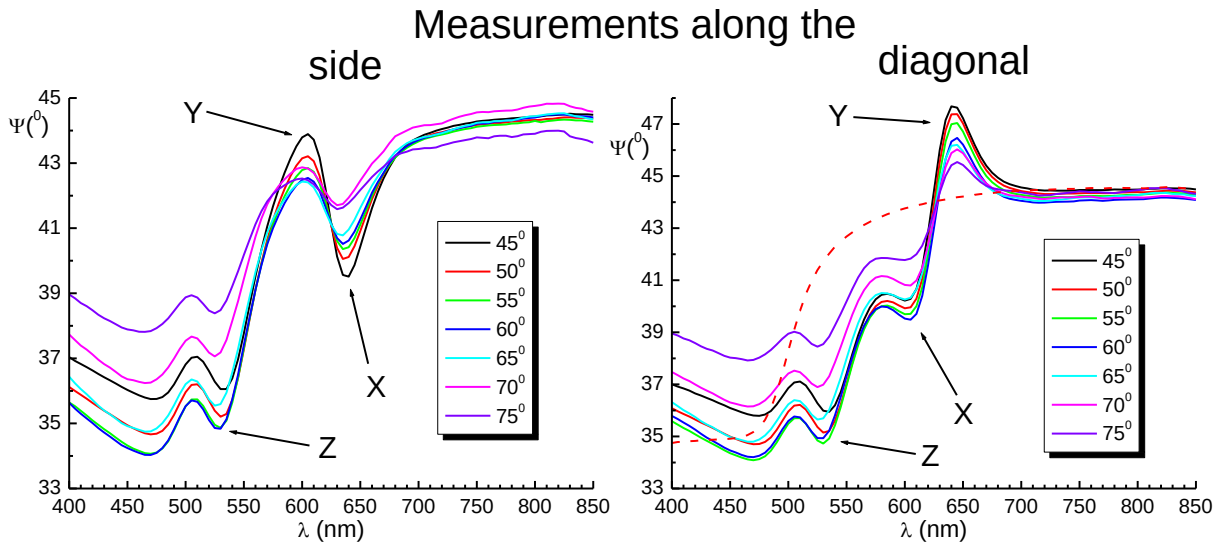

Figure 2 *Spectra of ellipsometric angle Ψ measured at different angles of incidence for two mutual orientations of the square lattice and the plane of incidence, the directions of which are indicated. The dashed line demonstrates the spectrum for a clean substrate, i.e. without lattice of nanoparticles.*

The analysis [3] further indicates that the minima in the spectra are connected to resonances of the X- and Z-components of the dielectric tensor while maxima are related to the resonance of the Y-component. All those features are indicated in Figure 2 and are clearly different at the two different orientations of the plane of incidence.

Previous results [1] demonstrated that standard treatment of ellipsometric results for considered plasmonic structures is incorrect. Application of standard models of Effective-Medium Approximation for layers of nanoparticles is incorrect too [4]. Direct assignment of features in ellipsometric spectra to resonances of the components of dielectric functions of deposited birefringent layer [3] is convenient but qualitative tool. Thus, as correct account of the polarizability renormalization of a single nanoparticle deposited on a layered surface inside of an ordered structure of nanoparticles, as appropriate construction of parametrized effective dielectric functions of the layer of nanoparticles are necessary for the analysis of ellipsometric results.

In spite of Rayleigh anomalies for both orientations of the lattice are rather far from the experimental spectral range and the approach developed in [1] gives only minor changes of the values of the components of the effective dielectric functions for both orientations, different positions of plasmonic resonances for different orientations are clearly visible. So, this question demands additional investigations.

3 Conclusions

Ellipsometry clearly reveals plasmonic resonances of the lattice of nanoparticles and demonstrates that their position depends on the mutual orientation of the plane of incidence of the exciting light and own vectors of the lattice. The reason of so clear difference demands further investigation.

4 References

[1] E. Bortchagovsky, Yu. Demydenko, A. Bogoslovskaya, J. Tang, F. Dai, M. Fleischer, I. Milekhin, A. Sharma, G. Salvan, and D. R. T. Zahn, Microellipsometry study of plasmonic properties of Metal-Insulator-Metal structures with ordered lattices of nanoparticles, J. Appl. Phys. 129:123104 (2021)

[2] R.M.A. Azzam and N.M. Bashara, Ellipsometry and polarized light (North-Holland, Amsterdam, 1977).

[3] E. Bortchagovsky and T. Mishakova, Exhibition of film's resonances in ellipsometric spectra and Berreman effect, submitted to Appl. Opt.

[4] E. G. Bortchagovsky, A. Dejneka, L. Jastrabik, V. Z. Lozovski, and T. O. Mishakova, Deficiency of standard Effective-Medium Approximation for ellipsometry of layers of nanoparticles, J. Nanomater. 2015:602844 (2015)

EXTENDED DYNAMICS AND LASING OF NANOEMITTERS ENHANCED BY DISPERSIVE CARBON NANOTUBES

Gennadiy BURLAK

CIICAp, Universidad Autónoma del Estado de Morelos, Av. Universidad 1001, Cuernavaca, Morelos 62210, México

**Corresponding author:gburlak@uaem.mx*

Abstract

We investigate the extended dynamics and laser emission of random nanoemitters attached in a three-dimensional (3D) array of dispersed carbon nanotubes (CNTs) enhanced by plasmonic-polariton excitations. We found that in such a composite system, the onset time of laser generation (instability) in the nanoemitters significantly depends on the plasmonic frequency of the nanotubes. In the case of CNTs with a high plasmonic frequency, surface plasmon-polaritons are excited macroscopically, which leads to strong cross-coupling of emitter radiation to re-excited plasmon-polariton fields. The latter leads to a significant decrease in the onset time of laser instability. We found a resonant change in the field structure in the system associated with plasmon-polariton generation when the field of emitters in 3D clusters is strongly coupled to the CNT field. The corresponding resonance is detected in the form of a strong and narrow peak of the inverse participation ratio. The position of this resonance weakly depends on the number of attached emitters.

1 Model and basic equations

We consider periodic array of single-walled parallel carbon nanotubes (CNT) and a number of radiating nanoemitters attached randomly between of CNTs. To investigate the dynamics of this complex nonlinear 3D system we use the Maxwell equations for electrical **E**(r,t) and magnetic **H**(r,t) fields, polarization **P**(t), and four-level laser populations $N_{0,1,2,3}(t)$ of nanoemitters (quantum dots) [1-4]. However such nonlinear 3D system cannot be solved analytically, therefore in this study we use the numerical FDTD simulations allowing obtaining the exact solutions for photonic radiating field.

1.1 Lasing in the system with carbon nanotubes

We consider single-walled CNTs and a number **N** of radiating emitters (quantum dots (QD)) are randomly placed between the nanotubes. We study the radiating in such a compound system (emitters with surrounding CNT) at different values of the plasma frequency ω_P when the surface plasmon-polaritons (SPP) in CNT can be generated. Fig.1 shows the integral output flux of field energy that can be written as $I(t) = \oint_S (\mathbf{K}\cdot\mathbf{n})dS$ where $\mathbf{K}$ is the Poynting vector.

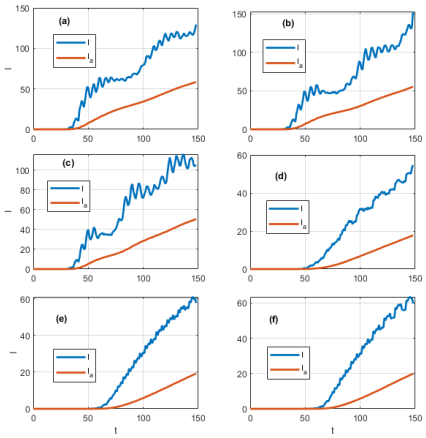

***Figure** 1. Integral intensity I(t) of field radiating by nanoemitters for different plasma frequencies ω_P.*

From Fig. 1 one can see that the flux of the field energy $I(t)$ from the CNT array significantly depends on ω_P of surrounding CNT. We can conclude that the frequency $\omega_c = \omega_p = 1.0\times10^8\,\mathrm{sec}^{-1}$ (when the plasmon-polaritons are generated) indicates the characteristic frequency that separates two regimes in considered compound system.

Fig.1 shows that the field dynamics and lasing of N random nanoemitters considerably depends on ω_P of surrounding CNT.

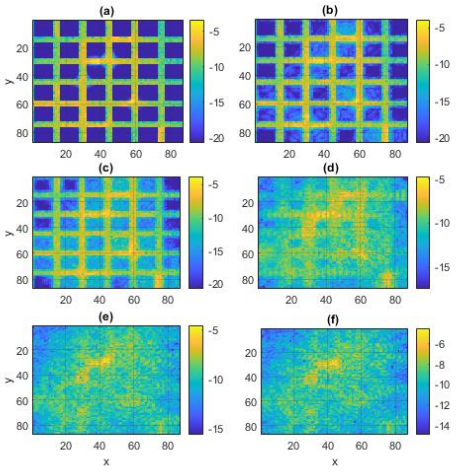

***Figure** 2. Spatial field distribution in the central plane at different ω_P of surrounding CNT.*

Fig.2 shows that at large ω_P the field is concentrated near the boundaries and gaps between the CNTs and practically

does not penetrate inside the nanotubes. At smaller values of $\omega_p <= 1.0\times10^8\ \mathrm{sec}^{-1}$ (see panels (d), (e), and (f)) the field **E** is near homogeneous, where only the point-like radiating emitters are visible. In such a ω_P frequency range the SPPs can not propagate. Because of the significantly inhomogeneous shape of the field distribution (Fig.2), it is important to quantify the characteristics of the spatial features of plasmon-polariton field to decide how much the photonic field state **E** is ordered. To do that we calculate the Inverse Participation Ratio (IPR) defined as the normalized integral over the square of the field energy that reads

$$IPR = \frac{L^3 \int |\mathbf{E}|^4 d^3 r}{\left(\int |\mathbf{E}|^2 d^3 r\right)^2} = \left(\frac{L}{\Lambda}\right)^3.$$

We numerically found that IPR has very sharp peak at $\omega_c = \omega_p = 1.0\times10^8\ \mathrm{sec}^{-1}$ (shown in Fig.3) that thus can be declared as critical frequency (resonance) of SPP generation. The position of ω_c is practically independent on the number of emitters N.

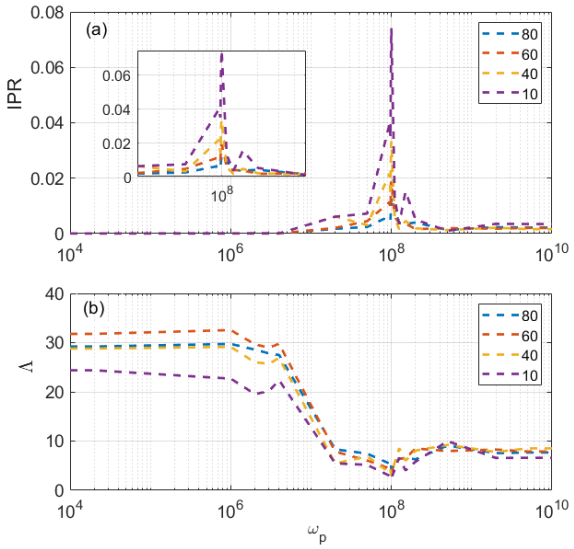

Figure 3. *(a) The Inverse Participation Ratio (**IPR**) of the radiating field in CNT lattice as function of the plasma frequency ω_p for different number of emitters. (b) The localization length of the field **Λ** in the CNT lattice as function of plasma frequency ω_p. We observe that IPR has very sharp peak at $\omega_p = \omega_c = 10^8 sec^{-1}$ that can be mention as a critical frequency and corresponds to surface PP generation. The position of ω_c is practically independent on the number of emitters N.*

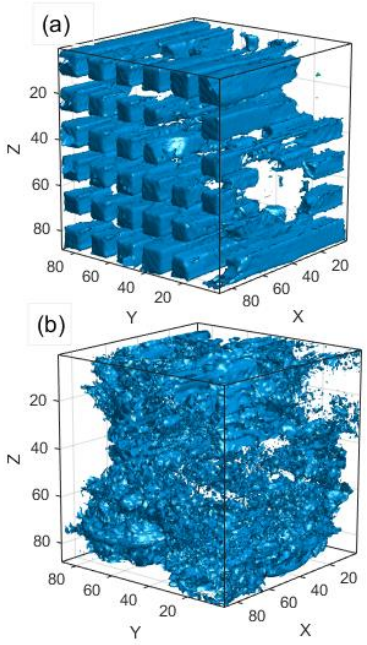

***Figure** 4. The spatial 3D structure of plasmon-polariton field in CNT array at different plasma frequency (a) $\omega_p = \omega_c = 10^8 sec^{-1}$ that corresponds to the incipient ordering state of field, and (b) disordered field state below the critical $\omega_p = 10^7 sec^{-1} < \omega_c$.*

2 Acknowledgement

This work was supported in part by CONACYT (Mexico) under the grant No. A1-S-9201.

3 References

[1] G. Burlak, Y.G. Rubo, Mirrorless lasing from light emitters in percolating clusters. PRA 92, 013812 (2015).

[2] G. Burlak, Cecilia Cuevas-Arteaga, Gustavo Medina-Ángel, Erika Martínez-Sánchez, and Yessica Y. Calderón-Segura, Plasmon-polariton

[3] oscillations in three-dimensional disordered nanotubes excited by a moving charge. Jour. Appl. Phys. 126, 013101 (2019),

[4] A. E. Siegman, Lasers (Mill Valley, California, 1986).

[5] Xunya Jiang and C. M. Soukoulis, Phys. Rev. Lett. 85, 70 (2000)..

DAMPING RATES OF DISSIPATIVE PROCESSES IN METAL PLASMONIC NANOPARTICLE

Krystyna KOLWAS

Group of Optical Characterisation of Micro- and Nanoobjects, Institute of Physics, Warsaw, 02-668, Poland

Krystyna.Kolwast@ifpan.edu.pl

Abstract

The scope of the present report is the closer look at the dynamics of damping processes in MNP in order to answer the question which plasmonic quantities are damped as such data do not result from the classical EM considerations. The model is based on the link between the classical EM description of plasmonic properties of MNP and the quantum picture in which MNPs are treated as "quasi-atoms" or quasi-particles (PQPs). The energy level structure with the zero energy level state for non-excited plasmon allows studying the system dynamics accounting for dissipative processes.

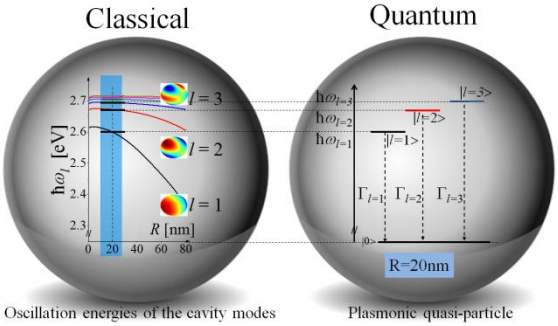

Figure 5 The starting scheme for modelling which relates the oscillation energies of LSP modes to the energy levels of quantum plasmonic quasi-particle

The evolution of the reduced density matrix of quantum open systems is ruled by the master equation in the Lindblad form which enables us to distinguish between damping processes of populations and coherences of multipolar plasmon oscillatory states and to establish the intrinsic relations between the rates of these processes. The size dependence of the rates of dephasing of the collective electron motion and of damping of populations are given for gold and silver MNPs on the base of the established classical-quantum relations of damping channels.

1 Introduction

Plasmonic properties of nanoscale structures lay the groundwork for many future technologies, applications and materials. Plasmonics is based on the excitations of surface plasmons understood as surface charge density oscillations, which form the standing waves of Localised Surface Plasmons (LSP) in the case of finite-size nanostructures. In spherical metal nanoparticles (MNPs) the basic properties of LSPs can be controlled by their radius and manifest in the scattering, absorption or extinction spectra in form of the maxima with size-dependent spectral position, spectral width and intensity. The maxima in the spectra reflect the resonant character of LSP excitations resulting from the size-dependent intrinsic properties of MNP [1]. Such spectra can be predicted by the classical Mie scattering theory when calculated for consecutive chosen radii. However, Mie scattering theory gives no direct information about the size-dependence of the pick position in the spectra.

2 Classical oscillation energies and damping rates of plasmonic cavity modes versus MNP radius

The dynamics of plasmon excitations is described by the important intrinsic functions of MNP's size such as resonant frequencies of the cavity modes and damping rates of such modes. The excitation of LSP is a resonance process which takes place when the frequency of the incoming light ω fits a self-frequency (-ies) of a plasmonic resonator $\omega_l(R)$ (of the cavity modes), where l, $l = 1,2,3,..$.

Therefore, the key issue is to find the intrinsic properties of a plasmonic cavity i.e. the size-dependent self frequencies of plasmon modes $\omega_l(R)$ but also the damping rates $\Gamma_l(R)$ of the oscillations. Such parameters characterise the plasmonic MNPs and can be found by looking for solutions of the self-consistent Maxwell equations in absence of the incoming light field in connection with the continuity relations at the sphere boundary [1]. The resulting dispersion relations for surface-localized fields define the complex, discrete eigenvalues $\hbar(\omega_l(R) - i\Gamma_l(R)/2)$. So the dynamics of surface localized EM fields: $E(r = R) = \exp(i\omega_l - \Gamma_l/2)t$) is unambiguously determined by the material properties of the MNP of a given size and its dielectric environment. Found in absence of the illuminating radiation, $\omega_l(R)$ and $\Gamma_l(R)$ inherently characterize an MNP of the radius R in the same way as the energy levels and the inverse of lifetimes characterize an atom or a molecule. In both cases, these quantities manifest in the spectra, when the systems are illuminated.

3 Quantum modeling of the plasmonic quasi-particle (PQP) decay dynamics

Let us ascribe [2] the oscillation energies $\hbar\omega_l(R)$ of the classical modes to the discrete energy levels, which are distinct from the zero-energy non-oscillatory level by the energies $\hbar\omega_l(R)$ (Fig. 1). The corresponding states of the

plasmonic systems S in the Hilbert space are $|l>$ with l = 1,2,3.... The only possible transitions are those with the absorption or emission of a photon with the energy $\hbar\omega_l$. Such transitions occur between the state $|l>$ and the non-oscillatory state $|0>$.

3.1 The density matrix and quantum master equation

To describe the state of the plasmonic system S we use the density matrix which is convenient in describing the quantum systems in mixed states and in time-dependent problems. The diagonal elements of the density matrix correspond to the probabilities $p_n = N_n/N$ of occupying a quantum states $|n>$, so they describe the relative populations of these states. The complex off-diagonal elements of the density matrix in the basis $|n>$, $|0>$ contain time-dependent phase factors that describe the evolution of the coherent superposition of the states.

As no physical system is absolutely isolated from its surroundings, the plasmonic system S has to be considered as an open quantum system which is a subsystem of a larger combined quantum system $S + E$, where E represents the environment to which the open system S is coupled. Following the main assumption of the basic theory of open quantum systems [3], the environment is assumed to be a large system with an infinite number of degrees of freedom. The interaction of the open system S with the environment causes an irreversible behavior of the open system S and leads to decoherence (randomization of phases) and dissipation of energy into the surroundings.

The dynamics of open systems in the case of Markov processes can be described by a quantum Markovian master equation in Lindblad form [3]:

$$\frac{\partial \rho^S(t)}{\partial t} = -\frac{i}{\hbar}\left[H, \rho^S(t)\right] - D[\rho^S(t)] \qquad (1)$$

where $\rho^s(t)$ is the reduced density matrix of the system S, and $D[\rho^s(t)]$ is the so-called dissipator:

$$D[\rho^S] = \frac{1}{2}\sum_\alpha \left(L_\alpha^\dagger L_\alpha \rho^S + \rho^S L_\alpha^\dagger L_\alpha - 2L_\alpha \rho^S L_\alpha^\dagger\right) \qquad (2)$$

Summation over α extends over all processes of coupling with the environment. The dissipator $D[\rho^s]$ describes the environmental influence on the system. The `jump' operators L_k describe a random evolution of the system which suddenly (at the time scale of the evolution) changes under the influence of the environment.

The first term on the right-hand side describes of eq. (1) the unitary evolution of the system S under the action of a Hamiltonian H.

3.2 Two-level system plasmonic system S_l

The simplest quantum system is a two-level system whose Hilbert space is spanned by two states, an excited state $|l>$ and a ground state $|0>$. The system S is then a sum of S_l of independent, open subsystems: $S = \sum_{l=1,2..} S_l$. Such description is a good approximation for many level systems, provided that the transitions to other than the ground state levels can be neglected so there is no coupling between the modes. Each system S_l is coupled to the environment independently. and all assumptions about the coupling of the S to the environment remain fulfilled for subsystems S_l. The form of the Lindblad equation guarantees, that also dynamics of each matrix operator $\rho^{S_l}(t)$, $\rho^S(t) = \sum_l \rho^{S_l}(t)$ is governed by the equation in the Lindblad form.

The Hamiltonian of a two-level system H_l, $H = \sum_l H_l$. Quantum properties of the cavity mode l are carried by the annihilation a_l and creation a_l^+ mode "amplitudes" (annihilation and creation operators of photons), which satisfy: $[a_l, a_l^+] = a_l a_l^+ - a_l a_l^+ = 1$. The Hamiltonian of the mode l: $H_F = 1/2\hbar\omega_l(a_l a_l^+ + a_l a_l^+) = \hbar\omega_l(a_l a_l^+ + 1/2)$. Dropping the zero-point energy $\hbar\omega/2$ from the Hamiltonian by redefining the zero of energy, we introduce the Hamiltonian H_l for the plasmonic QA in the form: $H_l = \hbar\omega_l\sigma_+\sigma_-$, where and σ_- and σ_+ and are the energy lowering (resulting in photon creation) and energy rising operators (resulting in photon annihilation) in the PQP system).

3.3 Dissipative processes

An excited plasmon, similarly as an excited atom, decays to the state of lower energy spontaneously emitting a photon. In the theory of open quantum systems, such decay is assumed to be due to the coupling of the system to the environment, which introduces radiative losses due to the spontaneous decay (coupling to the EM vacuum fluctuating fields) and heat losses due to the inevitable collisions of electrons in a metal (coupling to a heat-bath in a thermal equilibrium state with an infinite number of degrees of freedom). Dynamics of both coupling processes is assumed to be much faster than those of the open system S_l, so the dynamics of S_l (andthose of S) is Markovian. The jump operators describing these processes are:

$$L_{s,l} = \sqrt{\Gamma_l^s}\sigma_-, \quad L_{col,l} = \sqrt{\Gamma_l^{col}}\sigma_- \qquad (3)$$

where $\Gamma_l^s = \Gamma_l^r$ is the rate of radiative, spontaneous decay and $\Gamma_l^{col} = \Gamma_l^{nr}$ is the rate of nonraditive, collisional losses resulting in absorption and heat production.

3.4 Free evolution of populations and coherences

After algebra involving 2x2 matrices, the Lindblad master equation including radiative and nonradiative dissipation processes one can find the evolution of populations of the excited end ground state $\rho_{ll}(t), \rho_{00}(t)$ and of coherences $\rho_{l0}(t) = \rho_{00}^*(t)$ in the form:

$$\begin{aligned}
\rho_{ll}(t) &= \rho_{ll}(t_0)\exp\left(-\Gamma_l(t-t_0)\right), \\
\rho_{00}(t) &= \rho_{ll}(t_0)\left(1-\exp\left(-\Gamma_l(t-t_0)\right)\right) + \rho_{00}(t_0), \\
\rho_{0l}(t) &= \rho_{0l}(t_0)\exp\left(-i\omega_l - \Gamma_l/2)(t-t_0)\right), \\
\rho_{l0}(t) &= \rho_{l0}(t_0)\exp\left(i\omega_l - \Gamma_l/2\right)(t-t_0).
\end{aligned} \qquad (4)$$

where $\Gamma_l = \Gamma_l^r + \Gamma_l^{nr}$.

3.5 Conclusions:

The dephasing of coherences: $\Gamma_l^{coh} = 1/2\Gamma_l$ is twice as slower as damping of populations: $\Gamma_l^{pop} = \Gamma_l$.

The rates of population damping Γ_l^{pop} and Γ_l^{coh} depend on the size of a MNP. For gold and silver nanoparticles these rates can be accessed from our classical model based on the dispersion relation considerations [4]. In gold MNP of several nanometers the damping rates Γ_l^{pop} and Γ_l^{coh} are larger than those in silver, however in larger MNPs of tens of nanometers this relation changes.

4 References

[1] Kolwas, K.; Derkachova, A.; Shopa, M., Size characteristics of surface plasmons and their manifestation in scattering properties of metal particles. JQSRT, 110, 1490–1501 (2009)

[2] Kolwas, K., Decay Dynamics of Localized Surface Plasmons: Damping of Coherences and Populations of the Oscillatory Plasmon Modes, Plasmonics 14, 1629–1637 (2019)

[3] H. P. Breuer,. F.Petruccione, The theory of open quantum systems (Oxford University Press on Demand, 2002

[4] Kolwas, K., & Derkachova, A. Impact of the interband transitions in gold and silver on the dynamics of propagating and localized surface plasmons. Nanomaterials, 10(7), 1411 (2020)

AUTHORS INDEX